Technical Report Documentation Page

1. Report No. FHWA/TX-08/0-4829-1	2. Government Accession No.	3. Recipient's Catalog No.
4. Title and Subtitle Validating Mechanisms in Geosynthetic Reinforced Pavements		5. Report Date February 2008 6. Performing Organization Code
7. Author(s) Dr. J.G. Zornberg, Dr. J. Prozzi, Ranjiv Gupta, Dr. Rong Luo, Dr. J.S. McCartney, J.Z. Ferreira, Dr. C. Nogueira		8. Performing Organization Report No. 0-4829-1
9. Performing Organization Name and Address Center for Transportation Research The University of Texas at Austin 3208 Red River, Suite 200 Austin, TX 78705-2650		10. Work Unit No. (TRAIS) 11. Contract or Grant No. 0-4829
12. Sponsoring Agency Name and Address Texas Department of Transportation Research and Technology Implementation Office P.O. Box 5080 Austin, TX 78763-5080		13. Type of Report and Period Covered Technical Report September 2004–August 2007 14. Sponsoring Agency Code

15. Supplementary Notes
Project performed in cooperation with the Texas Department of Transportation and the Federal Highway Administration.
Project Title: Quantify the Benefits of Using Geosynthetics for Unbound Base Course

16. Abstract

Base reinforcement results from the addition of a geosynthetic at the bottom of or within a base course to increase the structural or load-carrying capacity of a pavement system. While there is clear evidence that geosynthetic reinforcements can lead to improved pavement performance, the identification and quantification of the parameters that contribute to such improvement has remained, at best, unclear. In addition, pavement structures deteriorate under the combined effects of traffic loading and environmental conditions such as moisture changes. The effect of moisture changes can be particularly detrimental in many locations of Texas, which are characterized by the presence of expansive clays. Consequently, this research focused on the assessment of the effect of geosynthetics on the pavement structural section and on its resistance to environmental changes.

It is well documented that the use of geosynthetics for unbound base courses can lead to improved performance and reduced costs in pavement systems. However, appropriate selection of geosynthetics is compromised by the difficulty in associating their relevant properties to pavement performance. Accordingly, important objectives of this research included: (i) determining the properties of geosynthetics that contribute to enhance the performance of pavement systems, and (ii) developing material specifications that incorporate the geosynthetic and soil properties that govern the pavement performance.

17. Key Words Geosynthetics, geogrids, geotextiles, reinforcement, soil-geosynthetic interaction, pavements, unbound base course, pullout test, confinement, stiffness	18. Distribution Statement No restrictions. This document is available to the public through the National Technical Information Service, Springfield, Virginia 22161; www.ntis.gov.

19. Security Classif. (of report) Unclassified	20. Security Classif. (of this page) Unclassified	21. No. of pages 268	22. Price

Form DOT F 1700.7 (8-72) Reproduction of completed page authorized

Validating Mechanisms in Geosynthetic Reinforced Pavements

Dr. J.G. Zornberg
Dr. J. Prozzi
Ranjiv Gupta
Dr. R. Luo
Dr. J.S. McCartney
J.Z. Ferreira
Dr. C. Nogueira

CTR Technical Report:	0-4829-1
Report Date:	February 2008
Project:	0-4829
Project Title:	Quantify the Benefits of Using Geosynthetics for Unbound Base Courses
Sponsoring Agency:	Texas Department of Transportation
Performing Agency:	Center for Transportation Research at The University of Texas at Austin

Project performed in cooperation with the Texas Department of Transportation and the Federal Highway Administration.

Center for Transportation Research
The University of Texas at Austin
3208 Red River
Austin, TX 78705

www.utexas.edu/research/ctr

Disclaimers

Author's Disclaimer: The contents of this report reflect the views of the authors, who are responsible for the facts and the accuracy of the data presented herein. The contents do not necessarily reflect the official view or policies of the Federal Highway Administration or the Texas Department of Transportation (TxDOT). This report does not constitute a standard, specification, or regulation.

Patent Disclaimer: There was no invention or discovery conceived or first actually reduced to practice in the course of or under this contract, including any art, method, process, machine manufacture, design or composition of matter, or any new useful improvement thereof, or any variety of plant, which is or may be patentable under the patent laws of the United States of America or any foreign country.

Notice: The United States Government and the State of Texas do not endorse products or manufacturers. If trade or manufacturers' names appear herein, it is solely because they are considered essential to the object of this report.

Engineering Disclaimer

NOT INTENDED FOR CONSTRUCTION, BIDDING, OR PERMIT PURPOSES.

Project Engineer: Darlene C. Goehl
Professional Engineer License State and Number: Texas No. 80195
P. E. Designation: Project Director

Acknowledgments

The authors express appreciation to TxDOT Project Director Darlene C. Goehl, members of the Project Monitoring Committee, and the district personnel who participated in the survey.

Table of Contents

List of Figures

List of Tables

Chapter 1. Introduction

1.1 Background

The use of geosynthetics has led to significant advances in pavement design but the proliferation of geosynthetic products and aggressive marketing from geosynthetic manufacturers has made it difficult for Texas Department of Transportation (TxDOT) personnel to quantify the geosynthetic benefits and the variables governing their design. In addition, pavement structures deteriorate under the combined effects of traffic loading and environmental conditions such as moisture changes. The effect of moisture changes can be particularly detrimental in many locations of Texas, which are characterized by the presence of expansive clays. Consequently, this research focused on the assessment of the effect of geosynthetics on the pavement structural section and its resistance to environmental changes. Further, a careful reevaluation of current design methodologies indicated little, if any, quantitative performance evaluation data is available on the response of geosynthetic-reinforced pavement sections constructed in most states including Texas. Accordingly, the overall goal of this research is to identify the material properties governing the design of geosynthetic-reinforced pavements and to develop appropriate material specifications. This project includes a number of research components, as follows:

i. Experimental, including determination of unconfined and in-soil properties of geosynthetics, particularly under low strains;

ii. Field monitoring, including visual inspection and dynamic testing of 32 test sections having three different geosynthetics and with lime and without lime treatment;

iii. Analytical, including modeling of longitudinal cracks caused due to moisture migration in the pavement and use of geosynthetics to prevent it.

1.2 Use of geosynthetic reinforcement to support loads in pavements

The load or stresses that the flexible pavements have to resist during their lifetime can be divided into two main categories: (i) due to traffic, and (ii) due to environmental factors. The loads due to traffic induce stresses in pavement that are complex in nature, as they are cyclic and occur for short duration. For simplicity, traffic is modeled as a vertical load that reduces in intensity with the increase of depth from the top of the pavement. Further, the repeated traffic loading causes accumulation of the stresses in the pavement leading to its permanent deformation. There are three critical points of stress within the pavement. Kerkhoven and Dormon (1953) first suggested the use of vertical compressive strain on the surface of subgrade as a failure criterion to reduce permanent deformation; Saal and Pell (1960) recommended the use of horizontal tensile strain at the bottom of asphalt layer to minimize fatigue cracking. The use of vertical compressive strain to control permanent deformation is based on the fact that plastic strains are proportional to elastic strains in paving materials. Thus, by limiting the elastic strains on the subgrade, the elastic strains in other components above the subgrade will also be controlled; hence, the magnitude of permanent deformation on the pavement surface will be controlled in turn. If the subgrade is weak and unable to resist this load, the top layers of

pavement need to be made rigid by increasing their thickness. The best strategy would be to strengthen the top layer to minimize the load transfer to the bottom. But asphalt and base course are expensive materials. In such a case, the geosynthetic can be used as additional reinforcement material to resist these loads and prevent growth of interface shear stresses, which may cause permanent deformation of the pavement.

The loads due to environmental factors primarily occur due to variation of moisture in the subgrade below the pavement. The seasonal variation of temperature and rainfall at a site can lead to change in subgrade moisture. Further, the edges of the pavement are prone to moisture variation as compared to the center of the pavement, which tends to remain at constant moisture or as compacted moisture level. If the subgrade below the pavement is expansive in nature, the soil would shrink and swell with the moisture variation causing additional stress on the pavement surface. The primary result of this moisture variation below the pavement is the formation of longitudinal cracks that are found predominantly on the edges of the pavement. To remedy this situation, some measures that have been suggested are lime or cement treatment of the soil, construction of trenches along the edge of pavement, and providing proper drainage to avoid ponding of the rainwater. Recently, the geosynthetics have been also used successfully along with lime treatment of the pavement to prevent the propagation of the micro cracks upward from the subgrade.

Even after appropriate consideration for the above loads, it is necessary to account for installation damage of the geosynthetics when they are used in pavement construction. The best approach is to implement good construction quality control. However, this is not always implemented and leads to different performance than expected based on the laboratory test results. Therefore, to completely understand the behavior of geosynthetic reinforced pavements, one not only needs to understand the loading conditions and the theoretical basis for underlying mechanisms but also needs to develop an appreciation for the effect of installation and construction conditions in the field on soil-geosynthetic interaction to fully quantify their performance.

1.3 Research objectives

The specific objectives of this study are to:

- Review current reinforced pavement design methodologies, with particular emphasis on their suitability for conditions typical of TxDOT pavements and Texas materials and environmental conditions
- Conduct an information survey summarizing the experience gained by TxDOT to date with the use of geosynthetic reinforcement in pavement systems
- Quantify the structural conditions of in-situ pavement sections constructed by TxDOT in order to identify the variables responsible for observed differential pavement performance
- Use the information collected in this study to validate existing methodologies or to develop a new methodology for the design of geosynthetic reinforced base courses
- Establish testing procedures and specifications based on quantification of soil-geosynthetic interaction under low strains

- Translate the finding of this research into construction and material guidelines suitable to TxDOT needs

1.4 Report outline

A review of the type of geosynthetics used in this research study along with their relevant properties is presented in Chapter 2. This section further discusses the governing mechanisms of geosynthetics in pavements and the field testing equipment required to measure the structural capacity of pavements. The survey conducted to document experience within the various TxDOT districts regarding geosynthetic reinforced pavement design is presented in Chapter 3. This chapter also explains the details of FM 2 road in Bryan district, which was the location of a field study involving 32 test sections. The geotechnical properties of soils along with the index and wide width tensile strength of geosynthetics used in this study are presented in Chapter 4. The details of equipment used for field testing, i.e., falling weight deflectometer (FWD) and rolling dynamic deflectometer (RDD) are presented in Chapter 5. Analysis of seasonal testing results obtained using these equipment in the test sections is also illustrated. Chapter 6 explains the mechanism of crack propagation in the pavement and numerical model used to understand the phenomenon. The moisture monitoring equipment used and results obtained from the data obtained is documented in Chapter 7. A review of current test specifications and guidelines for the suggested test are presented in Chapter 8. Chapter 9 presents a new test procedure, which is recommended to quantify soil-geosynthetic interaction in expeditious manner. Chapter 10 provides the conclusions from the current study and Chapter 11 recommends the direction in which further research should be conducted based on the current study. This report also includes a number of appendices, as follows: condition survey (Appendix A) and the pullout testing results (Appendix B).

Chapter 2. Background and Information Survey

2.1 Introduction

Base reinforcement results from the addition of a geosynthetic at the bottom or within a base course to increase the structural or load-carrying capacity of a pavement system. While there is clear evidence that geosynthetic reinforcements can lead to improved pavement performance, the identification and quantification of the parameters that contribute to such improvement has remained, at best, unclear. In addition, pavement structures deteriorate under the combined effects of traffic loading and environmental conditions such as moisture changes. The effect of moisture changes can be particularly detrimental in many locations of Texas that are characterized by the presence of expansive clays. Consequently, this research focused on the assessment of the effect of geosynthetics on the pavement structural section and on its resistance to environmental changes. To fully understand the significance of the research, an overview is provided herein on three key components of this study: (i) Geosynthetics, (ii) Function of geosynthetics in pavements, and (iii) Laboratory and field quantification of pavement performance. Then, the problems encountered when designing these pavements over expansive soils in Texas is addressed. Finally, a survey of TxDOT projects is presented, which was conducted to obtain the information regarding present state of practice among various districts of Texas. A major focus of this project was to understand and document the experience gained by TxDOT districts on use of geosynthetics in unbound base course of pavements, as this knowledge would provide significant lessons for future design and use. Attempt was made to frame the survey such that it complemented the information collected by review of the current literature on use of geogrid as reinforcement in flexible pavements.

2.2 Geosynthetics

Geosynthetics can be defined as planar products manufactured from polymeric material, which are used with soil, rock, or other geotechnical-engineering-related material as an integral part of a synthetic project, structure, or system (ASTM, 1995). Geosynthetics are widely used in many geotechnical and transportation applications. The geosynthetics market is strong and rapidly increasing due to the continued use of geosynthetics in well-established applications and, particularly, due to the increasing number of new applications that make use of these products. The strength of the geosynthetics market can be appreciated by evaluating the growth in the estimated amount of geosynthetics in North America over the years. The Industrial Fabrics Association International has estimated that approximately 734 million m^2 of materials were shipped in 2001 (Zornberg and Christopher, 1999).

Geosynthetics have numerous material properties. Many of the reported properties are important in the manufacture and quality control of geosynthetics; however, many others are also important in design. The material properties related to the manufacture and quality control of geosynthetics are generally referred to as index properties and those related to the design as design or performance properties. Considering their different properties, the several geosynthetic products can perform different functions and, consequently, they should be designed in order to satisfy minimum criteria to adequately perform these functions. The geosynthetic functions are separation, reinforcement, filtration, drainage, infiltration barrier, and protection.

Geosynthetics are manufactured in a factory-controlled environment. They are packaged in sheets, placed in a roll or carton, and finally transported to the site. At the project site the geosynthetic sheets are unrolled on the prepared surface, overlapped with each other to form a continuous geosynthetic blanket, and often physically joined to each other. The geosynthetic types are geotextiles, geomembranes, geogrids, geosynthetic clay liners (GCLs), geocomposite sheet drains, geocomposite strip (wick) drains, geocells, and erosion control products. While both geotextiles and geogrids have been used in pavement applications, the focus of this TxDOT study centers on the use of geogrids, as they have been the primary product used in projects involving pavements over subgrade soils sensitive to volumetric changes (i.e., heaving and shrinkage of soils).

2.2.1 Geogrids

Geogrids constitute a category of geosynthetics designed preliminary to fulfill a reinforcement function. They have found numerous applications in transportation projects (Zornberg and Christopher, 2000; Zornberg et al. 2001). Geogrids have a uniformly distributed array of apertures between their longitudinal and transverse elements. The apertures allow direct contact between soil particles on either side of the installed sheet, thereby increasing the interaction between the geogrid and the backfill soil.

Geogrids are composed of polypropylene, polyethylene, polyester, or coated polyester. The polyester geogrids and coated polyester geogrids are flexible, and typically woven or knitted. Coating is generally performed using PVC or acrylics to protect the filaments from construction damage. The polypropylene and polyethylene geogrids are rigid, and either extruded or punched sheet drawn. Figure 2.1 shows a number of typical geogrid products in the U.S. market.

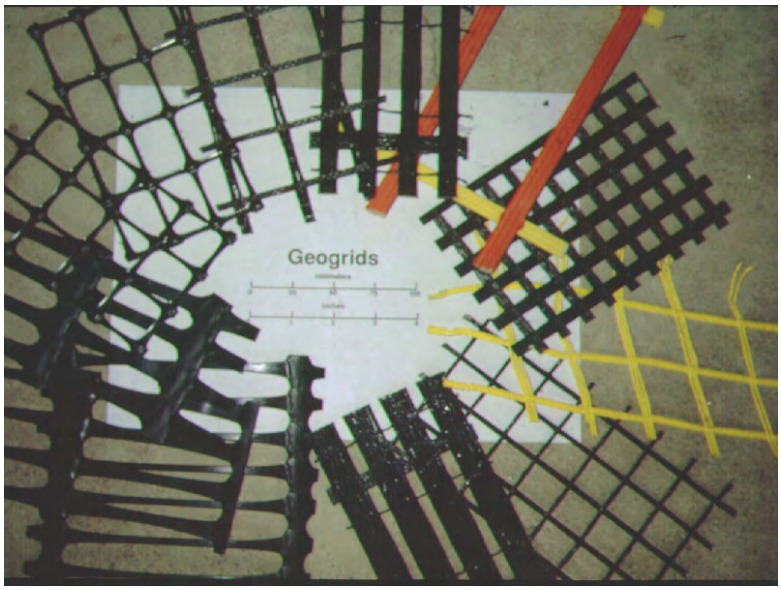

Figure 2.1: Geogrid Reinforcement Rigid geogrids are shown on the left side and flexible geogrids are shown on the right

2.2.2 Geotextiles

A geotextile is defined as a permeable geosynthetic made of textile materials. Among the different geosynthetic products, geotextiles are the ones that present the widest range of properties (Zornberg and Christopher 2006) and can be used to fulfill variety of functions for many different geotechnical, and transportation applications.

The polymers used in the manufacture of geotextile fibers include the following, listed in order of decreasing use: polypropylene (≈85%), polyester (≈12%), polyethylene (≈2%), and polyamide (≈1%). The most common types of filaments used in the manufacture of geotextiles include monofilament, multifilament, staple filament, and slit-film. If fibers are twisted or spun together, they are known as a yarn. The filaments, fibers, or yarns are formed into geotextiles using either woven or non-woven methods. Figure 2.2 shows a number of typical geotextiles. Woven geotextiles are manufactured using traditional weaving methods and a variety of weave types: plain weave, basket weave, twill weave, and satin weave. Non-woven geotextiles are manufactured by placing and orienting the filaments or fibers onto a conveyor belt, which are subsequently bonded by needle punching or by melt bonding.

Common terminology associated with geotextiles includes machine direction, cross machine direction, and selvage. Machine direction refers to the direction in the plane of the fabric in line with the direction of manufacture. Conversely, cross machine direction refers to the direction in the plane of fabric perpendicular to the direction of manufacture. The selvage is the finished area on the sides of the geotextile width that prevents the yarns from unraveling.

Figure 2.2: View of different types of geotextiles

2.3 Function of geosynthetics for pavements

Base reinforcement results from the addition of a geosynthetic at the bottom or within a base-course to increase the structural or load-carrying capacity of a pavement system by the transfer of load to the geosynthetic material. The two main benefits of the reinforcement are to (1) improve the service life and/or (2) obtain equivalent performance with a reduced structural

section. Base reinforcement could also be thought to provide a safety factor on the pavement load-carrying capacity, or weaker subgrade from design values or inaccuracies in the pavement design methodology. The primary mechanism associated with this application is lateral restraint or confinement (Holtz et al. 1998). The functions of geosynthetics in roadways include (Koerner 1998):

- Reinforcement: the addition of structural or load-carrying capacity to a pavement system by the transfer of load to the geosynthetic material.
- Separation: prevention of subgrade soil intruding into aggregate base (or sub-base), and prevention of aggregate base (or sub-base) migrating into the subgrade.
- Filtration: restricting the movement of soil particles, while allowing water to move from the filtered soil to the coarser soil adjacent to it during the performance life of the structure.
- Lateral Drainage (i.e., transmission): the lateral movement of water within the plane of the geosynthetic.

However, a certain geosynthetic product can perform different functions and similarly, the same function can often be performed by different types of geosynthetics. The geogrids generally have only one primary function of reinforcement in pavement design. In addition to this primary function, geotextiles can perform one or more secondary functions, which must also be considered when selecting the geotextile material for optimum performance. For example, a geotextile can provide separation of two dissimilar soils (e.g., gravel from clay in a road), but it may also provide filtration as a secondary function by minimizing the buildup of excess pore water pressure in the soil beneath the separator. A brief overview of specific functions performed by geogrids and geotextiles in pavement applications is given in next section. The improvement to the pavement system provided by geosynthetic reinforcement has been measured by a TBR or BCR ratio:

- TBR (Traffic benefit ratio): A ratio of the number of load cycles on a reinforced section to reach a defined failure state to the number of load cycles on an unreinforced section, with the same geometry and material constituents, to reach the same defined failure state. TBR is sometimes termed traffic improvement factor (TIF).
- BCR (Base course reduction): The percent reduction in the reinforced base, or sub-base, thickness from the unreinforced thickness, with the same material constituents, to reach the same defined failure state.

These ratios are specific to the product, material, geometry, failure criteria, and load used in the tests to quantify their values. Therefore, TxDOT must assess the applicability of these proposed ratios to project-specific materials, geometry, failure (or rehabilitation) criteria, and loading. Although research conducted to date has supported some of the design procedures, long-term performance information of projects based on these procedures is not available at this time such that confidence limits can be established. Therefore, an important goal of this project is to evaluate whether TxDOT should consider the use of reinforcements to improve the service life of pavement structures, or to go a beyond this initial step and use them to justify reducing the pavement structural section.

2.3.1 Reinforcement

Reinforcement is the synergistic improvement in the pavement strength created by the introduction of a geosynthetic into a pavement layer. While the function of reinforcement in the US has often been fulfilled by geogrids, geotextiles have been used extensively as reinforcement inclusions, particularly overseas, in transportation applications (Bueno et al. 2005a; Benjamin et al. 2007).

2.3.1.1 Mechanisms involved

The reinforcement function is developed primarily through the following three mechanisms (Holtz et al. 1998):

i. Lateral restraint through interfacial friction between geosynthetic and soil/aggregate. When an aggregate layer is subjected to traffic loading, the aggregate tends to move laterally unless it is restrained by the subgrade or geosynthetic reinforcement. Soft, weak subgrade soils provide very little lateral restraint, so ruts develop when the aggregate moves laterally. Interaction between the base aggregate layer and the geosynthetic transfers shear load from the base layer to a tensile load in the geosynthetic (Perkins and Ismeik, 1998).The geosynthetic being stiff in tension, limits the extensional lateral strains in the base layer. Further, a geosynthetic layer confines the base course layer thereby increasing its mean stress and leading to increase in its stiffness and shear strength. Both frictional and interlocking characteristics between the soil and geosynthetic are necessary to realize this mechanism. For a geogrid, this implies that the geogrid apertures and base soil particles must be sized properly. A geotextile with good frictional capabilities can provide tensile resistance to lateral aggregate movement (Figure 2.3a).

ii. Increased bearing capacity, i.e., by forcing the potential bearing surface failure plane to develop at alternate higher shear strength surface (Figure 2.3b).

iii. Membrane type of support of the wheel loads (Figure 2.3c). This tensioned membrane effect develops as a result of vertical deformations creating a concave shape in the geosynthetic. The tension developed in the geosynthetic helps support the wheel load and reduce the vertical stress on the subgrade, but significant rut depths are necessary to realize this effect.

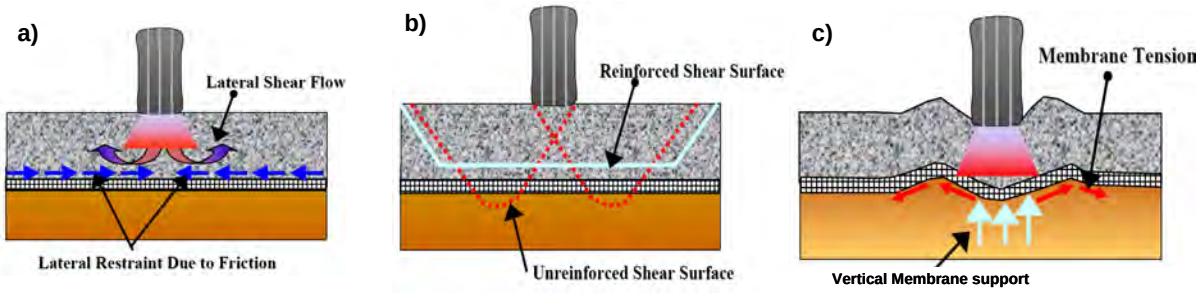

Figure 2.3: Reinforcement mechanisms induced by a geotextile used for base reinforcement: (a) Lateral restraint, (b) Increased bearing capacity, (c) Membrane-type support

2.3.2 Separation

Separation is the introduction of a flexible porous textile placed between dissimilar materials so that the integrity and the functioning of both the materials can remain intact or be improved (Koerner 2005). In pavement applications, separation refers to the geotextiles role in preventing the intermixing of two adjacent layers. For example, a major cause of failure of roadways constructed over soft foundations is contamination of the aggregate base course with the underlying soft subgrade soil as shown. A geotextile can be placed between the aggregate and the subgrade to act as a separator and prevent the subgrade and aggregate base course from mixing (Figure 2.4).

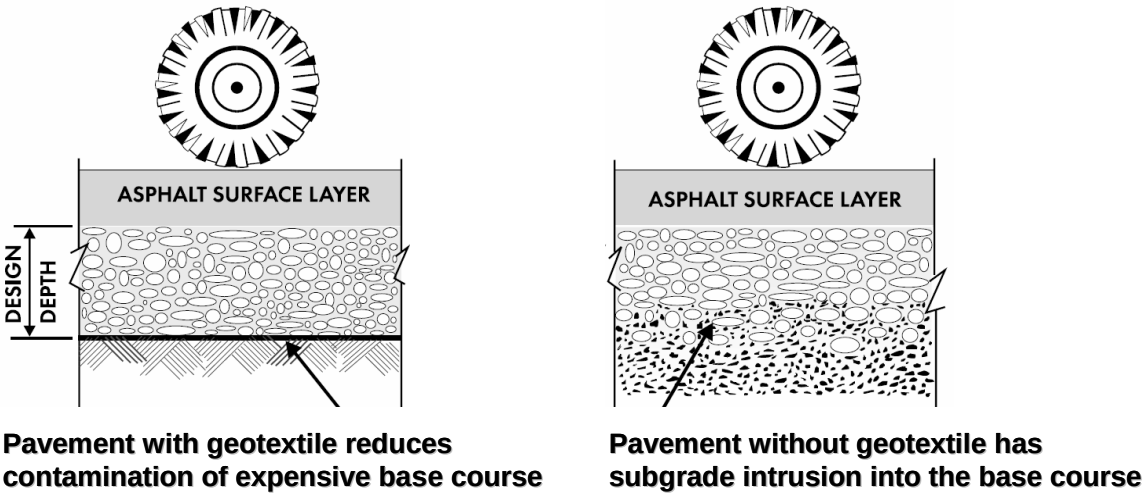

Figure 2.4: Separation function of a geotextile placed between the base aggregate and a soft subgrade

2.3.3 Filtration

Filtration is defined as the equilibrium geotextile-to-soil system that allows for adequate liquid flow with limited soil loss across the plane of the geotextile over a service lifetime

compatible with the application under consideration (Koerner, 2005). A common application illustrating the filtration function is the use of a geotextile in a pavement edge drain as shown in Figure 2.5. The geosynthetic-soil system should achieve an equilibrium that allows for adequate liquid flow under consideration. As the flow of liquid is perpendicular to the plane of the geosynthetic, filtration refers to the cross plane hydraulic conductivity or permittivity, which is defined as:

$$\psi = k_n / t$$

ψ is the permittivity, k_n is the cross-plane hydraulic conductivity, and t is the geotextile thickness at a specified normal pressure. The other important property for soil retention design using geotextiles is to compare the soil particle size characteristics to the 95% opening size of the geotextile (apparent opening size, AOS). The coarser sized particles eventually create a filter bridge that in turn retains the finer-sized particles, building up a stable upstream soil structure.

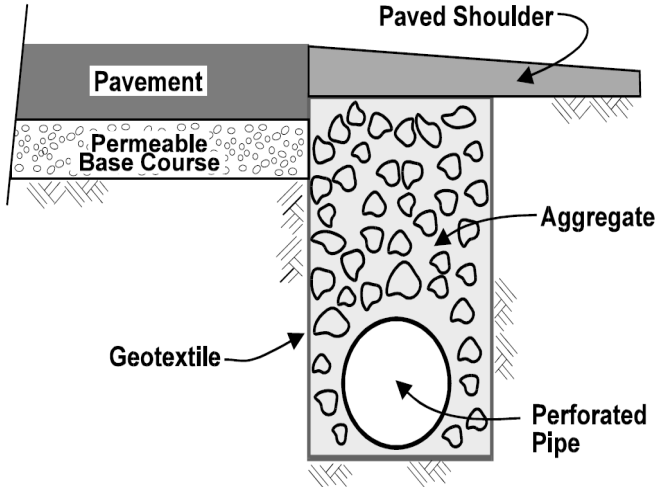

Figure 2.5: Filtration function provided by geotextile

2.3.4 Lateral Drainage

Drainage refers to the ability of geotextiles (typically thick nonwoven geotextiles) to provide an avenue for flow of water through the plane of the geotextile. As the geotextile thickness decreases with increasing normal stress, the in plane drainage of a geosynthetic is generally quantified by its transmissivity, which is defined as:

$$\theta = k_p t$$

θ is the transmissivity, k_p is the in plane hydraulic conductivity, and t is the geotextile thickness at a specified normal pressure.

2.3.5 Other Functions

Mitigation of crack propagation function (and sealing as secondary function) can be performed by a nonwoven geotextile when used in the overlay of the pavement. The asphalt layer is subjected to thermal cracking (due to environmental stresses) and reflection cracking (due to load-induced stresses). The geotextile acts as a stress relieving interlayer thus dissipating stresses before the crack induces stresses in the overlay. In addition, when a geotextile is impregnated with asphalt or other polymeric mixes it becomes relatively impermeable to both cross-plane and in-plane flow. As shown in Figure 2.6, the nonwoven geotextile can be placed on the existing pavement surface following the application of an asphalt tack coat. The geotextile has been reported not only to prevent cracks in the overlay but also to act as a waterproofing membrane minimizing vertical flow of water into pavement structure.

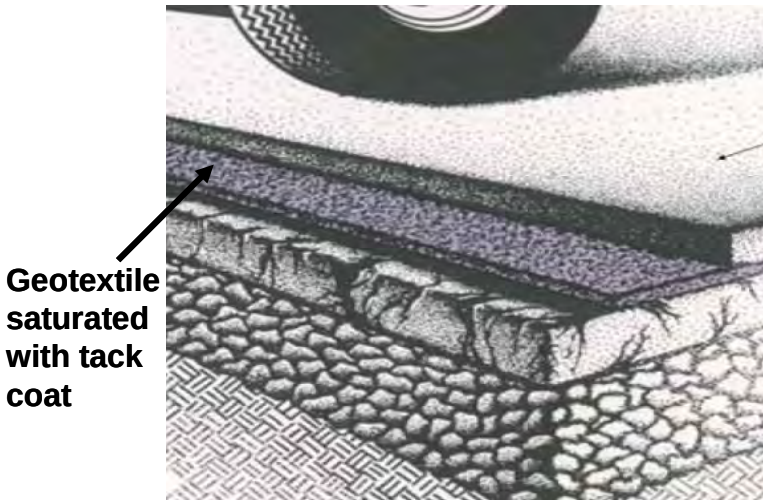

Figure 2.6: Geotextile used for mitigation of crack propagation in pavement overlay

2.4 Laboratory and field quantification of pavement performance

2.4.1 Laboratory Tests

Numerous tests are available to characterize the geosynthetic properties. The geosynthetic properties can be broadly categorized into five main categories, including a) Physical Properties, b) Mechanical Properties, c) Hydraulic Properties, d) Endurance Properties, and e) Degradation Properties. Because both geotextiles and geogrids are used in flexible pavements, the tests required to quantify them are explained.

2.4.1.1 Geotextile properties and test methods

Physical properties of the geotextiles generally serve as an index property and are not generally adopted directly in design. Table 2.1 shows common physical properties and their respective standards.

Table 2.1: Tests used to determine physical properties of geotextiles

Properties	Relevant standards
Specific gravity	ASTM D792 or D 1505
Mass per unit area (weight)	ASTM D5261 or ISO 9864
Thickness	ASTM D5199
Stiffness	ASTM D1388

The mechanical properties quantify the geotextiles' resistance to tensile stresses mobilized from applied loads or installation conditions. Some tests are performed with the geotextile in isolation while other tests are performed under the confinement of soil (often called performance tests). Table 2.2 summarizes tests available for quantification of mechanical properties of geotextiles.

Table 2.2: Tests used to determine mechanical properties of geotextiles

Tensile strength	Tear tests	Frictional behavior	Impact tests	Other tests
Grab tensile strength ASTM D4632	Trapezoidal test ASTM D4533	Direct shear device	Burst strength ASTM D3786	Compressibility
Narrow strip ASTM D751	Tongue tear test ASTM D751	Pullout device	Puncture tests	Fatigue strength
Wide width ASTM D 4595	Elmendorf tear test ASTM D1424			Seam strength
Confined tensile strength				

The tests required to determine *hydraulic, endurance and degradation properties* of geotextiles are summarized in Table 2.3. A number of tests are available for each one of these categories. The hydraulic response of geotextiles under unsaturated conditions has been the focus of recent advances (Bouazza et al. 2006). Some recent tests have been developed to accelerate the determination of endurance and degradation properties (e.g., creep) using time-temperature superposition methods (Bueno et al. 2005b; Zornberg et al. 2004).

Table 2.3: Tests used to determine hydraulic, endurance and degradation properties of geotextiles

Hydraulic Properties	Endurance Properties	Degradation Properties
Porosity (nonwoven)	Installation damage	Temperature degradation
Percent open area (woven)	Creep response	Hydrolysis degradation
Apparent opening size	Confined creep response	Chemical degradation Oxidative degradation
Permittivity	Stress relaxation	Radioactive degradation
Permittivity under load	Abrasion	Biological degradation
Transmissivity	Long-term clogging	Sunlight (UV)
Soil retention	Gradient ratio clogging	Synergistic effects
	Hydraulic conductivity ratio	General aging

2.4.1.2 Geogrid properties and test methods

In comparison to geotextiles, the geogrids are specifically used for reinforcement purposes in pavement. The test methods involved to quantify properties of geogrids in laboratory are listed in Table 2.4. Further discussion on these tests and their implication to pavement design is discussed in Chapter 8.

Table 2.4: Tests for geogrid properties

Physical Properties	Mechanical properties	Degradation properties
Structure	Single Rib test	Temperature effects
Junction type	Junction Strength	Oxidation effects
Aperture size	Wide width tensile strength	Hydrolysis effects
Thickness	Shear test	Chemical effects
Mass per unit area	Pullout test	Radioactive effects
Flexural rigidity	**Endurance properties**	Biological effects
Stiffness	Installation damage	Sunlight (UV) effects
	Tension-Creep behavior	Stress-crack resistance

2.4.2 Field Quantification of Pavement Performance

Unlike other civil structures, pavements are designed to deteriorate and fail in the field. Failure is expected to occur after the design period is reached, when the pavement condition falls below pre-established performance criteria. This deterioration process is the result of the combined effects of incremental load-associated and environment-related damage (Prozzi and Madanat, 2004). Thus, this research aimed at developing pavement design guidelines that would

account for both aspects, i.e., load-associated and environment-related damage of the pavement in the field. Load-associated response and performance is primarily evaluated by means of in-situ testing of field sections with the Rolling and Stationary Dynamic Deflectometer (RDD) and the Falling Weight Deflectometer (FWD). The potential for environment-related damage is primarily assessed through visual condition assessment, trenching, and monitoring moisture migration below pavement, which is explained in Chapter 7.

2.4.2.1 Rolling Dynamic Deflectometer (RDD)

The RDD was developed as a nondestructive testing (NDT) method for determining continuous deflection profiles of pavements (Bay and Stokoe, 1998; Lee and Stokoe, 2005). A schematic diagram of the RDD is shown in Figure 2.7a. Unlike other commonly used pavement testing methods, the RDD performs continuous rather than discrete deflection measurements. The ability to perform continuous measurements makes RDD testing very effective in quickly characterizing large sections of pavement while simultaneously providing a comprehensive picture of the pavement condition. This unique characteristic makes the equipment ideal for identification and quantification of localized problems such as joints, cracks and other discontinuities even before they can be visually detected at the pavement surface. The RDD was constructed by modifying the electro-hydraulic loading system on a Vibroseis truck. It applies sinusoidal dynamic forces to the pavement through specially designed loading rollers. The resulting deflections are measured by rolling sensors designed to minimize the influence of noise caused by rough pavement surfaces. When the RDD operates in a stationary mode, it becomes a Stationary Dynamic Deflectometer (SDD). A schematic diagram of the SDD is shown in Figure 2.7b. The SDD is a super-accelerated pavement testing device with which hundreds of thousands of load repetitions are applied in a matter of hours, hence, super-accelerated testing. Operated at 30 Hz, it can apply 10 times more load applications than the Texas Load Simulator (TxMLS) and 100 times more than the Heavy Vehicle Simulator (HVS). The load is typically applied dynamically to a steel loading frame, which has three circular steel loading pads (footing) in contact with the pavement surface. The dynamic load is created by a servo-hydraulic actuator, which generates harmonic loading at a pre-selected frequency, typically between 30 and 70 Hz. The load level can be varied significantly from one test to the next, and conditions ranging from moderate to allowable to overload levels can be generated. This footing attached to the loading framework can be custom-designed to simulate the loading configurations that are appropriate to address the specific objectives of each research project.

2.4.2.2 Falling Weight Deflectometer (FWD)

The Falling Weight Deflectometer (FWD) is a trailer-mounted device widely used for the dynamic non-destructive testing on pavement (Huang, 1993). During a field testing, the FWD applies dynamic loading similar to the moving wheel load to the pavement surface. The magnitude and duration of the applied dynamic loading can be controlled by changing the weight of the drop mass, the drop height, and the plate stiffness of the drop weight strikes. The pavement responses due to the FWD dynamic loading are measured in terms of vertical deflections using a number of geophones in a linear array. The deflection data produced by the FWD testing can be used to back-calculate the modulus of each pavement layer when incorporating the thicknesses of pavement layers. The back-calculated moduli may help pavement engineers estimate the bearing capacity of pavements, predict the pavement life, and make a plan for pavement maintenance and rehabilitation.

A number of computer programs have been developed for back-calculating the moduli of pavement layers based on the FWD deflection data. Most of the programs assume that the pavement structures is a multi-layer linear elastic system, such as WESDEF (Huang, 1993), MODULUS (Liu, 2001), EVERCALC (Turkiyyah). Some of these linear elastic programs are handy to use and provide fast estimate of the layer moduli. However, the assumption of linear elastic layers may result in significant errors in the predicted moduli when the subgrade is nonlinear elastic. A typical consequence is that the moduli of surface layer and of the subgrade are overestimated and the modulus of the intermediate layer is underestimated (Ullidtz, 1998). The finite element (FE) programs (such as ABAQUS and ANASYS) are much more powerful and versatile for accurately back-calculating the pavement layer moduli by effectively addressing various characteristics of pavement materials (Ullidtz, 1998). However, typical FE programs require considerable computation time and effort. In addition, a nonlinear model in FE program needs a large number of parameters, which may be hard to determine in practice. Odemark's method (Ullidtz, 1987 and 1998) is an appropriate alternative as this method not only addresses the nonlinearity of subgrade but also provides a fast algorithm. Based on Odemark's method, Gossain and Prozzi (2005) developed a nonlinear elastic program named VG to back-calculate pavement moduli with reduced computation time compared to the FE methods. The nonlinear program can calculate the degree of subgrade nonlinearity as well.

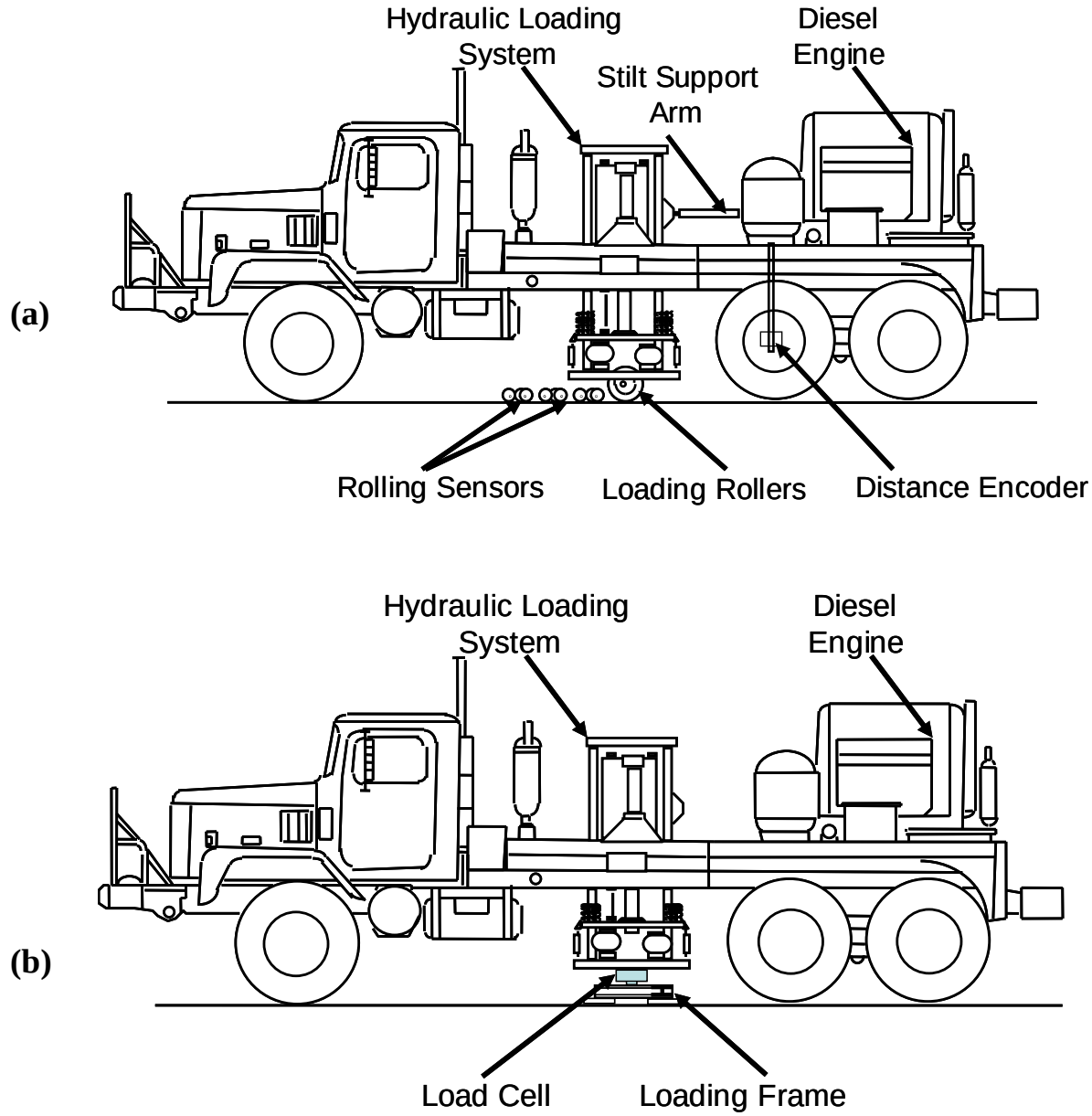

Figure 2.7: Field equipment: (a) Rolling Dynamic Deflectometer; (b) Stationary Dynamic Deflectometer

2.5 Background of expansive soils

Expansive soils are generally defined as soils that experience significant volumetric changes when subjected to moisture variation. Expansive soils are the results of a complex combination of conditions and processes for the parent materials, including basic igneous rocks and sedimentary rocks containing montmorillonite (Chen, 1988). Expansive soils found in the United States are primarily produced by the parent materials in the second category, such as

shales and clay stones. Volcanic ash and glass, which are the constituents of shales and clay stones, can be weathered to montmorillonite, a so-called “swelling clay” accounting for most of the expansive soil problems.

Expansive clay minerals, e.g. montmorillonite, have a large specific surface and carry a large net negative electrical charge that attracts the exchangeable cations (positive ions). These cations include Ca^{2+}, Mg^{2+}, H^{+}, K^{+}, NH_4^{+}, and Na^{+}, all of which are the most common exchangeable cations in clay minerals. The ability of clay to absorb cations from the solution can be quantified by the cation exchange capacity, which is defined as the charge or electrical attraction for cation per unit mass, in milli-equivalent per 100 g of soil. In the three most important groups of clay materials, montmorillonite, illite, and kaolinite, montmorillonite has the largest cation exchange capacity. As a result, expansive soils exhibit significant volume changes with the variation of the amount of present water.

2.5.1 Engineering Problems due to Expansive Soils

Problems associated with expansive soils are common worldwide, as have been reported in the United States, Australia, Canada, China, India, Israel, and South Africa (Chen, 1988). Expansive soils are found in 20 percent of the territory of the United States (Krohn and Slosson, 1980) specifically in Texas, Colorado, and Wyoming. The need to design and construct roadways on highly plastic clays is common in central and eastern Texas, where expansive clays are prevalent. The construction of roadways over highly plastic clay subgrades may lead to significant volume changes during subsequent cycles of wetting and drying. These volume changes induce vertical movements, accelerate the degradation of pavement materials, and ultimately shorten the service life of the roadway.

Climate has a direct effect on amount of shrink and swell experienced by expansive soils. The climate in which there is little annual rainfall—i.e., drier climates like central and west Texas—the soil has an annual soil moisture deficit and the soil swells when wetted. When the potential evapo-transpiration exceeds rainfall, a substantial amount of soil movement occurs around the edges of the pavement. Conversely, in wetter climates, like eastern Texas most structural damage occurs during periods of drought when the soil shrinks. Droughts in Houston (1979) and Dallas (1980) are examples of climate-induced structural damage. In Texas, more than half of the total damage caused by expansive soils occurs on highways and streets, which costs the Texas Department of Transportation (TxDOT) millions of dollars to repair every year (Jayatilaka and Lytton, 1997). Longitudinal cracking on the Farm-to-Market (FM) network is one of the most prevalent pavement distresses due to the volumetric change of the expansive subgrade. This type of “dry-land crack” initiates in the drying subgrade soil and reflects from the highly plastic subgrade through the pavement structure (Sebesta, 2002). Pavement and geotechnical engineers have for many years attempted to eliminate the dry-land cracking resulting from the expansive subgrade. A number of methods have been used to treat expansive soils, which can be grouped into three categories: i) alteration of expansive material by mechanical, chemical or physical means; ii) control of subgrade moisture conditions; and iii) geogrid reinforcement. Lime stabilization is the most extensively used alteration for modifying the expansive soils in the subgrade. The lime treatment thickness can vary from 0.25 m to 1 m. Other commercial stabilizers, for example, Roadbond EN1 and EMC Squared, have also been used for treating the expansive soils (Rajendran and Lytton, 1997). These non-calcium stabilizers have been shown to increase the strength and stiffness of the treated soil, reduce the swelling, decrease the permeability, and moderate the suction. Using vertical barriers is a typical method

for controlling the subgrade moisture conditions. Jayatilaka et al. (1997) found that installing impermeable geomembranes as vertical moisture barriers in pavement sections could reduce the moisture variation in expansive subgrade and then restrain pavement roughness. Also, geogrid reinforcement combined with the lime treatment is another effective method to prevent longitudinal cracking on Farm-to-Market (FM) roads caused by the shrinkage of expansive subgrade. In Texas, the geogrid is placed at the interface of the cement-treated or lime-treated sub-base and a 3 to 4 inch flexible base.

2.6 Survey

The previous sections described the background information regarding various components involved in this research. One of the major focuses of this project was to understand and document the experience gained by TxDOT districts on use of geosynthetics in unbound base course of pavements, as this would provide significant lessons for future design and use. Consequently, a survey of TxDOT projects was conducted to obtain the information regarding present state of practice among various districts of Texas. Attempt was made to frame the survey such that it complemented the information collected by review of the current literature on use of geogrid as reinforcement in flexible pavements.

2.6.1 Survey Form Details

The survey form was made in the form of a one page questionnaire as shown in Figure 2.8. The District engineers associated with the relevant projects were contacted. The survey forms were collected and the information obtained was analyzed. Attempt was made to assess the usage of geosynthetics in weak and expansive subgrade areas of Texas.

2.6.2 Participating TxDOT Districts

The survey response on 35 projects was obtained from 16 TxDOT districts. The participating districts were Fort Worth, Yoakum, Austin, Pharr, Wichita Fall, Lubbock, Beaumont, Abilene, Lufkin, El Paso, Dallas, San Angelo, Atlanta, Bryan, Paris, and Odessa. No response was obtained from TxDOT districts of Childress, Amarillo, San Antonio, Corpus Christi, Houston, Brownwood, Waco, Tyler, and Laredo. The number of projects reported, based on participating county of each district, are shown in Table 2.5.

Table 2.5: Number of projects from each county of participating TxDOT districts

S.NO.	County	District	Projects reported
1.	Fort Worth	Fort Worth	3
2.	Yoakum	Yoakum	1
3.	Williamson	Austin	1
4.	Hidalgo	Pharr	2
5.	Wichita	Wichita Fall	1
6.	Lubbock	Lubbock	1
7.	Jefferson	Beaumont	1
8.	Burnet	Austin	1
9.	Taylor	Abilene	1
10.	Angelina	Lufkin	1
11.	El Paso	El Paso	1
12.	Navarro	Dallas	1
13.	San Angelo	San Angelo	1
14.	Panola	Atlanta	4
15.	Titus	Atlanta	1
16.	Bowie	Atlanta	1
17.	Harrison	Atlanta	2
18.	Walker	Bryan	5
19.	Lamar	Paris	1
20.	Hunt	Paris	1
21.	Grayson	Paris	3
22.	Midland	Odessa	1

TxDOT SURVEY

PROJECT 0-4829: QUANTIFY THE BENEFITS OF USING GEOSYNTHETICS FOR UNBOUND BASE COURSE

PD: Darlene Goehl, Bryan District RS: Jorge Zornberg, CTR

Have you experienced cracking or swelling problems with pavements over high PI clays? ____YES ____NO

Have you experienced problems with weak subgrade? ____YES____NO (If No, skip to item #6)

Have you used geosynthetics as reinforcements in pavements? ____YES ____NO (If No, skip to item #6)

What kind of geosynthetics have you used? _____Geogrid _____Geotextile _____Other

Please provide details on the project/projects where geosynthetics were used? (If more than one project, kindly add details in separate page or table)

Project location:

Approximate length (miles):

Year of construction:

Brand/type of geosynthetics:

Why was this material used? (e.g. as base reinforcement, to span weak subgrade, other)

Additional Information/Comments:

Your Information:

Name: **E-mail:**

Position: **County:**

Tel: **Fax:**

Please e-mail this survey to: **@mail.utexas.edu** Thank you for your time!!

Figure 2.8: Survey form sent to TxDOT districts to assess geosynthetic usage

2.6.3 Analysis of Survey Results

Out of the 35 projects reported in the survey, 30 of the projects had problems due to cracking of pavement over high PI clay (as shown in Figure 2.9[a]) and 33 projects had problems due to pavement over weak subgrade, as shown in Figure 2.9(b). Analyzing the combined response, it was observed that 85% of the pavements had problems due to both of the aforementioned reasons, as shown in Figure 2.9(c). Geosynthetics were used in 26 projects to counteract these problems, and geogrid was the preferred geosynthetics, as shown in Figure 2.9(d). The results obtained from the preliminary survey are compiled in Table 2.6.

Table 2.6: Results obtained for survey conducted with TxDOT

	Cracking problem over pavements with high PI clay	Problems with weak subgrade	Use of geosynthetic over pavements
Yes	88%	94%	73.5%
No	12%	6%	26.5%

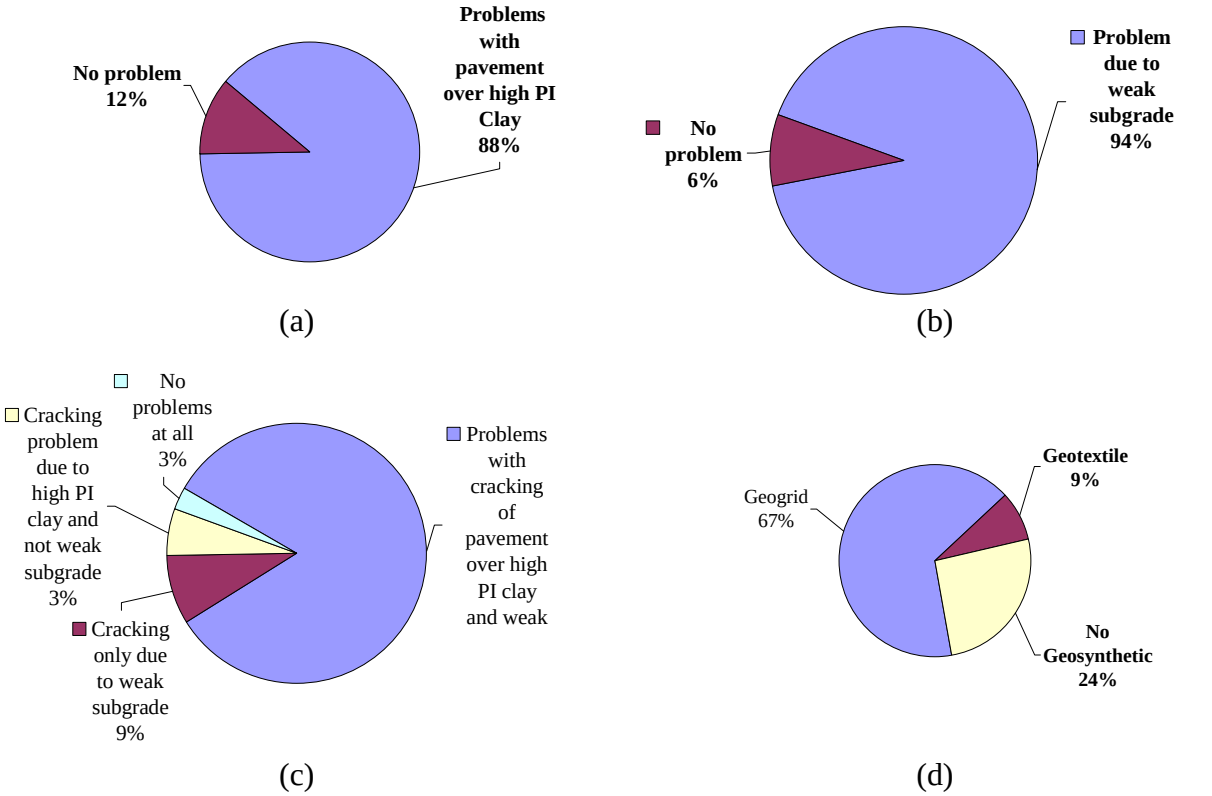

Figure 2.9: Survey results a) pavement sections over high PI clays having cracking problem b) problems with pavement section over weak subgrade c) areas with problem due to pavement over high PI clays and weak subgrade d) usage of various geosynthetics in pavements having problem with weak subgrade and over high PI clays

2.6.4 County Wise Analysis of Survey Responses

The county wise analysis of survey responses obtained was done to determine the status of current usage of geosynthetics throughout TxDOT districts. The results obtained from participating districts are shown in Figure 2.10.

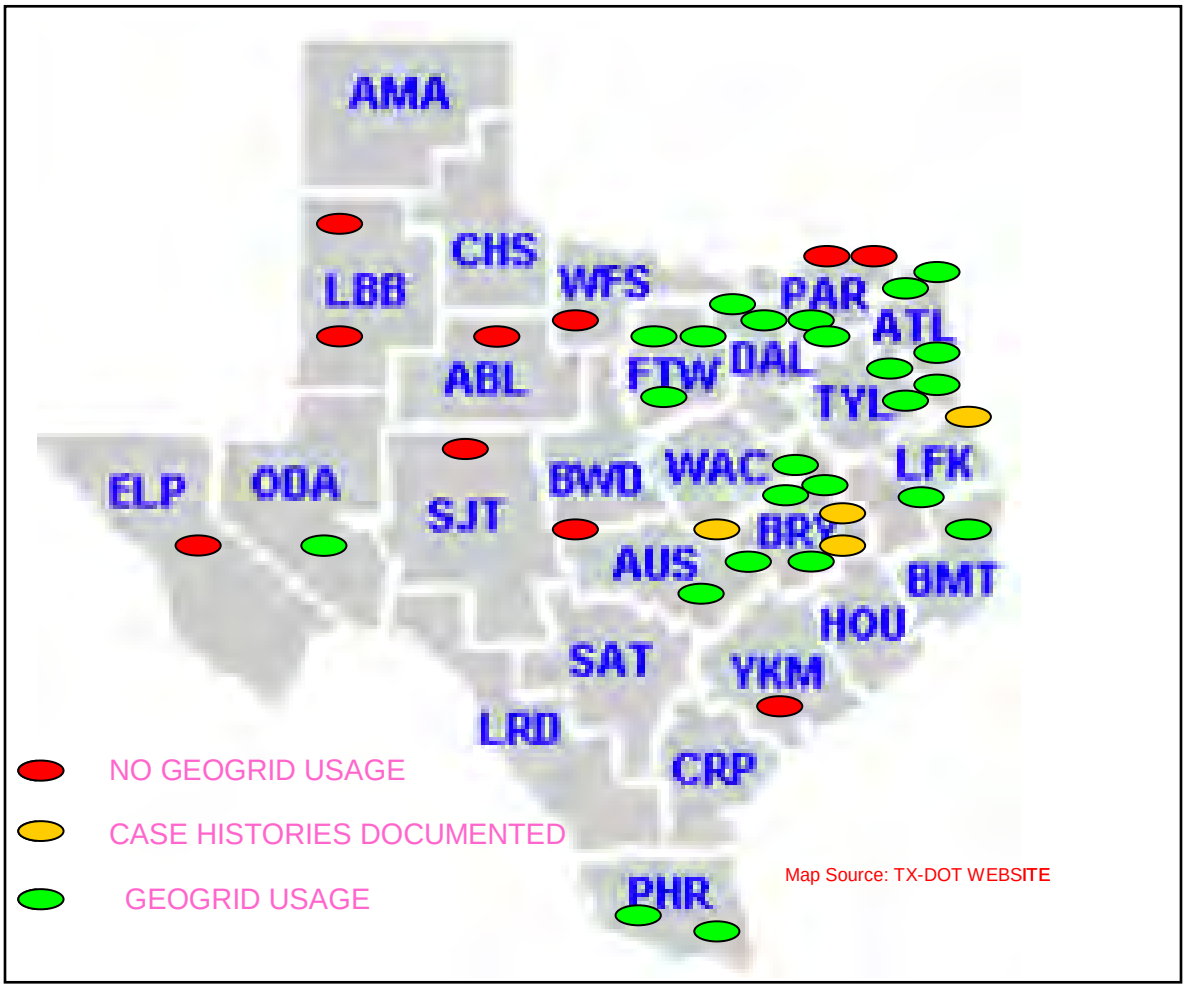

Figure 2.10: Map showing usage of geosynthetics in Texas based on districts that responded to the survey

2.6.4.1 Districts having no geosynthetic reinforcement in pavements

Districts having problems with pavements over high PI clay and weak subgrade—but did not use geosynthetics as reinforcement—were Yoakum, Wichita, Lubbock, Burnet, El Paso, Tom Green, Lamar, and Hunt.

2.6.4.2 Districts having geogrid as reinforcement in pavements

1. Fort Worth

The pavements in this area faced problems with cracking over high PI clays and weak subgrade. They used geogrids to span weak subgrade and provide benefit in reducing the severity of reflective cracking from the subgrade. The three projects executed in 2004-2005 were FM 2331 (4.3 miles), FM 917 (1.4 miles), and FM 157 (2.0 miles). The geogrid used was Tensar geogrid type 2. The pavement structure for the Johnson County section was 2”ACP, seal coat, 8” cement stabilized base and geogrid beneath the base. The FM 2331 section is between FM 4 and

SH 171. The FM 157 section is between US 67 and the Ellis County Line. The FM 917 section is in five separate section areas between SH 1774 and FM 2880.

2. Williamson

The area faced cracking problem with pavements over high PI clays and weak subgrade. The project was executed at US-79 (2.063 miles), west of Taylor, where layer of geogrid was introduced between lime-treated subgrade and flex base to reduce reflective cracking over high PI clays. As the construction is still going on, the long-term benefits from the project could not be evaluated right now.

3. Hidalgo

The pavements in this area had cracking problems when placed over high PI clay and weak subgrades. A test section was constructed in April 2001 on FM 1926, 0.66 miles long consisting of different geogrids each of 500 ft length. The grids used were Glass grid 8501, Hatelit C40/17, Pave dry 381, Star grid GPS, Bitutex composite by synteen, and Petro grid 4582. These were constructed to monitor ability of geosynthetic to prevent transverse and longitudinal cracks. This was mill and overlay section.

Further, a new project was started in March 2005 at FM 3462 that was 1.5 miles long. This material is being used to prevent cracks along the shoulders, which was evident before reconstruction.

4. Jefferson

The area engineer experienced problems with pavement over weak subgrades. The two layers of geogrids were used as base reinforcement to span weak subgrade. The project was executed at SH 73 and completed in 2000. It started from 0.5 miles west to Taylor Bayou to Chamber's county line. The total length of project was 17.686 miles and two products—Tensar and Tenax—were used.

5. Houston

The county experienced problems with cracking of pavements over high PI clays and weak subgrade. So geogrids were used to span weak subgrade. It was used at FM 357 (0.35 miles) at Wallace Creek in Houston County on a temporary detour for a bridge replacement project in 2005. Tensar geogrid was used. But the conditions were so poor that the subgrade had to be cement treated in addition to using geogrid.

6. Navarro

The county experienced problems with cracking of pavements over high PI clays and weak subgrade. The geogrids were used in northbound lane of IH 45, 1 mile south of US 287 in Corsicana for 0.2 miles, to span weak and wet subgrade over 12 inch of crushed concrete base. The project was completed in 20002. In the second project the 3-mile section of IH 45 from SH 14 to north of Richland creek in Navarro County was reinforced with geogrid in 2004. The grid was used to span soft subgrade covered with 6 to 10 inches of flexible base. The remaining section had 4-inch bond breaker and 13.5 inches of concrete pavement.

7. Panola

The county experienced problems with cracking of pavements over high PI clays and weak subgrade. The geogrid was used for spot treatment to act as reinforcement and mitigate subgrade cracking and span weak subgrade. Four projects were reported. The first project was executed on US 59 in 1991–1994. It used a nonwoven geotextile Phillips 66, 5 ft below the pavement. The three other projects were executed in 2004 where Tensar geogrid was used. These were FM 123 from US 79 to FM 31, FM 699 from US 59 to FM 2517, and FM 2517 from FM 699 to FM 31.

8. Titus

The county experienced problems with cracking of pavements over high PI clays and weak subgrade. The geogrids were used to mitigate subgrade cracking. A 0.52-mile section of FM 1402 from IH 30 to US 67 was reinforced in August 2004 using Tenax type 1 geogrid.

9. Bowie

The pavements in this county were experiencing problems due to cracking when placed over high PI clay and weak subgrade. The geogrids were used as base reinforcement and to mitigate subgrade cracking. US 259 was reinforced using Tensar BX 1100 geogrid with 0.59 miles of single placement and 0.19 miles of double placement in 2004.

10. Harrison

The two project details were available. In one project, executed in 1983 geotextile was used to span weak subgrade. In 4.3 mile section of FM 3251, layer of geotextile was placed directly below the flexible base. The geotextiles used were Typar 360, Mirafi 500X, and True-Tex MG 200. But the base failures occurred throughout the project. The reasons for failure were not clear. In other project geogrids were used for spot treatment. A section of FM 2199 from US 80 to IH20 was reinforced using geogrid type 1 to mitigate subgrade cracking in 2003.

11. Walker

The county had problems with cracking of pavements over high PI clays and weak subgrade. The main application of the geogrid was for base reinforcement purposes. Five projects were executed from 2001 to 2003 wherein Geogrid type 1 was used. The projects are listed here:

- FM 1696 (1.549 miles) between SH 75 to IH 45 in 2001
- FM 39 (7.854 miles) between US 190 and County Line in 2002
- FM 1428 (3.376 miles) between SH 21 and FM 2158 in 2003
- IH 45 (6.017 miles) between Leon county line and 0.2 miles north of MP 187
- FM 1375 (4.315 miles) between IH 45 West frontage road to 4 miles west

12. Grayson

The county had problems with cracking of pavements over high PI clays and weak subgrade. The geogrids were used in areas of high stress and signal intersection. Approximately 3 mile section of US 69 from Spur 503 to MLK at Denison were reinforced in 1999. A geotextile

was used under HMAC in US 82 from Coke to Beaver creek in 1998. Also grids were used for area widening in SH 121 from County line to SH 11 in Fanin. The project was completed in 2003.

13. Midland

The longitudinal cracking was observed in US 67 extending from Reagan County line to 3 miles west of it. The cracks were due to shrinkage occurring in the subgrade near the shoulder but later they continued across the roadway. The layer of Tensar geogrid was used between base and subgrade and project was completed in 2003.

14. Taylor

This county had problems with pavement section cracking when placed over high PI clays. They tried using geocomposite and glass grid. In both cases they ended up deleting it from the project due to the material not meeting the specifications set by TX-DOT.

2.6.5 Discussion of Survey Results

Based on the survey responses, it was found that most of the cracking occurred in pavements when they were constructed over high PI clays. Field district engineers attributed this to the weak subgrade below the pavement. They had attempted using geosynthetics in such case and both geogrids and geotextiles were used; though geogrid were more widely used as compared to geotextiles. Also most of the case studies where geosynthetics were used in the pavement were in the Forth Worth–Dallas area and Corpus Christi, which have problems due to high PI clays.

For majority of the projects, the geosynthetics were placed in the pavement during construction and no post construction performance evaluation was conducted making it difficult to quantify the benefits of use of geosynthetics in pavements. The geosynthetics products used on site ranged from geogrids (from more than one manufacturer), geotextiles to glass grids. They were also used at various locations within the pavement, i.e., at the base-subgrade interface, within the base and within the asphalt. Further, based on the comments received on the survey forms, it was found that the engineers had no specification on designing a geogrid reinforced roads. They only had a single TxDOT specification regarding testing methodology to be adopted to determine which geogrid should be used in pavement for reinforcement purposes, but no such specification existed for geotextiles. Further, the best location for the placement of geosynthetics and construction guidelines to place them in the field were not specified.

Therefore, it was concluded from the survey that though there was a lot of experience with usage of geosynthetics in pavements within the TxDOT but still there was no clear design methodology or post construction performance evaluation was adopted in the field. Therefore, based on the survey three sites were selected and post construction field monitoring was conducted to establish their performance as explained in Chapter 3.

Chapter 3. Field Testing and Monitoring Program

3.1 Introduction

The previous chapter described the background information regarding various components of this research and design practices adopted by TxDOT for the design of geosynthetic reinforced pavements. The survey of TxDOT projects was conducted to obtain the information regarding present state of practice among various districts of Texas. One of the major focuses of this project was also to document the field experience gained by TxDOT districts on the use of geosynthetics in unbound base course of pavements. Based on the survey results, three projects were selected for detailed field evaluation as explained in subsequent sections.

3.2 Field monitoring of projects identified from survey

This section describes the field performance of three pavement projects involving base reinforcement. In the first project, immediately after construction of the geogrid reinforced pavement, the longitudinal cracks were observed even before it was open to traffic. In the second project, contrastingly different performance was observed with two different geosynthetic products selected using project-specific specifications. The third project showed consistently good performance in various sections, but the good performance was not consistent with the results of dynamic field monitoring tests. The observations from the field studies further indicated the discrepancies in current design methods for geosynthetic reinforced pavements.

3.3 Description of case histories

3.3.1 Case History 1

Project description: SH 7 is located in Leon County of the Bryan district, Texas. In March 2005, it was planned to close the main section of the road for reconstruction and use the shoulder road as an alternative route. For this the shoulder was constructed consisting of lime stabilized subgrade, flexible base and one course of surface treatment with a layer of geogrid provided at subgrade-base interface.

Field observation: Longitudinal cracks were observed in the pavement section even before it was open to the traffic. So the forensic investigation of the site was planned to establish the reasons for premature failure of the road.

Site investigation: On visual inspection of the site, 2 inches (50 mm) wide longitudinal cracks were observed close to the junction of the recently constructed shoulder and previous main road section. The backhoe was then used to excavate the top portion and expose the cracked portion of the pavement. It was observed that there was no geogrid below the cracked portion of the pavement. Further, a bore hole was done at the location and soil samples were collected at 6 inches (0.15 m) interval to the depth of 3 feet (1 m). The top 1.5 feet (0.5 m) of the soil was found to be red colored sand followed by light brown clay. Preliminary investigation of the soil samples at site showed water content and plasticity index values as shown in Table 3.1. Further no shrinkage cracks were observed in the subgrade.

Table 3.1: Atterberg limit values for the soil samples collected at site

Depth of sample	Water content	Liquid limit	Plastic limit	Plasticity Index
(inches)	(%)	LL	PL	PI=LL-PL
0"-6"	9.7	17.7	14.1	3.6
6"-12"	17.7	23.6	19.0	4.6
12"-18"	13.7	23.3	20.0	3.3
18"-24"	20.3	37.1	23.2	13.9
24"-30"	24.3	38.5	24.1	14.4
30"-36"	24.8	43.8	31.1	12.7

Analysis and Result: The geogrid rolls supplied by the manufacturer were 9.8 ft (3m) wide but the proposed lane was about 14 ft (4.2 m) wide. The contractor had placed only one roll of the geogrid below the pavement, which left 4.2 ft (1.28 m) of the pavement unreinforced. While the section consisting of the geogrid reinforcement was performing well, the cracks developed in the unreinforced section of the pavement. Most of the cracks were observed at the junction of the unreinforced and reinforced section as shown in Figure 3.1. This provided field evidence that the geogrid reinforced pavements in expansive subgrade soils are less susceptible to cracking induced due to environmental loads than the unreinforced pavements.

Figure 3.1: Longitudinal cracks in the unreinforced section of FM 542 pavement

3.3.2 Case History 2

Project description: FM 1774 is located in Grimes County. In August 2002 as part of restoration of existing road, 9.120 miles (14.68 km) of the FM 1774 road from SH 90 to FM 2445, i.e., from station 993+34 to 1474+90 was reconstructed. During construction, the existing road was excavated and leveled to have 10 inches (0.25 m) of cement and lime stabilized subgrade, 7 inches (0.18 m) of flexible base, and one course of surface treatment. Site investigation and soil testing indicated presence of clay of high plasticity (PI=40) from stations 1289+00 to 1474+90. To reinforce the pavement at these locations an additional layer of geogrid was provided at subgrade-base interface. Two different geogrid types available in the market

were found to satisfy the project specifications. To evaluate the field performance both the geogrids were used, i.e., geogrid type 1 (polypropylene) from station 1299+58 to 1315+42 and geogrid type 2 (polyester) from station 1362+94 to 1474+90. The typical section of the geogrid reinforced pavement constructed at site was as shown in Figure 3.2.

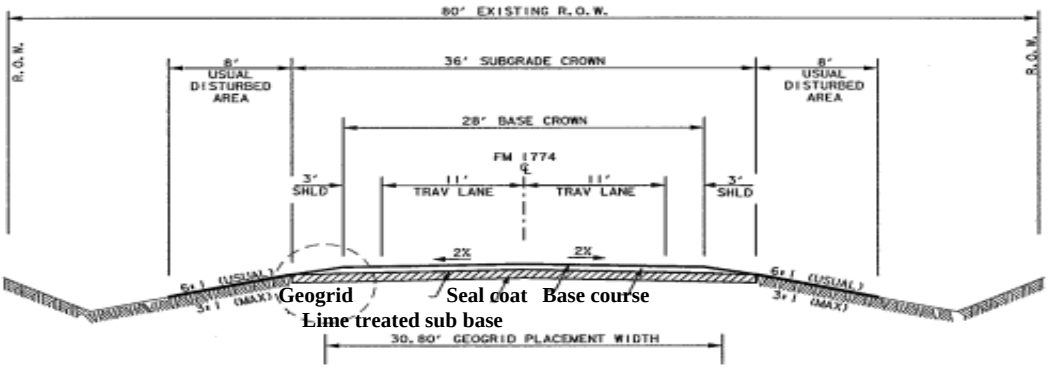

Figure 3.2: A typical geogrid reinforced pavement section at FM 1774

Observation: In summer of 2004, the longitudinal cracks were seen in the section reinforced with geogrid type 2 while the sections reinforced with geogrid type 1 were performing well. On excavating the cracked road sections of the pavement reinforced with geogrid type 2, it was observed that there was no longer bond between the longitudinal and transverse elements of the geogrid. Longitudinal cracks and slippage at junction of geogrids in section reinforced with geogrid 2 are as shown in Figures 3.3a and 3.3 b respectively.

Material properties: The material properties of both the grids were evaluated and compared with the project recommended specifications. These are as listed in Table 3.2.

Table 3.2: Comparison of Geogrid (type 1 and 2) properties with project specifications given by TxDOT

Geogrid type	Geogrid type 1	Geogrid type 2	Recommended
Aperture size, cm (inch)	3.5 (1.4)	4.3(1.7)	2.5-5.0 (1.0-2.0)
% Open area	75%	74%	70% min
Tensile Modulus at 2% strain , lb/ft	15306	27450	14000-20000
Junction efficiency	94%	35%	90% minimum

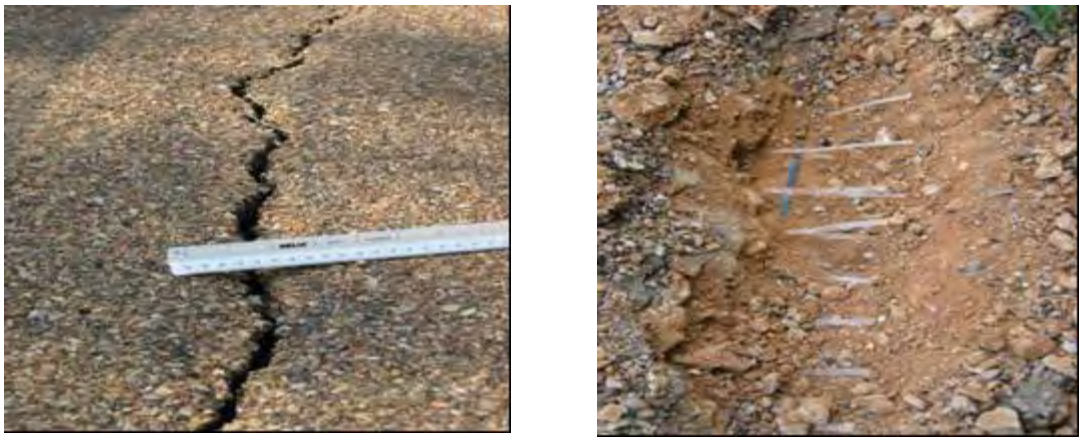

Figure 3.3: a) Longitudinal crack on the pavement reinforced with geogrid type 2 at FM 1774 (Bryan District) b) Slippage between longitudinal and transverse ribs at junction of geogrid type 2 at FM 1774 (Bryan District)

Analysis and Results: Though geogrid type 2 had higher strength in machine and cross machine direction than geogrid type 1, it had lower strength of the junctions. TxDOT specifications for geogrid products include both index properties (e.g., aperture size, percentage open area) and performance properties (e.g., tensile modulus, junction efficiency, ultimate strength in machine and cross-machine direction). A preliminary review of geogrid test results in well performing section showed junction efficiency (i.e., the ratio between the strength of the junction and the rib tensile strength) of 94% while the geogrid test result in a poorly-performing section shows a junction efficiency of only 35%. As current specifications require 90% junction efficiency, the inadequate junction efficiency value could be inferred as being the potential cause for the difference in pavement performance. However, closer inspection of the available test results indicated that the tensile modulus (at 2% strain) in the poorly-performing section is approximately twice as high as that in the well-performing section. Because the tensile modulus is a key property in current design methods, the need for additional material characterization to provide insight into the actual causes of the differences in pavement performance is required. For example, the tensile modulus in the cross-machine direction is rarely specified, but it is not less relevant than the tensile modulus in machine direction that is typically specified. Also the time - dependent response of polymeric material may lead to different results if tensile tests are conducted at different strain rates. Accordingly there is need of having additional laboratory tests that will capture the geogrid mechanism and provide independent verification of the geogrid properties that can better predict its performance in the field.

3.3.3 Case History 3

Project description: FM 1915 is located in Milam County, Texas. In 1996, longitudinal cracks were observed in the pavement section starting from Little River Relief Bridge to 2.5 miles (4 km) west of it. So the pavement was reconstructed such that all sections had 10 inches (0.25 m) of lime treated subgrade with a seal coat at top. Due to presence of clays of high plasticity at site it was planned to reinforce the pavement with a layer of geogrid at base and subgrade interface. Further to evaluate the performance of geogrid, two geogrid reinforced sections were constructed such that section 1 had a base course thickness of 8 inches (0.20 m) and section 2 had a base course thickness of 5 inches (0.127 m) along with a control section

having base course thickness of 8 inches (0.20 m). The details of each test section are as in Table 3.3 and typical contour view of the site is as shown in Figure 3.4.

Table 3.3: Details of three test sections constructed at FM 1915

Section	Section 1	Control section	Section 2
Material used	**Geogrid**	**No Geogrid**	**Geogrid**
Base course thickness, inches	8 (0.20)	8 (0.20)	5 (0.127)
PI	49	37	37
Extent of test section , miles	0.038-0.827	0.827-1.663	1.663 -2.480
Total length, ft (km)	4150 (1.26)	4397 (1.34)	4297 (1.31)

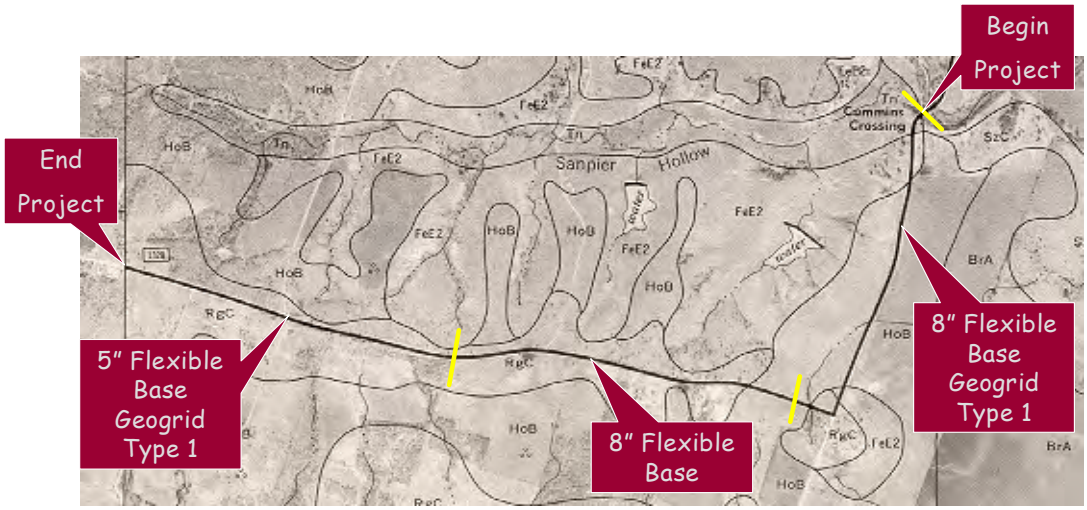

Figure 3.4: View of the limits of three sections at FM 1915

Field Testing: In July 2001, TxDOT performed falling weight deflectometer (FWD) testing on the entire 2.5 miles (4 km) of the pavement section. The tests were conducted at every 100 ft (30.48 m) interval starting from section 1. The FWD deflection data thus obtained was analyzed using the Modulus 6.0 software program developed by the Texas Transportation Institute (Scullion, 2004) and the elastic modulus for each pavement section layer was then back calculated. Table 3.4 summarizes the average values of modulus obtained for pavement layers of each section.

Table 3.4: Mean modulus (Mr) values obtained using Modulus 6.0, for various pavement layers for three test sections at FM 1915

Section	SECTION 1	CONTROL	SECTION 2
MODULUS, MPa	**Mean**	**Mean**	**Mean**
Seal coat	2068	2063	2020
Base course	1724	1660	1451
Sub base	443	380	302
Sub grade	139	134	132

Analysis: The results from the FWD testing showed higher values of the modulus for the base course and subgrade layer when geogrid reinforcement was used with 8 inches (0.20 m) thick flexible base course as compared to the control section. But the third section having geogrid reinforcement with 5 inches (0.127 m) base course thickness had lower base and sub base modulus as compared to the other two sections. These results lead to conclusion that the geogrid reinforcement would improve the performance of the pavement when used over the same base course thickness but the benefits would not be realized if the base course thickness was reduced.

When the FWD results were compared with the field visual assessment of the pavement, longitudinal cracks were observed in the control section. On other hand the two geogrid reinforced sections were found to be performing well without any surface cracking of pavement. The anomaly between the field observations and FWD testing is mainly due to the current pavement analysis procedures for FWD loading, which do not appropriately consider the effects of geogrid reinforcement layer. Presently the analysis is done by neglecting the geogrid layer and directly computing the modulus values for various pavement layers in the given section. These values are then compared to the modulus values for various pavement layers of a control section. The increase in the base course, sub base course, and subgrade modulus is attributed to the presence of the geogrid layer for a reinforced section when compared with a control section. This method of analysis can quantify the benefits for the same base course thickness but can be misleading if the base course thickness is varied. Due to drawbacks in current method, need for a better analysis method to quantify the benefits of geogrid reinforcement in the pavement that can adequately predict the field performance.

3.3.4 Conclusions from Case Histories

Forensic investigation conducted at a newly constructed pavement on FM 542 was reported. The longitudinal cracks were observed in the geogrid reinforced pavement before it was open to traffic. But when site was excavated near the cracks, no geogrid was found below the pavement section. Further investigation revealed that the contractor had laid 9.8 ft (3 m) roll of geogrid and the pavement being 14 ft (4.2 m) long, remaining 4.2 ft (1.28 m) section was unreinforced and was cracked. This study showed that use of geogrid can prevent cracking in the pavements.

Field performance of two geogrid reinforced pavement consisting of subgrade having clay of high plasticity are reported. The pavement had two different types of geogrid. Both the geogrids meet the project specifications set by TXDOT. Whereas one section reinforced with

geogrid type 1 (polypropylene) was found to be performing well, the other section reinforced with geogrid type 2 (polyester) showed longitudinal cracking. The review of the material properties leads to the preliminary conclusion that poor performance in the geogrid type 2 sections is due to inadequate junction efficiency but closer inspection indicated the higher tensile modulus of geogrid in this section. Because tensile modulus is an important property of geogrid, the need for better material characterization is stressed to predict the actual cause of difference in field performance.

In the third pavement, three sections were constructed. The two geogrid reinforced sections, i.e., section 1 and 2, had base course thickness of 8 inches (0.20 m) and 5 inches (0.127 m) respectively; whereas control sections (no geogrid reinforcement) had 8 inches (0.20 m) thick base course layer. FWD testing showed higher pavement modulus for the geogrid reinforced section with 8 inches (0.20 m) thick base course layer over the control section whereas lower modulus value were predicted for geogrid reinforced section having 5 inches (0.127 m) thick base course layer . This indicates better performance for the section 1 and poor performance of section 2 when compared with the control section. But field visual assessment showed cracking in the control section and the two geogrid reinforced section were performing well. The geogrid reinforced sections outperform the unreinforced sections though the FWD testing indicates otherwise. This shows the inadequacy in the present analysis technique for nondestructive testing to quantify the geogrid benefit in pavements.

In summary, there is adequate field evidence that geogrid reinforcement provides benefits by stabilizing pavement over clays of high plasticity. But still there is need for new laboratory tests that can provide insight into field performance of these sections. Further, new methods for the analysis of FWD testing need to be developed that can better predict the field performance of geogrid reinforced and unreinforced section.

3.4 Field test sections

The scope in the initial research project involved field evaluation of geogrid-reinforced pavements in completed TxDOT projects. However, soon after project initiation, the opportunity appeared for constructing test sections as part of a road reconstruction project (reconstruction of FM2 in Bryan District). Based on the lessons learnt from the field testing program conducted as explained in previous section, a field monitoring program for FM 2 project in Bryan district was developed. The field testing program included well-performing geosynthetic-reinforced sections, poorly-performing geosynthetic-reinforced sections, and unreinforced sections. Comparative evaluation of pavement reconstructed using at least 8 different reinforcement schemes (3 reinforcement products and unreinforced control section, with/without lime stabilization) was expected to lead to significant findings. Accordingly, and following advice from the project advisory board, a total of 32 test sections (4 reinforcement types x 2 stabilization approaches x 4 repeats) were constructed in FM2. Instrumentation was implemented in order to characterize the patterns of moisture migration under the pavement. Construction was completed in January 2006 and performance evaluation of the newly reconstructed road is being conducted with special focus on the 32 test sections. Field monitoring was conducted before reconstruction and immediately after reconstruction. However, post-construction field evaluation requires continued monitoring for at least two complete seasons. The main issues to be addressed in this study were to construct:

- Test sections with different geosynthetic types i.e. geogrid and geotextiles
- Test sections with different type of geogrids that would help in comparing performance of different products
- Control sections at the field to provide baseline for the study
- Sections having lime and no lime treatment
- Similar sections with number of repeats to account for variation in field due to environmental, construction and site factors

3.5 FM 2 description

3.5.1 Background

Texas Farm-to-Market Road No. 2 (FM 2) is located in Grimes County, in southeast Texas. The following figures show FM 2 relative to major metropolitan areas in Texas. The total length of the road is 6.4 miles, of which 2.4 miles lie towards the west of State Highway 6 (SH 6) at Courtney; the remaining 4 miles continue eastward and end at FM 362, as shown in Figure 3.5(a) and 3.5(b).

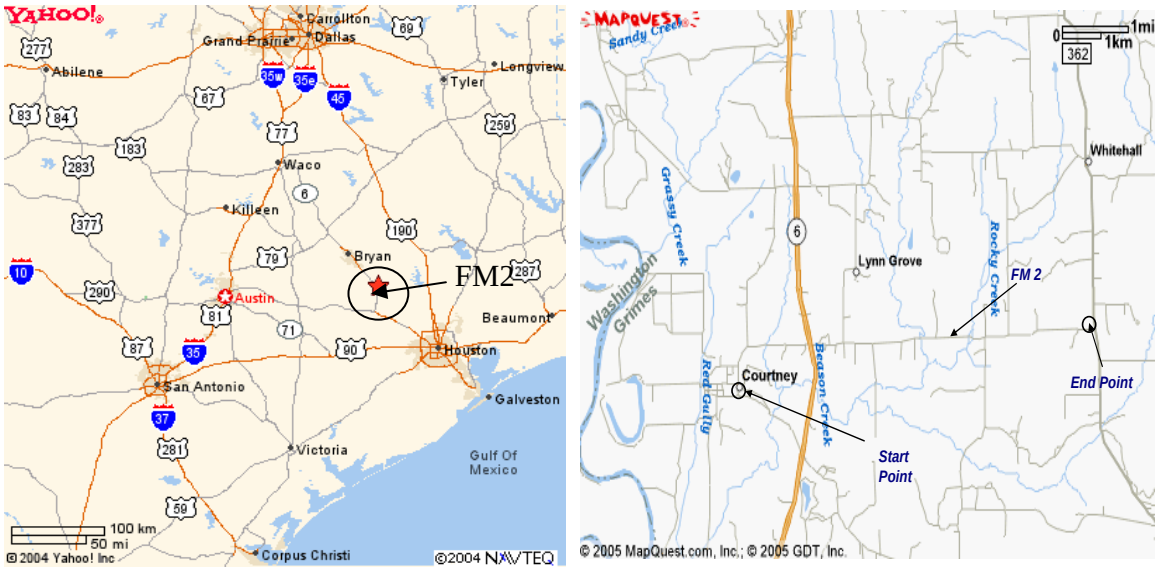

(a) (b)

Figure 3.5: a) Location of FM 2 Relative to major metropolitan areas in Texas
b) Layout of FM 2

3.5.2 Weather Conditions

FM 2 is located on the outskirts of city of Navasota in the Grimes county of Texas. The closest weather station to the site during year 2004 was located in College Station, the Bryan district of Texas. To get an initial estimate of the weather conditions at the site and surrounding areas, the weather information was collected from this station. The monthly average climate records of temperature and precipitation for last 30 years in Navasota (WSI Corporation, 2005)

were obtained and are as shown in Table 3.5. Based on the climate data, the average high temperature was around 96^{o} F in month of August and lowest temperature was 53^{o} F in month of January. The average annual precipitation was calculated to be 40.4 inches with high rainfalls in month of May, June, September and October. This climate data indicated that the site had two dry seasons in a year divided by two rainy seasons as shown in Figure 3.6.

Table 3.5: Navasota 30-year climate averages and records

Month	1	2	3	4	5	6	7	8	9	10	11	12
Temp. High (°F)	58	63	71	79	85	91	95	96	89	81	71	62
Temp. Low (°F)	37	40	48	57	64	69	72	71	66	56	48	39
Record High (°F)	88	90	99	95	101	104	108	110	106	100	91	85
Record Low (°F)	9	16	19	30	42	52	56	55	43	28	21	3
Mean Temp. (°F)	48	52	60	68	75	80	83	84	78	69	60	51
Rainfall (in.)	3	2.9	3	3.1	4.5	3.9	2.3	2.8	4.8	3.7	3	2.9

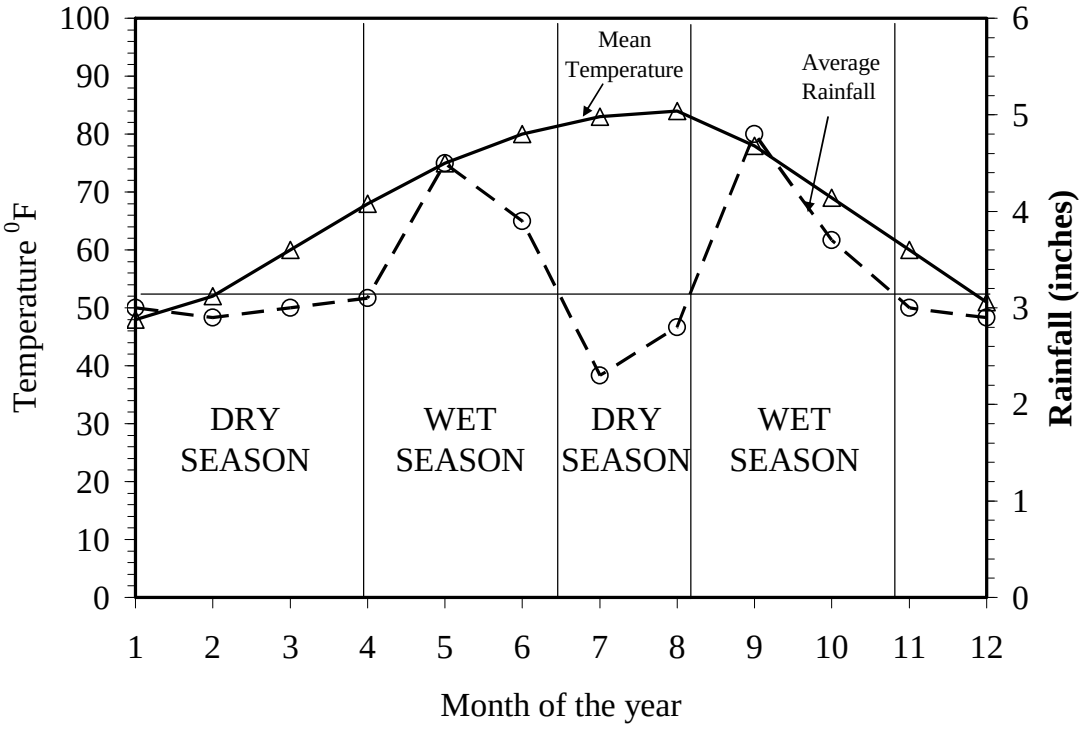

Figure 3.6: Wet and dry season at the site based on 30-year average climate data

3.5.3 Seasonal Variation of Moisture

The analysis of climatic data at the site showed the presence of wet and dry weather cycles during a given year. This seasonal variation of moisture at the site is known to cause distress in pavement due to presence of high PI clays. These expansive soils, containing the clay mineral montmorillonite, are widespread in this area and experience significant volumetric changes when subjected to changes in moisture conditions. The volumetric change of the expansive soil may cause serious road pavement distresses, such as excessive roughness, longitudinal cracking, and structural deterioration (Sebesta, 2002).

3.5.4 Average Annual Daily Traffic

Based on the traffic information provided by TxDOT for the FM 2 road, the average daily traffic (ADT) was 800 in 2002 and is expected to increase to 1300 vehicles in 2022. Of this, the trucks account for 6.6 percent of the ADT. The expected total number of equivalent 18-kip single axle load (ESAL) is 91,000 in one direction of the flexible pavement for a 20 year period from 2002 to 2022. The speed limit on FM 2 was 55 miles per hour.

3.6 Pre-construction field evaluation

Before the beginning of reconstruction of the FM 2 road, a field survey was conducted on January 4, 2005, to quantify the structural section of in-situ pavement. The main motivation of this preliminary field investigation was to identify the condition of subgrade and construct the field test sections such that they are constructed over similar ground conditions. Further, previous data collected by TxDOT on the site, which consisted of four pavement cores taken in March 2002, was obtained. It showed that FM 2 had a base course with an average thickness of 9.5 inches covered by a seal coat of 0.5 inches (Goehl, 2002). The basic work plan consisted of four main components:

1. Site Characterization
2. Visual inspection and Pavement Crack Characterization
3. Falling Weight Deflectometer (FWD)
4. Rolling Weight Deflectometer (RDD)

3.6.1 Site Characterization

3.6.1.1 Mile Marking

Mile markers in form of wooden pegs were placed every 0.5 miles starting from FM 362 to provide consistent reference points for current and future testing. These marks were used to match the data obtained by FWD and RDD testing as shown in Figure 3.7

3.6.1.2 Soil Sampling

The soil sampling was conducted every 0.5 miles. The samples were collected from the vicinity of the pavement to a depth of 1 foot. The samples consisted of the debris of asphalt from previous rehabilitation work conducted on the site. The samples obtained were not representative

of the actual subgrade soil but provided visual evidence of variation of soil throughout the pavement.

3.6.1.3 Soil processing and Index test

The soil samples obtained from the site were used to determine the in-situ water content for top 1 foot of soil. Further the soil was dried in the constant temperature room for 24 hours and then index tests were performed. Due to presence of debris the values were not representative of actual field conditions and it was decided to perform bore hole coring in the subsequent field trips. Further, a report containing previous borehole investigation conducted by TXDOT was obtained and the values reported are as in Table 3.6.

Table 3.6: Water content at various locations from TxDOT report

Core location		Water content	LL	PL
0.5 mi east of SH6	Top 3 ft	14	36	21
1.5 mi east of SH6	Top 1.5 ft	26	51	42
2.5 mi east of SH6	Top 1 ft	11	16	6
3.5 mi east of SH6	Top 5 ft	34	72	45

Based on the first field trip, the general topography and area with high PI clays were identified. This helped in planning the geosynthetic reinforced test sections on site.

3.6.1.4 Visual inspection and pavement crack characterization

Visual field inspection was conducted on FM2 starting from FM 362 westward to SH 6. Most sections of this road were found to be severely deteriorated. Various types of distresses, including fatigue cracking, edge cracking, longitudinal cracking, patching, pothole, and rutting, raveling, and lane-to-shoulder drop-off as were observed and are described in Chapter 5. The initial survey laid the basis for future condition survey of the site.

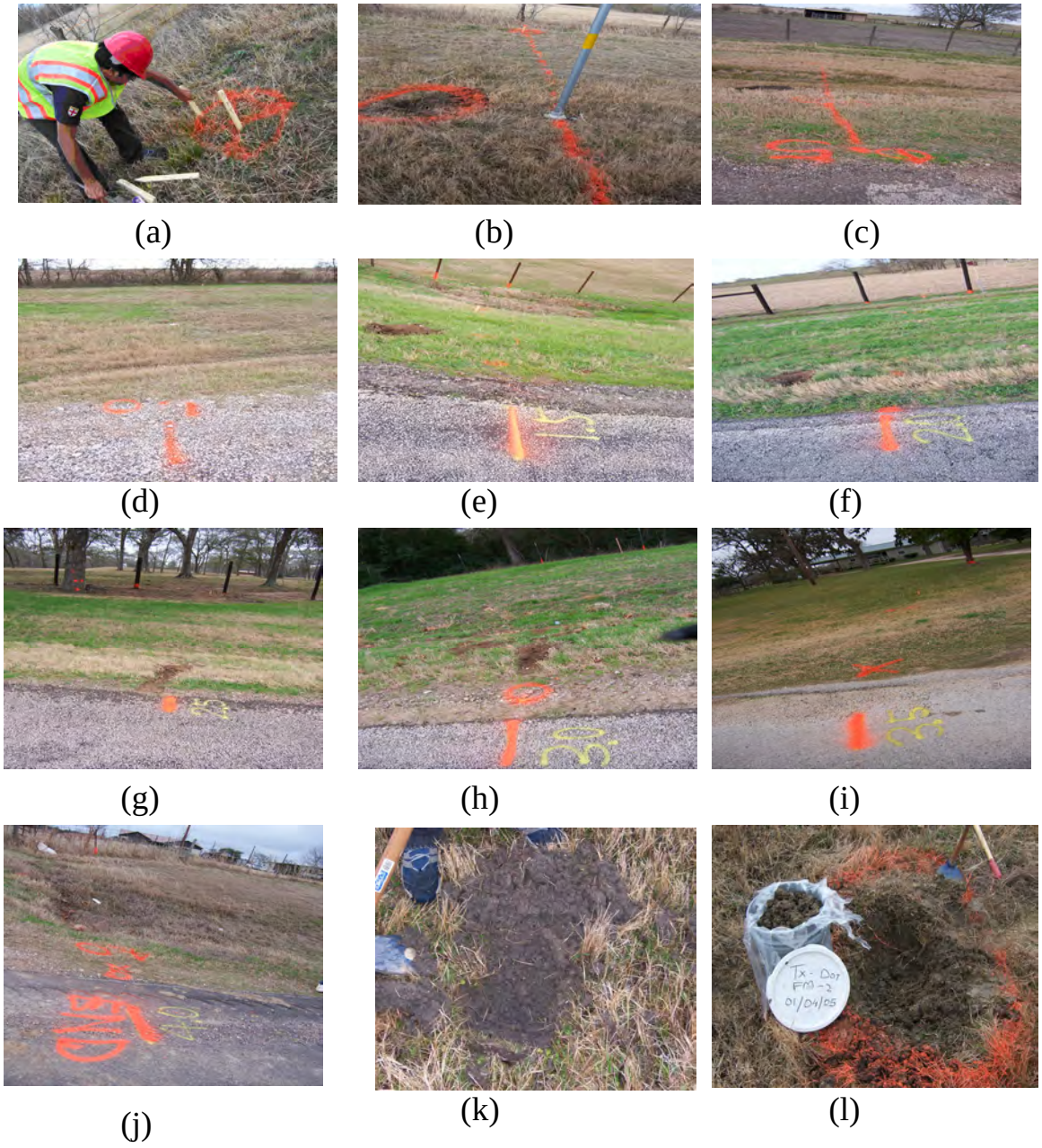

Figure 3.7: FM 2 pavement marking a) wooden peg b) 0 miles c) 0.5 mile d) 1.0 mile e)1.5mile f) 2.0 mile g) 2.5 mile h) 3.0 mile i) 3.5 mile j) 4.0 mile k) soil collection pit l) soil sampling at the site

3.6.2 Nondestructive Testing

Nondestructive pavement testing was done using RDD and FWD on FM 2 January 4–6, 2005. A total of 3.84 miles of section was tested starting from FM-362 end of the road and going towards SH-6. FWD test was done at every 300 ft and four different load levels. Simultaneously, RDD testing was done using two static load levels of 8 kips and 13 kips. The following analysis

presents the analysis of RDD and FWD test results that were used to determine the location of test sections to be placed in FM2. The basic issues addressed by pre-construction testing were to

- identify the subgrade characteristics
- determine location of test section
- quantify pavement characteristics before remedial action is done
- finalize the placement of repeats of each test sections in the pavement
- identify the subgrade characteristics and account for variability in design
- quantify pavement structural section before rehabilitation
- identify locations to construct the test sections
- finalize the placement of repeats of each test sections in the pavement to account for variability in sub-grade characteristics

The RDD truck consisted of three geophone sensors placed along the center line of the load bearing wheels at distances of 2.5", 38+2/16" and 56+1/6". The reading from the third geophone, which was farthest from the loading wheels, was assumed to be most representative of the subgrade characteristics. For FWD testing done at 300 ft spacing, the profile was assumed to have the same values of deflection for the next 300ft. The four load levels of 6 kips, 8 kips, 11 kips, and 15 kips were used at each measurement station. The values from the 8 kips load were assumed to be the most representative of typical axle wheel load for low volume roads and used in the analysis to calculate subgrade modulus of pavement Therefore, the deflection profiles obtained by RDD method and subgrade modulus obtained by FWD methods were plotted as shown in Figure 3.8. It was observed that where the RDD deflection was high, FWD modulus was low thereby indicating the weak material. Further 4 materials were placed in such a way that each material had the same range of deflection values from RDD and FWD tests. This was done to avoid a particular geosynthetics to be placed in weak subgrade throughout and other in a stronger subgrade.

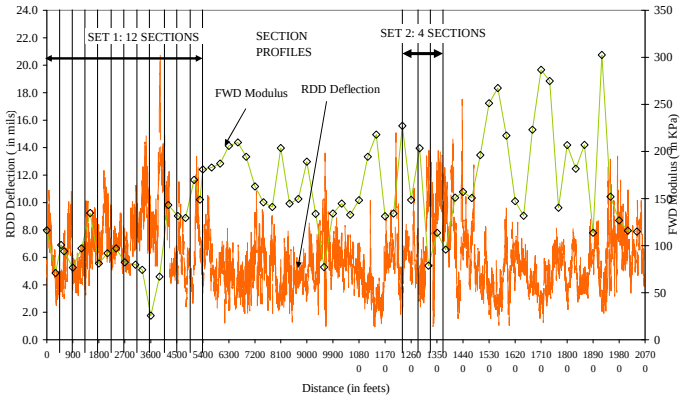

Figure 3.8: Recommended placement of test sections in one lane on FM 2

3.7 Reconstruction of FM2 site

Based on the preliminary investigation and TxDOT requirements the test sections were planned for construction on FM 2 site. The original pavement cross section as shown in Figure 3.9 was scarified and new cross sections were built as shown in Figure 3.10.

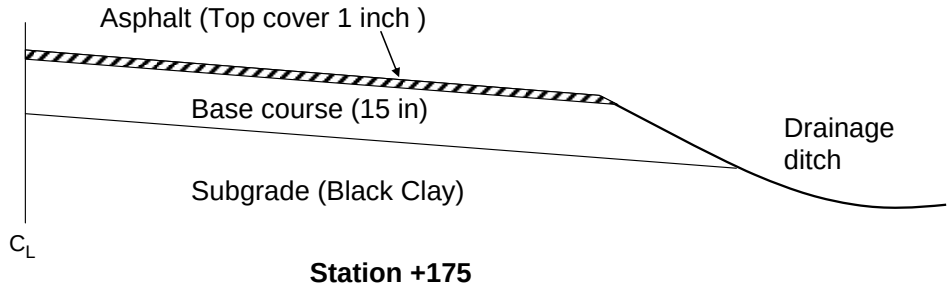

Figure 3.9: Existing pavement section at FM 2

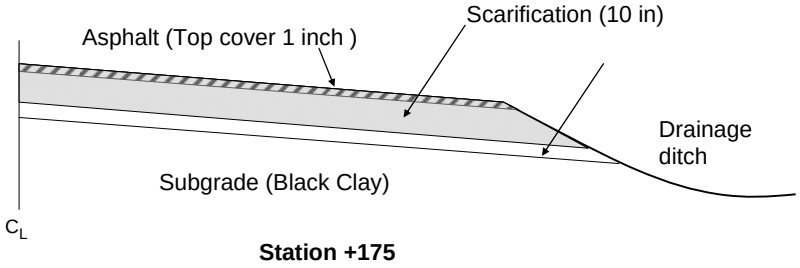

Figure 3.10: Scarification plan for FM 2

To prevent longitudinal cracking, TxDOT has proposed the use of geogrid reinforcement at the interface between the subgrade and base course and lime stabilization. The intention of this design is to use the geogrid to prevent translation of volume changes in the subgrade into the base course. The intention of the lime stabilization is to prevent volume changes in the near-surface soils and to provide a stiff layer beneath the new base course. During the rehabilitation of FM 2, several test sections were proposed to investigate different types of geogrids and the use or not of lime stabilization.

There are four basic proposed test section designs: unreinforced without lime stabilization, unreinforced with lime stabilization, reinforced without lime stabilization, and reinforced with lime stabilization. Figure 3.11(a) shows an unreinforced section without lime, which is used in this study as a control section. In this section, the scarified existing base course is re-compacted to at least RC = 95%. The new base course is also compacted to at least RC = 95%. Figure 3.11(b) shows an unreinforced section in which the scarified existing base course is lime stabilized. Figure 3.11(c) shows a reinforced section in which the scarified existing base course is not lime stabilized, while Figure 3.11(d) is also reinforced but the scarified existing base course is lime stabilized.

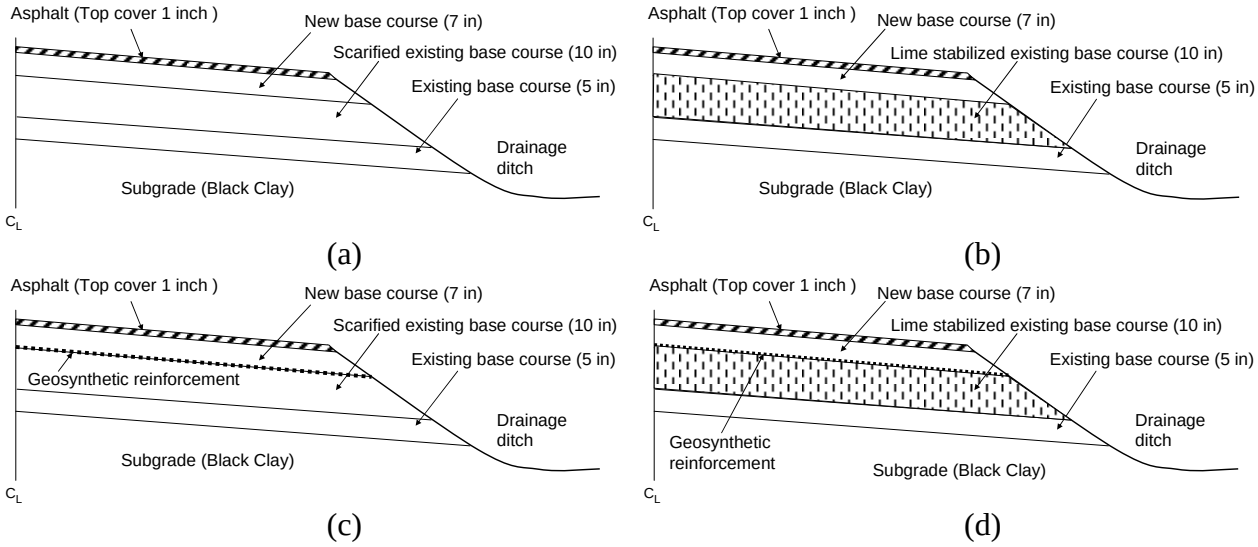

Figure 3.11: Pavement test sections at FM 2: (a) Unreinforced without lime stabilization; (b) Unreinforced with lime stabilization; (c) Reinforced without lime stabilization; (d) Reinforced with lime stabilization

3.8 Layout of test sections

Based on the analysis described, the initial plan for construction of test sections was submitted to the TxDOT. In the reinforced sections, three different geogrids were used in adjacent pavement test sections to investigate the possible advantages and disadvantages of different manufacturing designs. The four sections would be no geogrid (GG0) or control section, geogrid type 1 (GG1), geogrid type 2 (GG2), and geotextile (GG3) reinforced pavement section. Further, each of these sections would be constructed over lime-treated and non lime-treated base course. Therefore, eight such sections were constructed in field as shown schematically in Figure 3.12. Further, each of the 8 sections had 4 repeats at the site, totaling 32 such sections.

The field test sections were constructed in such a way as to accommodate at least one full length of the manufactured geosynthetic roll. The research team envisioned that the smaller test sections of different geosynthetic placed adjacent to each other would led to edge effects in the field. This would in turn influence the results obtained during post construction non-destructive test monitoring of performance in the test sections. The typical dimensions of the geosynthetic products used in the field are as shown in Table 3.7. Further, it was decided to construct equal number of test sections in both driving lanes of the pavement to account for the variability in the traffic conditions and also monitor performance of different geosynthetics when they are placed adjacent to each other.

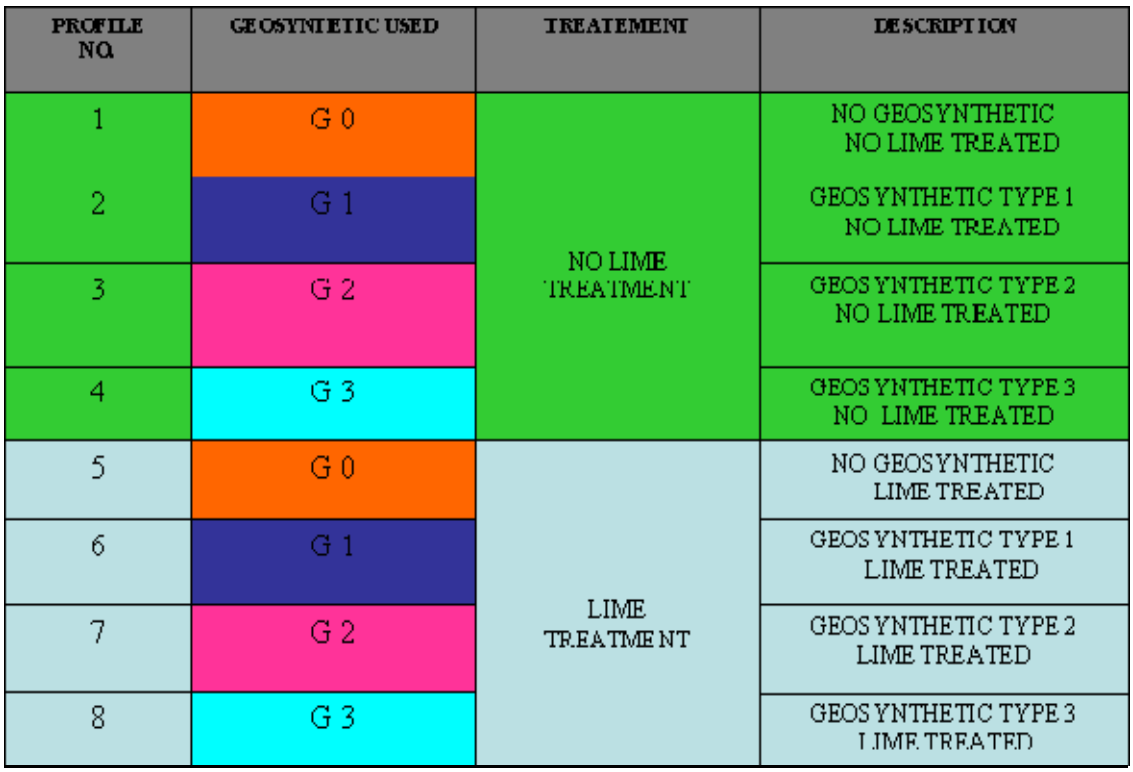

Figure 3.12: Schematic layout of test sections constructed at the FM 2 site

Table 3.7: Geosynthetic dimensions and rolls required for each test section

Geosynthetic used	Dimensions of roll		Number of rolls			Overlap
	Length (m)	Width (m)	Length wise	Width wise	Total	
GG1	75	3	2.0	2.0	4.0	Yes
GG2	50	3	3.0	2.0	6.0	Yes
GG3	92	4.6	1.5	1.0	1.5	No

FM 2 involved constructing a 30-feet-wide pavement section. Further, based on the contract restrictions, the research team was given permission to construct test sections between stations 223+39 and 162+83, and stations 98+19 and 78+35. So it was decided to construct 150 m (~450 ft) long test sections with first set of 24 test sections between station 221+00 and 167+00 and the second set of 8 test sections between stations 98+00 and 80+00. The number of rolls required for each of these test sections were calculated based on the site constraints of length and width of test section as shown in Table 3.10. The field layout and the numbering system adopted to distinguish various test sections is as shown in Figure 3.13 and has been followed in other sections of this report. The numbers 1 to 4 and 5 to 8 represent type of geosynthetic with lime treatment and no lime treatment respectively. Each section was further divided based on the driving lane as west bound (W) or east bound (E) and number of repeats as

a and b. Thus, section 2Wa indicates first test section in west bound lane with geosynthetic type 1.

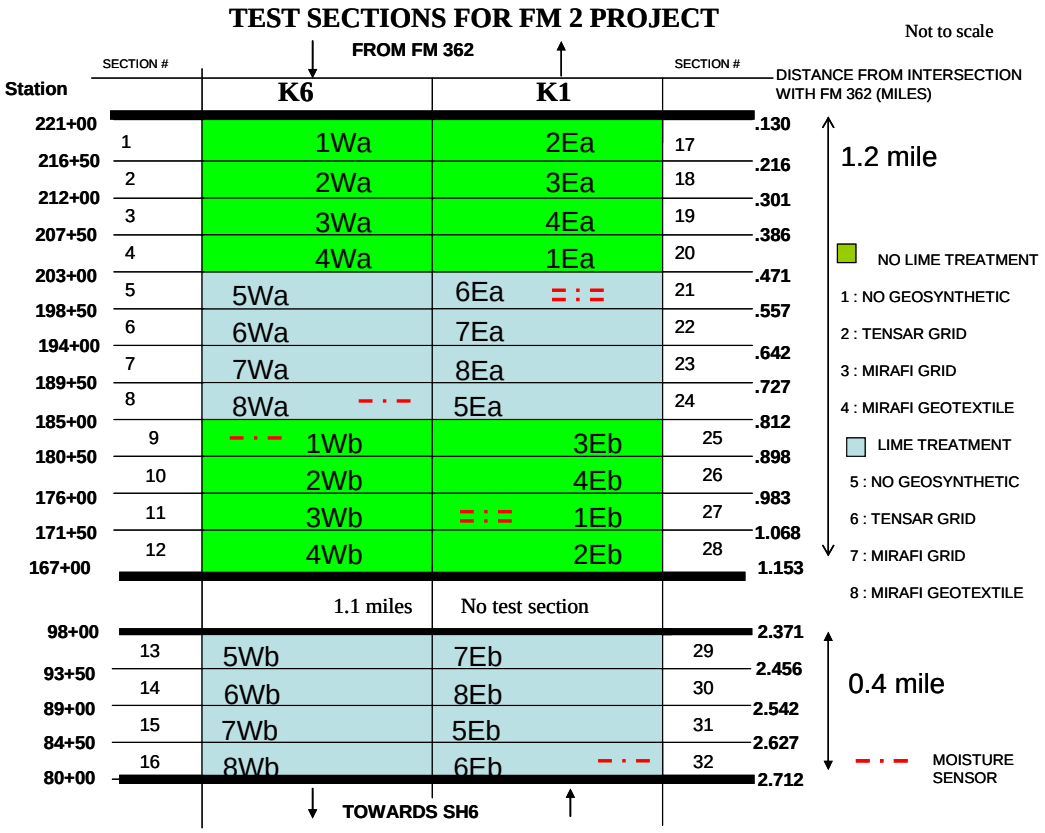

Figure 3.13: Station wise layouts of test section and numbering system

After constructing the test sections, the material characterization was carried for the both base course and subgrade soil followed by laboratory testing of geosynthetics used in test sections. Further, field monitoring of the test sections was done using FWD, RDD, visual inspection, and moisture monitoring and results obtained are shown in subsequent chapters. Based on the data collected from field testing, comparison was made regarding field performance of non-geosynthetic reinforced sections and geosynthetic reinforced sections.

Chapter 4. Material Characterization

4.1 Introduction

This chapter describes the properties of soil types and geosynthetics used in this project. The two main soil types of interest during the investigation of field test sections constructed at FM 2 were the base course and subgrade clay. As the subgrade clay was not readily available and variable properties throughout the entire 4 miles of the road, it was decided to conduct laboratory tests using a standardized soil called Fire Clay. A suite of geotechnical tests were conducted on these three soils as shown in Table 4.1. Further, three geosynthetic types were used in constructing the geosynthetic test sections. They were Tensar geogrid BX-1100, Mirafi geogrid BasX-11 and HP-570 Mirafi geotextile.

Table 4.1: Available data on soil used in FM 2 project

Test/Soil	BASE COURSE	FM 2 CLAY	FIRE CLAY
Specific Gravity	•	✓	✓
Grain Size Distribution	✓ Sieve test	✓ Sieve test	✓ Sieve + Hydrometer test
Atterberg limits		✓	✓
Compaction	✓ Standard Proctor test	✓ Standard Proctor test	✓ Standard Proctor test
Hydraulic Conductivity		✓ Flexible wall	•
SWRC		✓	✓

✓ Data available

4.2 Soil properties

4.2.1 Base Course

4.2.1.1 Source

The “Base Course” used on the FM 2 site was obtained from the Fuqua contractor’s yard in Navasota, Texas. It met the requirements of TX DOT Item 247, Flexible Base, type “A” Grade

1. The base course was transported from the contractor's yard to the geotechnical testing laboratory at UT Austin in two plastic drums of 55 gallon each.

4.2.1.2 Visual-Manual Soil Classification and Description

As per ASTM D 2488, the base course was classified as silty gravel with sand (GM).

4.2.1.3 Specific Gravity

The average specific gravity (Gs) of Base course was obtained as 2.68.

4.2.1.4 Grain Size Distribution

Using a standard sieve analysis procedure (ASTM D 422), 2000 grams of base course were used to determine the grain size distribution as shown in Figure 4.1. Values for D_{10}, D_{30}, D_{60}, in addition to the uniformity coefficient and the coefficient of gradation, are shown in Table 4.2.

4.2.1.5 Soil Classification

Based on the grain size distribution data presented in Table 4.2 and Figure 4.1, the values of Cc and Cu were calculated as shown in Table 4.2. As per ASTM D 2487, the base course was then classified as silty gravel with sand (GM-ML).

4.2.1.6 Maximum Dry Density

Standard proctor compaction tests (ASTM D 698) were performed on the Base Course materials. The results obtained from tests performed using the standard proctor procedures are summarized in Table 4.2. The curve obtained using the procedure is as shown in Figure 4.2. The optimum water content, in addition to the corresponding maximum dry density is presented in Table 4.2.

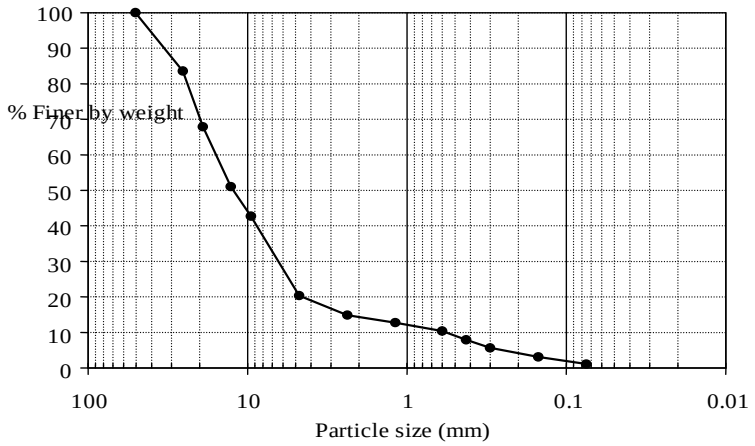

Figure 4.1: Grain size distribution curve for base course material used at FM 2

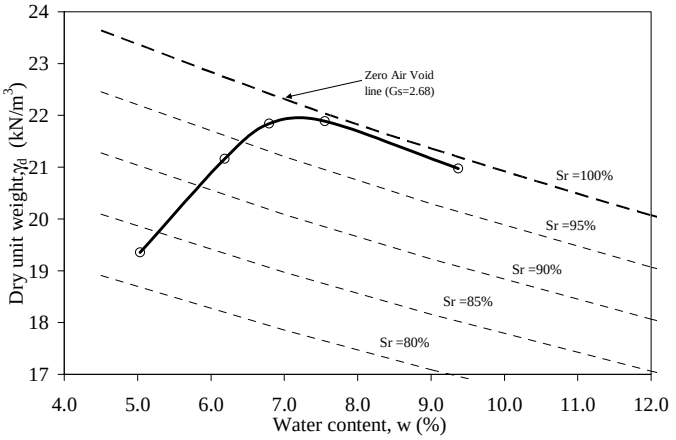

Figure 4.2: Standard Proctor Compaction curve for base course used on FM 2

Table 4.2: Properties of base course used on FM 2

Test	Index Parameter	Value	ASTM Standard
Soil Classification		GM-ML	D 2487
Specific Gravity	Specific Gravity, Gs		D 845-02
Particle size analysis	D_{10} , mm	0.6	D 422
	D_{30} , mm	6.0	D 422
	D_{60} , mm	10.8	D 422
	Uniformity coefficient, C_u	18.0	
	Coefficient of gradation, C_c	5.6	
Standard Proctor Compaction	Optimum water content, %	7.5	D 698
	Maximum dry unit weight, γ_d (kN/m^3)	22.0	D 698

4.2.2 FM 2 Clay

4.2.2.1 Source

The "FM 2 Clay" soil was obtained from the construction site in May 2005. The clay was excavated with a backhoe from a depth of approximately 5 feet near the station 184 close to the lane K6 on FM 2. The clay was transported to the laboratory at the University of Texas in two 55-gallon plastic drums. It was dried by placing it on metal trays in a temperature-controlled room at a temperature of 914º F (490º C) for 48 hours. The dried soil was then broken down with a hammer and passed through a soil crushing machine (Chipmunk Jaw Crusher model VD 67,

Bico Inc., Burbank, CA). The soil was then sieved and particles passing the #10 sieve were set aside for testing. Particles not passing the #10 sieve were reprocessed using the soil crushing machine until the material passed the #10 sieve.

4.2.2.2 Visual-Manual Soil Classification and Description

According to ASTM D 2488, FM 2 Clay is classified as gray clay (CH) with high plasticity, high dry strength, no dilatancy, and high toughness.

4.2.2.3 Specific Gravity

The average specific gravity (Gs) of FM 2 Clay was obtained as 2.70.

4.2.2.4 Grain Size Distribution

Using a standard sieve analysis procedure (ASTM D 422), 2000 grams of FM 2 clay were used to determine the grain size distribution. The data are presented in Table 4.3 and further illustrated in Figure 4.3. Values for D_{10}, D_{30}, and D_{60}, in addition to the uniformity coefficient and the coefficient of gradation, are presented in Table 4.3

4.2.2.4 Atterberg Limits

Atterberg limits were determined according to ASTM D 4318 for FM 2 clay. The values for the plastic limit and the liquid limit measured are reported in Table 4.3.

4.2.2.5 Soil Classification

Using the plasticity chart and ASTM D 2487, FM 2 clay was classified as clay of high plasticity (CH).

4.2.2.6 Maximum Dry Density

Standard proctor compaction tests (ASTM D 698) were performed on the FM 2 Clay. Results obtained from tests performed using the standard proctor procedures are summarized in Tables 4.3. The curve corresponding to the procedure was plotted in Figure 4.4. The optimum water contents, in addition to the corresponding maximum dry densities, are presented in Table 4.3.

4.2.2.7 Hydraulic Conductivity Test

Hydraulic conductivity test on FM 2 clay specimens prepared using standard proctor test was conducted using flexible wall permeameter. The results obtained are as listed in Table 4.3. The hydraulic conductivity of FM 2 clay varied with compaction water content as shown in Figure 4.5.

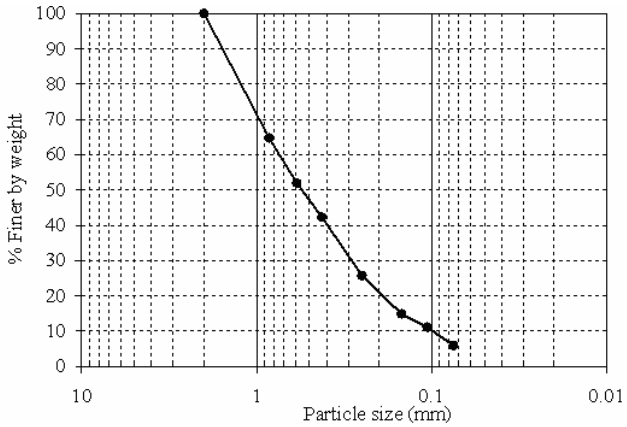

Figure 4.3: Grain size distribution of FM 2 clay

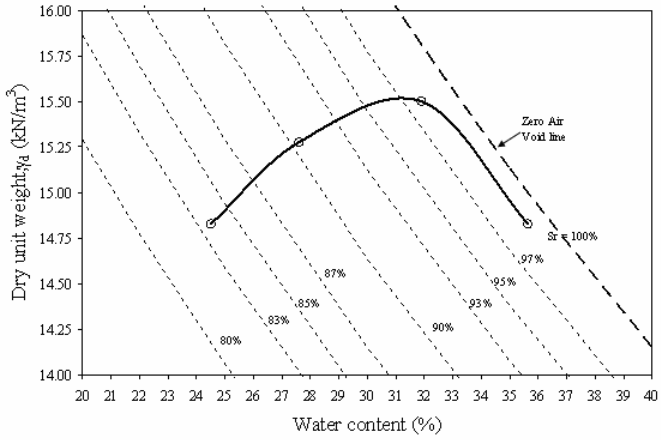

Figure 4.4: Standard Proctor compaction test on FM 2 clay

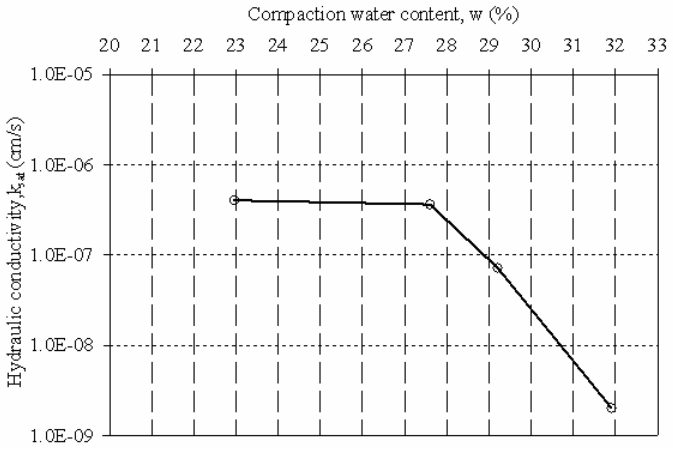

Figure 4.5: Hydraulic conductivity of FM 2 soil

Table 4.3: Properties of clay obtained from FM 2

Test	Index Parameter		Value	ASTM Standard
Soil Classification			CH	D 2487
Specific Gravity	Specific Gravity, Gs		2.7	D 845-02
Particle size analysis	D_{10}, mm		0.1	D 422
	D_{30}, mm		0.3	
	D_{60}, mm		0.7	
	Uniformity coefficient, C_u		7.0	
	Coefficient of gradation, C_c		1.3	
Atterberg Limits	Liquid Limit, LL (%)		33	
	Plastic Limit, PL (%)		72	
	Plasticity Index, PI (%)		39	
Standard Proctor Compaction	Optimum water content, %		32	D 698
	Maximum dry unit weight, γ_d (kN/m^3)		15.5	
Hydraulic Conductivity of Saturated soil using Flexible wall permeameter	Water content	Dry density	k_{sat}	
	(%)	kN/m^3	cm/s	
	23.0	13.0	4.0 X 10^{-7}	
	27.6	13.5	3.5 X 10^{-7}	
	29. 0	15.0	7.0 X 10^{-8}	
	32.0	15.0	2.0 X 10^{-9}	

4.2.3 Fire Clay

4.2.3.1 Source

The “Fire Clay” soil was obtained from the Elgin Butler Brick Company, 365 FM 696 in Elgin, Texas.

4.2.3.2 Visual-Manual Soil Classification and Description

According to ASTM D 2488, Fire Clay is classified as gray fat clay (CH) with high plasticity, high dry strength, no dilatancy, and high toughness.

4.2.3.3 Specific Gravity

The specific gravity was measured on two samples of Fire Clay. The tests were done according to ASTM D 854 and the average of the two values was used as a representative value for the specific gravity as reported in Table 4.4.

4.2.3.4 Hydrometer Analysis

Two hydrometer tests (ASTM D 422) were performed to determine the grain size distribution of a 50 g sample of Fire Clay as shown in Figure 4.6

4.2.3.5 Atterberg Limits

Atterberg limits were determined according to ASTM D 4318 for a sample of the Fire Clay as shown in Figure 4.7. Table 4.4 shows data pertaining to the liquid limit and plastic limit of soil.

4.2.3.6 Soil Classification

Using the plasticity chart in Figure 4.7 and ASTM D 2487, Fire Clay is classified as a CH fat clay material.

4.2.3.7 Maximum Dry Density

Standard and modified proctor compaction tests (ASTM D 698 and D 1557) were performed on the Fire Clay. The curves corresponding to both procedures were plotted in Figure 4.8. The optimum water contents, in addition to the corresponding maximum dry densities are presented in Table 4.4.

4.2.3.8 Hydraulic Conductivity

The soil water retention curve and variation of hydraulic conductivity with degree of saturation as obtained by Olsen and Daniel (1979) is as shown in Figure 4.9 and 4.10 respectively.

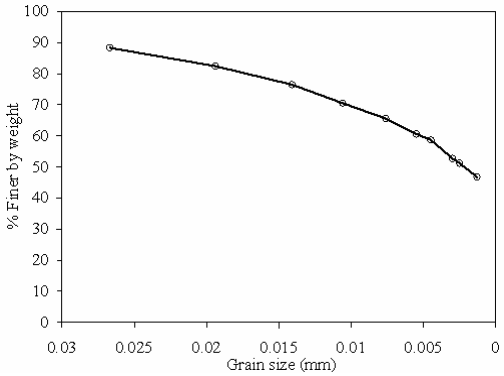

Figure 4.6: Grain size distribution of Fire Clay

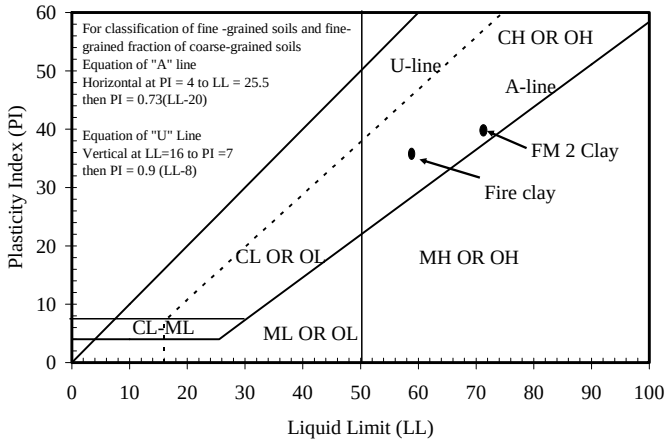

Figure 4.7: Plasticity Chart

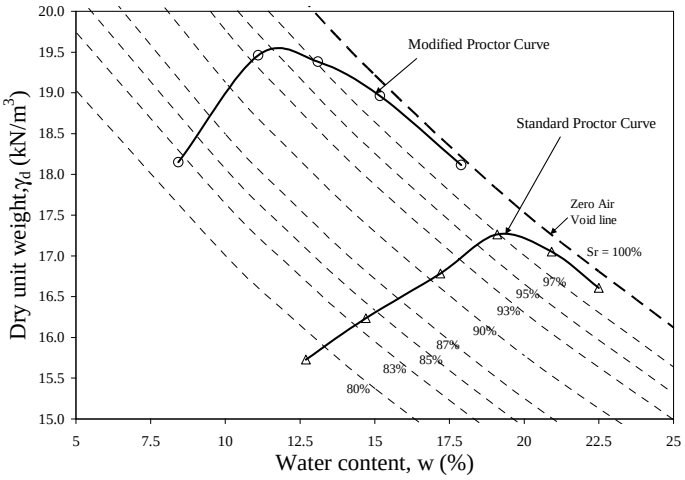

Figure 4.8: Standard and Modified Proctor compaction tests on Fire Clay

Table 4.4: Properties of Fire Clay

Test	Index Parameter	Value	ASTM Standard
Soil Classification		CH	D 2487
Specific Gravity	Specific Gravity, Gs	2.7	D 845-02
Atterberg Limits	Liquid Limit, LL (%)	23	
	Plastic Limit, PL (%)	59	
	Plasticity Index, PI (%)	36	
Standard Proctor Compaction	Optimum water content, %	19	D 698
	Maximum dry unit weight, γ_d (kN/m^3)	18	
Modified Proctor compaction	Optimum water content, %	11	D 1557
	Maximum dry unit weight, γ_d (kN/m^3)	20	

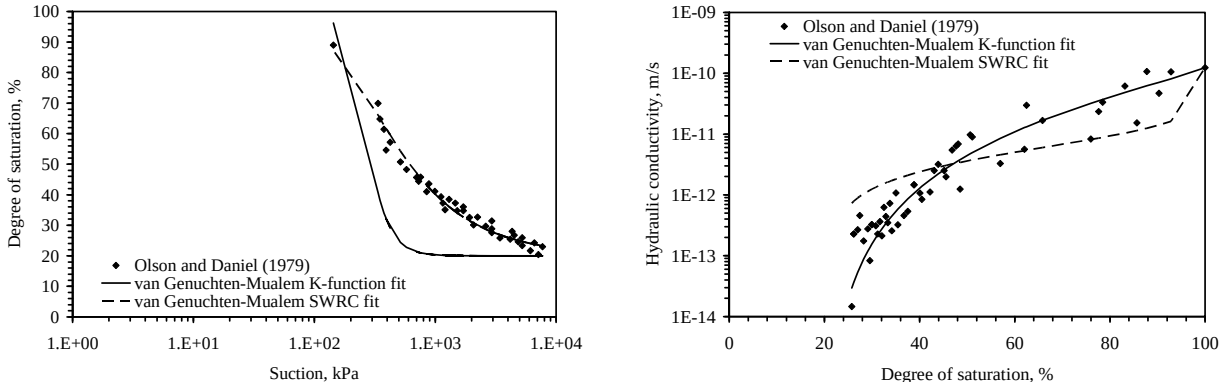

(a) (b)

Figure 4.9: a) SWRC for Fire Clay b) Hydraulic conductivity function for Fire Clay

4.3 Geosynthetics

4.3.1 Introduction

The geosynthetics used in this study consisted of two geogrids and one geotextile. Geogrid 1 (GG1) is a biaxial polypropylene geogrid manufactured by Tensar Corporation named BX 1100. Geogrid 2 (GG2) is a biaxial polyethylene geogrid with a protective coating manufactured by Mirafi and named as Bas X grid 11. Geotextile (GG3) is a polypropylene woven geotextile manufactured by Mirafi and branded as HP 570. The average index properties of these geosynthetics as reported by the manufacturers in both machine direction (MD) and cross-machine direction (XMD) are shown in Table 4.5

Table 4.5: Manufacturer's specification for the geosynthetics used in FM 2 project

Manufacturers' specification		GG1		GG2		GG3
Index Properties		**MD**	**XMD**	**MD**	**XMD**	**MD**
Aperture dimension	**mm**	25.0	33.0	25.4	25.4	0.6 (AOS)
Min. Rib Thickness	**mm**	0.76	0.76			
Tensile strength at 2% strain	**kN/m**	4.1	6.6	7.3	7.3	14.0
Tensile strength at 5% strain	**kN/m**	8.5	13.4	13.4	13.4	35.0
Ultimate tensile strength	**kN/m**	12.4	19.0	29.2	29.2	70.0

4.3.2 Index Testing of Geosynthetics

One roll of each geosynthetic used in FM 2 project was obtained from the construction site. The index properties of geogrids were tested as per the current TxDOT specifications. The tests included percent open area, rib thickness, single rib tensile test, and junction efficiency test. Further, wide width tensile testing of the geosynthetics was also conducted.

4.3.2.1 Percent Open Area

The percent open area of both the geogrids was measured by using a camera. The geogrid specimen was placed over the scanning table and the percentage of empty area as the ratio of total covered area was calculated using a Lab view program.

4.3.2.2 Rib Thickness

The rib thickness of both the geogrids in machine and cross machine direction was calculated using a vernier caliper. The average of five readings for thickness of the rib for both geogrids was reported.

4.3.2.3 Single Rib Tensile Testing

The single rib tensile testing was conducted for two geogrids as per ASTM (GRI) standard. The specimen consists of a single rib of the geogrid consisting of five junctions. The junctions at the ends were clamped using the serrated jaw grip to prevent slipping and crushing of the specimen. It was then attached to the load frame such that one rib had three junctions in the direction of concern. The test is conducted by moving the crosshead at speed of 50 mm/minute. The average maximum rib tensile strength and average geogrid tensile strength were calculated as

$$T_{rib} = \frac{\sum_{i=1}^{n} T_i}{n} \tag{4.1}$$

$$T_{grid} = (T_{rib})(n_{rib}) \tag{4.2}$$

where T_{rib} is the average maximum tensile strength (kN), T_i is the maximum rib tensile strength (kN), T_{grid} is the average geogrid tensile strength (kN/m) strength of i^{th} specimen, and n is the total number of test specimens. Finally, the average secant modulus at 2% strain ($M_{2\%}$) was calculated as

$$M_{2\%} = \frac{\frac{n_{rib}}{n}\sum_{i=1}^{n} T_{2\%}}{0.02} \tag{4.3}$$

where n is the total number of test specimens and $T_{2\%}$ is the tensile strength of the i^{th} specimen at 2% elongation.

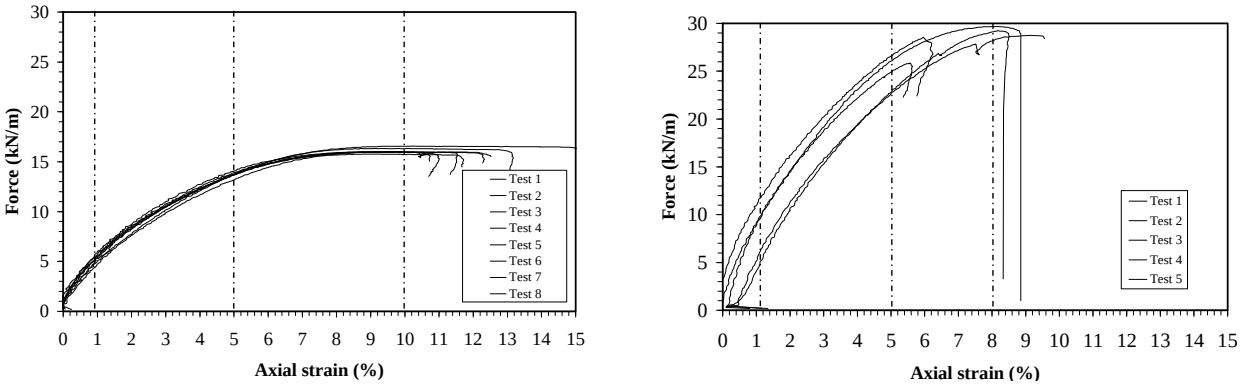

(a) (b)

Figure 4.10: Single rib tensile test for GG1 geosynthetic a) Machine direction b) Cross-machine direction

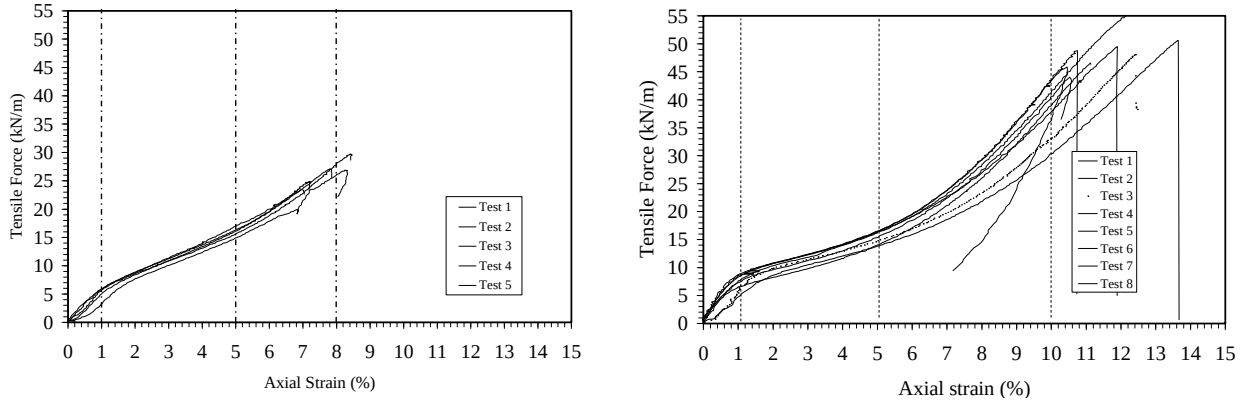

(a) (b)

Figure 4.11: Single rib tensile test for GG2 geosynthetic a) Machine direction b) Cross-Machine direction

4.3.2.4 Junction strength

The junction strength of both geogrids was tested using a tensile testing machine capable of moving at a constant rate of extension of 1.97 inches/minute (50 mm/minute). The specimen was prepared by cutting the junctions from each side of the geogrid to allow for the maximum amount of transverse ribs on each side of the junction to be tested. The specimen was mounted so that the center "T" was attached to the rib clamp and the transverse rib was attached on both sides of the junction to the junction clamp. The average maximum junction tensile strength was calculated as

$$J_{rib} = \frac{\sum_{i=1}^{n} J_i}{n} \tag{4.4}$$

$$J_{grid} = (J_{rib})(n_{junction}) \tag{4.5}$$

where J_{rib} is the average maximum junction tensile strength (kN), J_i is the maximum junction tensile strength of ith specimen (kN), n is the total number of test specimens, J_{grid} is the average geogrid junction strength (kN/m), and $n_{juction}$ is the number of junction per meter. Further, the junction strength efficiency ($E_{junction}$) was calculated as

$$E_{junction} = \frac{J_{rib}}{T_{rib}} X100 \tag{4.6}$$

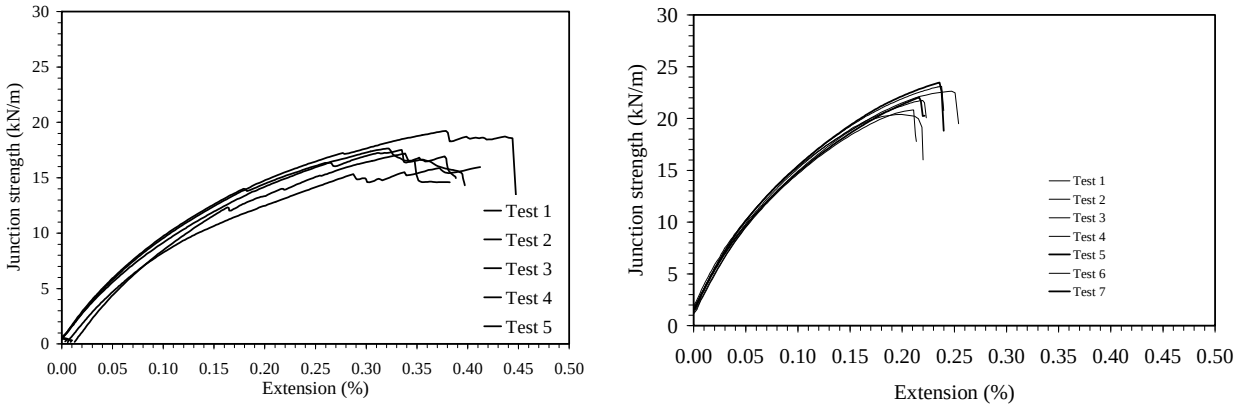

Figure 4.12: Junction strength of GG1 geosynthetic in a) Machine direction b) Cross-machine direction

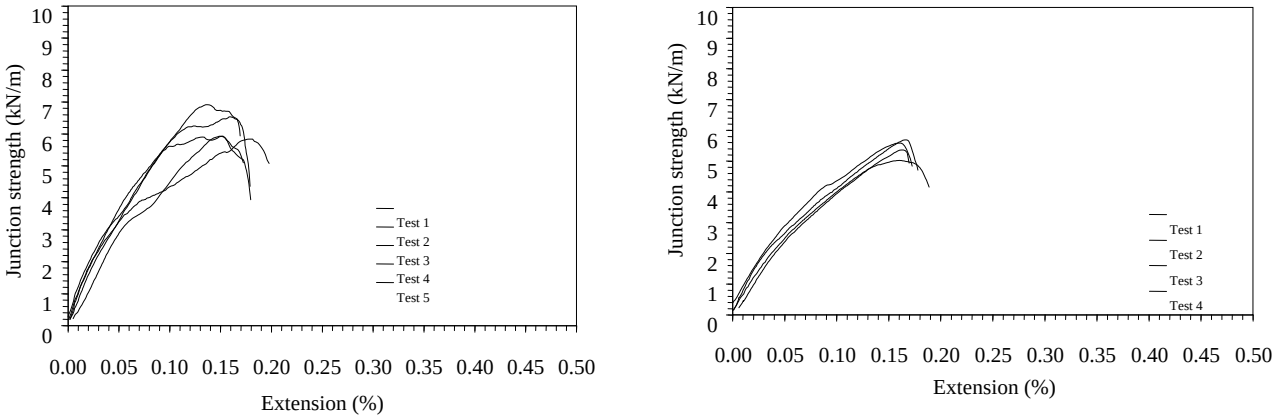

Figure 4.13: Junction strength of GG2 geosynthetic in a) Machine direction b) Cross-machine direction

Table 4.6: Junction efficiency of geogrids

Geogrid type	Ultimate Tensile Strength, kN/m	Junction Strength, kN/m	Junction efficiency (%)
GG1 MD	24.6	28.8	100.0
GG1 XD	18.6	15.3	82.6
GG2 MD	22.0	5.7	26.0
GG2 XD	57.9	7.0	12.2

4.3.3 Wide Width Tensile Testing

Wide width tensile testing was conducted on the three geosynthetics as per ASTM 4595 standard. The geosynthetics were tested in both machine and cross machine direction. Further the effect of strain rate on the tensile strength of these geosynthetics was evaluated by conducting tests at 1%, 5%, 10%, and 20% strain per minute. The average tensile strength obtained at each strain rate for each geosynthetic is reported in Table 4.3. The results indicated that the tensile strength of geogrids at low strains (1%) was independent of the strain rate at which test was conducted and there was slight increase in strength at higher strain levels of 5% and 10%. But the geotextiles showed strain dependency and the ultimate tensile strength increased with increase in the strain rate of testing. The values of tensile strength obtained using single rib tensile strength showed agreement with those obtained using the wide width tensile testing.

Table 4.7: Tensile strength of geogrids

Geosynthetic	Test Direction	% Strain at Max Load	Stiffness at 1% Strain	Stiffness at 2% Strain	Stiffness at 5% Strain	Stiffness at 10% Strain	Stiffness at Maximum Load
			(kN/m)	(kN/m)	(kN/m)	(kN/m)	(kN/m)
			1	2	5	10	
GT 3	MD	19	624	614	520	487	440
GT 3	XD	20	829	744	533	441	363
GG 2	MD	12	527	379	278	300	289
GG 2	XMD	13	579	446	282	316	366
GG 1	MD	14	368	287	199	132	97
GG 1	XD	10	531	437	323	232	226

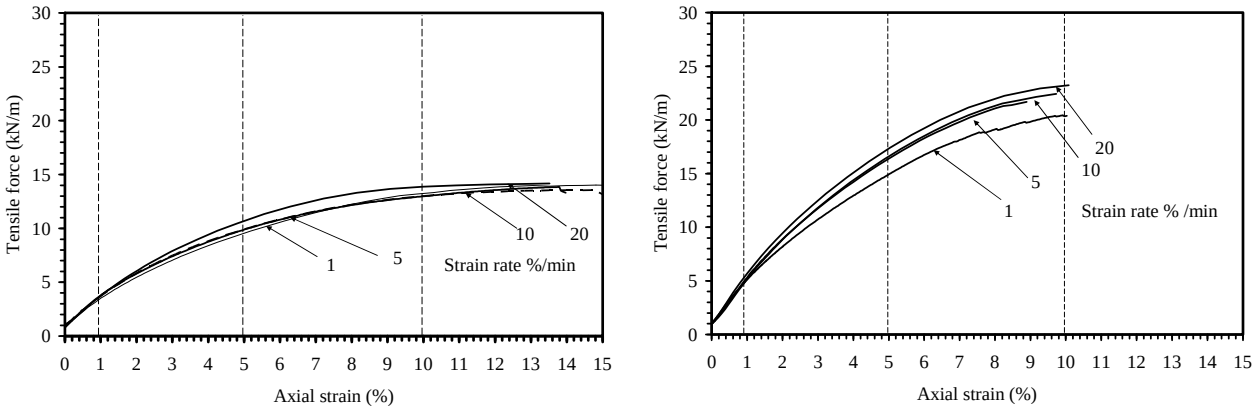

(a) (b)

Figure 4.14: Wide width tensile test on GG1 a) Machine direction b) Cross machine direction

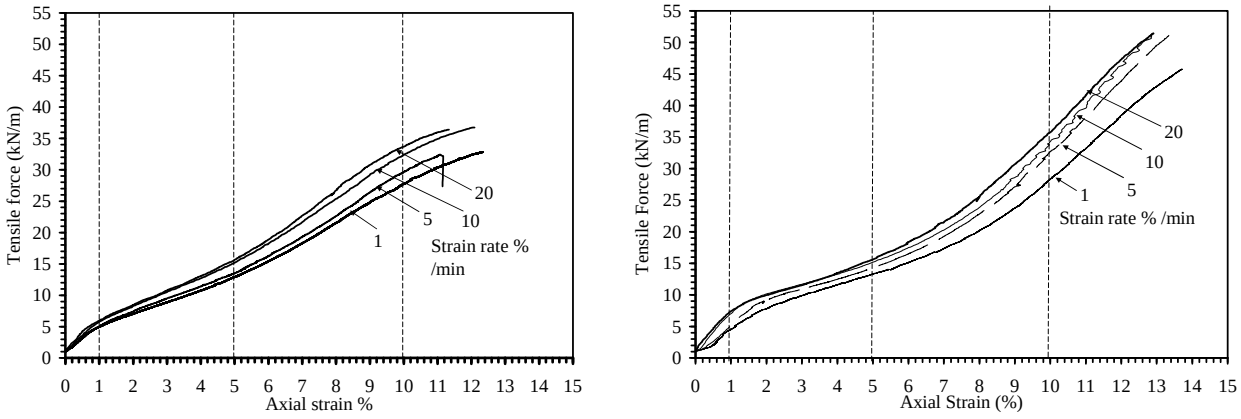

(a) (b)

Figure 4.15: Wide width tensile test on GG2 a) Machine direction b) Cross machine direction

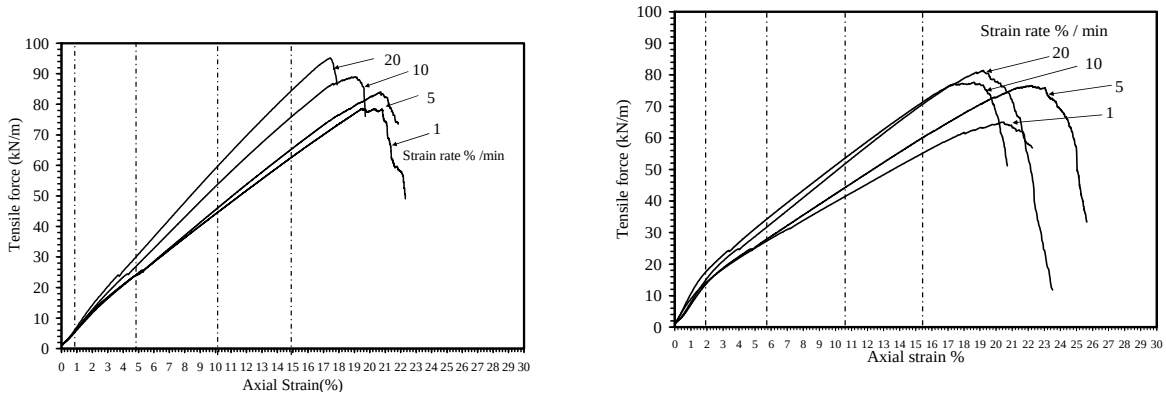

(a) (b)

Figure 4.16: Wide width tensile test on GG3 a) Machine direction b) Cross machine direction

The tests conducted to quantify property of geosynthetics used in the field section were further analyzed in light of current TxDOT specifications in Chapter 8. Their relative advantages and disadvantages to understanding the mechanisms involved in pavement design are also discussed later.

Chapter 5. Field Monitoring

5.1 Introduction

To quantify the structural conditions of in-situ pavement sections constructed by TxDOT on FM 2, a comprehensive field testing program was designed and conducted to characterize the conditions of the experimental pavement sections. The experimental pavement sections included sections with and without lime treatment, sections without geosynthetic reinforcement, and sections with different types of geosynthetic reinforcement. Two geogrids and one geotextile materials were used. Falling Weight Deflectometer (FWD) testing and the Rolling Dynamic Deflectometer (RDD) testing were performed on all experimental sections in different years and seasons. Elevation surveys were conducted to evaluate the seasonal change of pavement elevation because of the volumetric change of subgrade soil. All the testing information, data analyses, and results are summarized in this chapter.

5.2 FWD testing

5.2.1 Background of FWD Testing

The Falling Weight Deflectometer (FWD) is a trailer-mounted device widely used for the dynamic non-destructive testing on pavement (Huang, 1993). During a field testing, the FWD applies impact dynamic loading that produces a load wave similar to that of the moving traffic wheel load to the pavement surface. The FWD lift weights to predetermined heights and then drops them on a loading plate, which transfers the impulse force to the pavement. The magnitude and duration of the applied dynamic loading can be controlled by changing the weight of the drop mass, the drop height, and the plate stiffness of the drop weight strikes. The force imparted to the pavement is measured by the load cell, which is located directly above the load plate.

The pavement under the loading plate is deformed into a dish or bowl shape by the impulse force generated by the FWD (Schmalzer, 2006). The shape of the deformed pavement surface is called a deflection basin. The pavement responses due to the FWD dynamic loading are measured in terms of vertical deflections using a number of geophones in a linear array. The distances between geophones used in this testing are: The shape of the deflection basin can be plotted based on the vertical deflections measured by the geophones.

The deflections measured by the geophones indicate the overall pavement bearing capacity and the quality of subgrade. Analyzing pavement deflection data is the most efficient method to compare relative changes of the structural conditions between test stations (Bendana et al., 1994). The change in pavement structural conditions with time and traffic can also be examined by studying the surface deflection change over time periods. Generally, higher

deflections indicate weaker pavement system. The sensors far away from the loading plate typically record the response of the deeper layers, and the deflections measured by the sensors close to the loading plate represent the composite effects of all pavement layers.

The deflection data produced by the FWD testing can be used to back-calculate the modulus of each pavement layer when incorporating the thicknesses of pavement layers. The back-calculated moduli may help pavement engineers estimate the stress-strain distribution within the pavement under given loads, the bearing capacity of the pavement, predict the pavement life, and make a plan for pavement maintenance and rehabilitation.

The typical FWD has a distance measurement instrument (DMI) and temperature sensors. The DMI is a high-accuracy odometer that measures the distance of the FWD traveled along the road. The temperature sensors include an air temperature sensor and an infrared surface-temperature sensor. The air temperature and pavement temperature can be used to correct pavement material stiffness due to temperature effects.

5.2.2 FWD Testing Performed on FM 2

After the reconstruction of the pavement structure on FM 2, four FWD tests were performed on both eastbound (K1) and westbound (K6) lanes. The tests were conducted in February 2006, August 2006, November 2006, and February 2007. Table 5.1 lists the numbers of test stations in each FWD test. The typical distance between two neighboring test stations was 50 ft. The FWD tests were performed not only on the experimental sections but also on the other sections on FM 2. However, the following data analyses focus on the test stations in the experimental sections only. With a total length of 450 ft, each experimental section had approximately nine FWD test stations within it.

Table 5.1: Numbers of FWD test stations

Test Time	Number of Test Stations	
	Eastbound (K1)	Westbound (K6)
February 2006	139	170
August 2006	165	176
November 2006	159	167
February 2006	145	166

At each test station, the FWD applied four levels of dynamic loading to the pavement surface through a loading plate with a radius of 150 mm. The magnitude of the applied dynamic load was controlled by changing the drop height. The pavement vertical deflections were measured by seven geophones (sensors). The distance between two adjacent sensors was 12 in (304.8 mm). The deflection data produced by the FWD as well as the other testing information were collected in one file with an extension of .FWD for each test.

5.2.3 Deflection Data Analysis

The deflection data generated in the FWD tests were analyzed to evaluate the pavement condition. The larger the defection values, the weaker the pavement. At each test station, every geophone measured a deflection value. Therefore, there were seven deflection data points at each load level at each test station. These deflections are labeled from W1, at the loading plate center, through W7, which was measured by the furthest geophone from the loading plate center. Three deflection parameters were of the most interest for our study, including W1, W1-W2, and W7. W1 reflects bearing capacity of the entire pavement structure. W1-W2 is the Surface Curvature Index (SCI), which is a general indicator of pavement/base stiffness and suggests the consistency of the pavement condition (TxDOT, 2002). W7 reflects and correlates to the subgrade stiffness. A pavement structure can by diagnosed according to Table 5.2 in terms of Surface Curvature Index and W7 (TxDOT, 2002). The values in Table 5.2 are based on the assumption that the data collection load level is 9000 lbs, ±500 lbs, and that the sensor spacing at 12" intervals.

Table 5.2: Pavement diagnosis based on FWD deflection data

Sensor W7	Surface Curvature Index (SCI) (W1-W2)			Pavement Diagnosis
	Surface Treatment	Thin Asphalt (<3")	Thick Asphalt (>3")	
<1.30	<20	<15	<10	Good base, stiff subgrade
	20-40	15-30	10-20	Marginal base, stiff subgrade
	>40	>30	>20	Thin and/or soft base, stiff subgrade
1.3-1.9	<20	<15	<10	Good base, marginal subgrade
	20-40	15-30	10-20	Marginal base, marginal subgrade
	>40	>30	>20	Thin and/or soft base, marginal subgrade
>1.9	<20	<15	<10	Good base, soft or wet subgrade
	20-40	15-30	10-20	Marginal base, soft or wet subgrade
	>40	>30	>20	Thin and/or soft base, soft or wet subgrade

Figures 5.1 through 5.24 show the deflection data (W1, W1-W2, and W7) in the experimental sections on both eastbound and westbound of the four FWD tests. As the surface layer of the pavement structure on FM 2 is surface treatment, the critical values of the W1-W2 are 20 and 40. For all the FWD tests performed on FM 2, the values of W1-W2 (load level 9000 lbs) at most test stations are less than 20 mil. According to Table 5.2, all experimental sections on FM 2 have a base layer of good quality. The value of W7 changed from less than one to close

to three, which indicates the variability of subgrade quality along the experimental sections. The values of W7 at load level 9000 ± 500 lbs in the FWD test performed in August 2006 are generally higher than those in the other three tests. The possible reason is that there was a significant amount of rain in August 2006, which made the subgrade wet and soft. The values of W1, W1-W2, and W7 are larger under higher loading levels. However, the effect of geosynthetics reinforcement is not clearly reflected by the deflection data.

In order to clarify the joint effects of lime treatment and geosynthetic reinforcement, the mean and standard deviation of W1, W1-W2, and W7 were calculated for every experimental section. Only the deflection data of five test stations in the middle of each section were selected for the purpose of eliminating the effect of adjacent sections. If there were less than five FWD test stations in one experimental section, the deflection data for all test stations in this section were used to calculate the mean and standard deviation. Figures 5.25 to 5.48 present the mean and the deflection range within one standard deviation (from mean- standard deviation to mean + standard deviation) of W1, W1-W2, and W7 in every test.

It was expected that the lime-treated sections had significantly lower W1, W1-W2, and W7 than the sections without lime treatment. However, the averages W1, W1-W2, and W7 of some lime-treated sections are larger than the experimental sections without lime treatment. Only the deflection data generated in the FWD test performed in August 2006 on Westbound FM 2 clearly suggest that the lime-treated sections are stronger than the sections without lime. The deflection data of other tests have some clue of better performance of lime-treated sections, but the evidence is not convincing.

To study how deflections change with time, the average values of W1, W1-W2, and W7 of all FWD test were plotted together to analyze the effect of time on the three parameters. Figures 5.49 through 5.54 illustrate the average values of W1, W1-W2, and W7 in every test. It was expected that the pavement deflections generated by the FWD tests would increase with time. However, no evidence has been found that the latest FWD test, performed in February 2007, measured larger deflections than those generated by any one of the previous tests. Figures 5.51 and 5.54 show that most experimental sections have the largest average values of W7 in the test performed in August 2006 on both eastbound and westbound. This fact indicates again that the subgrade may be softer and wetter in August 2006 than the winter seasons.

On either eastbound lane or westbound lane, there are two repetitions of experimental sections. Therefore, there are in total four repetitions of each experimental section on both lanes of FM 2. As stated in previous chapter, the letter “W,” “E,” “a” and “b” are used to distinguish the different repetitions. If treating the repetitions as variable, every section from No. 1 to No. 8 has four values of W1 in every FWD test. For example, the No. 1 section has four W1 values in each test, one for Section 1Wa, one for Section 1Wb, one for Section 1Ea, and one for Section 1Eb. As four FWD tests have been conducted on both eastbound and westbound lanes, every section from No. 1 to No. 8 have 16 W1 values (4 repetitions times 4 tests), as well as 16 W1-W2 values, and 16 W7 values. Figures 55, 56 and 57 show the 16 values of W1, W1-W2, and

W7 at Section 1 through Section 8. The deflections at one section generated by different FWD tests were shifted slightly in the figures to make the illustration clearer. In the three figures, the same markers at one section indicate the four repetitions in one FWD test. The same markers were expected to group together at each section because they have the same pavement structure. However, the studied deflection values varied significantly between repetitions at one section in one test. This fact indicates that the quality of the experimental sections is not consistent. It is also clear in these figures that the deflections did not increase with time.

In summary, based on the analysis on the FWD deflection data, the lime treated sections had lower deflection values than sections without lime treatment.

5.2.4 Modulus Back-Calculation

A number of computer programs have been developed for back-calculating the moduli of pavement layers based on the FWD deflection data. Most the programs assume that the pavement structure is a multi-layer linear elastic system, such as WESDEF, MODULUS, and EVERCALC. Some of these linear elastic programs are user-friendly and provide fast estimate of the layer moduli. The finite element program, such as ABAQUS and ANASYS, are more powerful and versatile for accurately back-calculating the pavement layer moduli by incorporating nonlinear properties of materials. However, typical finite element programs require considerable computation time and effort. In addition, a nonlinear model in finite element program may need a large number of parameters, which may be hard to determine in engineering practice.

The software MODULUS 6.0 was used to back-calculate the moduli of pavement layers based on the FWD deflection data. MODULUS was developed by Texas Transportation Institute (TTI) and has been used since the early 1990s to evaluate pavement structure and to provide layer modulus values for structural design (Liu and Scullion, 2001). The early versions of MODULUS were based on DOS platform. The latest version, MODULUS 6.0, is coded based on the Windows technology for user to analyze FWD deflection data in Windows system.

According to the pavement structure information provided by TxDOT, the pavement of FM 2 has a one-inch surface treatment, 7-inch new base, 15-inch existing based and subgrade. If treating the thin surface treatment as a separate layer, significant errors may occur during the modulus back-calculation process. The reason is that MODULUS is not designed for thin-surface pavement structures. Therefore, the surface treatment layer was combined with the new base, which became the top layer with a total thickness of 8 in. (200 mm) in the back-calculation process. The second layer in the back-calculation was the existing base with a thickness of 15 in (380 mm). Figures 5.58 to 5.81 present the back-calculated moduli of the surface layer (treatment plus new base), second layer (existing base), and subgrade based on the deflection data generated by every FWD test.

5.3 RDD testing

5.3.1 Background of Rolling Dynamic Deflectometer

The Rolling Dynamic Deflectometer (RDD) is a mobile, truck-mounted device used for nondestructive testing of highway and airport (Bay and Stokoe, 1998). This research prototype device was developed at The University of Texas at Austin in cooperation with the Texas Department of Transportation (TxDOT) and the Federal Highway Administration (FHWA). The RDD testing is able to provide a continuous profile of pavement conditions, which is a major advantage over other nondestructive testing methods. Most nondestructive and destructive testing techniques can only perform testing at discrete pavement locations. A continuous profile measured by the RDD offers an informative picture of the entire pavement sections. Another advantage of the RDD is that the testing can be performed in the presence of traffic.

The RDD was converted from a Vibroseis truck that is used in exploration geophysics to apply large dynamic forces to the ground for the purpose of generating seismic waves for oil prospecting. The gross weight of the RDD is approximately 50 kips (222 kN). The RDD has four major components: i) an electro-hydraulic dynamic loading system; ii) a force measurement system; iii) a array of rolling sensors that are located underneath the RDD; and iv) a distance measurement system (Lee, 2006). During the testing, the RDD applies both dynamic and static forces to the pavement surface simultaneously through two polyurethane loading rollers. The applied forces are measured by four load cells located between the loading rollers and the upper loading platform. A typical RDD loading function in the testing consists of a steady-state sinusoidal dynamic force and a static hold-down force.

The array of rolling continuously measures the dynamic deflections due to the sinusoidal loading so that the continuous deflection profiles can be obtained. The continuous deflection profiles provide virtually 100% coverage of the entire project length. The RDD is able to measure the dynamic deflection of the pavement surface as the RDD rolls along the test path when using well-designed rolling sensors. The RDD rolling sensors are geophones mounted on a 3-wheel cart. As a contact-type sensor, each RDD rolling sensor uses gravity as the reference to measure the pavement deflection.

During the testing, the travel distance of the RDD is measured by a rotary optical encoder. A PC-based data acquisition system records individual analog signals from the load cells, rolling sensors and the distance encoder. Therefore, all measurements are post-processed after field testing to obtain the continuous deflection profile. A typical continuous deflection profile contains the coordinates of the surveyed points in terms of the RDD travel distance and the pavement deflection at each survey point.

5.3.2 RDD Testing Performed on FM 2

Two RDD tests have been performed on FM 2. The first RDD testing was conducted in January 2005 before the pavement of FM 2 was reconstructed. The second RDD testing was in February 2006 after the pavement reconstruction of FM 2.

The first RDD testing was conducted only on the westbound lane (K6). An operating frequency of 35 Hz was used. During the testing, two different levels of loading were applied to the pavement surface, respectively. The lower load level had a static force of eight kips and a peak-to-peak dynamic force of four kips. The higher load level consisted of a static force of 13 kips and a peak-to-peak dynamic force of 6 kips. These continuous deflection profiles were used to determine the locations of experimental sections, which were desired to be built on the subgrade with approximately the same quality.

The second RDD testing was performed on both westbound lane (K6) and eastbound lane (K1). Two load levels were used in the testing: low load and high load. The low load had a static force of nine kips and a dynamic peak-to-peak force of 2 to 3 kips. The loading frequency of the low load was 35 Hz. The RDD tested all 32 experimental sections at the low load level. The high load had a loading frequency of 30 Hz, and it was composed of a static force of 11 kips and a dynamic peak-to-peak force of 4 kips. Only some of the experimental sections were tested by RDD at the high load level, including 4 sections on the eastbound lane (K1) and 12 sections on the westbound lane (K6).

5.3.3 Data Analysis of RDD Deflection

1. Average Deflection of Experimental Sections

The RDD deflection profile at any load level contains a large amount of survey points. For example, deflections at 145 points were surveyed by the RDD in Section 1Wa, which has a length of 450 ft on the westbound lane. The average and the 95% confidence interval of deflection in every experimental section were calculated at both low load level and high load level. Figures 5.4, 5.5, 5.6 and 5.7 present the calculated results. As the RDD did not test all sections at the high load level, a number of sections do not have the deflection data at the high load, as shown in Figures 5.6 and 5.7.

The lime-treated sections, whose labels begin with 5.5, 5.6, 5.7, or 5.8, were expected to have lower deflections. However, the calculation results in Figures 5.4 through 5.7 do not follow the intuitive expectation. Some lime-treated sections had higher average deflection than that of the section without lime treatment. For example, the average deflection of Section 1Wa is supposed to be higher than the average deflection of Section 5Wa because both sections were exactly the same except Section 5Wa was treated with lime; however, the calculation showed the opposite result. The same trend applied when comparing the average deflection values of Section 2Wa and Section 6Wa, Section 3Wa, and Section 7Wa, and Section 4Wa and Section 8Wa.

The computed average deflections do not reflect the benefit of geosynthetic reinforcement. The geosynthetic-reinforced sections were expected to have lower deflection, but this expectation is not illustrated in Figures 5.4 to 5.7. Some sections without geosynthetics had lower deflection values. An example can be found in Figure 5.4: when comparing Sections 1Wa, 2Wa, 3Wa and 4Wa, Section 1Wa was expected to have the highest deflection because it was not reinforced by geosynthetics while the other three were all reinforced by different types of geosynthetics. However, Section 1Wa had the lowest average deflection value among the four sections without lime treatment. Another example is the four lime-treated sections: Sections 5Wa, 6Wa, 7Wa, and 8Wa. Section 5Wa without geosynthetic reinforcement was supposed to have the highest deflection, but Figure 4 shows that Section 5Wa had the lowest average deflection compared to the other three sections.

2. Correlation between RDD Deflection and FWD Deflection

Statistical analysis was conducted to study the relationship between the deflections measured by the RDD and the deflections surveyed by FWD. In order to avoid the effects of climate and pavement age, only the results of the second FWD testing were selected to compare to the second RDD testing measurements. Both selected FWD and RDD tests were performed on the same day in February 2006.

First of all, the average FWD W1 deflection of all experimental sections was plotted against the average RDD deflection, as presented in Figures 5.8 and 5.9. These two figures show that the FWD W1 deflection and the RDD deflection were approximately linearly correlated. Therefore, a linear model was used to predict the FWD W1 deflection (dependent variable) based on the available RDD deflection data (independent variable). Besides the RDD deflection data, additional explanatory variables were used in the linear model, including the high load level, the westbound lane (K6) and the lime treatment. Except for the RDD deflection data, the other three regressors were dummy variables in the regression analysis. A dummy variable, also known as indicator or bound variables, takes the values 0 or 1 to indicate the absence or presence of some categorical effect. For example, Section 6Eb had an average FWD W1 of 16.80 mils and an average RDD deflection of 31.20 mils at the low load level; Section 6Eb was treated by lime and was on the eastbound lane (K1); therefore, for this section, the variable lime had a value of 1, the variable of high load had a value of 0, and the variable K6 had a value of 0.

The first regression model started from the following form:

$$W1 = \beta_0 + \beta_1 \cdot RDD + \beta_2 \cdot \text{lime} + \beta_3 \cdot HighLoad + \beta_4 \cdot K6 \qquad (5.1)$$

in which:

$W1$ = the average FWD W1 deflection of every experimental section;

RDD = the average RDD deflection of every experimental section;

lime = the dummy variable of lime treatment, if the section was treated by lime, then this variable has a value of 1; otherwise the value is 0;

HighLoad = the dummy variable of high load level in the RDD testing, if the section was tested at the high load level in the RDD testing, this variable has a value of 1; otherwise the value is 0;

$K6$ = the dummy variable of westbound lane, if the section is on the westbound lane (K6), this variable has a value of 1; otherwise the variable has a value of 0; and

β_0 through β_4 = parameters to be estimated.

The model estimation results are summarized in Table 5.3. The t-statistic for β_0 is as small as 0.150, which indicates that the intercept is not statistically significant in this model. This fact is satisfactory and follows intuitive expectation because a section with a zero RDD deflection is expected to have a zero FWD W1 deflection. In other words, if extending the trend lines, these lines should go through the origin (0, 0). According to engineering judgment, these lines should not have an intercept, which supports the regression results in this statistical analysis.

The average RDD deflection has a large t-statistic value, which suggests this independent variable is statistically significant. The estimated parameter has a positive sign indicating a higher RDD deflection is associated with a higher FWD W1 deflection. The lime treatment and the high load level are also statistically significant in this analysis. The predicted FWD W1 deflection has a lower value on a section with lime treatment. A high load level used in the RDD testing leads to a larger FWD W1 deflection than a low load level based on the estimated β_3. The westbound lane (K6) is not statistically significant in this model. This finding indicates that the pavement and subgrade quality are approximately the same on both lanes (K1 and K6). Therefore, it is reasonable to remove the dummy variable of westbound lane from the regression model.

Table 5.3: Estimation Results of Model with Four Variables

Parameter	Parameter Description	Parameter Estimate	T-Statistic	R-Square
β_0	Intercept	6.91E-01	0.150	Multiple R: 0.646 R Square: 0.418 Adjusted R Square: 0.362
β_1	Average RDD deflection	6.06E-01	4.671	
β_2	Lime treatment (dummy variable)	-3.87E+00	-2.647	
β_3	High load level in RDD testing (dummy variable)	3.13E+00	1.973	
β_4	Westbound lane (dummy variable)	2.69E+00	1.548	

The second regression model was developed without the dummy variable of westbound lane, as in the following form:

$$W1 = \beta_0 + \beta_1 \cdot RDD + \beta_2 \cdot \text{lime} + \beta_3 \cdot HighLoad \quad (5.2)$$

The number of the independent variable reduces from four to three because the variable of westbound lane is not statistically significant in the first regression model. The estimation results of the second model are shown in Table 5.4. The intercept is statistically insignificant, which is reasonable because a zero RDD deflection should be associated with a zero FWD W1 deflection and the intercept should be zero. The three regressors are all statistically significant. The signs of the estimated parameters are the same as the parameters estimated in the first model. The R-square of the second model does not decrease considerably because of the remove of the dummy variable of westbound lane.

Table 5.4: Estimation Results of Model with Three Variables

Parameter	Parameter Description	Parameter Estimate	T-Statistic	R-Square
β_0	Intercept	4.88E+00	1.289	Multiple R: 0.620 R Square: 0.384 Adjusted R Square: 0.341
β_1	Average RDD deflection	5.09E-01	4.407	
β_2	Lime treatment (dummy variable)	-3.51E+00	-2.392	
β_3	High load level in RDD testing (dummy variable)	3.41E+00	2.129	

In order to characterize possible effect of the geogrid reinforcement in the regression, a third model was developed in the following form:

$$W1 = \beta_0 + \beta_1 \cdot RDD + \beta_2 \cdot \text{lime} + \beta_3 \cdot HighLoad + \beta_5 \cdot TG + \beta_6 \cdot MG + \beta_7 \cdot MT \qquad (5.3)$$

where:

TG = dummy variable of Tensor Geogrid, if the section was reinforced by Tensor Geogrid, this variable has a value of 1, otherwise zero;

MG = dummy variable of Mirafi Geogrid, if the section had a layer of Mirafi Geogrid, this variable has a value of 1, otherwise zero; and

MT = dummy variable of Mirafi Geotextile, if the section was reinforced by Mirafi Geotextile, this variable has a value of 1, otherwise zero.

The estimation results are presented in Table 5.5. The first three independent variables remain their significance in this model. The inclusion of the three variables of geosynthetics does not change the statistical insignificance of the intercept. All Tensor Geogrid, Mirafi Geogrid, and Mirafi Geotextile are not statistically significant in this model. The estimation results of this model suggests that the lime treatment considerably affect the correlation between FWD W1 deflection and the RDD deflection, and that the geosynthetic reinforcement does not have a significant effect on the prediction of FWD W1 deflection based on the RDD deflection data.

Table 5.5: Estimation Results of Model with Six Variables

Parameter	Parameter Description	Parameter Estimate	T-Statistic	R-Square
β_0	Intercept	5.04E+00	1.304	Multiple R: 0.664 R Square: 0.441 Adjusted R Square: 0.357
β_1	Average RDD deflection	4.45E-01	3.733	
β_2	Lime treatment (dummy variable)	-3.48E+00	-2.399	
β_3	High load level in RDD testing (dummy variable)	3.22E+00	2.024	
β_5	Tensor Geogrid	5.94E-01	0.286	
β_6	Mirafi Geogrid	3.01E+00	1.471	
β_7	Mirafi Geotextile	3.49E+00	1.659	

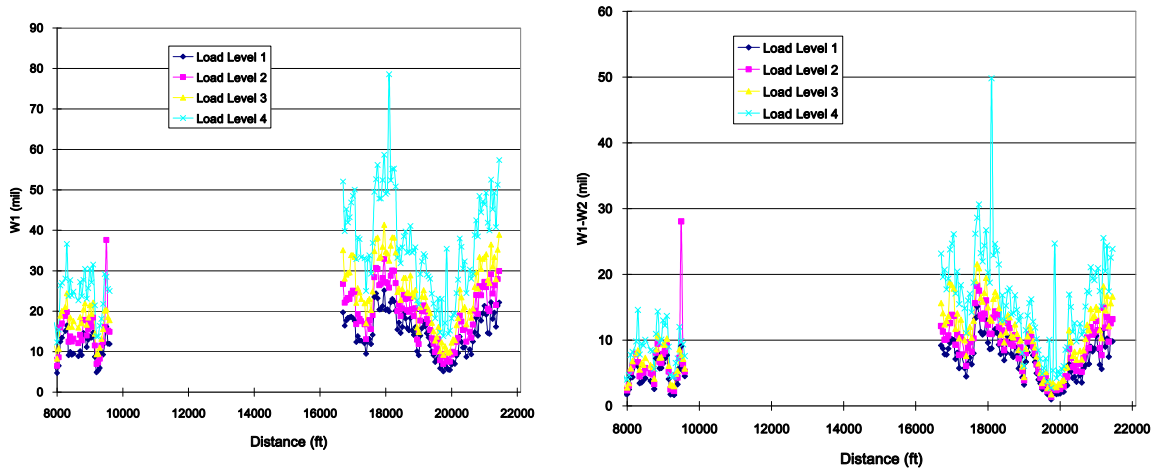

Figure 5.1: Eastbound Lane FWD Test in February 2006 a) W1 b) W1-W2

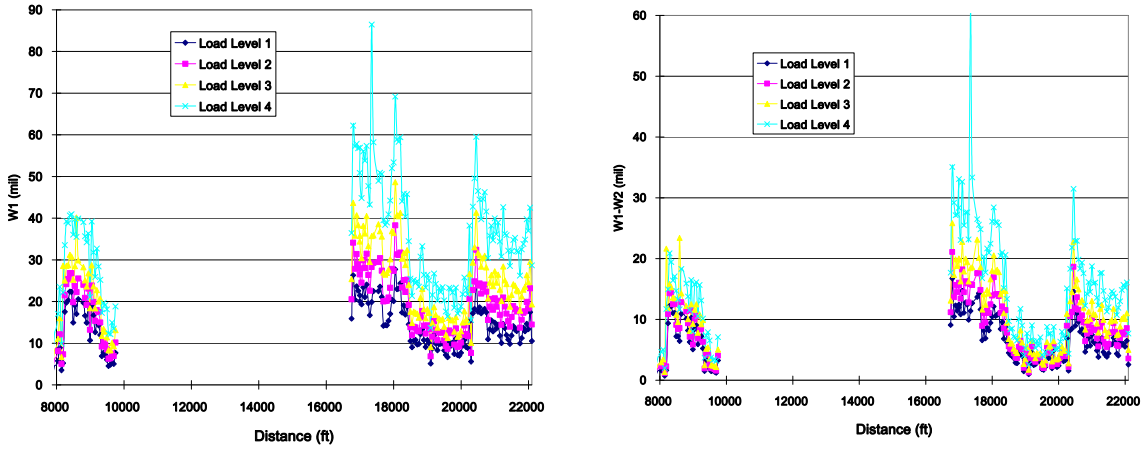

Figure 5.2: Westbound Lane FWD Test in February 2006 a) W1 b) W1-W2

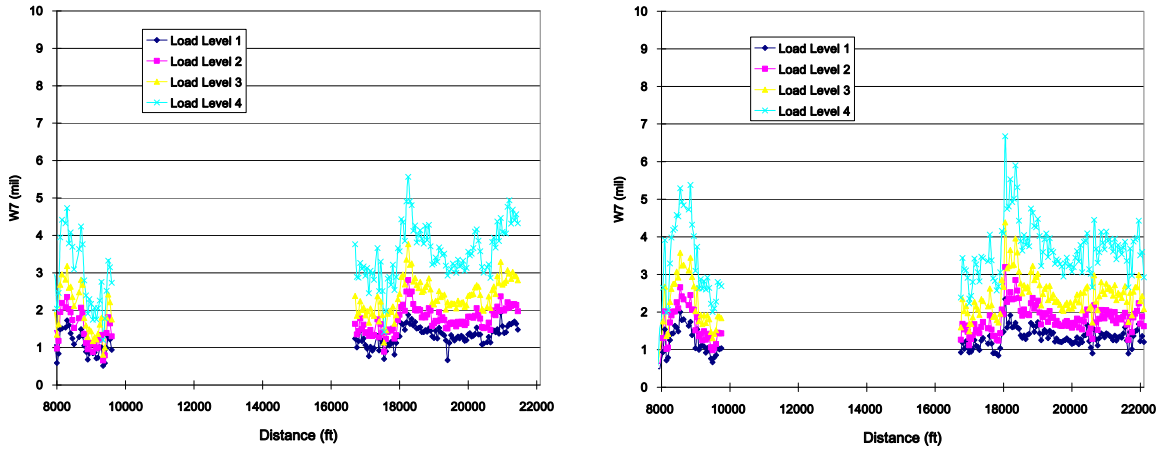

Figure 5.3: W7 load for FWD test in February 2006 a) Eastbound b) Westbound

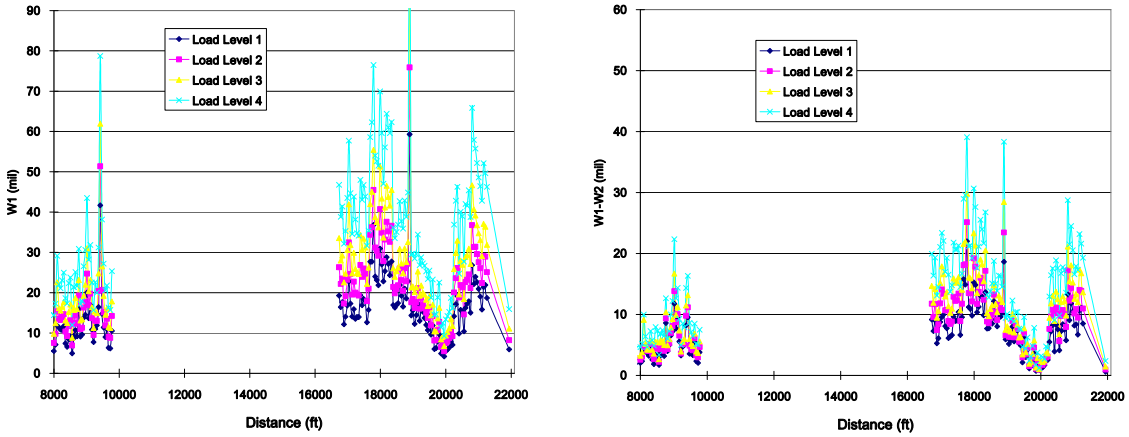

Figure 5.4: Eastbound Lane FWD Test in August 2006 a) W1 b) W1-W2

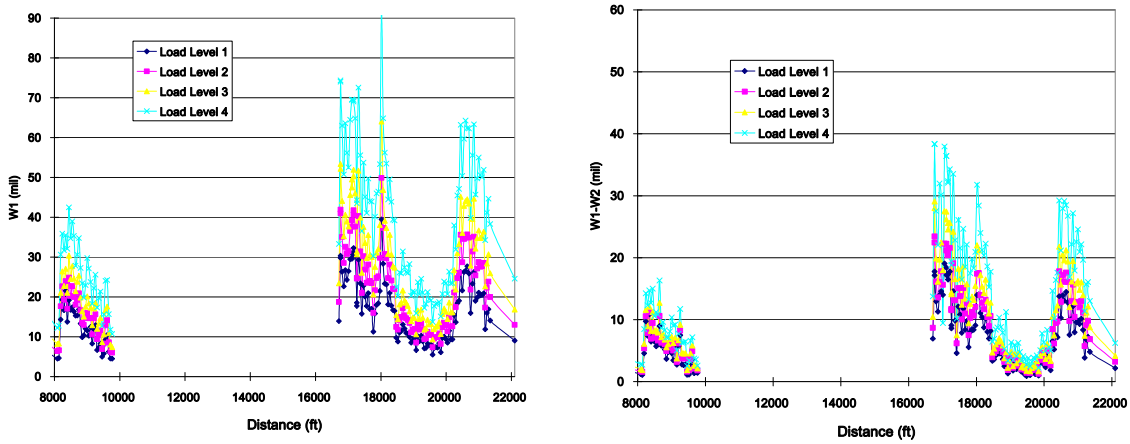

Figure 5.5: Westbound Lane FWD Test in August 2006 a) W1 b) W1-W2

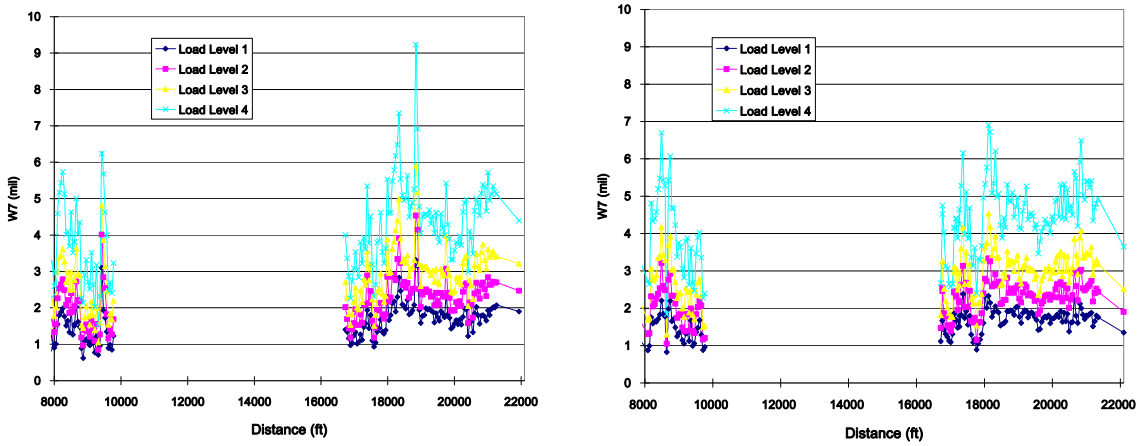

Figure 5.6: W7 load for FWD test in August 2006 a) Eastbound b) Westbound

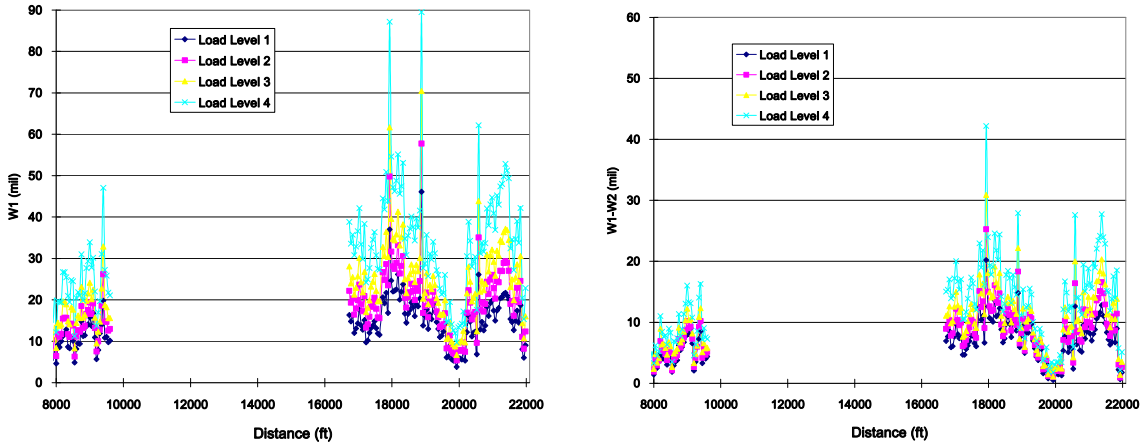

Figure 5.7: Eastbound Lane FWD Test in November 2006 a) W1 b) W1-W2

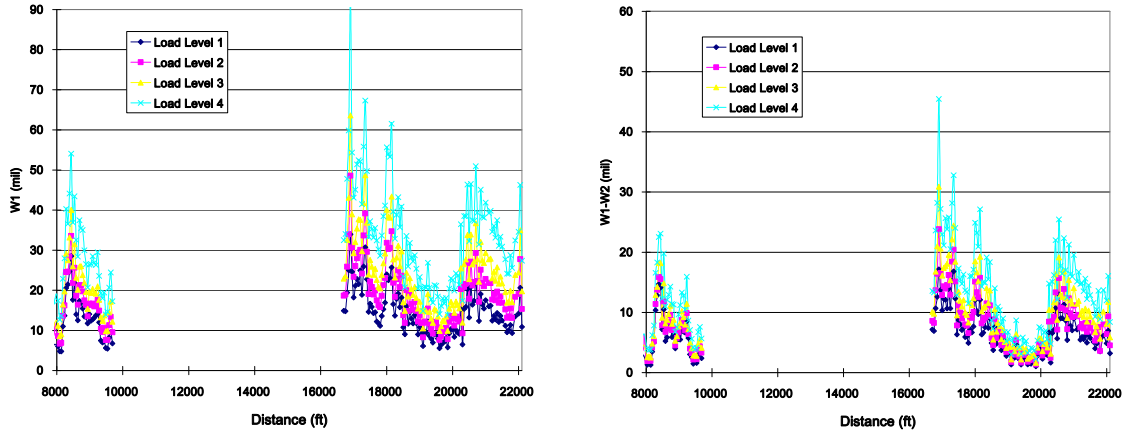

Figure 5.8: Westbound Lane FWD Test in November 2006 a) W1 b) W1-W2

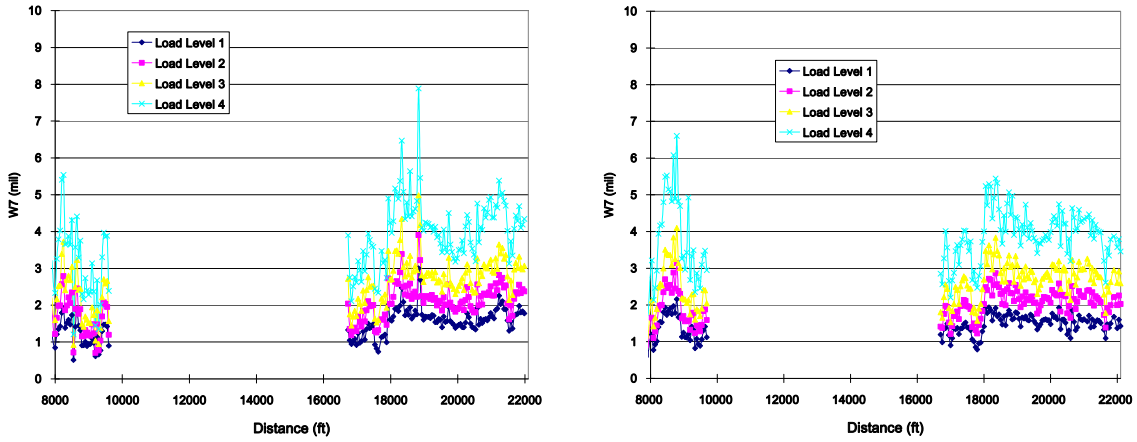

Figure 5.9: W7 load for FWD test in November 2006 a) Eastbound b) Westbound

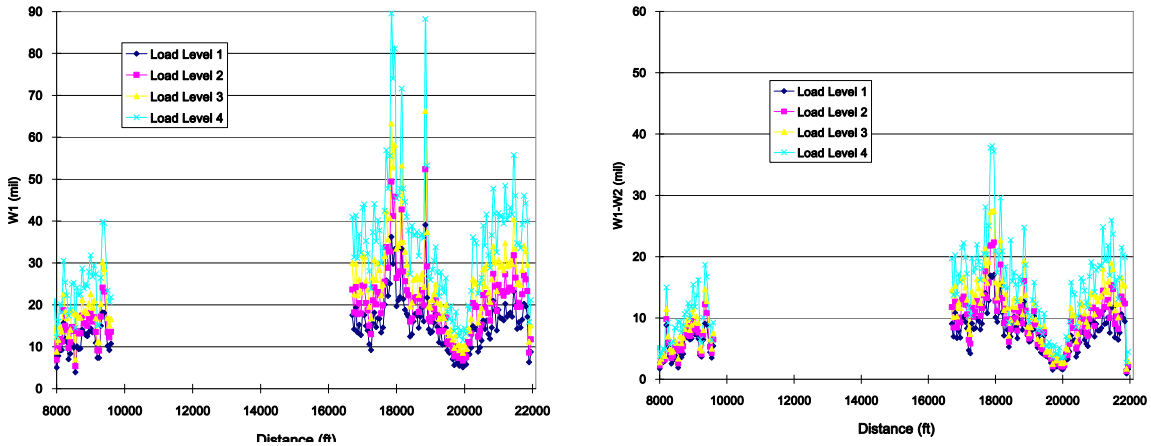

Figure 5.10: Eastbound Lane FWD Test in February 2007 a) W1 b) W1-W2

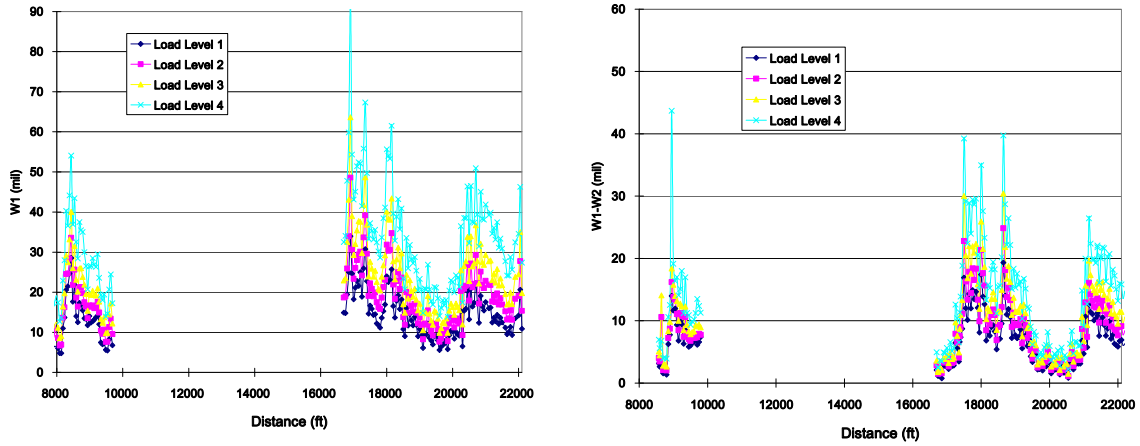

Figure 5.11: Westbound Lane FWD Test in February 2007 a) W1 b) W1-W2

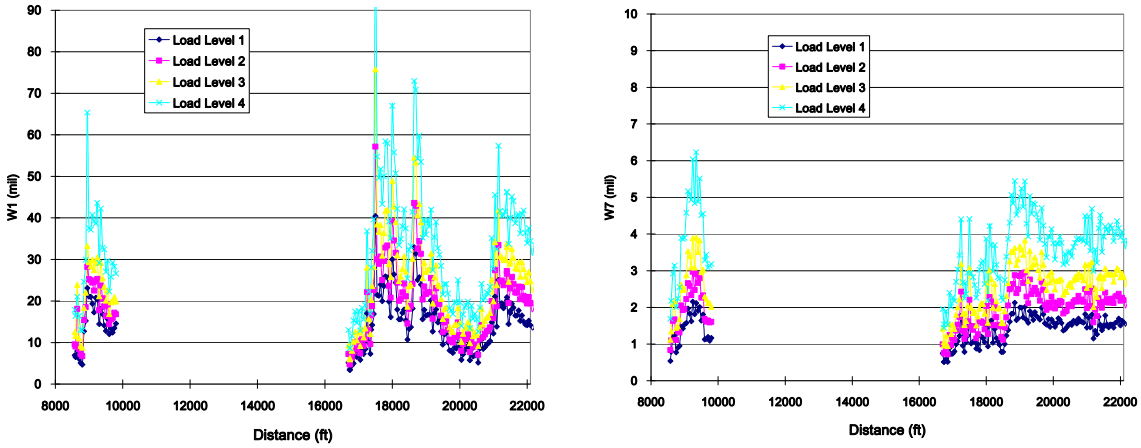

Figure 5.12: W7 load for FWD test in February 2007 a) Eastbound b) Westbound

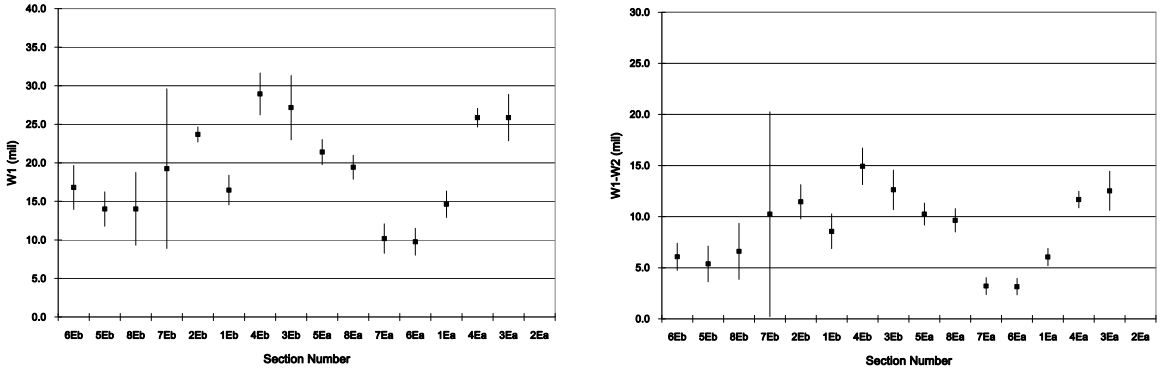

Figure 5.13: Mean and Standard deviation in Eastbound Lane for February 2006 a)W1 b) W1-W2

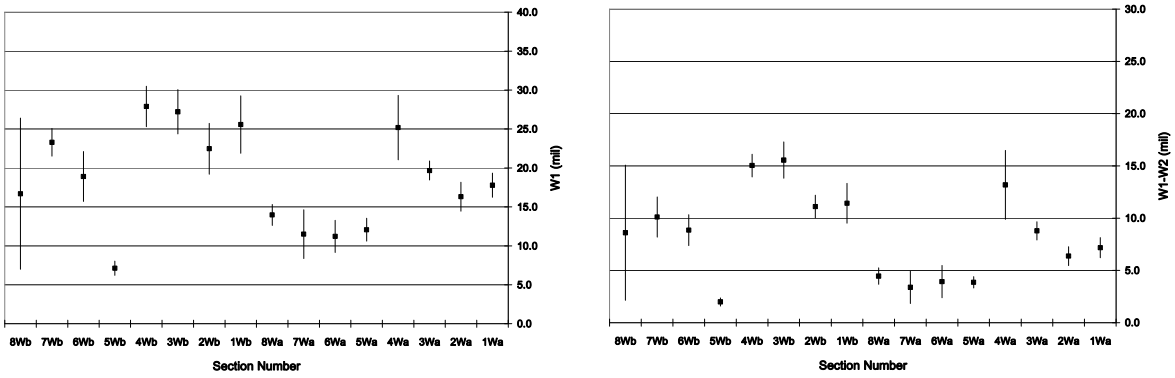

Figure 5.14: Mean and Standard deviation in Westbound in February 2006 a) W1 b) W1-W2

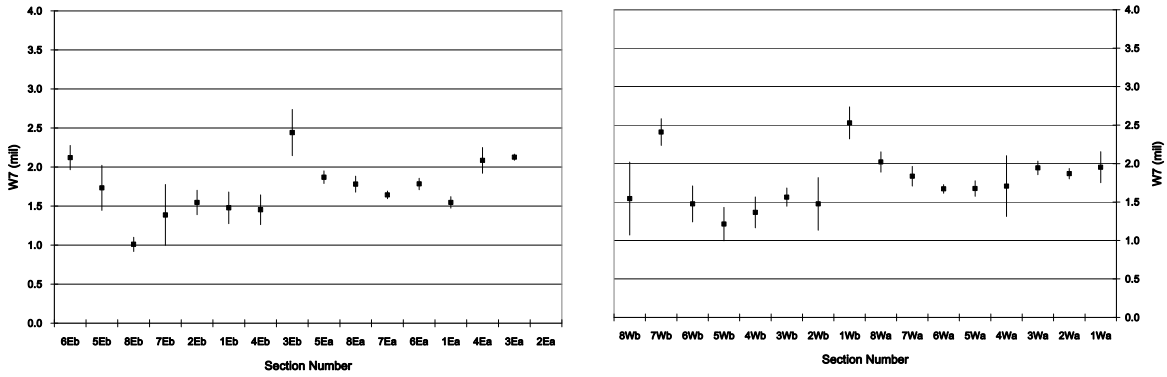

Figure 5.15: Mean and Standard deviation for W7 load in February 2006 a) Eastbound b) Westbound

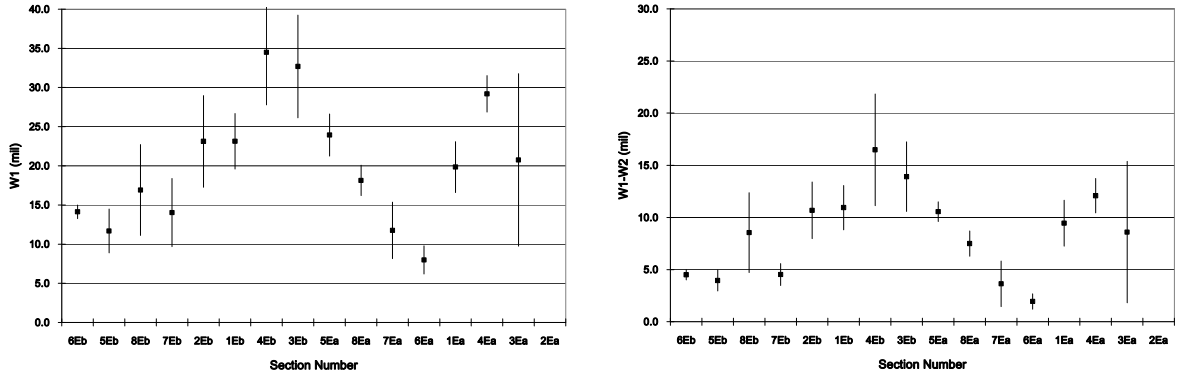

Figure 5.16: Mean and Standard deviation in Eastbound Lane in August 2006 a) W1 b) W1-W2

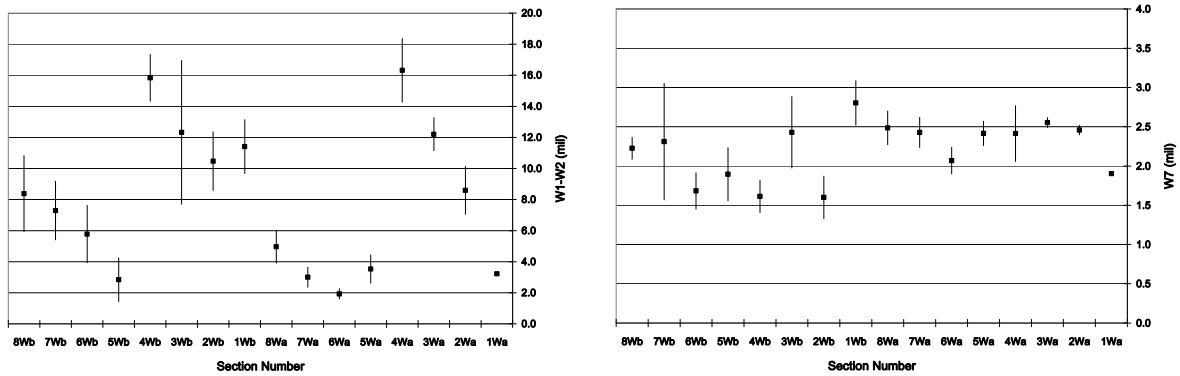

Figure 5.17: Mean and Standard deviation in Westbound in August 2006 a) W1 b) W1-W2

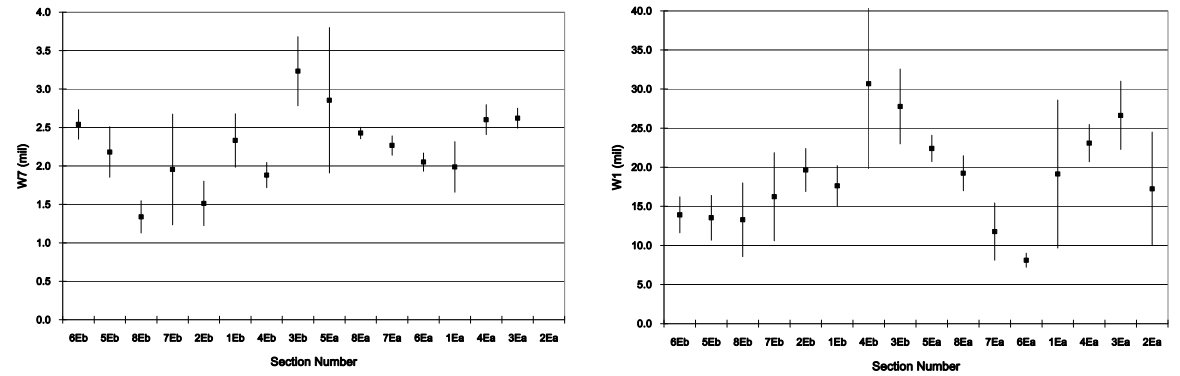

Figure 5.18: Mean and Standard deviation for W7 load in August 2006 a) Eastbound b) Westbound

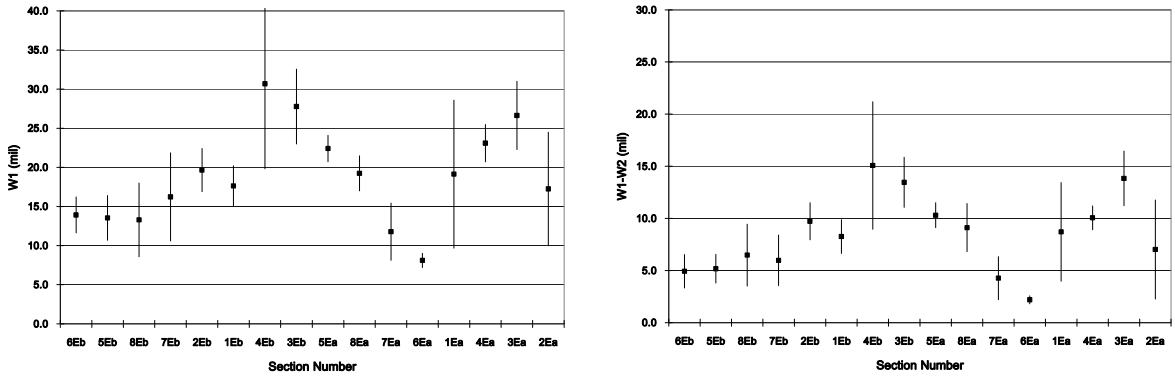

Figure 5.19: Mean and Standard deviation in Eastbound Lane in November 2006 a) W1 b) W1-W2

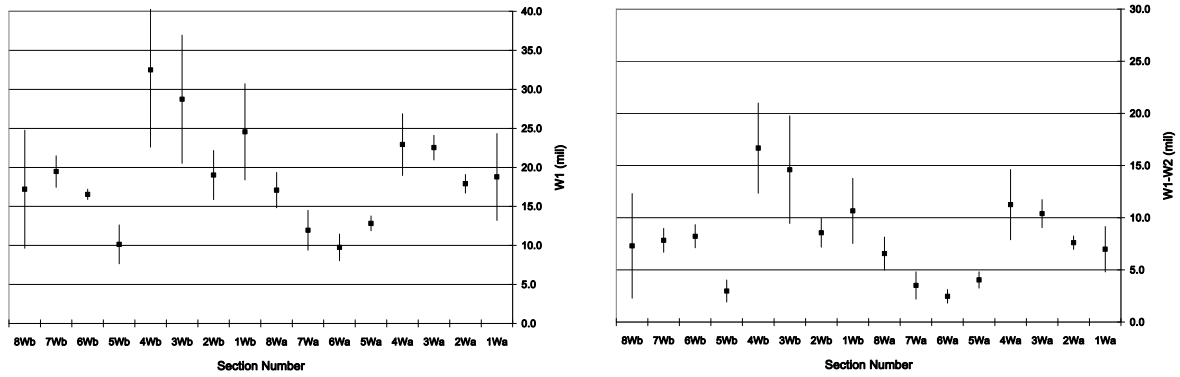

Figure 5.20: Mean and Standard deviation in Westbound in November 2006 a) W1 b) W1-W2

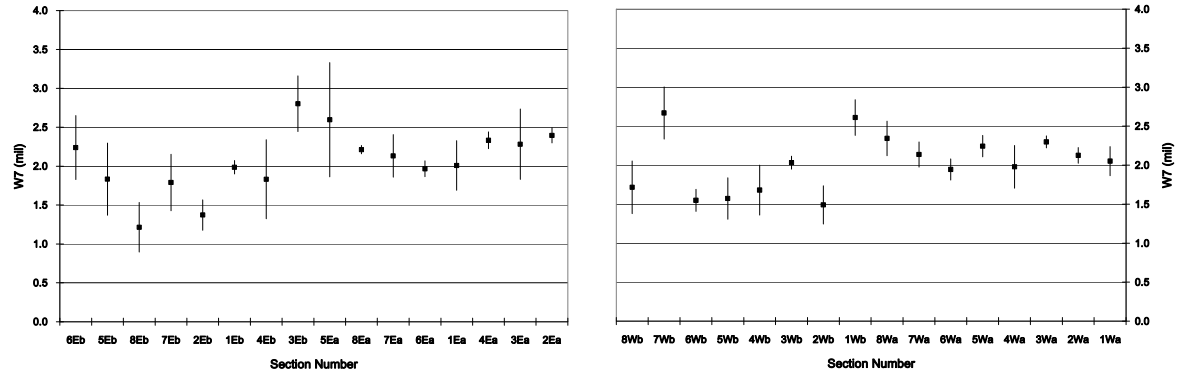

Figure 5.21: Mean and Standard deviation for W7 load in November 2006 a) Eastbound b) Westbound

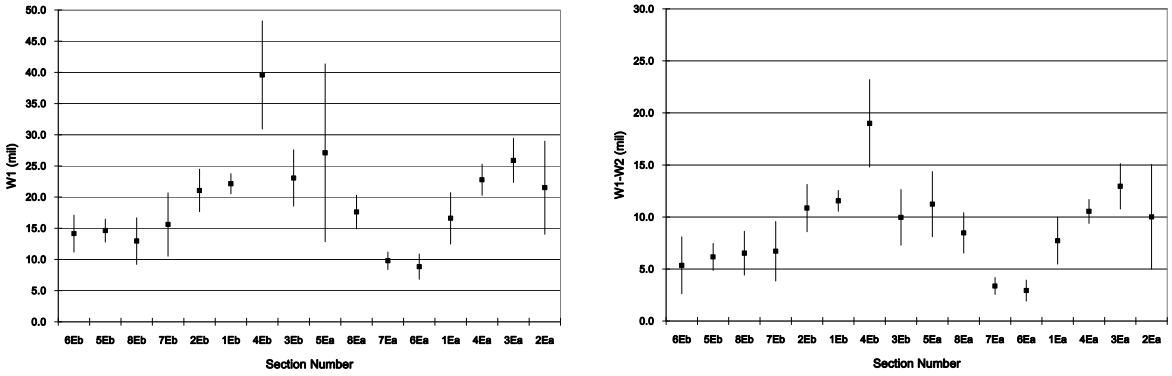

Figure 5.22: Mean and Standard deviation in Eastbound Lane in February 2007 a) W1 b) W1-W2

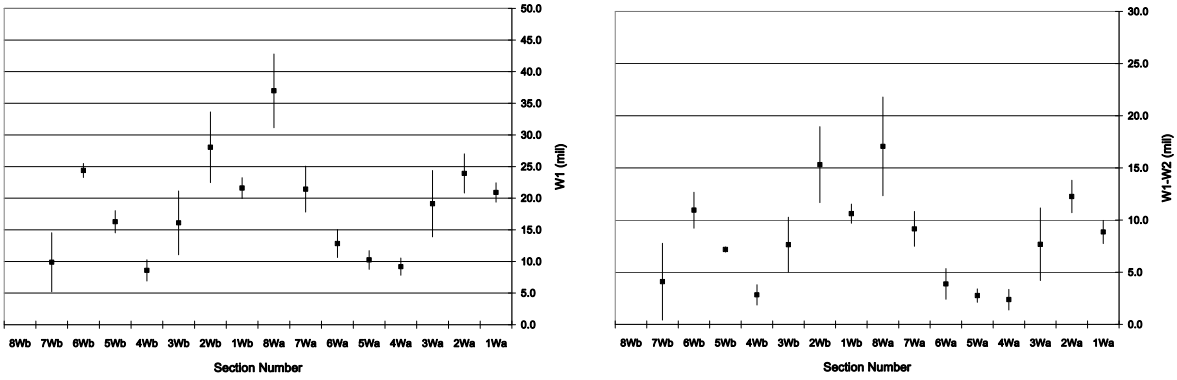

Figure 5.23: Mean and Standard deviation in Westbound in February 2007 a) W1 b) W1-W2

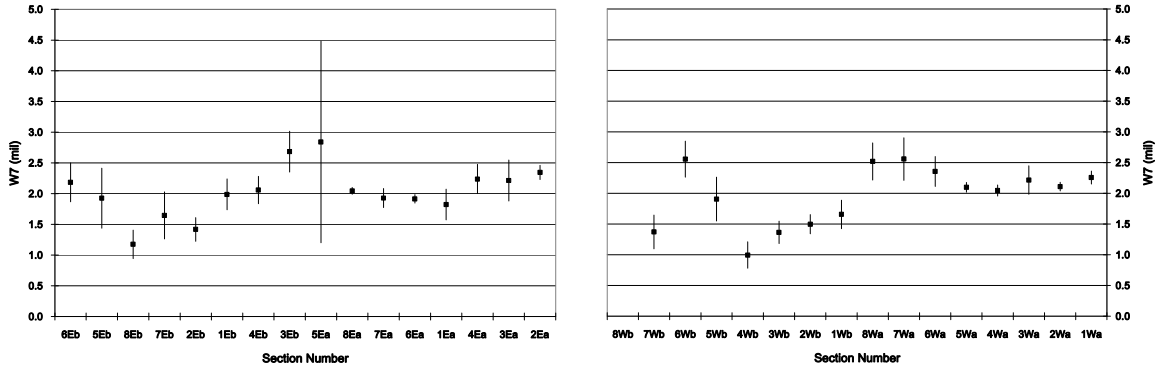

Figure 5.24: Mean and Standard deviation for W7 load in February 2007 a) Eastbound b) Westbound

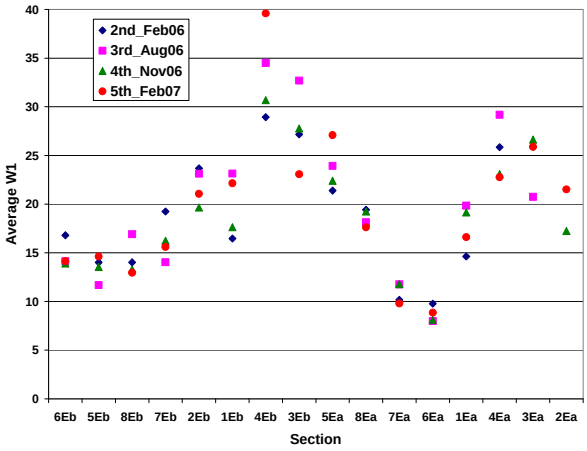

Figure 5.25: Average Values of W1 on Eastbound

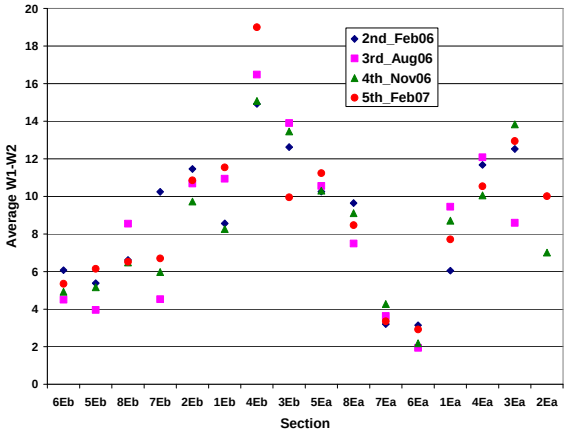

Figure 5.26: Average Values of W1-W2 on Eastbound

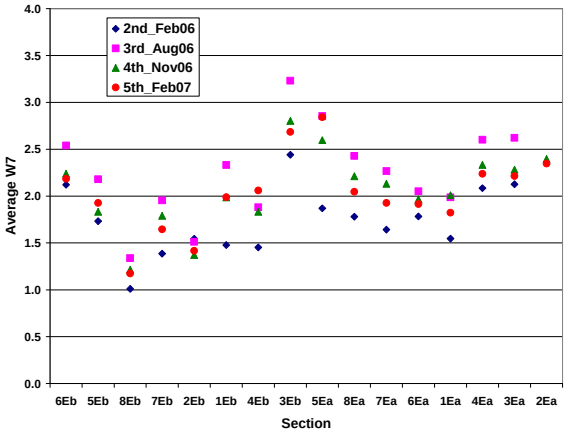

Figure 5.27: Average Values of W7 on Eastbound

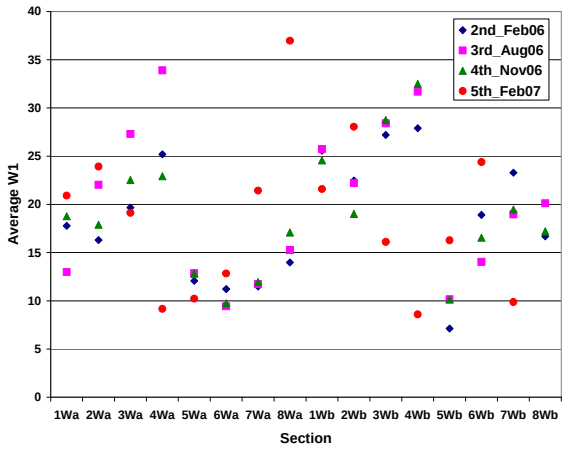

Figure 5.28: Average Values of W1 on Westbound

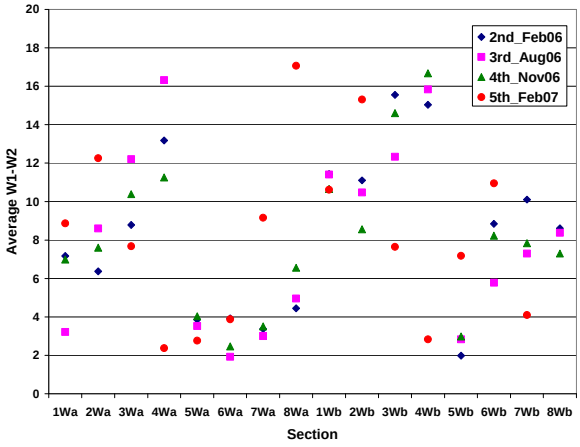

Figure 5.29: Average Values of W1-W2 on Westbound

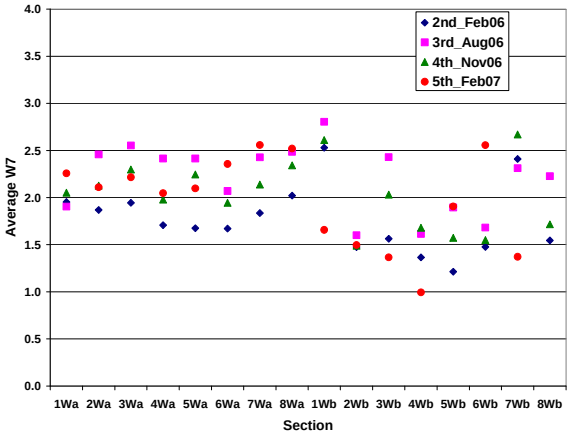

Figure 5.30: Average Values of W7 on Westbound

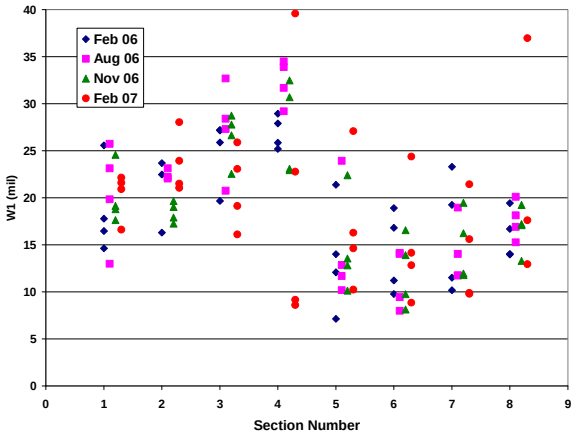

Figure 5.31: Average Values of W1 at Section No. 1 to No. 8

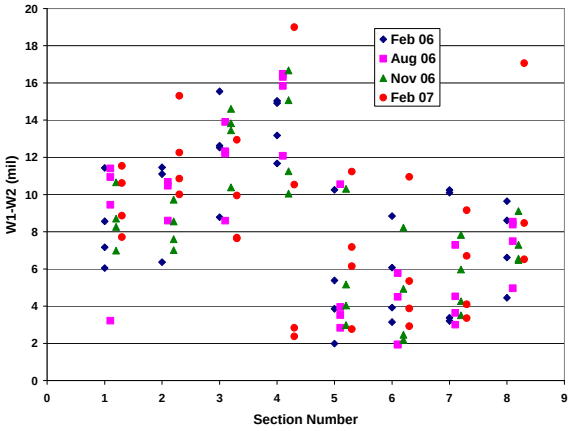

Figure 5.32: Average Values of W1-W2 at Section No. 1 to No. 8

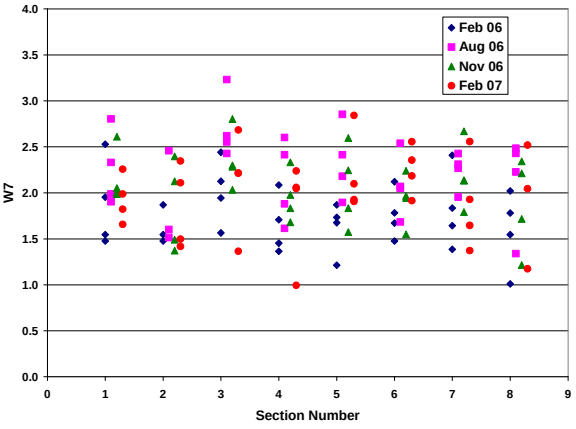

Figure 5.33: Average Values of W7 at Section No. 1 to No. 8

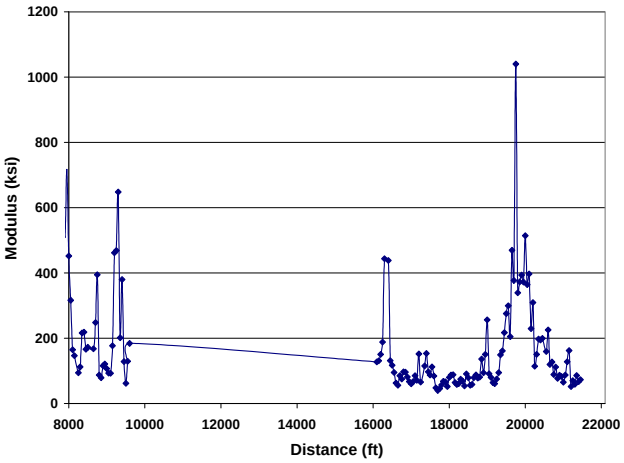

Figure 5.34: Back-Calculated Surface Modulus on Eastbound for February 2006

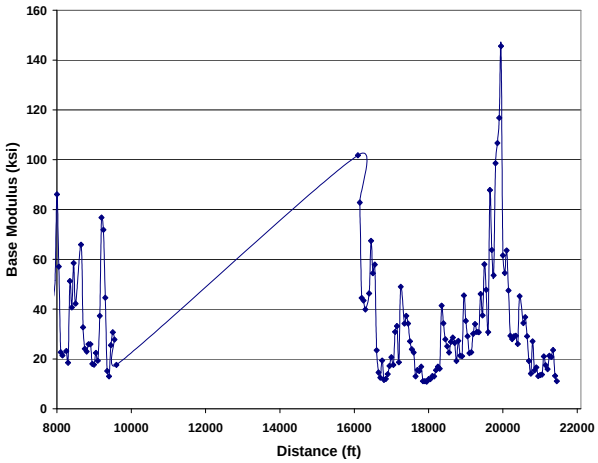

Figure 5.35: Back-Calculated Base Modulus on Eastbound for February 2006

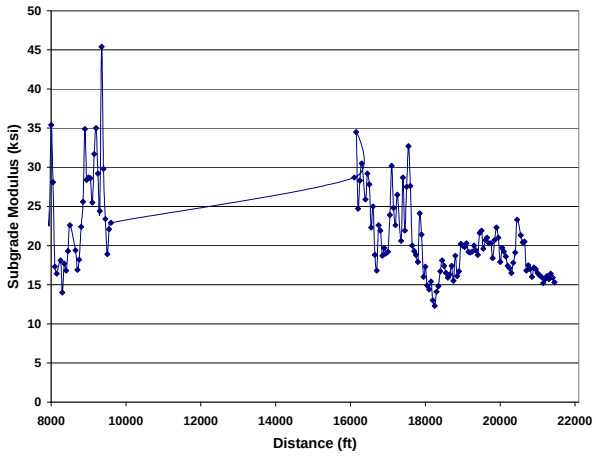

Figure 5.36: Back-Calculated Subgrade Modulus on Eastbound for February 2006

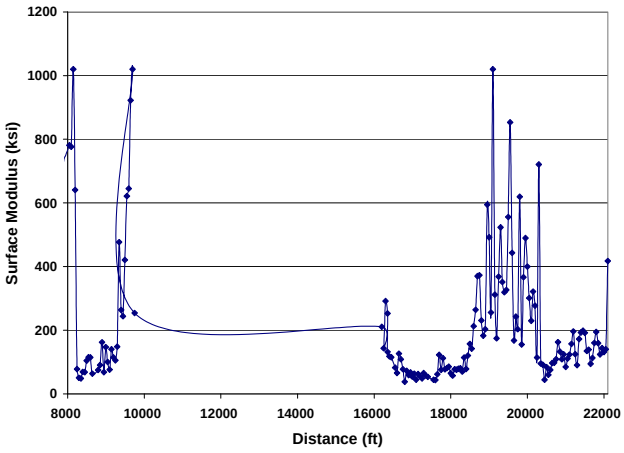

Figure 5.37: Back-Calculated Surface Modulus on Westbound for February 2006

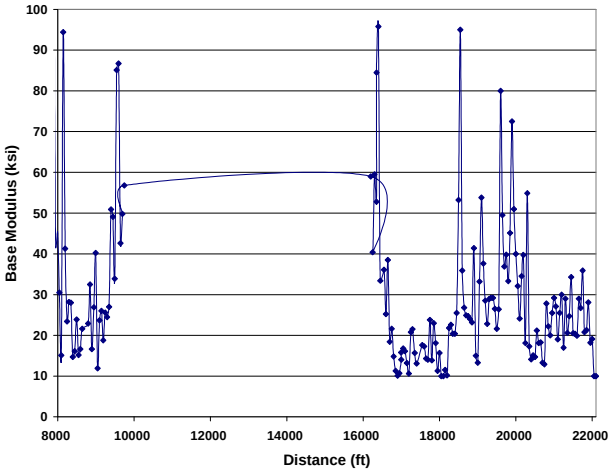

Figure 5.38: Back-Calculated Base Modulus on Westbound for February 2006

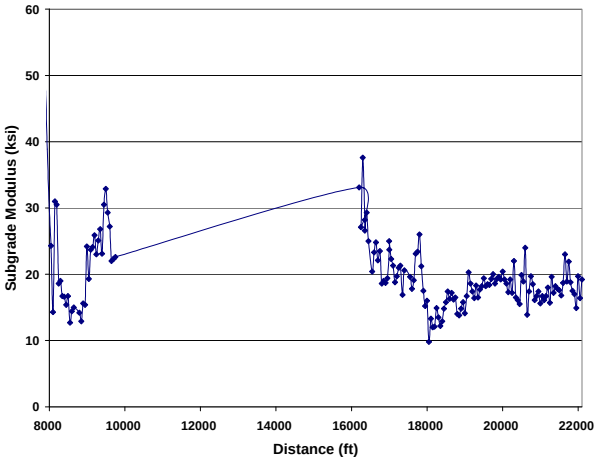

Figure 5.39: Back-Calculated Subgrade Modulus on Westbound for February 2006

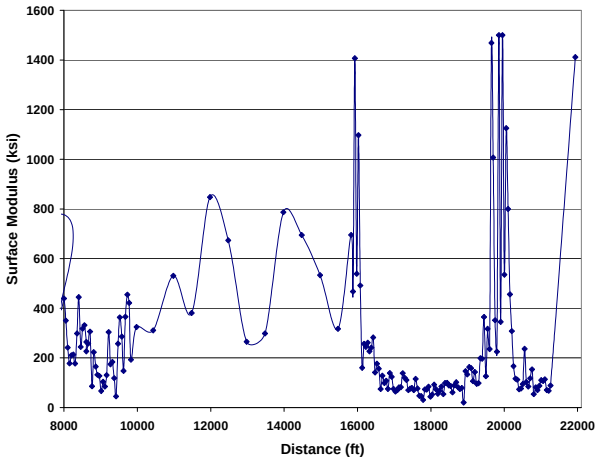

Figure 5.40: Back-Calculated Surface Modulus on Eastbound for August 2006

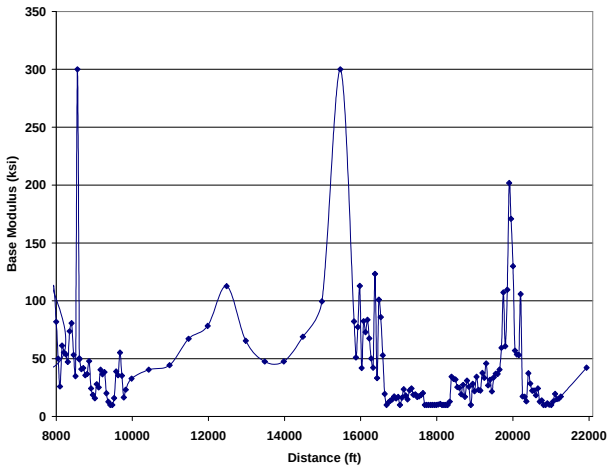

Figure 5.41: Back-Calculated Base Modulus on Eastbound for August 2006

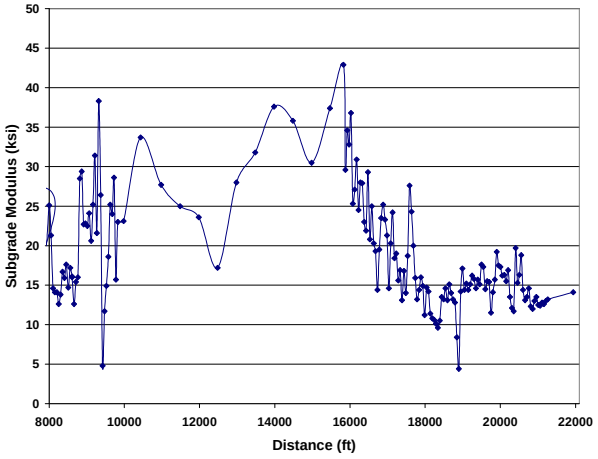

Figure 5.42: Back-Calculated Subgrade Modulus on Eastbound for August 2006

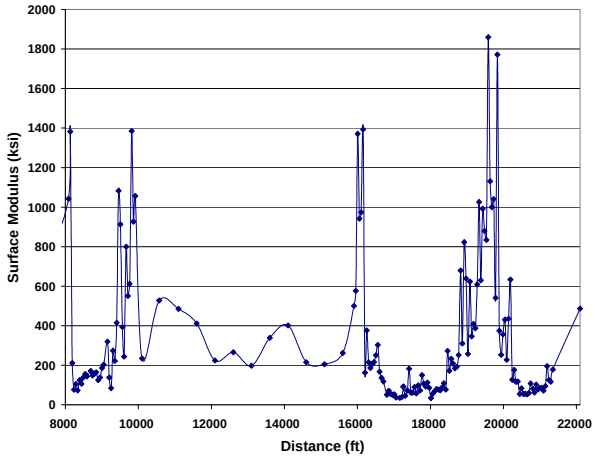

Figure 5.43: Back-Calculated Surface Modulus on Westbound for August 2006

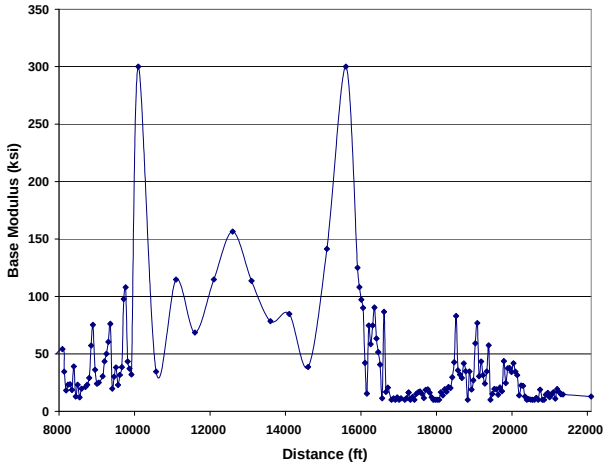

Figure 5.44: Back-Calculated Base Modulus on Westbound for August 2006

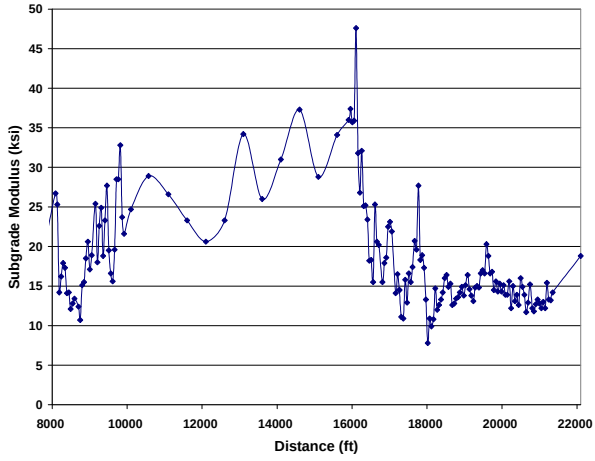

Figure 5.45: Back-Calculated Subgrade Modulus on Westbound for August 2006

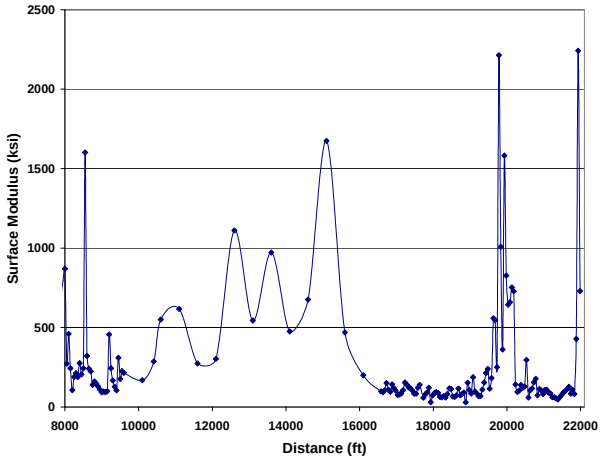

Figure 5.46: Back-Calculated Surface Modulus on Eastbound for November 2006

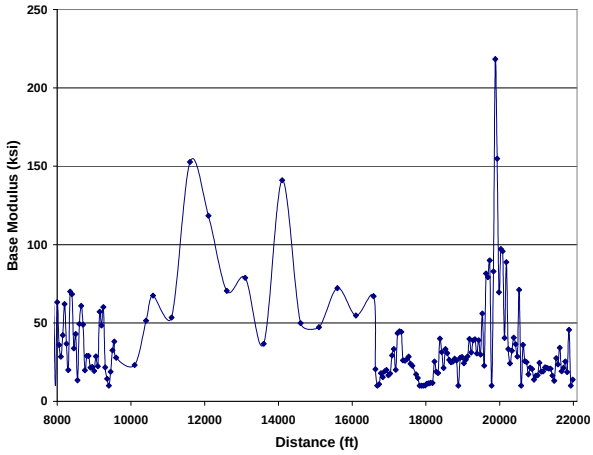

Figure 5.47: Back-Calculated Base Modulus on Eastbound for November 2006

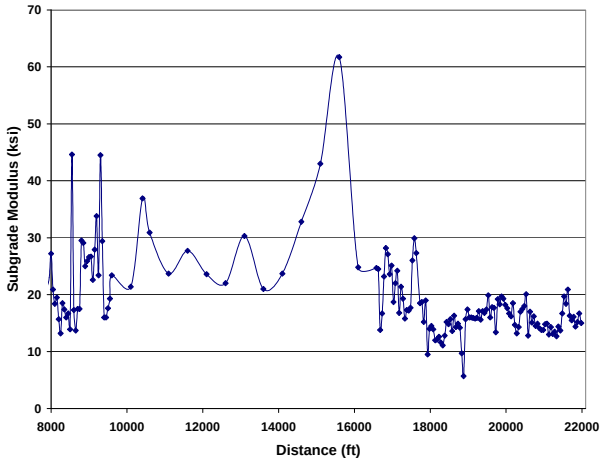

Figure 5.48: Back-Calculated Subgrade Modulus on Eastbound for November 2006

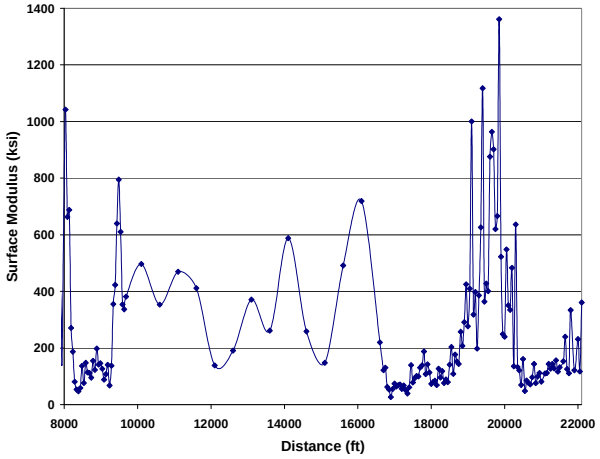

Figure 5.49: Back-Calculated Surface Modulus on Westbound for November 2006

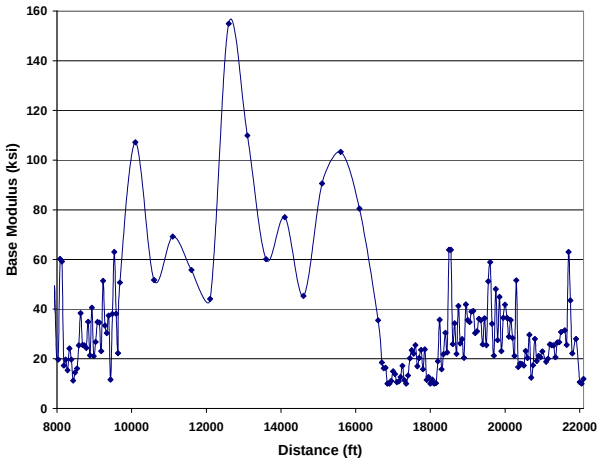

Figure 5.50: Back-Calculated Base Modulus on Westbound for November 2006

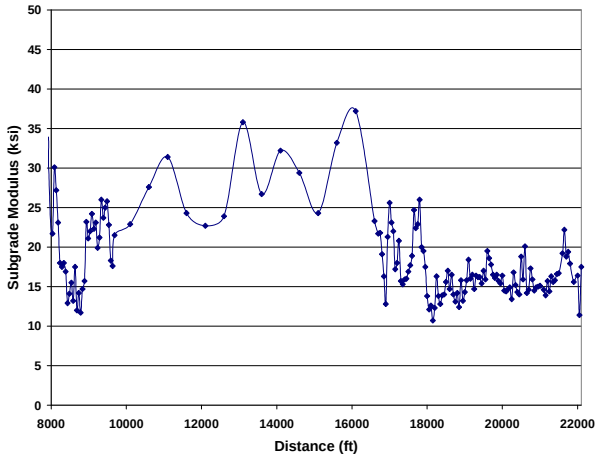

Figure 5.51: Back-Calculated Subgrade Modulus on Westbound for November 2006

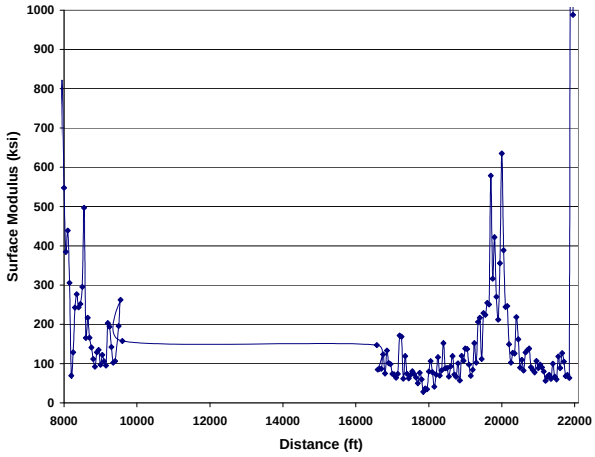

Figure 5.52: Back-Calculated Surface Modulus on Eastbound for February 2007

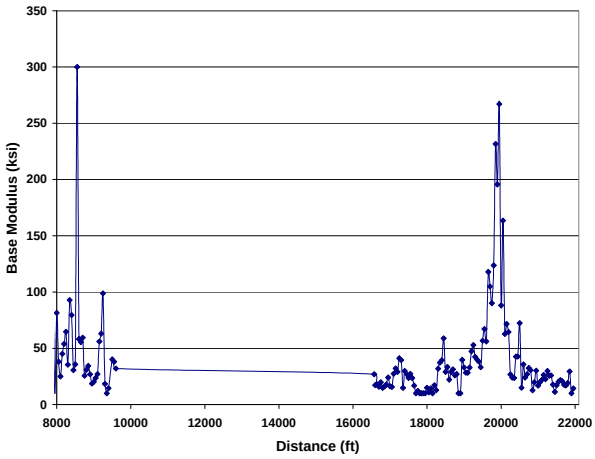

Figure 5.53: Back-Calculated Base Modulus on Eastbound for February 2007

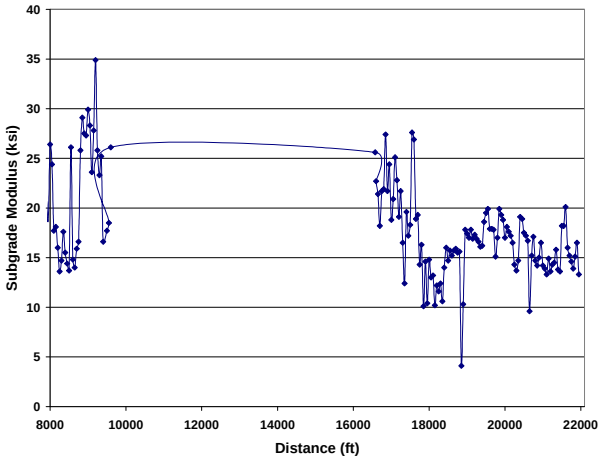

Figure 5.54: Back-Calculated Subgrade Modulus on Eastbound for February 2007

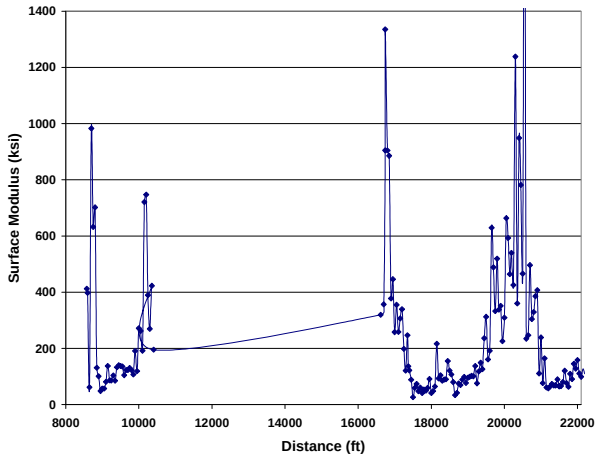

Figure 5.55: Back-Calculated Surface Modulus on Westbound for February 2007

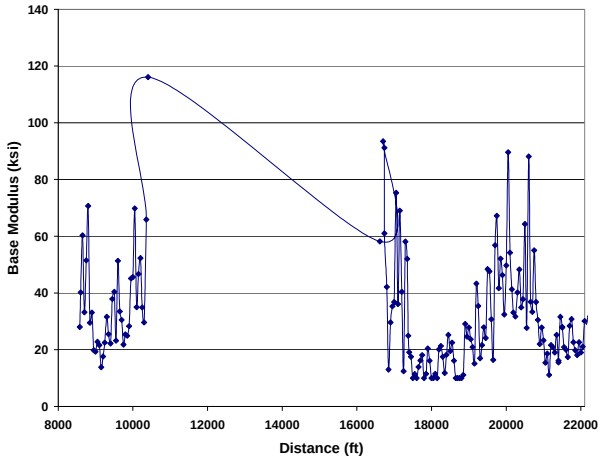

Figure 5.56: Back-Calculated Base Modulus on Westbound for February 2007

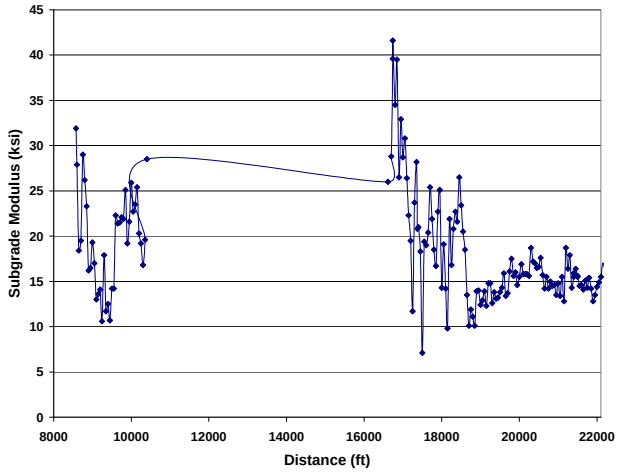

Figure 5.57: Back-Calculated Subgrade Modulus on Westbound for February 2007

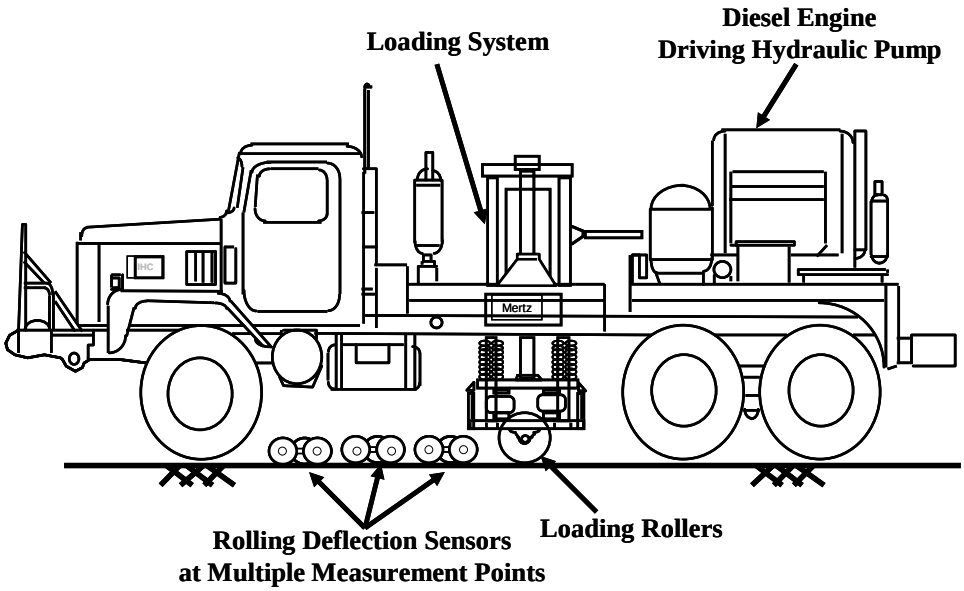

(a) Rolling Dynamic Deflectometer

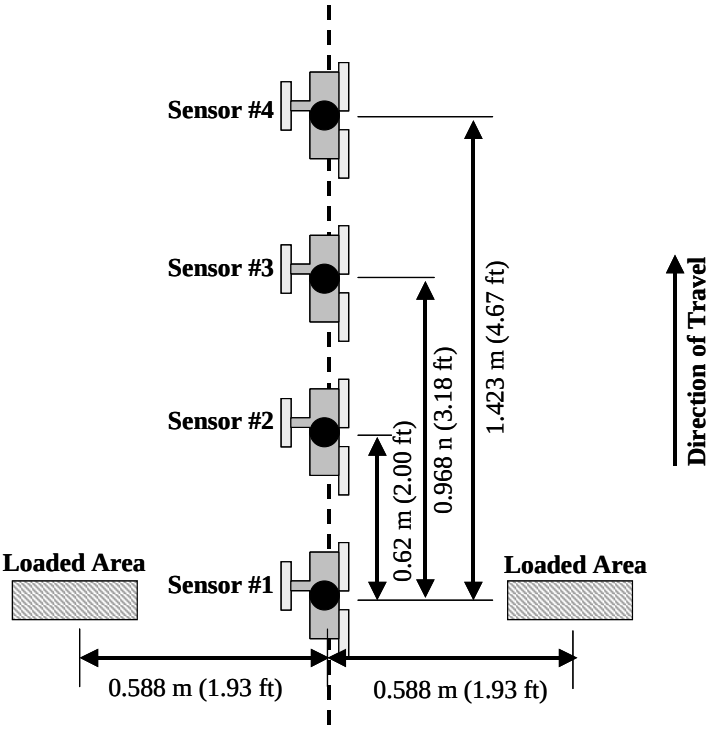

(b) Typical Rolling Sensor Configuration for RDD Testing

Figure 5.58: General RDD arrangement with rolling sensor array (Lee et al., 2005)

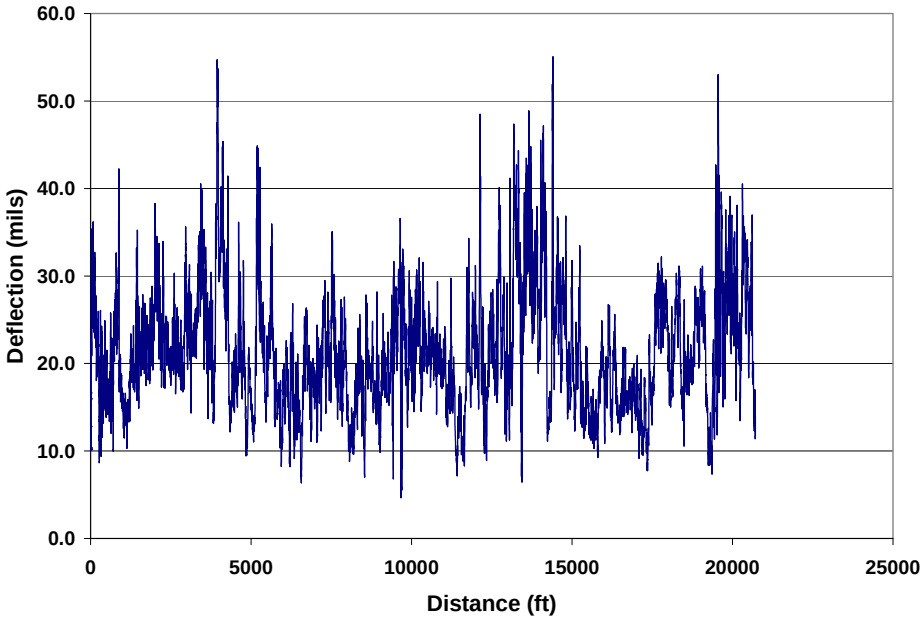

Figure 5.59: Sensor #1 deflection profile at low load level

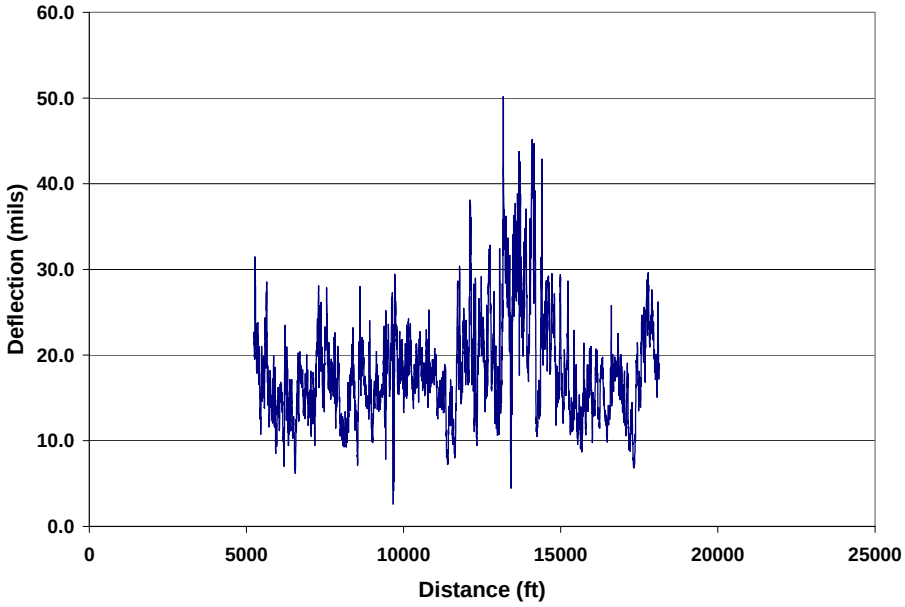

Figure 5.60: Sensor #1 deflection profile at high load level

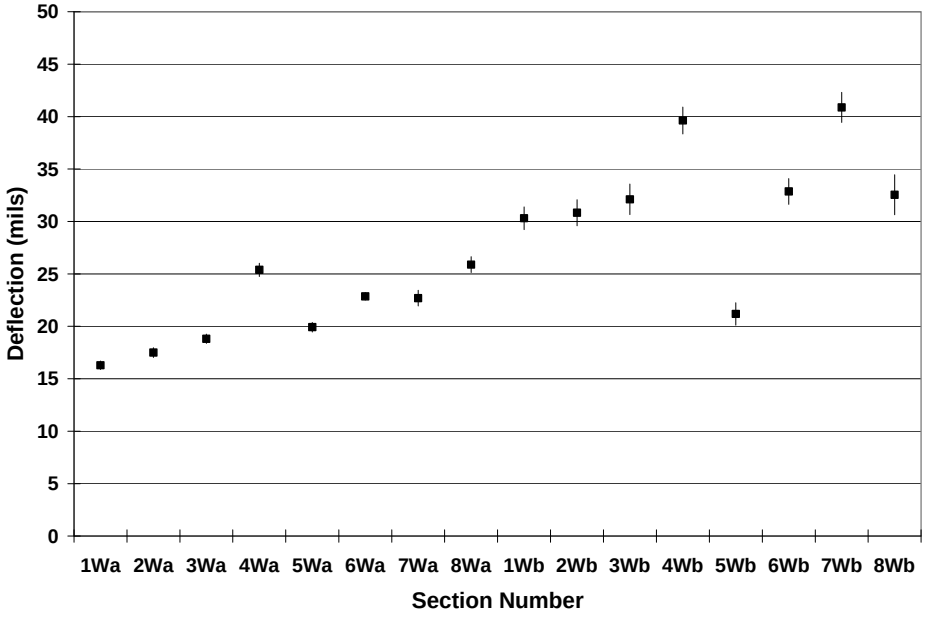

Figure 5.61: Average and 95% confidence interval of deflection in experimental sections on westbound lane (K6) at low load

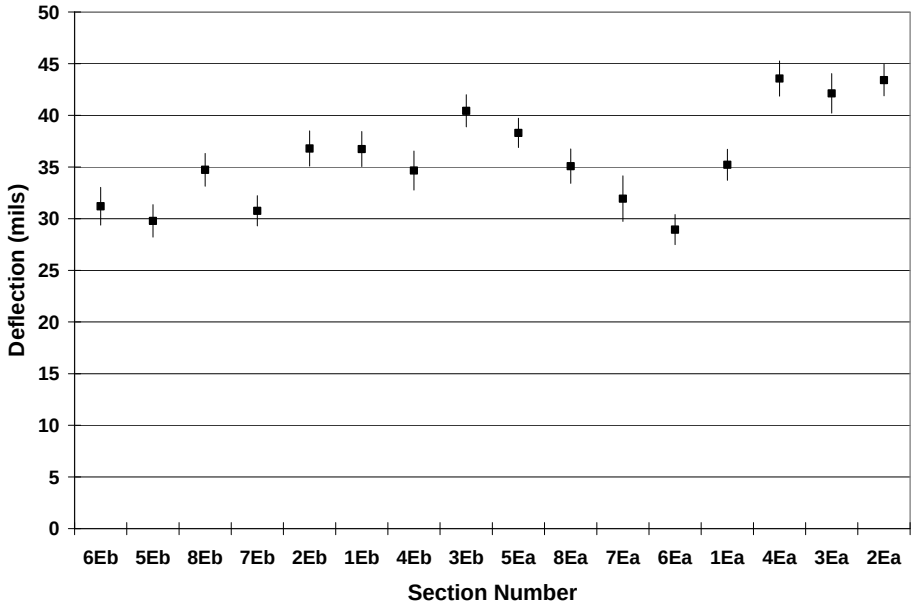

Figure 5.62: Average and 95% confidence interval of deflection in experimental sections on eastbound lane (K1) at low load

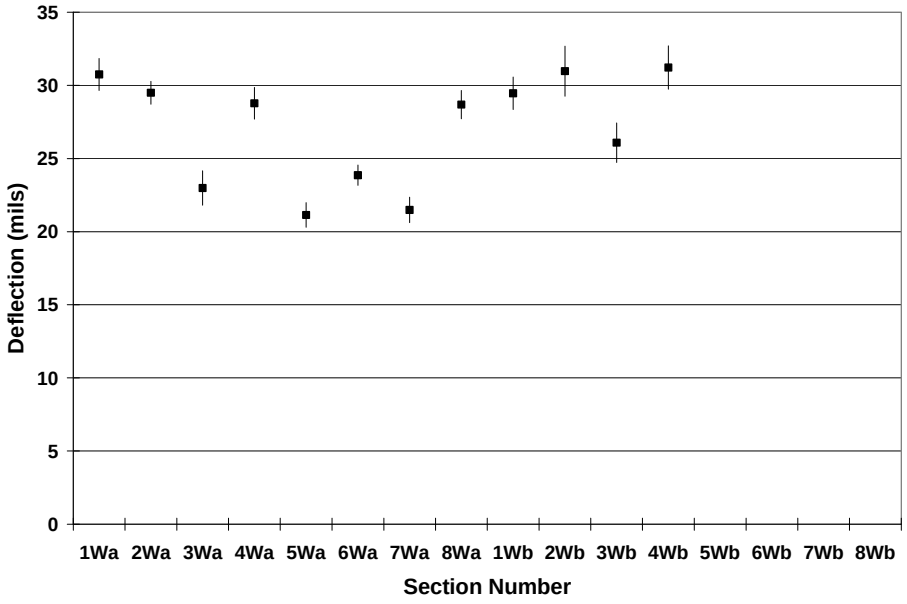

Figure 5.63: Average and 95% confidence interval of deflection in experimental sections on westbound lane (K6) at high load

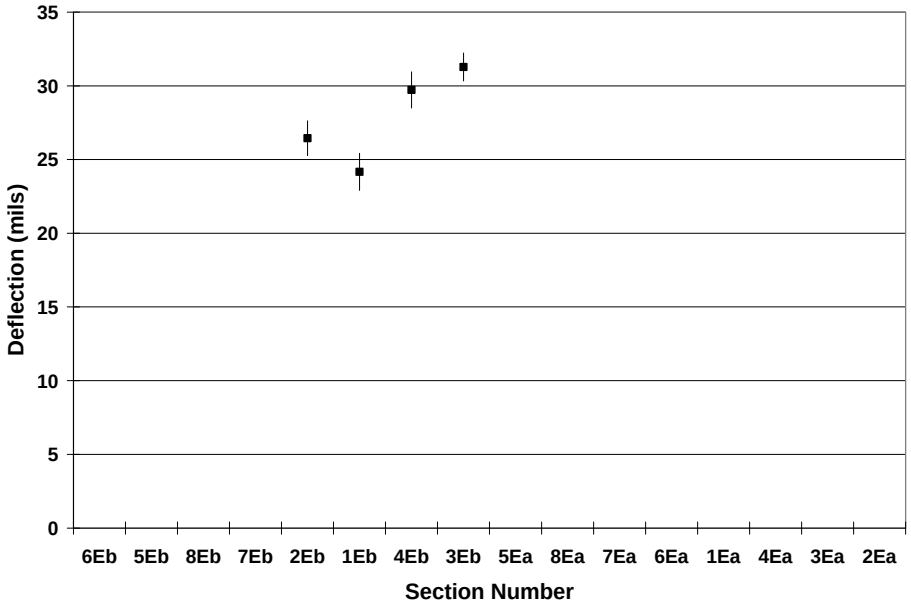

Figure 5.64: Average and 95% confidence interval of deflection in experimental sections on eastbound lane (K1) at high load

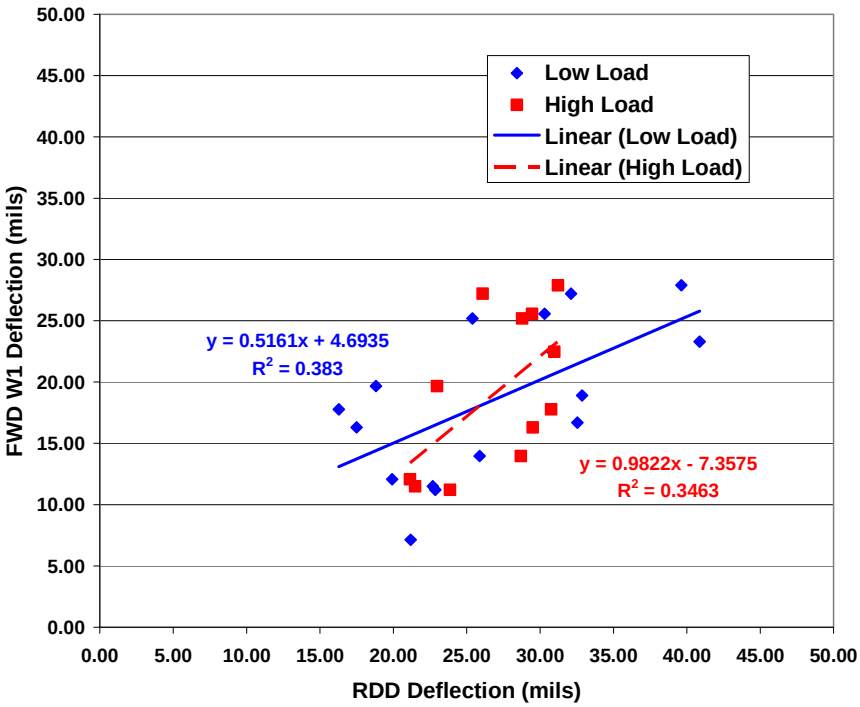

Figure 5.65: Relationship between FWD W1 deflection and RDD deflection on westbound lane (K6)

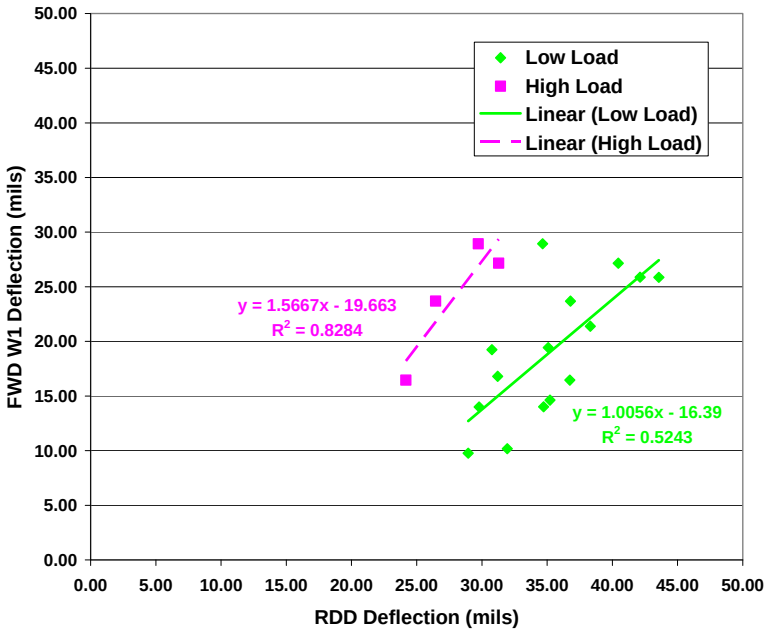

Figure 5.66: Relationship between FWD W1 deflection and RDD deflection on eastbound lane (K1)

Chapter 6. Modeling Geosynthetic Pavement

6.1 Introduction

Expansive soils are soils that experience significant volumetric changes when subjected to changes in moisture conditions. The volumetric change of this type of soil can produce serious problems to pavement and foundations. Expansive soils are found in 20 percent of the territory of the United States (Jayatilaka and Lytton, 1997). Texas, Colorado, and Wyoming have the most severe degree of expansive soils. In Texas, pavements have suffered from expansive soils in the subgrade for decades. Longitudinal cracking is one of the most prevalent pavement distresses due to the volumetric change of the expansive subgrade. This type of cracking, so-called "dry-land crack," is considered to initiate in the drying subgrade soil and then to reflect from the highly plastic subgrade through the pavement structures (Sebesta, 2002). Fortunately, recent practice of using geogrid reinforcement to address this problem has shown promising results in Texas. The geogrids were installed beneath a flexible base on FM roads and were anchored on the subbase layer or the subgrade. However, despite preliminary success of geogrids in limiting longitudinal cracks, little is known about the mechanisms leading to propagation of the longitudinal cracks to the surface of the pavement. Accordingly, the benefit of using geosynthetic treatment has not been properly quantified.

This chapter uses the linear elastic fracture mechanics (LEFM) to study the propagation of desiccation cracks in the subgrade into pavement layers and the mechanism of geogrid preventing cracks from coming through. The next section reviews the stress analysis on saturated and unsaturated soils, which is followed by the estimate of soil suction profiles. The subsequent section studies the finite element modeling of pavement structure over shrinking subgrade and the crack development in the pavement. The next section uses the linear elastic fracture mechanics theory to study the benefit of geogrid-reinforcement for pavement. The final section summarizes the study approach and the main findings.

6.2 Stress-strain analysis in expansive subgrade

To study the crack initiation in expansive subgrade, it is necessary to analyze the stress/strain state in the subgrade soil. The subgrade soil consists of unsaturated soil, which is above the water table, and saturated soil, that is under the water table. This section will start with the stress analysis on the saturated soil, whose theory is well established and accepted, and will extend to the mechanical behavior and the volumetric change theory of unsaturated soil.

6.2.1 Stress Analysis on Saturated Soil

The equilibrium conditions for a saturated soil can be described by the effective stress, $(\sigma - u_w)$, in which σ is the total stress, and u_w is the pore-water pressure. This stress variable has the following tensor form:

$$\begin{bmatrix} \sigma_{11} - u_w & \sigma_{12} & \sigma_{13} \\ \sigma_{21} & \sigma_{22} - u_w & \sigma_{23} \\ \sigma_{31} & \sigma_{32} & \sigma_{33} - u_w \end{bmatrix}$$

in which

u_w = pore-water pressure;

$\sigma_{11} - u_w$ = effective stress in the x_1 direction;

$\sigma_{22} - u_w$ = effective stress in the x_2 direction;

$\sigma_{33} - u_w$ = effective stress in the x_3 direction; and

σ_{12}, σ_{23}, σ_{31}, σ_{13}, σ_{32}, σ_{21} = shear stress components.

The shear stress components have the following relationships under equilibrium conditions:

$$\sigma_{12} = \sigma_{21} \tag{6.1}$$

$$\sigma_{23} = \sigma_{32} \tag{6.2}$$

$$\sigma_{31} = \sigma_{13} \tag{6.3}$$

Assuming that the saturated soil behaves as an isotropic and linearly elastic material, the effective stress variable is used to formulate the constitutive relations with respect to the generalized Hooke's law. Equations 6.4, 6.5 and 6.6 give the elastic constitutive relations in the x_1, x_2, and x_3 directions:

$$\varepsilon_{11} = \frac{\sigma_{11} - u_w}{E} - \frac{\nu}{E}(\sigma_{22} + \sigma_{33} - 2u_w) \tag{6.4}$$

$$\varepsilon_{22} = \frac{\sigma_{22} - u_w}{E} - \frac{\nu}{E}(\sigma_{11} + \sigma_{33} - 2u_w) \tag{6.5}$$

$$\varepsilon_{33} = \frac{\sigma_{33} - u_w}{E} - \frac{\nu}{E}\left(\sigma_{11} + \sigma_{22} - 2u_w\right) \tag{6.6}$$

where

ε_{11} = normal strain in the x_1 direction;

ε_{22} = normal strain in the x_2 direction;

ε_{33} = normal strain in the x_3 direction;

E = modulus of elasticity with respect to a change in the effective stress; and
ν = Poisson's ratio for the soil structure.

6.2.2 Stress Analysis on Unsaturated Soil

In contrast to saturated soil, an unsaturated soil has more than one independent stress variable because of the presence of soil suction. Soil suction is a measure of a soil's affinity for water (Chen, 1988). In another word, suction is a parameter indicating the intensity with which it will attract water. Generally, soil with less water content has higher soil suction. The soil suction, commonly called "total suction," is quantified in terms of the relative humidity. Total suction consists of two parts: matric suction and osmotic suction. Matric suction is derived from the negative water pressure associated with the capillary phenomenon. Osmotic suction arises from the soluble salts in the soil water that produce the osmotic repulsion forces.

Fredlund and Morgenstern (1976) used two stress state variables to describe the equilibrium condition and to formulate the constitutive equations of an unsaturated soil. The two stress variables are net normal stress, $(\sigma - u_a)$, and the matric suction, $(u_a - u_w)$, in which σ is the total normal stress, u_a is the pore-air pressure, and u_w is the pore-water pressure. Consequently, the stress state of the unsaturated soil can be expressed by two independent stress tensors:

$$\begin{bmatrix} \sigma_{11} - u_a & \sigma_{12} & \sigma_{13} \\ \sigma_{21} & \sigma_{22} - u_a & \sigma_{23} \\ \sigma_{31} & \sigma_{32} & \sigma_{33} - u_a \end{bmatrix}$$

and

$$\begin{bmatrix} u_a - u_w & 0 & 0 \\ 0 & u_a - u_w & 0 \\ 0 & 0 & u_a - u_w \end{bmatrix}.$$

These two tensors cannot be combined to one because they have different constitutive relations that depend on the soil properties.

Assuming that the unsaturated soil is isotropic and linearly elastic, the constitutive relations can be formulated in terms of the two stress state variables, $(\sigma - u_a)$ and $(u_a - u_w)$, as shown in Equations 6.7, 6.8 and 6.9:

$$\varepsilon_{11} = \frac{\sigma_{11} - u_a}{E} - \frac{\nu}{E}(\sigma_{22} + \sigma_{33} - 2u_a) + \frac{u_a - u_w}{H} \tag{6.7}$$

$$\varepsilon_{22} = \frac{\sigma_{22} - u_a}{E} - \frac{\nu}{E}(\sigma_{11} + \sigma_{33} - 2u_a) + \frac{u_a - u_w}{H} \tag{6.8}$$

$$\varepsilon_{33} = \frac{\sigma_{33} - u_a}{E} - \frac{\nu}{E}(\sigma_{11} + \sigma_{22} - 2u_a) + \frac{u_a - u_w}{H} \tag{6.9}$$

where

E = modulus of elasticity for the soil structure with respect to a change in the net normal stress, $(\sigma - u_a)$; and

H = modulus of elasticity for the soil structure with respect to a change in matric suction, $(u_a - u_w)$.

Every constitutive equation for the unsaturated soil can be explained as an extension of each corresponding constitutive relation for the saturated soil because of the additional stress variable, matric suction, in addition to the normal stress.

Equations 6.7, 6.8 and 6.9 can also be written in incremental forms:

$$d\varepsilon_{11} = \frac{1}{E} d(\sigma_{11} - u_a) - \frac{\nu}{E} d(\sigma_{22} + \sigma_{33} - 2u_a) + \frac{1}{H} d(u_a - u_w) \tag{6.10}$$

$$d\varepsilon_{22} = \frac{1}{E} d(\sigma_{22} - u_a) - \frac{\nu}{E} d(\sigma_{11} + \sigma_{33} - 2u_a) + \frac{1}{H} d(u_a - u_w) \tag{6.11}$$

$$d\varepsilon_{33} = \frac{1}{E} d(\sigma_{33} - u_a) - \frac{\nu}{E} d(\sigma_{11} + \sigma_{22} - 2u_a) + \frac{1}{H} d(u_a - u_w) \tag{6.12}$$

Therefore, the incremental volumetric change of an unsaturated soil can be calculated by adding the incremental strains in the three directions:

$$\frac{dV}{V} = d\varepsilon_v = d\varepsilon_{11} + d\varepsilon_{22} + d\varepsilon_{33} \tag{6.13}$$

in which dV is the volume change of the unsaturated soil, V is the soil volume at initial state, and $d\varepsilon_v$ is the incremental volumetric strain.

Let x_1 be the transverse direction perpendicular to the vehicle travel direction on the pavement, x_2 be the longitudinal direction that is the vehicle travel direction, and x_3 be the vertical direction. Assume that the initial condition is right after the subgrade construction, when the subgrade soil is intact and without any crack. Therefore, the initial strains are zero in all three directions. During the desiccation process of the unsaturated soil in the pavement subgrade, the lateral strain (the strain in horizontal directions, ε_{11} and ε_{22}) remain zero before crack initiation because of lateral constraint. The field data collected by Konrad et al. (1997) confirmed that drying soils experience a restrained desiccation so that the lateral strains were maintained zero until a crack initiated in the soil. Consequently, the incremental horizontal strains in both transverse (x_1) and longitudinal direction (x_2) remain zero before cracking, which means:

$$\varepsilon_{11} = \frac{\sigma_{11} - u_a}{E} - \frac{\nu}{E}(\sigma_{22} + \sigma_{33} - 2u_a) + \frac{u_a - u_w}{H} = 0 \tag{6.14}$$

$$\varepsilon_{22} = \frac{\sigma_{22} - u_a}{E} - \frac{\nu}{E}(\sigma_{11} + \sigma_{33} - 2u_a) + \frac{u_a - u_w}{H} = 0 \tag{6.15}$$

Because of symmetry, $\sigma_{11} = \sigma_{22}$, hence Equation 6.14 can be rewritten as:

$$\varepsilon_{11} = \frac{\sigma_{11} - u_a}{E} - \frac{\nu}{E}(\sigma_{11} + \sigma_{33} - 2u_a) + \frac{u_a - u_w}{H} = 0 \tag{6.16}$$

Rearrange Equation 6.16, and the following equation can be reached:

$$\sigma_{11} - u_a = \frac{\nu}{1-\nu}(\sigma_{33} - u_a) - \frac{E}{H}\frac{1}{1-\nu}(u_a - u_w) \tag{6.17}$$

in which $(\sigma_{11} - u_a)$ is the incremental tensile stress in the transverse direction. As the pore-air pressure is atmospheric for most practical engineering problems, the net normal stress in the vertical direction, $\sigma_{33} - u_a$, equals to σ_{33} by setting atmospheric pressure zero. The total vertical stress, σ_{33}, so-called the overburden pressure, is produced by the self-weight of the soil and the pavement covered on the soil, and it can be calculated by:

$$\sigma_{33} = \gamma_a h_a + \gamma_b h_b + \gamma_s h_s \tag{6.18}$$

in which

γ_a = unit weight of mass asphalt;

γ_b = unit weight of mass base material;

γ_s = unit weight of mass soil;

h_a = thickness of asphalt layer;

h_b = thickness of base; and

h_s = depth of point A from the top of the subgrade.

The overburden pressure results in compressive horizontal stress, which increases as the depth of the soil. In the meantime, the matric suction in the soil reduces the compressive horizontal stress. At shallow depth, relatively small matric suction may reduce the compressive net normal stress to zero or even to be negative. If the soil cannot sustain any tensile stress, cracks will develop as the net normal horizontal stress, $\sigma_{11} - u_a$, approaches zero. However, soils are considered to have a certain amount of tensile strength, σ_t, and this tensile strength has been used in the crack criterion that predicts the onset of large tensile cracks by comparing the tensile strength with the net normal horizontal stress (Lee et al., 1988; Morris et al., 1992; Ayad et al., 1997). Even though microcracks may build up and coalesce in early stages, this criterion is well accepted that if $\sigma_{11} - u_a$ exceeds the tensile strength of the soil σ_t, a large scale tension crack will develop. Ayad et al. (1997) did an experiment to measure the tensile strength of an intact clay deposit at the experimental site of Saint-Alban, Quebec, Canada. The value of the tensile strength of the Saint-Alban clay was evaluated to be 9 kPa.

6.2.3 Volumetric Change Theory of Unsaturated Soil

One may doubt this volumetric change formulation because this theory is based on the assumption that the unsaturated soil is a linearly elastic material, but soil behaves with high plasticity in engineering practice. However, Equations 6.10 through 6.13 indicate the important information that the volumetric change of soil can be produced by either net normal stress or matric suction or both. The relationships may not be linear between soil's volume change and the normal stress or the matric suction, but the volumetric compliances with respect to net normal stress and matric suction can be determined by lab experiments. Morris et al. (1992) stated a constitutive equation as:

$$d\varepsilon_v = \frac{dV}{V} = C_t d(\sigma - u_a) + C_a d(u_a - u_w) \tag{6.19}$$

in which

$$C_t = \frac{1}{V}\frac{\partial V}{\partial(\sigma - u_a)};$$

$C_a = \frac{1}{V}\frac{\partial V}{\partial(u_a - u_w)}$; and

σ = mean normal stress.

C_t and C_a are referred to as volumetric deformation coefficients, which are constants for linearly elastic case only. Fredlund and Rahardjo (1993) graphically presented the constitutive surfaces for an unsaturated soil, which indicate that the volumetric deformation coefficients vary from one stress state to another in a nonlinear manner on the curved constitutive surface. The logarithm of the two stress variables are found to be linearly related to the volumetric strain of an unsaturated soil. Lytton et al. (1977, 1995, 2004) developed a model to estimate the volumetric strain of an elemental volume of soil:

$$\frac{\Delta V}{V} = -\gamma_h \log_{10}\left(\frac{h_f}{h_i}\right) - \gamma_\sigma \log_{10}\left(\frac{\sigma_f}{\sigma_i}\right) - \gamma_\pi \log_{10}\left(\frac{\pi_f}{\pi_i}\right) \quad (6.20)$$

where

$\frac{\Delta V}{V}$ = volumetric strain;

h_i = initial value of matric suction;

h_f = final values of matric suction;

σ_i = initial value of mean principle stress;

σ_f = finial value of mean principle stress;

π_i = initial value of osmotic suction;

π_f = finial value of osmotic suction;

γ_h = matric suction compression index;

γ_σ = mean principal stress compression index; and

γ_π = osmotic suction compression index.

Because the osmotic suction rarely changes in pavement subgrade soil, the volumetric change produced by the osmotic suction variation (the last term on the right hand side of

Equation 6.20) can be ignored. In addition, considering a newly constructed pavement structure without traffic loading, the mean principle stress can also be neglected. Therefore, the matric suction is the only independent variable that determines the volumetric change of the subgrade soil in a pavement, and Equation 6.20 can be reduced to:

$$\frac{\Delta V}{V} = -\gamma_h \log_{10}\left(\frac{h_f}{h_i}\right) \tag{6.21}$$

If the expansive soil is allowed to free swell and free shrinkage, the volumetric strain will evenly distributed in every direction; in other words, the strain in each direction (x_1, x_2, and x_3 direction) will be the same. However, because of the lateral constraint of the soil, the vertical strain (strain in x_3 direction) is usually larger than the horizontal strain (strain in x_1 and x_2 direction). Lytton (1994) presented a crack fabric factor, f, to estimate the vertical strain based on the volumetric strain:

$$\frac{\Delta H}{H} = f \cdot \frac{\Delta V}{V} \tag{6.22}$$

The back-calculated values of f is 0.5 when the soil is drying and is 0.8 when the soil is wetting.

The matric suction compression index (γ_h) can be estimated by an empirical procedure developed by McKeen (1980). This method predicted γ_h using percent fine clay, plasticity index (PI), and cation exchange capacity (CEC). Percent fine clay is calculated by dividing the fine clay (finer than 2 micron) content by percentage passing No. 200 sieve. The cation exchange capacity can be determined by a routine test procedure in agricultural laboratories, or it can be estimated by empirical relationships developed by Mojekwu (1979) as shown in Equations 6.23 and 6.24:

$$CEC = (PL)^{1.17} \quad meq/100g \tag{6.23}$$

$$CEC = (LL)^{0.912} \quad meq/100g \tag{6.24}$$

where

PL = plasticity limit, in percent; and
LL = liquid limit, in percent.

Based on the percent fine clay, PI and CEC, McKeen's method calculates the activity (Ac) and cation exchange activity (CEAc) as in Equations 6.25 and 6.26:

$$Ac = \frac{PI}{\%\ clay} \tag{6.25}$$

$$CEAc = \frac{CEC}{\%\ clay} \quad meq/100g \tag{6.26}$$

The calculated Ac and CEAc are used to obtain a guide number of γ_h in the Chart for the Prediction of Suction Compression Index (Figure 6.1) developed by McKeen. The guide numbers in Figure 6.1 are γ_h for soils with 100 percent fine clay. To obtain the value of γ_h for a real soil, the guide numbers determined by Figure 6.1 is reduced by multiplying the percent fine clay. Finally, the obtained suction compression index need to be corrected to compensate for the different initial volume of soil mass during a wetting or drying process by Equations 6.27 and 6.28 (Lytton, 2004):

$$\gamma_{h(swell)} = \gamma_h e^{\gamma_h} \tag{6.27}$$

$$\gamma_{h(shrinkage)} = \gamma_h e^{-\gamma_h} \tag{6.28}$$

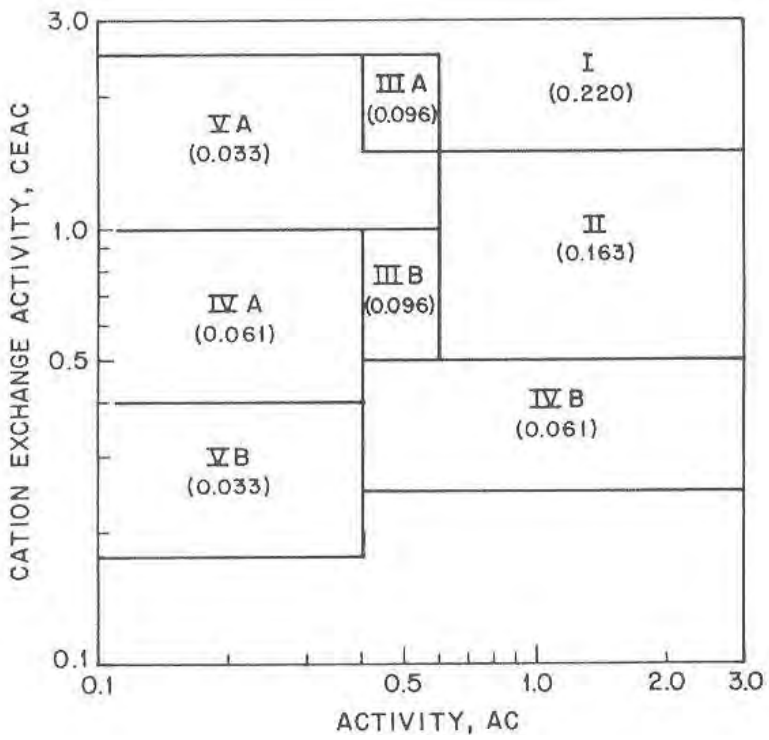

Figure 6.1: Chart for the prediction of suction compression index (McKeen, 1980)

For lime treated soil, Lytton (2004) proposed a method to estimate the plasticity index (PI) and the liquid limit (LL) as shown in Equations 6.29 and 6.30:

$$PI_{\lim e-treated} = PI_{untreated}\left(\frac{9-\%\lim e}{9}\right) \tag{6.29}$$

$$LL_{\lim e-treated} = \frac{PI_{untreated}}{a} + b \tag{6.30}$$

Parameters a and b in Equation 6.30 depend on soil mineral classification, which is shown in Figure 6.2. Typical values of a and b corresponding to each soil mineral classification are given in Table 6.1. Then the suction compression index can be calculated by McKeen's method following the steps described.

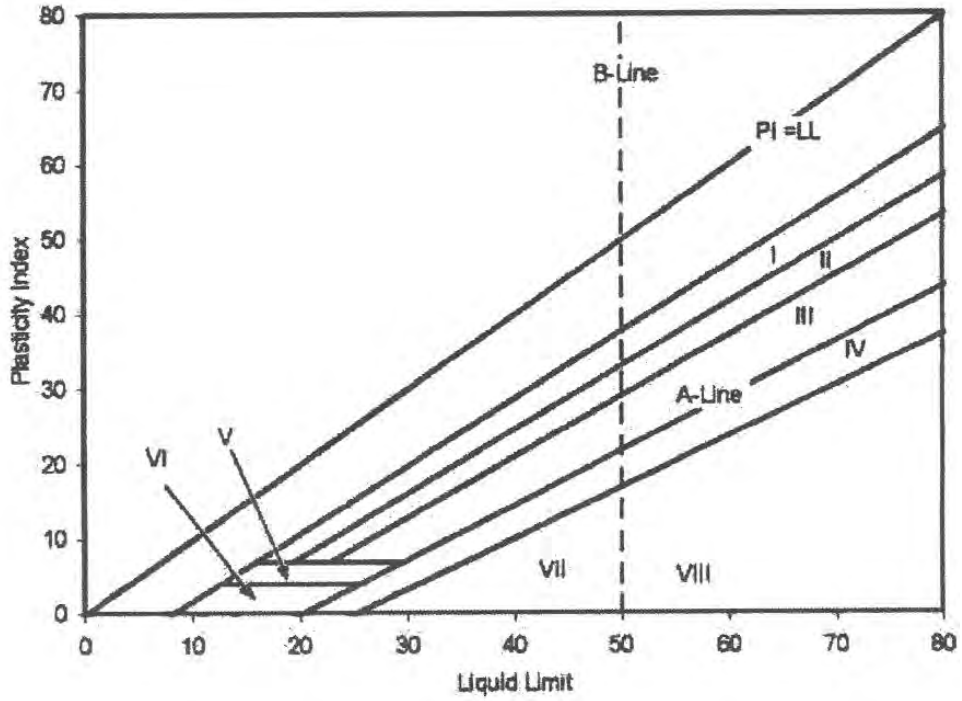

Figure 6.2: Mineral classification (Lytton, 2004)

Table 6.1: Typical values of a and b corresponding to mineral classification (Lytton, 2004)

Group	*a*	*b*
I	0.83	11
II	0.81	14
III	0.73	20
IV	0.68	25
V	0.68	25
VI	0.68	25

For the untreated FM 2 soil, the soil properties were determined by laboratory test and are given in Table 6.1. Consequently, the percent fine clay is calculated to be 22%, Ac is 1.77, CEC is 49, and CEAc is 2.22. The guide number of γ_h is estimated to be 0.220, and the final corrected γ_h for use is 0.0461. If the soil is treated with 6% lime, as the parameters a and b are 0.73 and 20 respectively (because the soil is in the III mineral classification), $PI_{\text{lime}-treated}$ and $LL_{\text{lime}-treated}$ can be calculated by Equations 6.29 and 6.30, and their values are 13 and 39, respectively. Therefore, Ac is 0.59 and CEAc is 1.28, so the guide number of γ_h is 0.033 based on Figure 6.1. The final corrected γ_h is 0.0072. These values of suction compression index are important for pavement modeling use in later sections.

6.2.4 Estimation of Suction Profile

To study the shrinkage crack development in the subgrade soil during the decrease of water content and increase of matric suction, it is desirable to estimate the shrinkage stress generated between two steady state suction profiles. Knowing two steady sate suction profiles, Lytton's model (Equations 6.21 and 6.22) can be used to predict the total strain that occurs between the two steady states based on the suction change. Therefore, the shrinkage stress produced by the suction change can be estimated using the stress-strain constitutive relationship of the subgrade soil. Based on the stress distribution, the reflection of shrinkage crack can be modeled in the subgrade up through the pavement surface.

Matric suction can be measured using filter paper in the laboratory as given in ASTM (2003), which is a simple and economical method for the suction range from 10 to 100,000 kPa. In this test method, the soil specimen is placed with filter papers in an airproof container for seven days. This duration is sufficient to allow different vapor pressures inside the container to reach equilibrium, including pore-water vapor pressure in the specimen, pore-water vapor pressure in the filter paper, and partial water vapor pressure in the air. Subsequently, a calibration relationship is developed between the filter paper water content with soil suction based on the type of the used filter paper and the test procedure. Finally, the suction of the specimen can be determined using the measured mass of the filter papers and the calibration relationship.

The axis-translation technique is another method to directly measure the matric suction in the laboratory. This measurement was originally proposed by Hilf in 1956 for both undisturbed and compacted soil specimens (Fredlund and Rahardjo, 1993). In the test procedure, a closed pressure chamber is used to contain the unsaturated soil specimen. A pore-water pressure measuring probe connects a tube full of deaired water and the soil specimen. The water in the tube has a tendency to go into tension and then produces negative water pressure, which is

measured by a gauge. Increasing the air pressure in the closed chamber will result in higher tendency of the water to go into tension. Once achieving equilibrium, the matric suction of the soil can be determined based on the difference between the air pressure in the chamber and the measured negative water pressure.

Tensiometer is a commonly used device in the field to directly measure the negative pore-water pressure in a soil. The tensiometer allows the equilibrium achieved between the soil and the measuring system. At equilibrium, the water in the tensiometer has the same negative pressure as the pore-water in the soil. Currently different types of tensiometer are available for use in the field (Fredlund and Rahardjo, 1993). Mitchell (1979, 1980) proposed a theoretical model to simulate the effects of climate (evaporation and infiltration) as a sinusoidal form with frequency n, as shown in Equation 6.31:

$$u(0,t) = U_e + U_0 \cos(2\pi nt) \tag{6.31}$$

in which

$u(0,t)$ = matric suction at ground surface, in pF (kPa=0.0981×10^{pF});

U_e = equilibrium suction, in pF;

U_0 = amplitude of suction change at ground surface, in pF;

n = number of suction cycles per second; and
t = time in seconds.

Furthermore, Mitchell developed a model to describe the suction $u(y,t)$ at any time t and depth y:

$$u(y,t) = U_e + U_0 \exp\left(-\sqrt{\frac{n\pi}{\alpha}}y\right)\cos\left(2\pi nt - \sqrt{\frac{n\pi}{\alpha}}y\right) \tag{6.32}$$

in which:

y = soil depth;

α = soil diffusion coefficient, $= \frac{\gamma_w}{\gamma_d}\frac{p}{c}$,

γ_w = water density;

γ_d = soil dry density;

p = unsaturated permeability; and
c = inverse slope of log suction (in pF) vs. gravimetric water content.

The equilibrium suction in a specific location can be estimated based on the Thornthwaite Moisture Index (TMI) (Wray et al., 2005). TMI (Thornthwaite, 1948) is a parameter characterizing the moisture balance in a specific location taking account of rainfall, potential evapotranspiration and the depth of available moisture stored in the rooting zone of vegetation. TMI is calculated by Equation 6.33, and the calculation procedure includes three steps: i) determining monthly potential evapotranspiration; ii) allocating available water to storage, deficit and runoff on a monthly base; and iii) summating monthly runoff moisture depth, deficit moisture depth and evapotranspiration to obtain annual values.

$$TMI = \frac{100R - 60DEF}{E_p} \tag{6.33}$$

where

R = runoff moisture depth;

DEF = deficit moisture depth; and

E_p = evapotranspiration.

Wray (1978) developed a TMI map of Texas based on historical mean of TMI, as shown in Figure 6.3. As the TMI value is determined, the corresponding equilibrium suction, U_e, can be estimated using the Figure 6.4 (Wray, 2005) or a regression equation, Equation 6.34 (Lytton, 2004).

$$U_e = 3.5633\exp(-0.0051TMI) \tag{6.34}$$

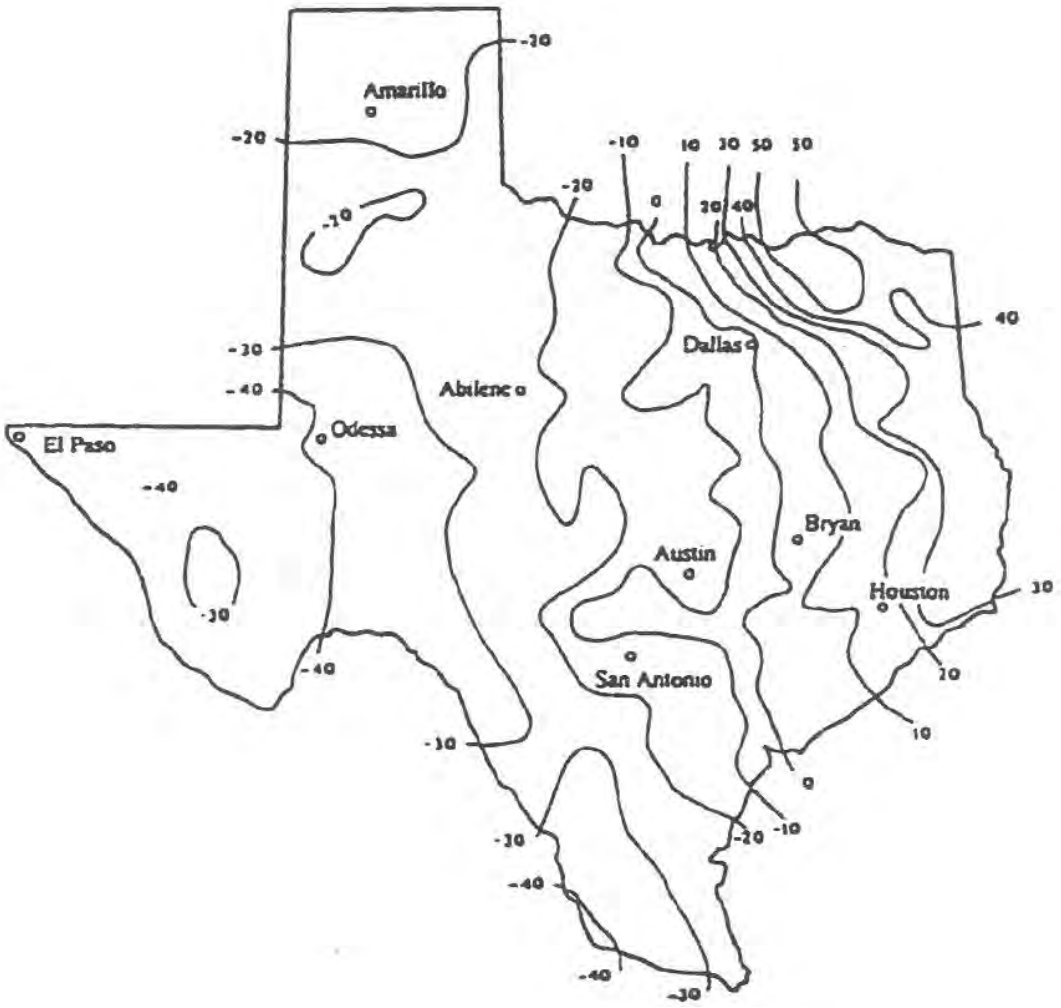

Figure 6.3: Thornthwaite Moisture Index spatial distribution in Texas (Wray, 1978)

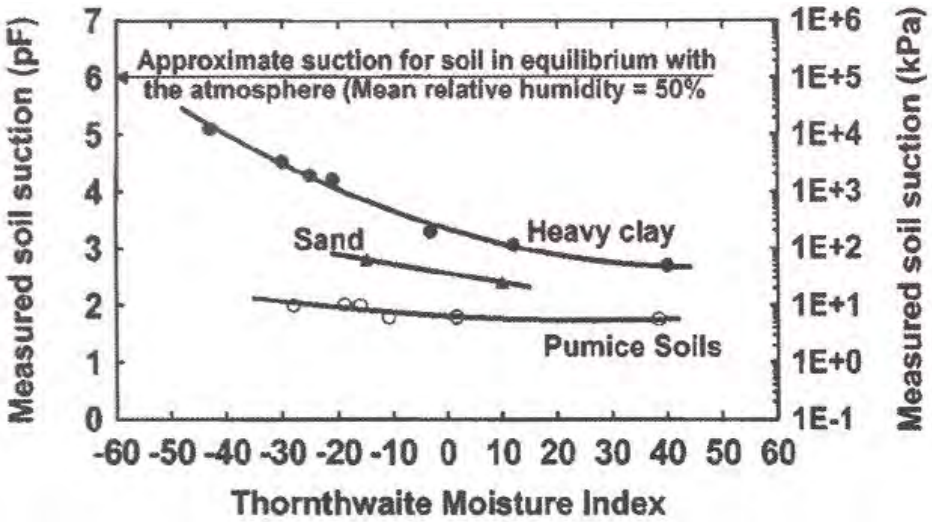

Figure 6.4: Variation of soil suction of road subgrade with Thornthwaite Moisture Index (Wray, 2005)

As FM 2 is located close to Bryan, its TMI value is approximately 6 based on Figure 6.3, and its equilibrium suction, U_e, is estimated to be 3.45 pF using Figure 6.4 or Equation 6.34. The amplitude of suction change at ground surface, U_0, is assumed to be 1.05 pF, and the frequency number n in Equation 6.32 equals to 1 cycle per year. The soil diffusion coefficient α was determined by laboratory test to be 0.0005 cm^2 per second. Therefore, the soil suction profile in each month can be predicted using Mitchell's model (Equation 6.32) as shown in Table 6.2.

Table 6.2: Predicted suction profile in pf in each month in FM 2 area

Month No.	Depth (m)								
	0	0.5	1.0	1.5	2.0	2.5	3.0	3.5	4.0
1	4.36	3.90	3.67	3.56	3.50	3.48	3.46	3.46	3.45
2	3.98	3.71	3.58	3.51	3.48	3.47	3.46	3.45	3.45
3	3.45	3.45	3.45	3.45	3.45	3.45	3.45	3.45	3.45
4	2.93	3.19	3.32	3.39	3.42	3.43	3.44	3.45	3.45
5	2.54	3.00	3.23	3.34	3.40	3.42	3.44	3.44	3.45
6	2.40	2.93	3.19	3.32	3.39	3.42	3.43	3.44	3.45
7	2.54	3.00	3.23	3.34	3.40	3.42	3.44	3.44	3.45
8	2.93	3.19	3.32	3.39	3.42	3.43	3.44	3.45	3.45
9	3.45	3.45	3.45	3.45	3.45	3.45	3.45	3.45	3.45
10	3.98	3.71	3.58	3.51	3.48	3.47	3.46	3.45	3.45
11	4.36	3.90	3.67	3.56	3.50	3.48	3.46	3.46	3.45
12	4.50	3.97	3.71	3.58	3.51	3.48	3.47	3.46	3.45

If the soil is under a flexible impermeable cover, e.g. flexible pavement, the suction is different under the pavement center line from the pavement edge (shoulder). Mitchell (1979) obtained the analytical solution of steady state suction within the soil body under a flexible impermeable cover of length L. The suction under the impermeable cover has an approximate relationship with the suction at the cover edge:

$$u_y(x) \approx U_e + (u_y - U_e)\frac{\cosh\frac{\pi x}{2a}}{\cosh\frac{\pi L}{4a}} \tag{6.35}$$

where

$u_y(x)$ = suction at the location with a distance of x from the pavement centerline in the depth y;

x = distance from the pavement centerline;

u_y = suction at the pavement edge in the depth y;

L = pavement width; and

a = soil active zone depth, under which the soil suction has a constant value of U_e.

Using Equation 6.35, the horizontal suction profile can be predicted based on the vertical suction profile. Consequently, the suction distribution under a flexible impermeable pavement is obtained at each steady suction state.

6.3 Crack development in pavement

Based on the stress/strain analysis and volumetric change theory of the expansive soil, this section will approach the crack development in pavement structure due to the matric suction change in expansive subgrade. Theories of fracture mechanics will be applied to this study, before which necessary background information of fracture mechanics will be provided. Because the pavement is infinitely long in the longitudinal direction, the problem can be reduced to a 2-D plane strain problem for convenience.

6.3.1 Crack Development in Subgrade

Assume the subgrade is intact without any large cracks right after construction, which is the initial condition in this analysis. At the initial situation, both pavement and subgrade are in equilibrium condition. As the moisture content decreases in the subgrade soil, the matric suction increases, which produces tensile stress in the soil. The magnitude of the tensile stress produced by the matric suction change can be estimated by Lytton's model (Equations 6.21 and 6.22) and the constitutive relation of the soil based on two steady state suction profiles. As the tensile stress reaches the tensile strength of the subgrade soil, a crack will initiate.

To determine the location and propagation of the crack, it is necessary to study the stress distribution in the soil before the crack initiation. A 2-D plane strain finite element (FE) model was developed in a commercial FE program, ABAQUS, to simulate the stress field in the pavement and subgrade when the subgrade soil is shrinking. The modeled pavement structure consisted of an asphalt layer, base, and subgrade. Each pavement layer was assumed to be homogenous, isotropic, linearly elastic, weightless, and bonded to the underlying layer. Table 6.3 shows the detailed information of the modeled pavement structure. Because of symmetry, only half-wide pavement was studied. The subgrade width and depth were 12 m and 6 m, respectively, for the purpose of applying proper boundary conditions. The constructed pavement model in ABAQUS is shown in Figure 6.5.

Table 6.3: Pavement structure

Layer	Thickness (m)	Young's Modulus (MPa)	Poisson's Ratio
Asphalt	0.025	2,500	0.35
Base	0.25	350	0.35
Subgrade	6	75	0.35

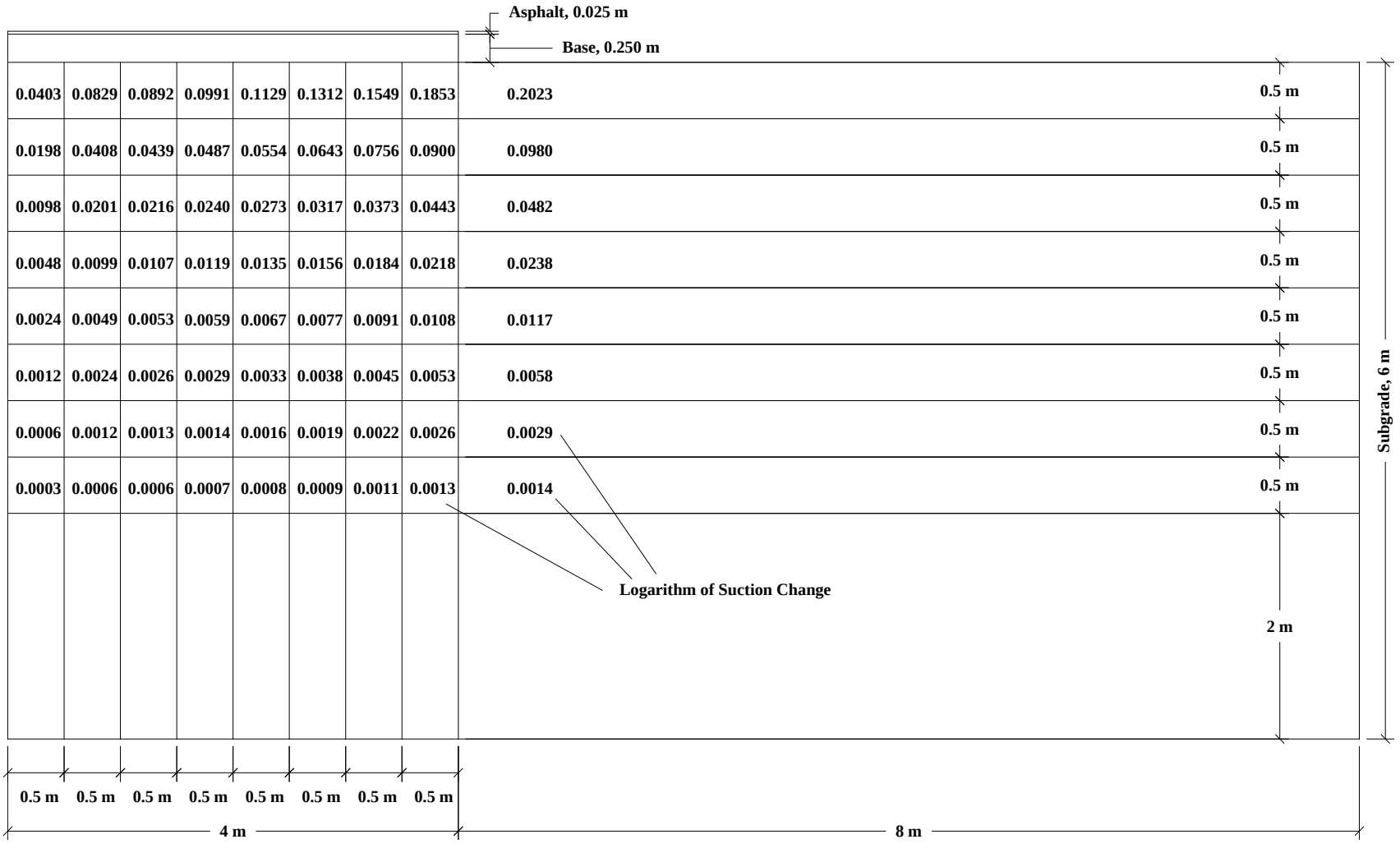

Figure 6.5: Pavement structure modeled in ABAQUS

The boundary conditions for the pavement model were i) no horizontal displacement at the centerline of the asphalt layer, the base, and the subgrade, because of symmetry; ii) no vertical displacement at the bottom of the subgrade, because the geometric size in depth is large enough for the subgrade; and iii) no horizontal displacement at the far end of the subgrade, which satisfies the condition of no horizontal strain before cracking together with the first boundary condition.

Two steady state suction profiles were chosen from the predicted suction profiles in FM 2 area shown in Table 6.2. To capture the critical case, suction profiles in month No. 6 and No. 12 were selected because these two suction profiles represent the driest season and the wettest season, respectively, in terms of extreme suction values. Based on the vertical profiles, the horizontal profile for each steady state was predicted using Equation 6.35. Subsequently, the logarithm of suction change at each location of the soil was calculated from the wet season to the dry season in order to use Lytton's model (Equation 6.21). The logarithm of suction change was simulated using thermal expansion in ABAQUS, that is, the initial temperature of the subgrade soil was assumed to be zero, and the final temperature was the logarithm of the suction change. Because the suction change varies from different locations in the subgrade soil, the subgrade was partitioned into a number of grids, and each grid had a value of "final temperature" that simulated the logarithm of suction change at that location. The number in each grid shown in Figure 6.5 is the "final temperature" at that place. The thermal expansion coefficient in the simulation was one half of the suction compression index (γ_h) based on Equation 6.22. The generated mesh distribution was designed to provide adequate accuracy without consuming too much computational effort. The mesh size is 20 mm for the pavement and the subgrade under the pavement; for the subgrade not under the pavement, biased seed was used to obtain denser mesh close to the pavement and sparser mesh in the regions far from the pavement. All elements were 4-node bilinear plane strain quadrilateral with reduced integration (CPE4R) to increase the rate of convergence. In total, 94,000 elements were generated to simulate this model.

Simulation results showed that in the subgrade soil, the largest positive normal stress in the transverse direction (x_1 direction) developed in the upper part close to the interface of the subgrade and the base. Figure 6.6 shows the distribution of the normal stress in transverse direction in the pavement and the upper part of the subgrade soil in the undeformed shape. Because the ABAQUS sign convention is that tensile stresses are positive and compressive stresses are negative, the stress distribution indicated that the largest tensile stress in the subgrade presented in the area close to the pavement shoulder and close to the base-subgrade interface with a magnitude of around 0.5 MPa. This area has the highest possibility to generate cracks. Therefore, the horizontal location of crack initiation was determined to be 0.6 m in the horizontal direction away from the pavement shoulder. The vertical location of the initial crack should be close to the base-subgrade interface and will be determined in later sections.

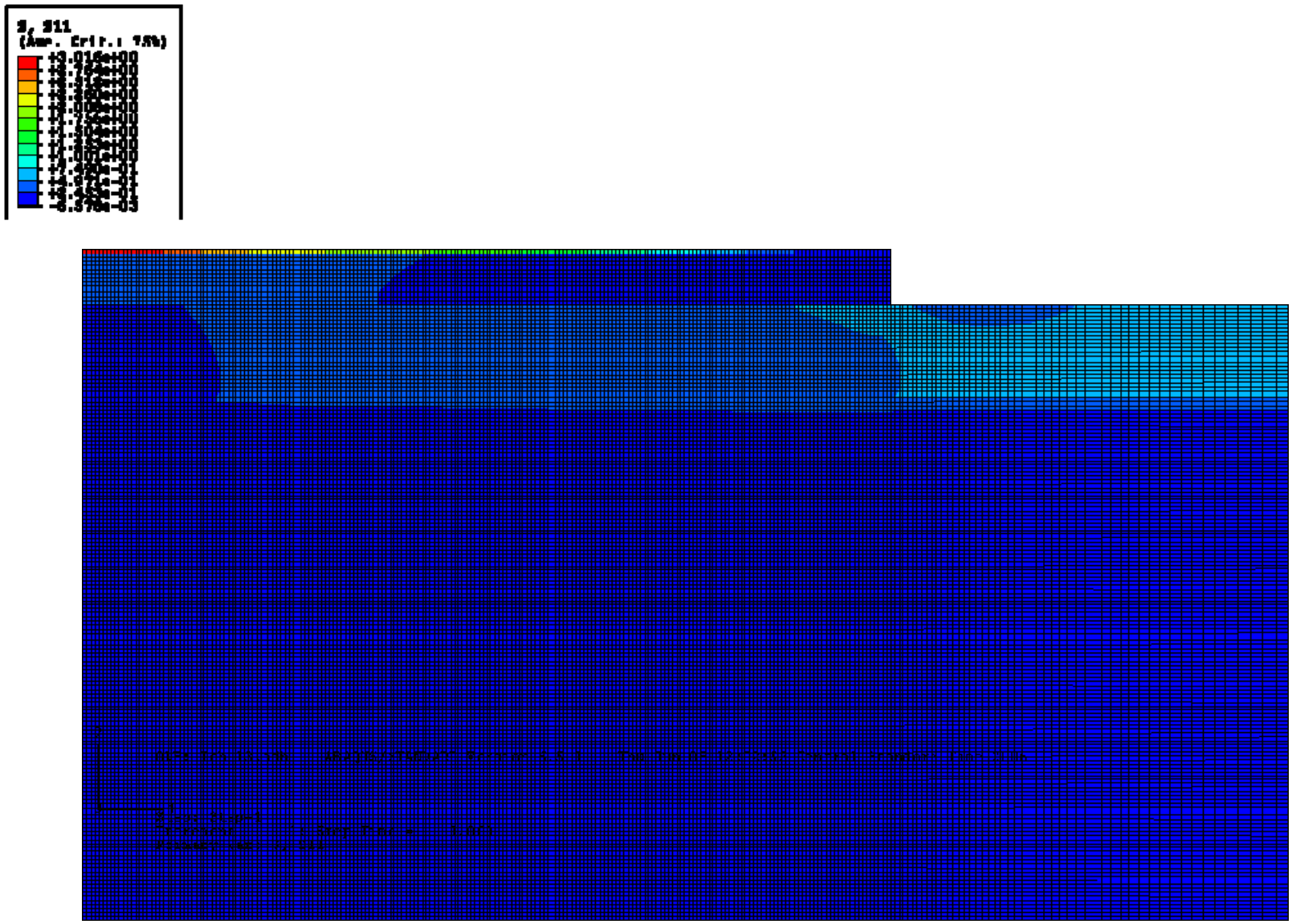

Figure 6.6: Distribution of pavement normal stress in transverse direction

6.3.2 Fundamentals of Crack Propagation

As the crack appears in the subgrade, it is of interest to study how the crack develops to three basic "modes," Mode I, II and III, corresponding to different loading conditions as shown in Figure 6.7 (Lawn, 1993). Mode I (opening mode) corresponds to normal separation of crack under the effect of tensile stress applied normally to the crack plane; model II (sliding mode) corresponds to the in-plane shearing of the crack in a direction normal to the crack front; mode III (tearing model) corresponds to anti-plane shearing parallel to the crack front.

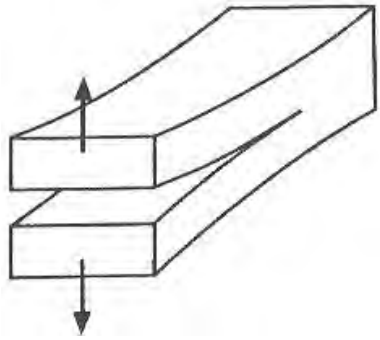

Mode I: Opening Mode

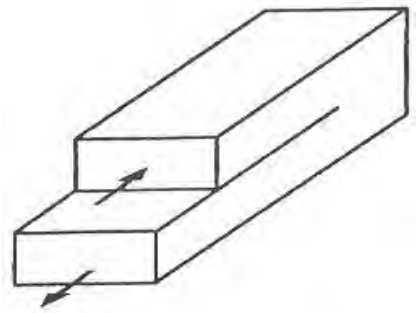

Mode II: Sliding Mode

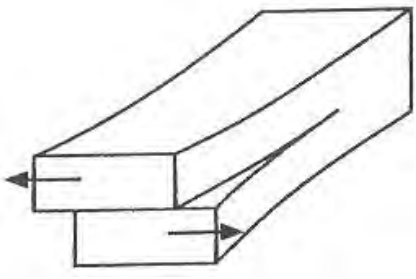

Mode III: Tearing Mode

Figure 6.7: Three fracture modes (Lawn, 1993)

Because stress concentrations occur in the vicinity of the crack tip, a stress intensity factor, K, is used to quantify the components of stress and displacement at the crack tip. Each crack propagation mode has a stress intensity factor, i.e. K_I, K_{II}, K_{III}, respectively. For linear elastic crack tip field, the stress and displacement solutions were developed by Irwin for each crack mode with respect to rectangular coordinates and polar coordinates in Figure 6.3 (Paris et al. 1965; Lawn 1993). The Irwin crack-tip solutions are given in Equations 6.36, 6.37 and 6.38, in which E is Young's Modulus, ν is Poisson's ratio, and

for plane stress: $\kappa = \dfrac{3-\nu}{1+\nu}$, $\nu' = 0$, $\nu'' = \nu$;

for plane strain: $\kappa = 3-4\nu$, $\nu' = \nu$, $\nu'' = 0$.

Mode I:

$$\begin{Bmatrix} \sigma_{xx} \\ \sigma_{yy} \\ \sigma_{zz} \end{Bmatrix} = \frac{K_I}{\sqrt{2\pi r}} \begin{Bmatrix} \cos\left(\frac{\theta}{2}\right)\cdot\left[1-\sin\left(\frac{\theta}{2}\right)\cdot\sin\left(\frac{3\theta}{2}\right)\right] \\ \cos\left(\frac{\theta}{2}\right)\cdot\left[1+\sin\left(\frac{\theta}{2}\right)\cdot\sin\left(\frac{3\theta}{2}\right)\right] \\ \sin\left(\frac{\theta}{2}\right)\cdot\cos\left(\frac{\theta}{2}\right)\cdot\cos\left(\frac{3\theta}{2}\right) \end{Bmatrix} \text{k}$$

$$\begin{Bmatrix} \sigma_{rr} \\ \sigma_{\theta\theta} \\ \sigma_{r\theta} \end{Bmatrix} = \frac{K_I}{\sqrt{2\pi r}} \begin{Bmatrix} \cos\left(\frac{\theta}{2}\right)\cdot\left[1+\sin^2\left(\frac{\theta}{2}\right)\right] \\ \cos^3\left(\frac{\theta}{2}\right) \\ \sin\left(\frac{\theta}{2}\right)\cdot\cos^2\left(\frac{\theta}{2}\right) \end{Bmatrix}$$

$$\sigma_{zz} = \nu'\left(\sigma_{xx}+\sigma_{yy}\right) = \nu'\left(\sigma_{rr}+\sigma_{\theta\theta}\right)$$

$$\sigma_{xz} = \sigma_{yz} = \sigma_{rz} = \sigma_{\theta z} = 0$$

$$\begin{Bmatrix} u_x \\ u_y \end{Bmatrix} = \frac{K_I}{2E}\sqrt{\frac{r}{2\pi}} \begin{Bmatrix} (1+\nu)\cdot\left[(2\kappa-1)\cos\left(\frac{\theta}{2}\right)-\cos\left(\frac{3\theta}{2}\right)\right] \\ (1+\nu)\cdot\left[(2\kappa+1)\sin\left(\frac{\theta}{2}\right)-\sin\left(\frac{3\theta}{2}\right)\right] \end{Bmatrix}$$

$$\begin{Bmatrix} u_r \\ u_\theta \end{Bmatrix} = \frac{K_I}{2E}\sqrt{\frac{r}{2\pi}} \begin{Bmatrix} (1+\nu)\cdot\left[(2\kappa-1)\cdot\cos\left(\frac{\theta}{2}\right)-\cos\left(\frac{3\theta}{2}\right)\right] \\ (1+\nu)\cdot\left[-(2\kappa+1)\cdot\sin\left(\frac{\theta}{2}\right)+\sin\left(\frac{3\theta}{2}\right)\right] \end{Bmatrix}$$

$$u_z = -\frac{\nu'' z}{E}\cdot(\sigma_{xx}+\sigma_{yy}) = -\frac{\nu'' z}{E}\cdot(\sigma_{rr}+\sigma_{\theta\theta}) \tag{6.36}$$

Mode II:

$$\begin{Bmatrix} \sigma_{xx} \\ \sigma_{yy} \\ \sigma_{xy} \end{Bmatrix} = \frac{K_{II}}{\sqrt{2\pi r}} \begin{Bmatrix} -\sin\left(\frac{\theta}{2}\right)\cdot\left[2+\cos\left(\frac{\theta}{2}\right)\cdot\cos\left(\frac{3\theta}{2}\right)\right] \\ \sin\left(\frac{\theta}{2}\right)\cdot\cos\left(\frac{\theta}{2}\right)\cdot\cos\left(\frac{3\theta}{2}\right) \\ \cos\left(\frac{\theta}{2}\right)\cdot\left[1-\sin\left(\frac{\theta}{2}\right)\cdot\sin\left(\frac{3\theta}{2}\right)\right] \end{Bmatrix}$$

$$\begin{Bmatrix} \sigma_{rr} \\ \sigma_{\theta\theta} \\ \sigma_{r\theta} \end{Bmatrix} = \frac{K_{II}}{\sqrt{2\pi r}} \begin{Bmatrix} \sin\left(\frac{\theta}{2}\right)\cdot\left[1-3\sin^2\left(\frac{\theta}{2}\right)\right] \\ -3\sin\left(\frac{\theta}{2}\right)\cdot\cos^2\left(\frac{\theta}{2}\right) \\ \cos\left(\frac{\theta}{2}\right)\cdot\left[1-3\sin^2\left(\frac{\theta}{2}\right)\right] \end{Bmatrix}$$

$$\sigma_{zz} = \nu'(\sigma_{xx}+\sigma_{yy}) = \nu'(\sigma_{rr}+\sigma_{\theta\theta})$$

$$\sigma_{xz} = \sigma_{yz} = \sigma_{rz} = \sigma_{\theta z} = 0$$

$$\begin{Bmatrix} u_x \\ u_y \end{Bmatrix} = \frac{K_{II}}{2E}\sqrt{\frac{r}{2\pi}} \begin{Bmatrix} (1+\nu)\cdot\left[(2\kappa+3)\cdot\sin\left(\frac{\theta}{2}\right)+\sin\left(\frac{3\theta}{2}\right)\right] \\ -(1+\nu)\cdot\left[(2\kappa-3)\cdot\cos\left(\frac{\theta}{2}\right)+\cos\left(\frac{3\theta}{2}\right)\right] \end{Bmatrix}$$

$$\begin{Bmatrix} u_r \\ u_\theta \end{Bmatrix} = \frac{K_{II}}{2E}\sqrt{\frac{r}{2\pi}} \begin{Bmatrix} (1+\nu)\cdot\left[-(2\kappa-1)\cdot\sin\left(\frac{\theta}{2}\right)+3\sin\left(\frac{3\theta}{2}\right)\right] \\ (1+\nu)\cdot\left[-(2\kappa+1)\cdot\cos\left(\frac{\theta}{2}\right)+3\cos\left(\frac{3\theta}{2}\right)\right] \end{Bmatrix}$$

$$u_z = -\frac{\nu'' z}{E}(\sigma_{xx}+\sigma_{yy}) = -\frac{\nu'' z}{E}(\sigma_{rr}+\sigma_{\theta\theta}) \tag{6.37}$$

Mode III:

$$\sigma_{xx} = \sigma_{yy} = \sigma_{rr} = \sigma_{\theta\theta} = \sigma_{zz} = 0$$

$$\sigma_{xy} = \sigma_{r\theta} = 0$$

$$\begin{Bmatrix} \sigma_{xz} \\ \sigma_{yz} \end{Bmatrix} = \frac{K_{III}}{\sqrt{2\pi r}} \begin{Bmatrix} -\sin\left(\frac{\theta}{2}\right) \\ \cos\left(\frac{\theta}{2}\right) \end{Bmatrix}$$

$$\begin{Bmatrix} \sigma_{rz} \\ \sigma_{\theta z} \end{Bmatrix} = \frac{K_{III}}{\sqrt{2\pi r}} \begin{Bmatrix} \sin\left(\frac{\theta}{2}\right) \\ \cos\left(\frac{\theta}{2}\right) \end{Bmatrix}$$

$$u_x = u_y = u_r = u_\theta = 0$$

$$u_z = \frac{4K_{III}}{E}\sqrt{\frac{r}{2\pi}}\left[(1+\nu)\sin\left(\frac{\theta}{2}\right)\right] \tag{6.38}$$

The stress intensity factor, K, depends on the applied loading and specimen geometry, for example, the size of the crack. Consequently, the stress intensity factor determines the stress intensity of the local field.

The Irwin crack-tip solution is important to determine the crack propagation from the energy release point of view. For a crack configuration in Figure 6.8, let U_E be the strain energy in the system and the crack length be a prior to extension. The strain energy release may be presented in an integral form over the crack surfaces immediately behind the crack tip per unit width of front:

$$\delta U_E = 2\int_{a+\delta a}^{a} \frac{1}{2}\left(\sigma_{yy}u_y + \sigma_{xy}u_x + \sigma_{zy}u_z\right)dx, \ (u = \text{constant}) \tag{6.39}$$

In Equation 6.39, the factor 2 indicates the displacement of the two crack surfaces; the factor 1/2 means the proportionality between tractions and corresponding displacements; the stresses σ_{ij} correspond to $r = x - a$, $a \le x \le a + \delta a$, $\theta = 0$; and the displacements u_i corresponds to $r = a + \delta a - x$, $\theta = \pi$. Define the strain energy release rate as:

$$G = -\left(\frac{\partial U_E}{\partial a}\right)_u \tag{6.40}$$

Substituting the Irwin crack-tip solutions (Equations 6.36, 6.37 and 6.38) into Equation 6.39 and proceeding to the limit $\delta a \to 0$, the strains energy release rate may be integrated as:

$$G = \frac{K_I^2}{E'} + \frac{K_{II}^2}{E'} + \frac{K_{III}^2(1+\nu)}{E} \tag{6.41}$$

in which $E' = E$ in plane stress and $E' = E/(1-\nu^2)$ in plane strain.

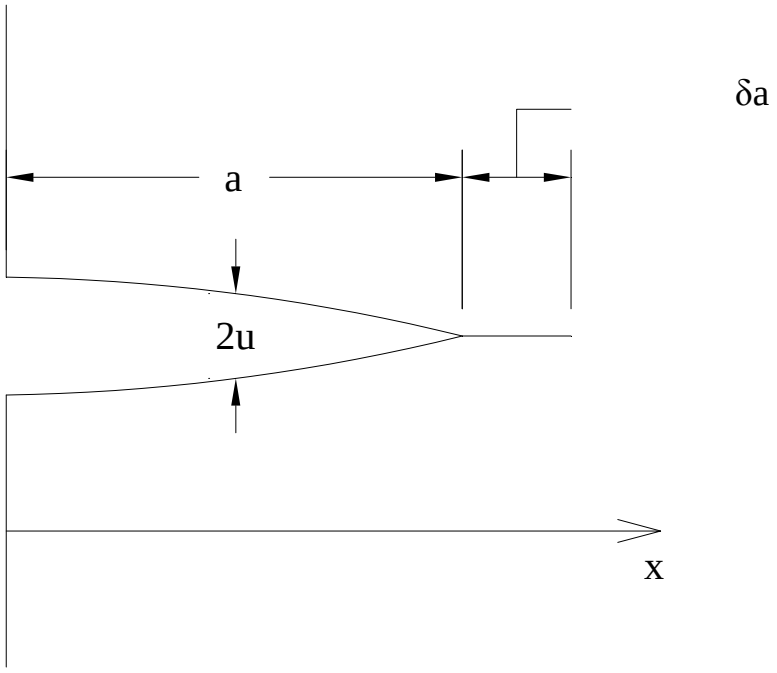

Figure 6.8: Crack Increment in Specimen of Unit Thickness

At energy equilibrium, the strain energy release rate, G, equals to the surface energy of the generated two crack surfaces, $2\gamma_s$ (γ_s is the surface energy of one crack surface). When $G = 2\gamma_s$, the corresponding stress intensity factor, K_c, is called the fracture toughness of the material, which is a constant material property and can be measured experimentally. Consequently, the fracture criterion is that: when the stress intensity factor is larger than the fracture toughness of a material, the crack is unstable and will propagate to release energy until energy equilibrium; and when the stress intensity factor is smaller than the fracture toughness, the crack remains stable.

For a crack in a linear elastic body, the strain energy release rate (G) and the stress intensity factor (K) can be quantified using a path-independent integral, which is called J integral (Rice, 1968). The J integral is defined as:

$$J = \int_{\Gamma} \left(W dy - \mathbf{T} \frac{\partial \mathbf{u}}{\partial x} ds \right) \tag{6.42}$$

where

W = the strain energy density, $W = \int_0^{\varepsilon} \sigma_{ij} d\varepsilon_{ij}$;

Γ = any curve surrounding the crack tip;

$\mathbf{T}$ = the traction vector defined according to the outward normal along Γ, $T_i = \sigma_{ij} n_j$;

$\mathbf{u}$ = the displacement vector;

y = direction normal to the crack line; and

ds = differential element of arc length along Γ.

In the linear elastic case, the J integral is identical to the strain energy release rate G and can be related to the stress intensity factors. Therefore, the J integral is widely accepted as a quasi-static fracture mechanics parameter for linear response.

6.3.3 Fracture Toughness of Pavement Materials

According to the fracture criterion, if the stress intensity factor is larger than the material fracture toughness, the crack will propagate; otherwise the crack will be stable. Unfortunately, fracture toughness for soils and pavement materials (HMA, crushed stone, lime-treated soil, etc.) has not been well defined to date.

Harison et al. (1994) used a ring test to measure the mode I fracture toughness (K_{IC}) of two compacted soils from Kentucky. They found K_{IC} varied significantly with the soil type and water content. For the first test clay, K_{IC} decreased from 0.200 to 0.020 $MPa \cdot \sqrt{m}$ as the water content increased from 3% to 23%. For the second test clay, K_{IC} varied from 0.028 to 0.005 $MPa \cdot \sqrt{m}$ as the water content increased from 3% to 16%.

Konrad et al. (2001) reported the fracture toughness (K_{IC}) of frozen base and subbase soils in pavement with different ice content. The measured fracture toughness increased as the increase of ice content and soil average grain size. For a given volumetric ice content, the fracture toughness of frozen crushed stone was found to be larger than that of the frozen sand. At the temperature 23º F (-5º C), the fracture toughness of crushed stone samples with an average dry density of 2070 kg/m^3 and a porosity of 22% increased approximately linearly from 0.05 to 0.40 $MPa \cdot \sqrt{m}$ as the volumetric ice content increased from 6% to 14.2%; the K_{IC} of the frozen

sand with dry density varying from 1490 to 1690 kg/m^3 increased from 0.04 to 0.70 $MPa \cdot \sqrt{m}$ when the volumetric ice content increased from 8% to 28%.

Mobasher et al. (1997) tested K_{IC} of asphalt concrete and asphalt-rubber mixture at different binder content and two temperatures (30º F and 19º F) (-1 ºC and -7 ºC). For most specimens in their test, the measured K_{IC} decreased as the increase of temperature but increased when the binder content increased. For asphalt concrete, the measured K_{IC} values varied from 0.77 to 1.17 $MPa \cdot \sqrt{m}$; for asphalt rubber, the K_{IC} value was from 0.60 to 1.06 $MPa \cdot \sqrt{m}$.

Because the fracture toughness of soil and pavement materials reported in the literature is not a constant but depends on a number of variables (temperature, material property, etc.), it is difficult to precisely predict whether the initial crack will grow or not by using the fracture criterion. However, in order to study the crack propagation process, this study conservatively assumed the fracture toughness of each pavement material to be constant and to be close to the lower value presented in the literature. The assumed fracture toughness for asphalt, base, and subgrade soil is 1.000, 0.100, and 0.050 $MPa \cdot \sqrt{m}$, respectively. If the crack stress intensity factor is larger than the assumed fracture toughness, the crack may not definitely propagate but have a higher possibility to grow. This approach will also be used in later section to demonstrate the benefit of geogrid reinforcement.

6.3.4 Crack Propagation Process

To study the crack development in the pavement, an initial crack was introduced to the upper part of subgrade. As stated in previous section, the horizontal location of the initial crack was assumed to be 0.06 m away from the pavement shoulder. The vertical location of the initial was selected by a few trials based on the strain energy release condition, that is: i) introduce the initial crack at different vertical locations with the same horizontal location, ii) calculate the J integral and stress intensity factors, iii) compare the magnitude of the stress intensity factors and select the vertical location with the largest mode I stress intensity factor (K_I). The initial crack length was assumed to be 0.025 m. All the J integral and stress intensity factors can be calculated in ABAQUS.

Based on the FE model constructed in previous section, the initial crack was introduced to the subgrade without changing the load and boundary conditions. The crack was modeled as a seam with specified crack tips and crack fronts from the Interaction Module of ABAQUS/CAE. The seam, defined as an edge in this two-dimensional part in this model, was originally closed

but can open during the analysis. ABAQUS/CAE places overlapping duplicate nodes along the seam when the mesh is generated. All the elements in the FE model were eight-node biquadratic plane strain (CPE8R) elements. By using these collapsed second-order elements, a mesh singularity can be obtained at the crack tips. In order to create a $1/\sqrt{r}$ singularity in strain at the crack tips, a value of 0.25 was used for the midside node parameter, which moved the midside nodes on the element sides adjoining the collapsed edge to the quarter points of the elements. In addition, the element sides at the crack tips were collapsed with single-node-type degenerate element control.

The J integral and stress intensity factors are evaluated in ABAQUS along contours. Each contour is a ring of elements completely surrounding the crack tip from one crack face to the opposite crack face. A number of contours can be specified to calculate contour J integral. The first contour integral was determined using all the elements within the crack front and one layer of element outside the crack front. Additional contour integrals were computed by adding a single layer of elements to the group of elements that were used to calculate the previous contour integral. ABAQUS automatically finds the elements that form each ring at the crack tip. Each contour provides an evaluation of the J integral and stress intensity factors. Even though the J integral is path independent, each contour provides a different estimate on J integral because of the approximate nature of the finite element solution. Therefore, a finer mesh is needed at the crack tip. Even with fine mesh at the crack tip, the first few contours may vary and be inaccurate. To obtain the contour integral with a high level of accuracy, more contours should be requested until the value of contour integral appears approximately constant from one contour to the next. In this study, the crack tip regions were partitioned to facilitate the generation of focused meshes. In the Step Module of ABAQUS/CAE, history outputs with 20 contours were requested for each crack tip to calculate the J integral and the stress intensity factors.

Before studying the development of initial crack, 10 trial cracks were placed at different vertical location to find the most possible vertical location of the initial crack. Even though the subgrade top has the largest tensile stress, the initial crack is less possible to occur there because the pavement has little tensile stress prior to the initial crack presence and tends to keep the soil intact. Therefore, the initial crack is most possible to occur in the upper part of the subgrade, which has relatively large tensile stress, but not at the interface of the base and subgrade. All the trial cracks were placed at 0.6 m horizontally away from the pavement shoulder with the same crack length, 0.025 m, but different vertical location. Define d as the vertical distance from the upper crack tip to the interface of the base and subgrade. In the first trial, d is 0.01 m; in the second trial, d is 0.035 m (0.025 m lower than the first trial crack); and so on. All the stress intensity factors, including K_I and K_{II}, at the crack tips were calculated. The mode I stress intensity factor K_I was of special interest because it directly related to the longitudinal crack on

the pavement. The calculation results are showed in Table 6.4. The mode I stress intensity factor K_I at both crack tips reached the maximum when d is 0.16 m. In summary, the initial crack was determined to be 0.16 m in the vertical direction from the interface of the base and subgrade and 0.6 m in the horizontal direction from the pavement shoulder.

Table 6.4: Trail crack stress intensity factors

No.	d (m)	Crack Tip	K_I ($MPa \cdot \sqrt{m}$)
1	0.010	Upper tip	0.080
		Lower tip	0.084
2	0.035	Upper tip	0.087
		Lower tip	0.087
3	0.060	Upper tip	0.089
		Lower tip	0.089
4	0.085	Upper tip	0.089
		Lower tip	0.089
5	0.110	Upper tip	0.089
		Lower tip	0.089
6	0.135	Upper tip	0.090
		Lower tip	0.089
7	0.160	Upper tip	0.091
		Lower tip	0.090
8	0.185	Upper tip	0.090
		Lower tip	0.090
9	0.210	Upper tip	0.090
		Lower tip	0.089
10	0.235	Upper tip	0.089
		Lower tip	0.089

The stress intensity factor at the upper and the lower tips of the initial crack were 0.091 and 0.090 $MPa \cdot \sqrt{m}$, respectively, both of which were larger than the assumed fracture toughness of the subgrade soil (0.050 $MPa \cdot \sqrt{m}$). Consequently, the initial crack was assumed to grow in both directions. Figure 6.9 records the crack developing progress from the initial

crack (Crack 1) to the finial crack (Crack 7) whose crack tip reached the asphalt layer. The stress intensity factors at both crack tips varied at each crack progress stage, but they were always larger than the fracture toughness of the pavement materials. This fact does not mean that the crack will definitely propagate but does indicate that the desiccation crack had a very high possibility of causing the longitudinal crack on the pavement surface.

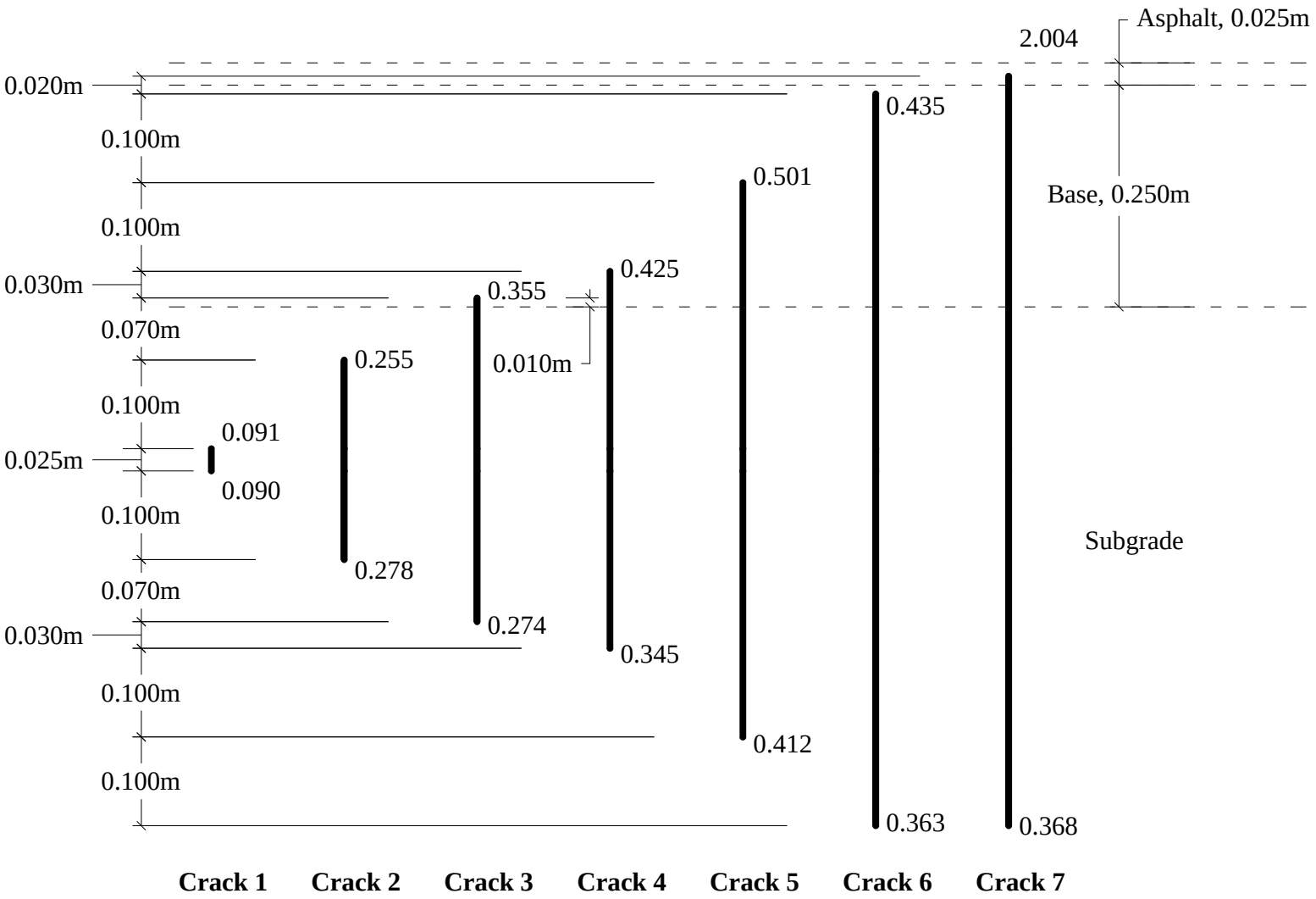

Figure 6.9: Stress intensity factors of crack in pavement without geogrid (Unit: MPa·m$^{0.5}$)

6.4 Benefit of geogrid reinforcement

6.4.1 Mechanism of Geogrid Reinforcement

Geogrid is defined by the American Society for Testing and Materials (ASTM) as "*a planar product manufactured from polymeric material used with soil, rock, earth, or other geotechnical engineering related material as an integral part of man-made project, structure, or system.*" Geogrids are manufactured in a factory-controlled environment. They are packaged in sheets, placed in rolls or cartons, and finally transported to the sites. At the project sites, the geogrid sheets are unrolled on the prepared surface, overlapped with each other to form a continuous geogrid blanket, and often physically joined to each other.

Geogrids have high tensile strength so they have been used to reinforce the pavement and particularly, to be placed at the interface of base and subgrade to prevent cracks developing from the shrinking subgrade. The base material interlocks the subgrade soil through the geogrid apertures, the geogrid can be assumed to be fully bonded with pavement materials. When the crack initiated in the subgrade develops upward, the crack may go through the geogrid as the geogrid is not a physical barrier but has apertures. However, the geogrid has to deform with the crack opening, and a small deformation of a rigid geogrid results in a significant force. Consequently, the geogrid applies this force directly to the crack faces, as illustrated in Figure 6.10. This force tends to close the crack and to reduce the stress intensity factor at the crack tip, which is the basic mechanism of geogrid preventing crack development.

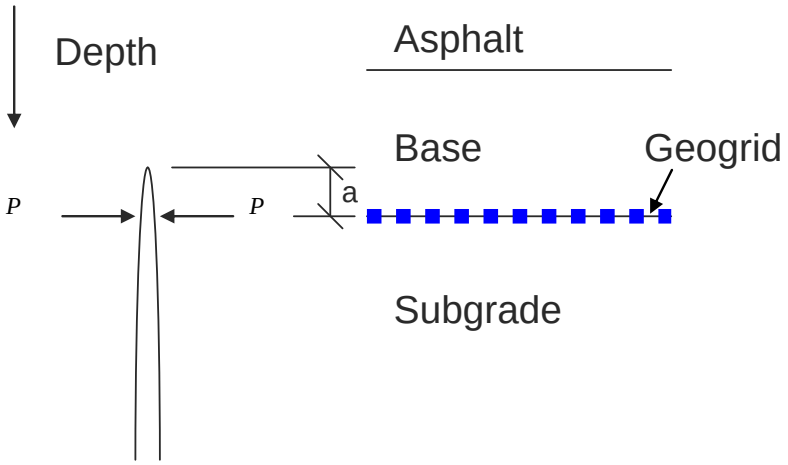

Figure 6.10: Mechanism of geogrid preventing crack

The magnitude of the stress intensity factor reduction can be analytically calculated using the so-called M-integral conservation law. Freund (1978) studied four plane elastic crack problems with concentrated force applying perpendicularly to the crack faces. The stress

intensity factors were calculated simply and directly by using the conservation law. Tada et al. (2000) gave detailed mathematical solutions to the stress intensity factors of the problem. In the literature, the concentrated force is applied to the crack surfaces in the outward direction to let the crack grow. On the contrary, in the geogrid-reinforcement problem, the geogrid applies force to the crack surfaces in the inward direction to let the crack close. The geogrid-reinforcement force results in a reduction of the stress intensity factor with the same magnitude as the one in the literature. In summary, there are two forces applied on the surfaces of the desiccation crack in the geogrid-reinforcement pavement: one is the shrinking stress in the soil, which is the driving force for the crack propagation; another is the geogrid-reinforcement force, which limits the crack growth. If the geogrid can reduce the stress intensity factor of the upper crack tip to a value that is below the fracture toughness of the base, the crack will stop developing upward to the pavement surface.

6.4.2 Modeling and Benefit of Geogrid

Based on the finite element model constructed in ABAQUS, the geogrid was placed at the interface of the base layer and subgrade as reinforcement. The one-dimensional truss element was selected to model the geogrid because the geogrid was a slender structure that supports loading only along the horizontal direction but cannot resist any bending. In the 2D finite element model, the truss elements representing geogrid reinforcement were “embedded” in the “host” pavement elements using the embedded element technique offered by ABAQUS. The embedded truss elements had identical displacement to the host solid elements, that is, the embedded elements were full bonded to the surrounding materials. This technique fairly simulated the situation that a crack goes through the geogrid without breaking it.

The geogrid was given a fixed Poisson’s ratio of 0.5 and different elastic moduli of 400, 1000 and 4000 MPa . An initial crack was introduced to the geogrid-reinforced pavement model at exactly the same position (0.6 m horizontally away from the pavement shoulder and 0.16 m vertically away from the subgrade top). The stress intensity factors at the crack tips were calculated and presented in Figure 6.11, in which three stress intensity values show at the each crack tip: the first number is the stress intensity factor at that crack tip when the modulus of the geogrid is 400 MPa ; the second number is the stress intensity factor when the geogrid modulus is 1000 MPa ; and the third number is when the geogrid modulus is 4000 MPa . Compared to Figure 6.9, Figure 6.11 shows that the geogrid reinforcement reduced the stress intensity factors at the tips of Crack 1 (initial crack) and Crack 2, but the stress intensity factors still exceeded the fracture toughness of the subgrade soil. Therefore, the crack was assumed to be extended in both directions until the upper crack tip advanced into the base course and was 0.01 m away from the geogrid. All geogrids with different moduli demonstrated significant reinforcement benefit by reducing the stress intensity factor at the upper crack tip from 0.355 (see Figure 6.8) to no more

than 0.100 $MPa \cdot \sqrt{m}$. The geogrid with higher stiffness showed better performance in the reinforcement.

The results showed that the geogrid can successfully reduce the stress concentration at the crack tip and therefore significantly decrease the likelihood of crack growing upward. The stress intensity factor of the lower tip of the crack was still larger than the assumed soil toughness so that the crack may extend in the downward direction. However, as the stress intensity factor of the upper crack tip was decreased to the level below the fracture toughness of the base material, the crack is much less possible to develop toward the pavement surface. These findings indicate that the geogrid may allow the crack to extend in the subgrade but considerably constrain the desiccation crack to propagate toward the pavement surface. In another words, geogrid reinforcement can successfully reduce the longitudinal crack on the pavement surface caused due to the shrinkage of expansive subgrade.

6.5 Conclusions

This study analyzed the stress field in the expansive subgrade due to the matric suction changes. A finite element model was developed to simulate the stress distribution in a pavement over shrinking subgrade. The linear elastic fracture mechanics theory was used to the study the crack propagation from the subgrade upward to the pavement. The desiccation crack was modeled in ABAQUS, and stress intensity factors were calculated at the crack tips.

The mechanism of geogrid reinforcement was studied from the fracture mechanics point of view. The geogrid was modeled as “embedded elements” to function as reinforcement in the solid pavement element at the interface of base and subgrade. A number of geogrids with different elastic moduli were selected for the purpose of study the effect on the benefit of geogrid reinforcement. The stress intensity factors of the crack in the pavement with different geogrid were computed by ABAQUS and were compared with that of the crack in the pavement without geogrid.

Results show that the geogrid can significantly reduce the stress intensity factor at the crack tip in the base, which means the shrinkage crack is much less likely to propagate through the base layer toward the pavement surface. The geogrid with higher stiffness may provide more reinforcement by further reducing the stress intensity factor, but the additional benefit is not significant. These findings support current practice in Texas of using geogrid reinforcement for the control of shrinkage cracks that develop in the subgrade and propagate to the surface. As such, it is the first step into the quantification of this mechanism.

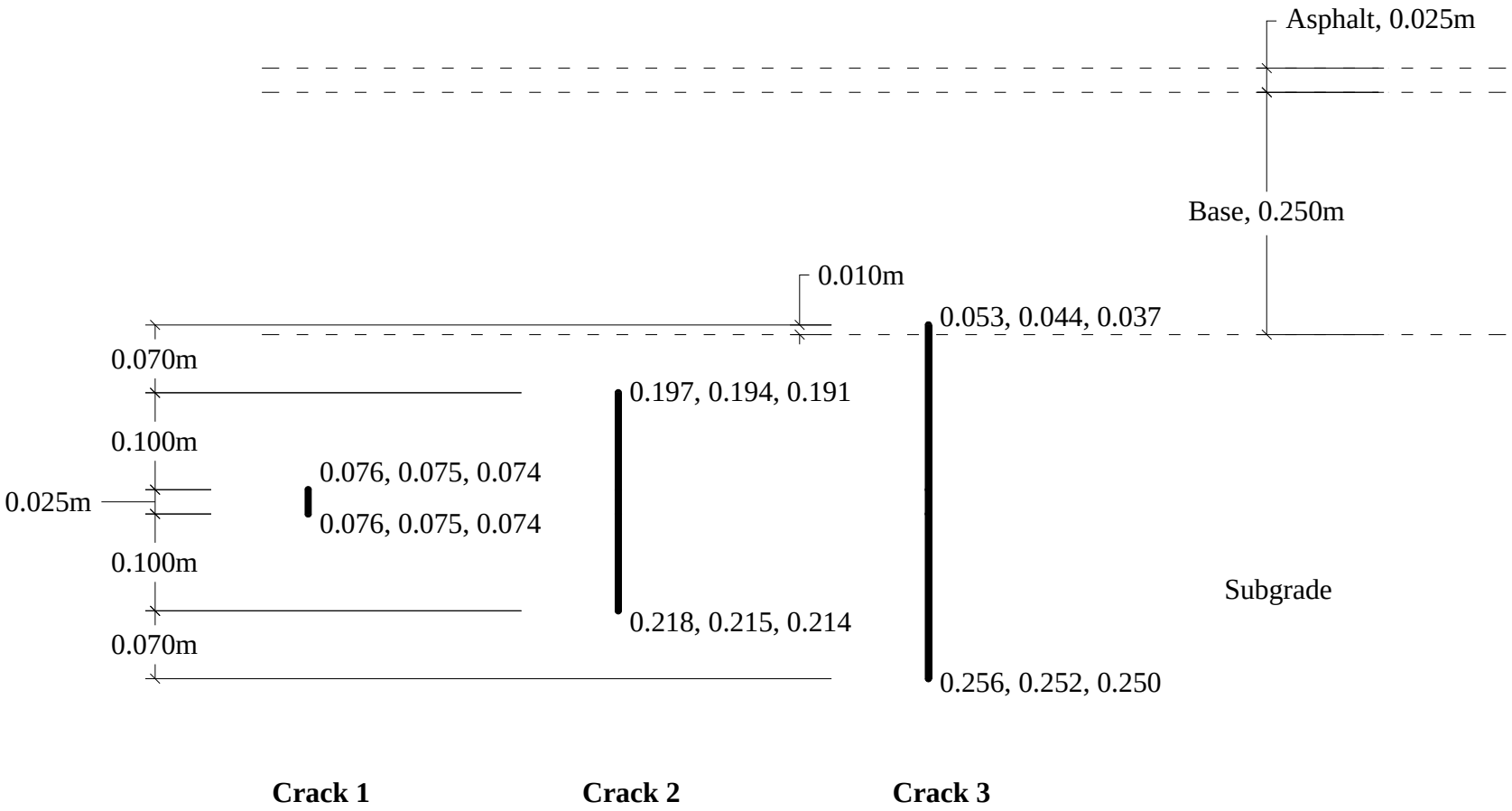

Figure 6.11: Stress Intensity Factors of Crack in Geogrid-Reinforced Pavement (Unit: MPa·m$^{0.5}$)

Chapter 7. Moisture Migration in Geosynthetic Reinforced Pavements

7.1 Introduction

The Texas Department of Transportation (TxDOT) has observed longitudinal cracking in flexible pavements constructed atop expansive clay subgrades. Clays are considered expansive when they experience volume change upon wetting and drying, and are often characterized by a plasticity index (PI) greater than 20. Longitudinal cracks occur parallel to the roadway and can extend a significant distance. Further, they have often been observed by TxDOT to extend through the base course into the subgrade. These cracks are undesirable, as they provide a pathway for moisture infiltration and increased ease of base course particle migration, both of which accelerate roadway degradation (Sebesta et al. 2004). A mechanism of longitudinal cracking relevant to flexible pavements atop expansive clay subgrades is differential volume change across the width of the roadway. This occurs due to moisture infiltration from rainstorms or moisture removal due to evapotranspiration. Due to the low structural stiffness of flexible pavements compared to concrete pavements, stress redistribution due to differential movement may result in brittle failure of the pavement system. As this mechanism is independent of vehicle loading, it may be used to explain several pavement failures observed by TxDOT before opening to traffic. An improved understanding of the migration of moisture in highway subgrades will enhance implementation of strategies for prevention of longitudinal cracking in pavements.

7.2 Mechanism of crack formation

A strong linkage between moisture migration and longitudinal cracking has not been well established in the literature. Accordingly, the goal of this research was to investigate the migration of moisture under the pavement in order to assess the likelihood of differential shrinkage and swelling between the center and edges of the pavement. Specifically, the horizontal and vertical components of the volumetric strain due to shrinkage and swelling may impose tensile, shear, and bending stresses at the point under the pavement at which moisture does not fluctuate. An exaggerated representation of the vertical component of subgrade movement is shown in Figure 7.1(b). The first case shows the edges of the pavement bending downwards, as the subgrade soil in the shoulder shrinks during drying. The second case shows the edges of the pavement bending upwards as the subgrade in the shoulder swells during wetting. In both cases, differential movement between the shoulders and the centerline of the road will lead to longitudinal cracks that are closer to the edge of the pavement, similar to those observed in Figure 7.1.

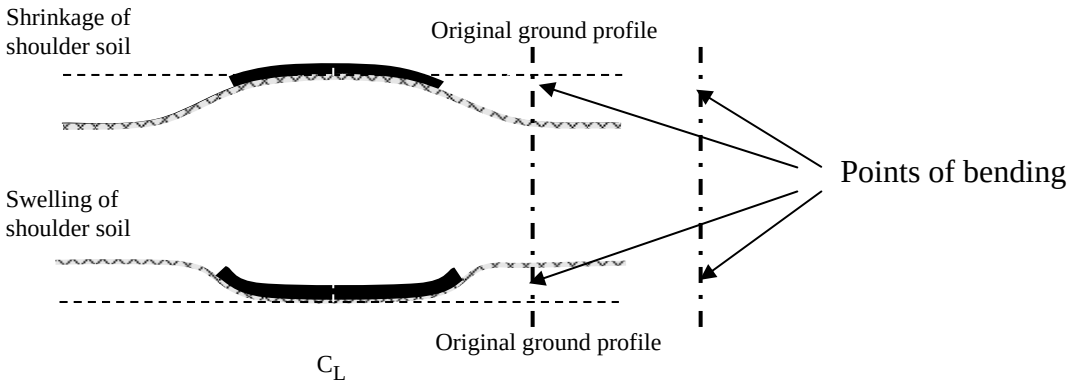

Figure 7.1: Conceptual model for subgrade volume change

The effects of volume change in expansive clay subgrades on pavement performance have been addressed by removal of the expansive clay, placement of a stiff pavement structure over the expansive material, or by lime treatment of the subgrade. Removal of soil over the length of a roadway is cost-prohibitive, and the swell pressures of expansive soil can be high enough to exceed the tensile strength of concrete. Lime treatment has been found to be inadequate in expansive clays containing sulfates. In these clays, growth of ettringite mineral crystals has been observed upon the addition of lime (Mitchell and Dermatas 1992). Ettringite crystal growth has been observed to lead to significant volume changes in the subgrade. Although this issue has been addressed by allowing time for ettringite crystal formation before compaction of the lime treated soil, problems have still been encountered due to inadequate dosing of lime and spatial variability in the sulfate concentration along the length of a roadway. In response to the difficulties encountered in conventional treatment options, TxDOT has investigated the use of geogrid reinforcement for subgrade reinforcement. Geogrids have been observed to work well on several roads in eastern Texas over the past five years, such as FM1915 in Millam County and SH7 and FM 2 in Bryan district (Zornberg et al. 2008). Geogrids have been proposed to increase the stiffness of the subgrade, to help bridge cracks, to limit the passage of cracks from the subgrade into the base course, and to increase the tensile resistance of the pavement. The normal stress on the geogrid is negligible compared to that in retaining wall and embankment applications, so conventional geogrid design methodologies are inappropriate. Additional research is needed to define the material properties that lead to an improvement in pavement performance.

An ongoing research project at The University of Texas at Austin has focused on the investigation of geosynthetic reinforcement of subgrades, mechanisms of longitudinal cracking, and moisture migration in clay subgrades. This project includes a full-scale field monitoring component. Specifically, several geosynthetic-reinforced test sections were installed during the rehabilitation of the FM 2 road, near Navasota, TX. Horizontal and vertical profiles of moisture sensors were installed in several of the test sections at FM 2. This chapter describes the details of the moisture sensor installation and calibration, presents results from moisture sensors installed into the subgrade component of several pavement profiles at FM 2, and evaluates trends in the moisture data useful for investigation of the mechanism of longitudinal cracking.

7.3 Pavement rehabilitation

Texas Farm-to-Market Road No. 2 (FM 2) is located in Grimes County (southeast Texas) as explained in Chapter 3. The following figures show FM 2 relative to major metropolitan areas in Texas.

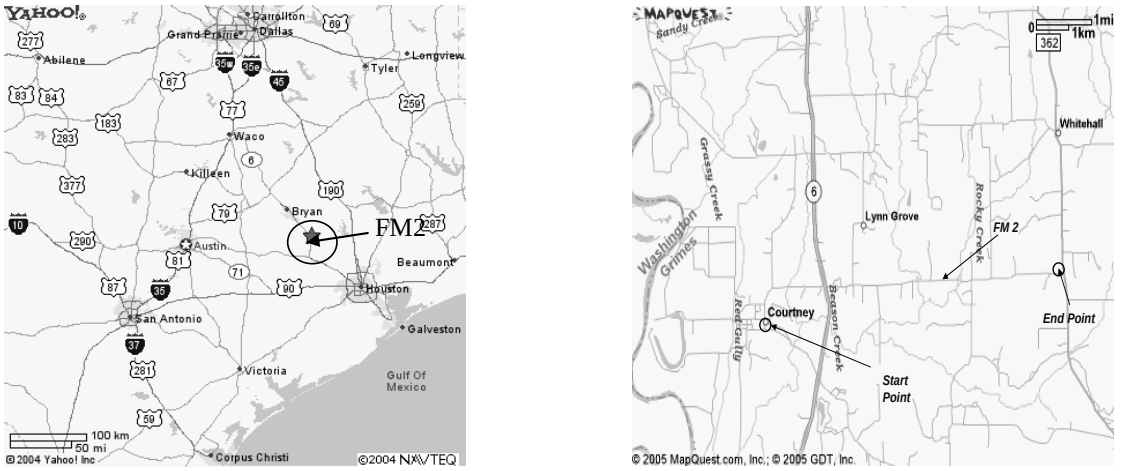

(a) (b)

Figure 7.2: (a) Location of FM 2 relative to major metropolitan areas in Texas; (b) Layout of FM 2

A typical pavement cross section of the FM 2 pavement before rehabilitation is shown in Figure 7.3. The roadway was severely deteriorated before rehabilitation, with longitudinal cracking and rutting. Degradation was likely due to both water seepage through the cracked asphalt and water infiltration into the subgrade clay. Due to the relatively thick existing base course layer (0.4 m), TxDOT decided to scarify only the top 0.25 m of this material. The proposed scarification plan for the new pavement test sections is shown in Figure 7.3. The roadway has a slope of 3% from the centerline to the edge of the road, and there is approximately a 0.8 m drop-off from the edge of the pavement to the trough of the drainage ditch.

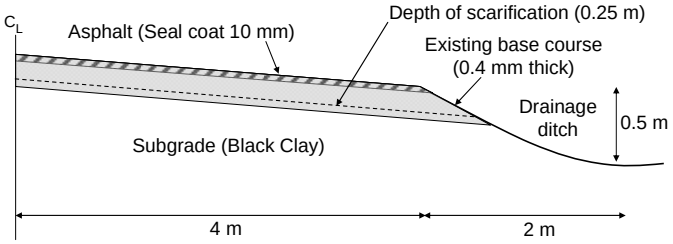

Figure 7.3: Original pavement cross-section at FM 2 with scarification plan

After scarification, TxDOT decided to treat the soil with lime before re-compaction to provide a stiff foundation for the new flexible pavement. After scarification, lime treatment, and compaction of the existing base course, a layer of geogrid reinforcement was placed onto the road. This was followed by an additional 175 mm of compacted base course and a seal coat of asphalt. It should be noted that the existing subgrade was not included in the scarification or lime treatment plans, likely due to workability issues with the clay of high plasticity. Accordingly, the

overall goal of the rehabilitation plan at FM 2 was to stiffen the road above the expansive clay subgrade. Of the possible mechanisms of geogrid reinforcement, the intention of using the geogrid in this rehabilitation was to prevent translation of volume changes in the subgrade into the base course. Construction occurred during the summer of 2005, and finished in Fall 2005.

The University of Texas at Austin proposed a modification to this rehabilitation program to by changing the type of geogrid at different sections, and by not using lime treatment in some of the sections. Specifically, eight test sections were proposed to investigate different types of geogrids and the use or not of lime stabilization, as summarized in Table 7.1. These test sections include an unreinforced section and three geosynthetic-reinforced sections. Geosynthetic types 1 and 2 are geogrids while geosynthetic type 3 is a woven geotextile. The eight pavement cross sections were repeated four times each (for a total of 32 sections) throughout the length of the road in order to account for changes in behavior due to location and environmental conditions (slope, soil conditions, vegetation). The location of the different pavement cross sections along the length of the road are shown in Figure 4. Moisture sensors were installed into the subgrade soil at several locations along FM 2 to monitor typical moisture migration patterns under the pavement and in the shoulders. This study focuses on the results from two vertical profiles of moisture sensors installed at Stations 199 and 184, and one horizontal profile installed at Station 84, as shown in Figure 7.4.

Table 7.1: Pavement cross-section descriptions in FM 2 project

Pavement test section	Lime treatment*	Geosynthetic
1	Yes	No reinforcement
2	Yes	Geogrid 1
3	Yes	Geogrid 2
4	Yes	Woven geotextile
5	No	No reinforcement
6	No	Geogrid 1
7	No	Geogrid 2
8	No	Woven geotextile

* Lime treatment used for scarified pre-existing base course

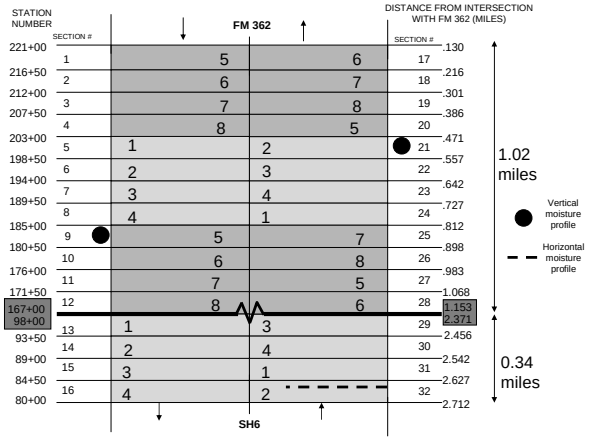

Figure 7.4: FM 2 layout with moisture sensor profile installation locations

The clay subgrade at FM 2 varies along the four miles of pavement. Cores of the first 3 meters of soil were obtained at three locations. The thicknesses of the soil layers at the moisture sensor installations are shown in Figure 7.5(a). Two predominant clays were noted: a red clay with medium plasticity index (PI=35) and a black-gray clay with high plasticity index (PI=50). The black-gray clay is common in the Bryan district and is colloquially referred to as "Backlands." At the end of the borings (around 3 meters) an intact sandy clay layer was collected. A survey was conducted to obtain an elevation profile of the pavement-shoulder surface at Station 199, as shown in Figure 5(b). The soil profile at this location is also included in this figure. The seal coat of asphalt extends to ±4.0 m and partially covers the run-out of the base course. Vertical profiles of the porosity of the black clay at Station 199 for two times during the year are shown in Figure 5(c). The average porosity (n) is 0.45 and the dry density (ρ_d) corresponding to this porosity is 1500 kg/m^3 (assuming that the soils are saturated and G_s = 2.7). A shrinkage curve was obtained for an intact core of the black clay, as shown in Figure 5(d). The shrinkage limit (SL) is 13.

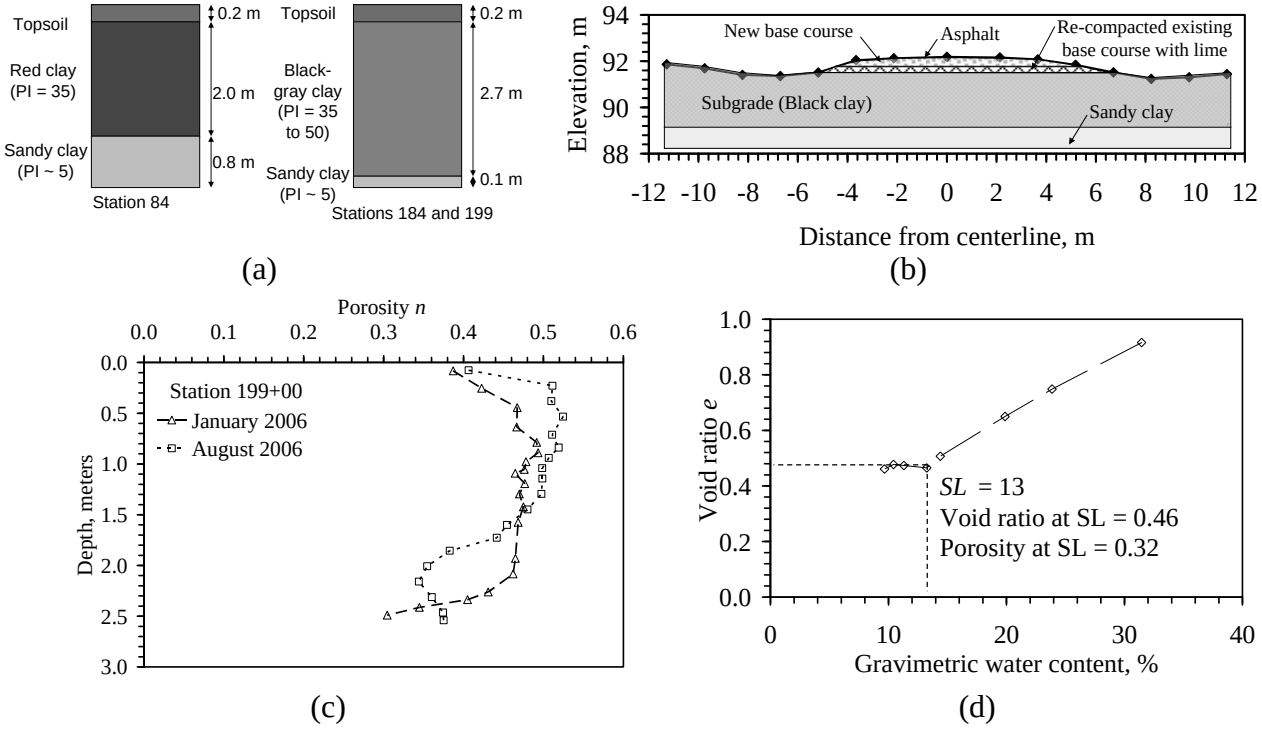

Figure 7.5: (a) Boring summary; (b) Elevation profile at Station 199; (c) Porosity profile; (d) Shrinkage curve

The travel time for moisture to pass from the shoulder to the center of the pavement can be estimated using the hydraulic conductivity of clay when saturated (K_s). The hydraulic conductivity of a core of the black clay (having a gravimetric water content w = 28% or porosity n = 0.43) was determined to be $7x10^{-10}$ m/s using a flexible wall permeameter. The hydraulic conductivity of the red clay remolded at its optimum water content is $5x10^{-9}$ m/s, about an order of magnitude more permeable than the black clay. The lower PI of the sandy clay indicates that it is more permeable than the overlying clays, indicating it may be a secondary boundary for moisture entry into the subgrade.

7.4 Moisture sensors

ECH_20 sensors, obtained from Decagon, Inc., were used in this study to infer the gravimetric water content at particular locations in the subgrade. These sensors consist of a capacitor circuit embedded within a protective resin. The sensors measure the time required for the capacitor to charge upon application of a potential difference (Decagon 2006). The soil acts as the dielectric material between the capacitor plates, so the time required to charge the capacitor is sensitive to the dielectric permittivity of the soil. Changes in the relative amounts of air and water in the soil during wetting and drying, as well as changes in density during shrinkage/swelling, result in changes in dielectric permittivity. The charge time of the capacitor is correlated in this study with the gravimetric water content of the soil, as this parameter is only sensitive to changes in the mass of water (assuming that the mass of solids is constant). Although the soil may be saturated during swelling, the mass of water will increase as the density increases. For a saturated soil, changes in gravimetric water content are directly proportional to changes in the void ratio. The ECH_20 sensors have low power requirements compared to other moisture sensors (time domain reflectometry, neutron gauge), are relatively small, are inexpensive, and can be used with conventional data loggers such as the Decagon EM50 or the HOBO data loggers.

The procedures for installation were different for the horizontal and vertical arrays of sensors. The horizontal array was installed in compacted red clay, while the vertical arrays were installed in quasi-undisturbed conditions. Accordingly, the moisture sensors were calibrated for compacted red clay in the lab, and separately for the black clay in-situ. A barrel of red clay was dried in the lab and several 3 kg samples were conditioned to a range of gravimetric water contents expected in the field (5 to 25%). Specimens of the red clay were compacted to a dry density (ρ_d) of 1600 kg/m^3 in a rectangular mold sized to fit the sensor with 30 mm of clearance on each side. A piston compactor was used to control the energy imparted to the soil during compaction, and the moisture sensor was placed into the middle of three lifts. After compaction, a measurement was made with the moisture sensor. The relationship between the gravimetric water content of the red clay and the sensor reading is shown in Figure 7.6(a). In a strict sense, this calibration curve is valid for the unsaturated red clay at this particular dry density. Accordingly, it may not provide the exact water content for the clay after swelling or shrinkage occurs. Nonetheless, this calibration equation provides a first estimate of the water content in the subgrade. For the black clay, the sensor output was correlated with the gravimetric water content of a sample of soil obtained from the location at which the moisture sensor was installed, as shown in Figure 7.6(b). The average porosity and dry density from the borings that were conducted at the time of installation are also shown. A linear calibration equation was obtained for this soil, falling above the 1:1 line. The range in gravimetric water content of 29 to 41 shown in this figure reflects the initial gravimetric water content during installation of the moisture sensors. This calibration curve also includes data from sensors from arrays at other locations in the black clay that are not discussed here.

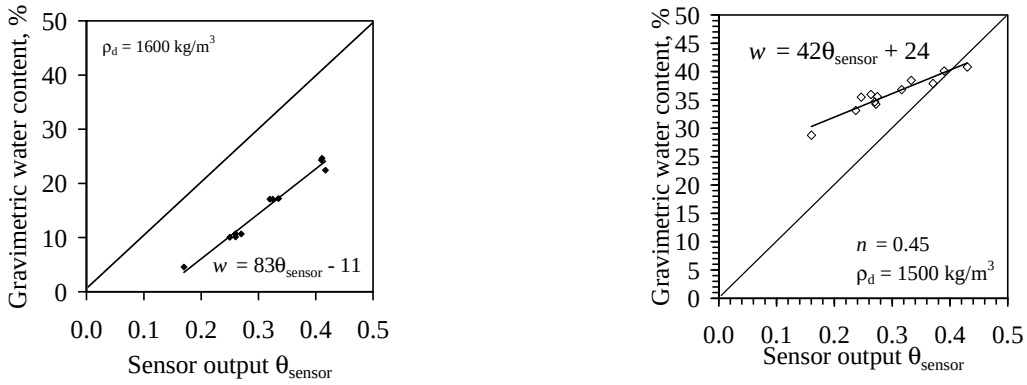

Figure 7.6: Moisture sensor calibration: (a) Calibration for remolded red clay; (b) Calibration for in-situ black clay

7.4.2 Moisture Sensor Installation

The pavement profile and horizontal sensor locations at Station 84 are shown in Figure 7.7(a), while those for the vertical profiles at Stations 184 and 199 are shown in Figures 7.7(b) and 7.7(c). The low hydraulic conductivity of the asphalt seal coat ($<10^{-9}$ m/s) and the slope of the roadway indicate that rainfall onto the pavement will runoff into the drainage ditch, so it is considered impermeable. The drainage ditch is assumed to be the primary infiltration pathway into the subgrade. The horizontal array of sensors is useful to assess the movement of water under the road, while the vertical arrays are useful to assess moisture fluctuations in the soil profile without the influence of the pavement boundary.

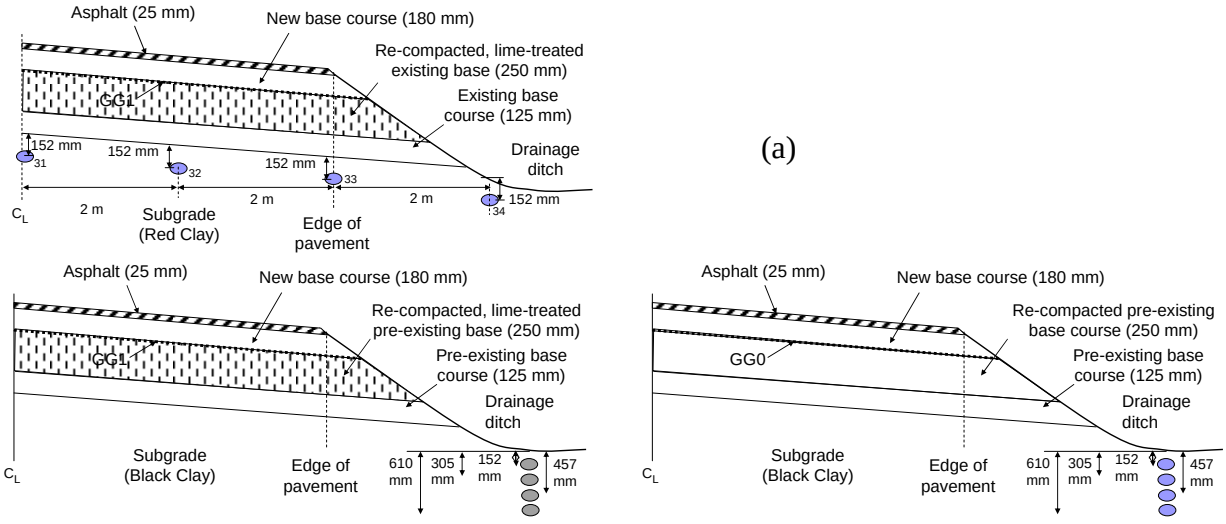

Figure 7.7: Sensors: (a) Horizontal array at Station 84; (b) Vertical array at Station 184; (c) Vertical array at Station 199

The moisture sensors in the horizontal array at Station 84 were installed in remolded soil (consistent with the calibration). For this location, a trench perpendicular to the direction of the

road was excavated through one of the lanes using a backhoe [Figure 7.8(a)]. Care was taken to separate the base course and the subgrade for later replacement of the road section [Figure 7.8(b)]. The soil was leveled at the sensor locations [Figure 7.8(c)], the sensors were placed as indicated in Figure 7.7(a), and the subgrade was carefully backfilled around the sensors. The sensor cables were passed through a corrugated plastic tube to a mailbox containment system [Figure 7.8(d)]. The cables were connected to a datalogger inside the mailbox containment system for easy access [Figure 7.8(e)]. The moisture sensors in the vertical sensor arrays at Stations 184 and 199 were installed into intact soil by creating a pilot holed for the sensor. After digging a 0.75 m deep hole at the monitoring location, a saw blade was used to create a small slit into the soil using several blows from a rubber mallet [Figure 7.8(f) and 7.8(g)]. After carefully removing the saw blade, the moisture sensor was inserted into the slit, and soil was backfilled over the sensor end [Figure 7.8(h) and 7.8(i)]. The subgrade was then backfilled into the hole and compacted by hand using the hammer.

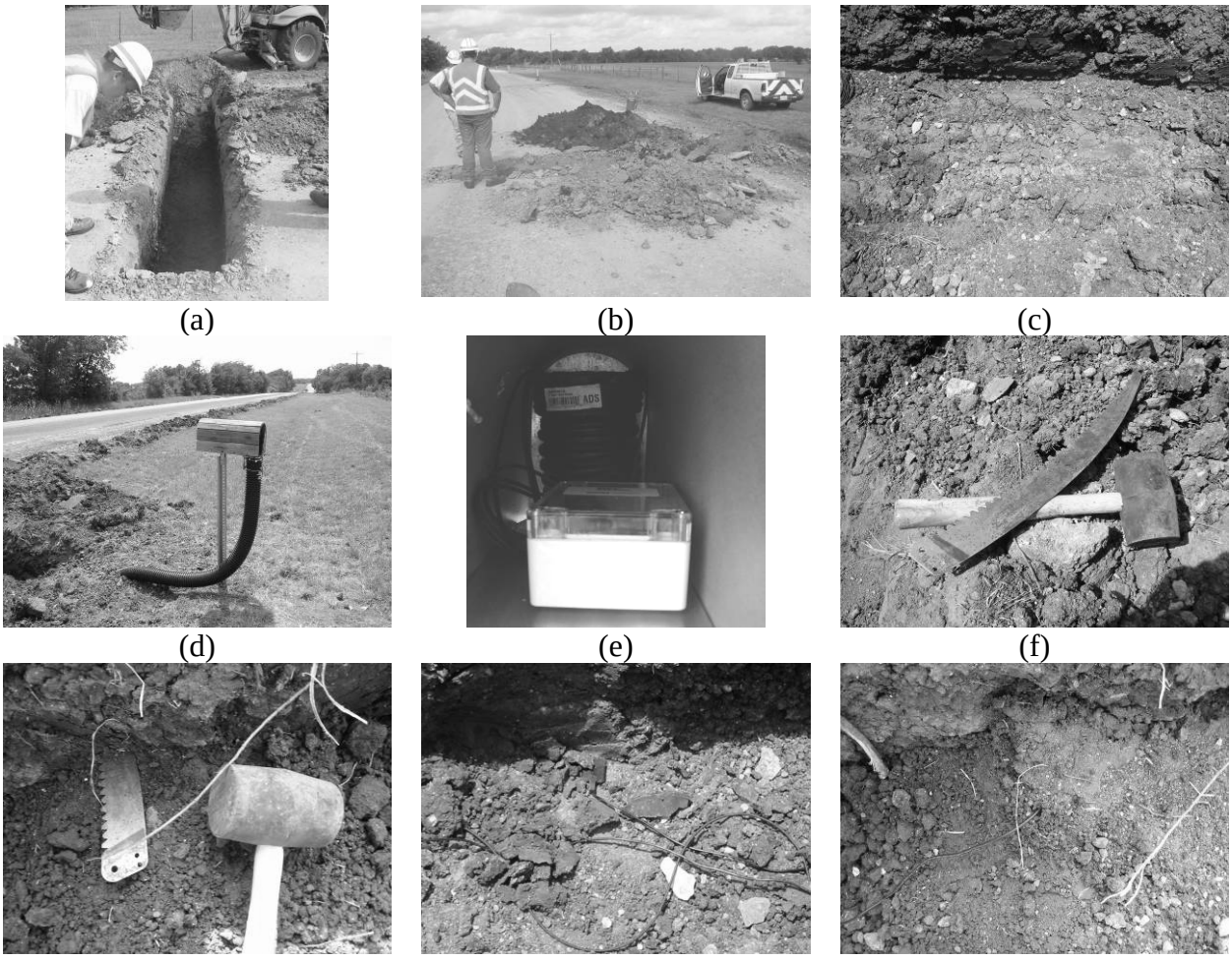

Figure 7.8: Moisture sensor installation procedures: (a) Trenching; (b) Separation of base and subgrade; (c) Leveling of installation site; (d) Protective tubing and datalogger containment system; (e) Datalogger; (f) Tools for pre-insertion of sensor; (g) Pre-insertion; (h) Installed sensor; (i) Compaction near sensor head

7.5 Field monitoring results

7.5.1 Weather Data

Although the closest weather station to the site is at Hempstead, approximately 3 miles from the road, this weather station has only been in operation since January 2006. Accordingly, the historic weather patterns were obtained from a weather station located in College Station, which is also in the Bryan district of Texas. The monthly average records of temperature and precipitation for last 30 years in College Station (WSI Corporation 2005) are shown in Figure 7.9. The average high temperature was around 97º F (36° C) in August and average low temperature was 37º F (3° C) in January. The average annual precipitation was calculated to be 40 in. (1013 mm), with high rainfall amounts in May, June, September, and October. The site has two dry seasons in a year divided by two rainy seasons.

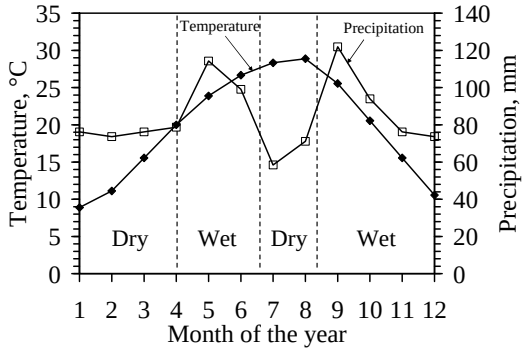

Figure 7.9: Average monthly climate data based on 30 years of weather records from College Station

Daily weather data from the station in Hempstead, TX was more useful for day-to-day assessment of the environmental conditions at the FM 2 site. The precipitation is shown in Figure 7.10(a). This figure indicates that periods of intense rain occurred between October and February of 2006, while periods of little rainfall were observed in the late spring and late summer. The temperature and relative humidity at Hempstead are shown in Figure 7.10(b). This figure indicates that the relative humidity fluctuates between 50 and 92%, while the temperature ranges from 32 to 88º F (0 to 31° C).

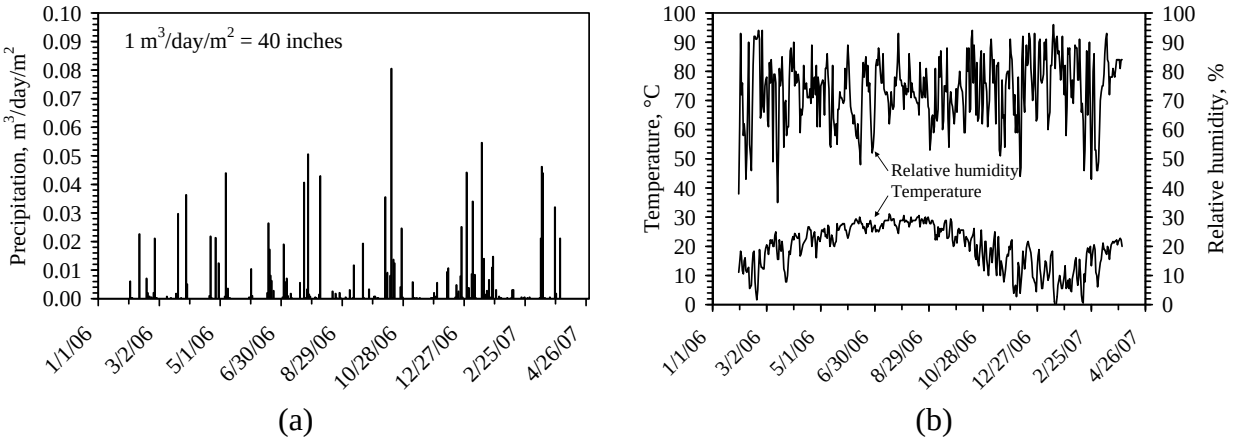

Figure 7.10: Weather data at Hempstead: (a) Precipitation data; (b) Temperature and relative humidity data

7.5.2 Gravimetric Profiles from Bore Holes

The samples obtained from split-tube samples during the borings were used to determine the in-situ water content profiles at different times of the year. The gravimetric water content profiles at the times of two different borings are shown in Figure 7.11(a) and 7.11(b) for Stations 184 and 199. The soil has a relatively dry surface layer (with $w < SL$), likely due to the onset of a dry period. However, the gravimetric water content values deeper in the profiles from January 2006 are representative of relatively dry conditions, while the profiles from August are representative of relatively wet conditions. However, the gravimetric water content difference is not significantly different for the two periods.

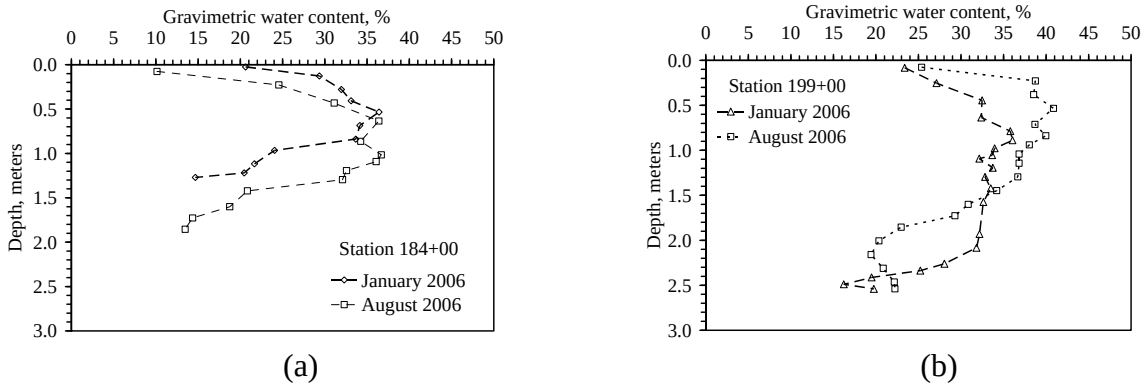

Figure 7.11: Gravimetric water content profiles from the boreholes: (a) Station 184 (b) Station 199

7.5.3 Horizontal Moisture Profile Results from Sensors

The monitoring results for the horizontal array at Station 84 are shown in Figure 7.12(a). The installation time for Station 84 was May 26, 2005, which was before the roadway had been

rehabilitated (construction finished in fall 2005). The data logger did not start working consistently until July 28, 2005 due to an issue with the batteries. Discussion with the site operators indicates that the site was relatively dry during construction in the summer of 2005. This dry period is reflected in the significant drop in gravimetric water content measured by Sensor 34 in the drainage ditch. The shrinkage curve for this soil was not obtained, but a gravimetric water content of 20% during this dry period is likely close to the shrinkage limit. After December of 2005, the moisture sensor 34 in the ditch showed significant fluctuations in water content, ranging from 16% to 46%. However, the water content inferred by the three sensors under the road was about 30% and did not fluctuate. A slight increase in water content was observed by the sensors under the pavement, likely due to spatial equilibration of gravimetric water content after construction. Despite the difference in moisture fluctuations between the subgrade in the drainage ditch and that under the pavement, no longitudinal cracks have been observed to date. This location is geogrid-reinforced, and the base course is lime treated, so the pavement is relatively stiff. As the soil at this location is relatively wet under the pavement, an extended dry period would be required to cause different movement. However, there has not been an extended dry period in the time since construction.

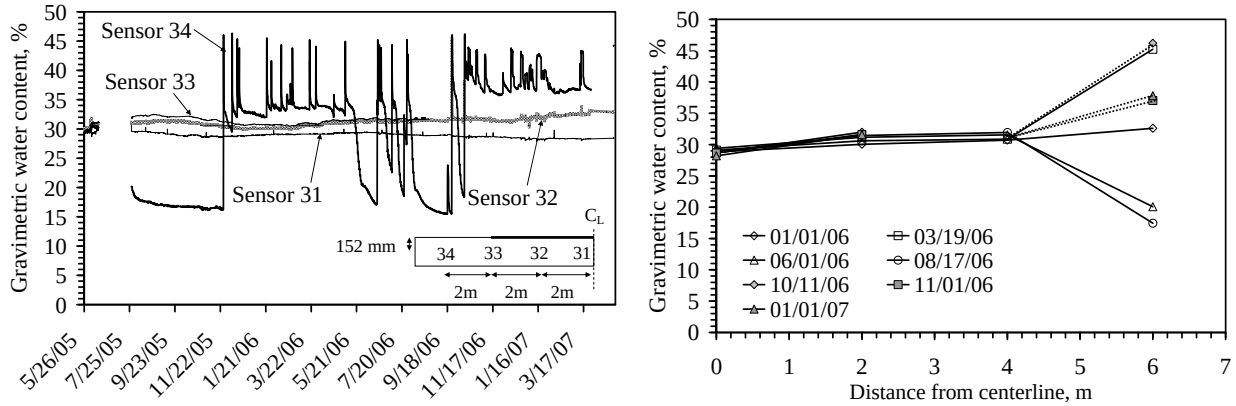

(a) (b)

Figure 7.12: Moisture data for Station 84 (red clay): (a) Time series for each sensor (b) Horizontal moisture isochrones

A comparison between the precipitation and the gravimetric water content at the shoulder of Station 84 is shown in Figure 7.13. The spikes in water content in the clay in the drainage ditch are generally consistent with the timing of rainfall events at Hempstead (5 miles from FM 2), although there are some obvious inconsistencies (10/20/2006). There was a dry period in the summer of 2006 during which the soil dried, but the rest of 2006 and 2007 were relatively wet.

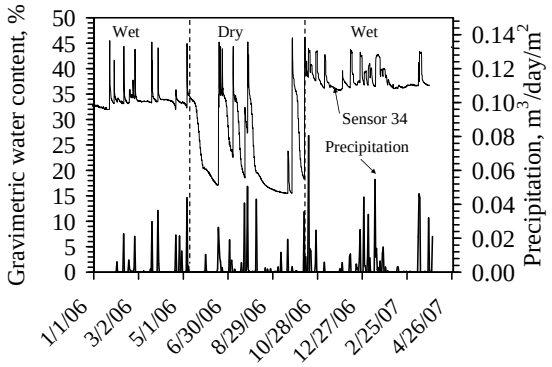

Figure 7.13: Comparison between gravimetric water content in the drainage ditch with precipitation (Station 84)

7.5.4 Vertical Moisture Profiles

Horizontal moisture sensor arrays were also installed under the road at several other locations, but the installations were damaged by lawnmowers and rodents. Accordingly, vertical arrays of sensors were installed in the drainage ditch at Stations 184 and 199 one year after the installation of the sensors at Station 84. These installations were installed to infer the range of water contents in the field, as well as the rate of movement of wetting or drying fronts in the subgrade under the shoulder. The time series for the sensors at Station 184 are shown in Figure 7.14(a), and vertical moisture profiles at different times are shown in Figure 7.14(b). The water content at this location was observed to vary between 26% and 43%, consistently above the shrinkage limit (13). In particular, the sensor at 610 mm routinely showed an increase in water content of 5% in the period of 2-3 days. Using the saturated hydraulic conductivity (k_s) obtained in the laboratory, this travel time is associated with a gradient of 3400 [$i = d/(k_s t)$]. This high gradient is due to wetting of a relatively dry soil. A longer time is required for the soil to dry than to wet, as the hydraulic conductivity of unsaturated soil is less than saturated soil, and as the gradient due to evapotranspiration is lower than that associated with wetting of a dry soil. The surface of the soil shows a wider variation in water content than deeper in the profile. This location has no shade from trees, so dry conditions are expected.

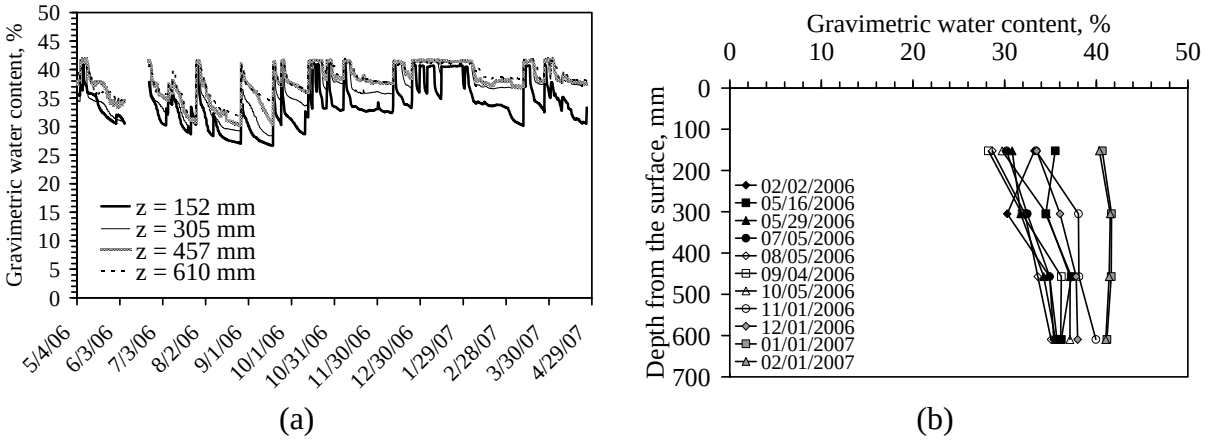

(a) (b)

Figure 7.14: Gravimetric water content data for Station 184: (a) Time series for each sensor (b) Isochrones

The gravimetric water content time series for the vertical array of sensors at Station 199 is shown in Figure 7.15(a), and selected moisture profiles are shown in Figure 7.15(b). All the sensors showed similar trend in gravimetric water content with time. The gravimetric water content was observed to vary between 30% and 43%. This location is shaded by trees, and ponded water was routinely observed during most field trips to the site, which indicates why the subgrade in the drainage ditch did not reach as low of gravimetric content values as that at Station 184.

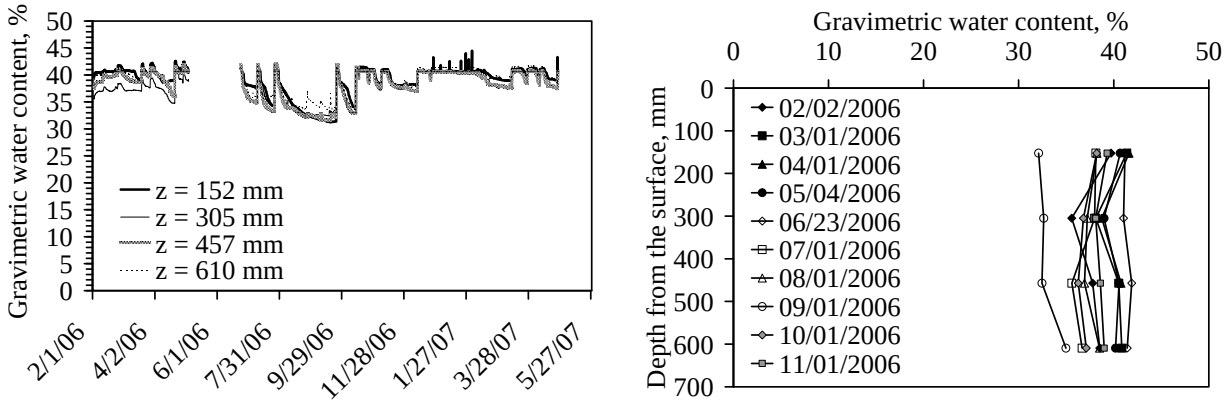

(a) (b)

Figure 7.15: Gravimetric water content data for Station 199: (a) Time series for each sensor (b) Isochrones

The daily changes in gravimetric water content for Stations 184 and 199 are shown in Figures 7.16(a) and 7.16(b). Positive increases in water content of 14% were observed during the course of a day, during heavy rainfall (with ponding) occurring after a dry period. However, significant negative changes in gravimetric water content are less likely (e.g., less than 3% changes in water content were observed in a day) due to the lower hydraulic conductivity of unsaturated soils.

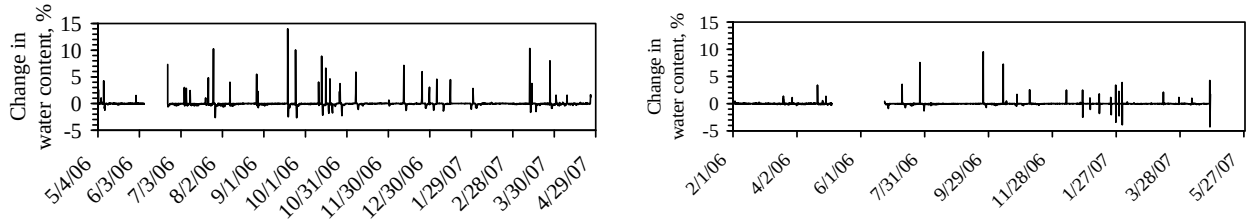

Figure 7.16: Change in water content of the surface sensor (152 mm): (a) Station 184 (b) Station 199

A comparison between the gravimetric water content measured by the sensors closest to the ground surface in the drainage ditch at Stations 84 and 199 is shown in Figure 7.17. The timing of the changes in water content is similar for the two sites, despite the different soil types. The magnitude of moisture variation is similar for the two sites, with large changes in gravimetric water content occurring over the period of several days.

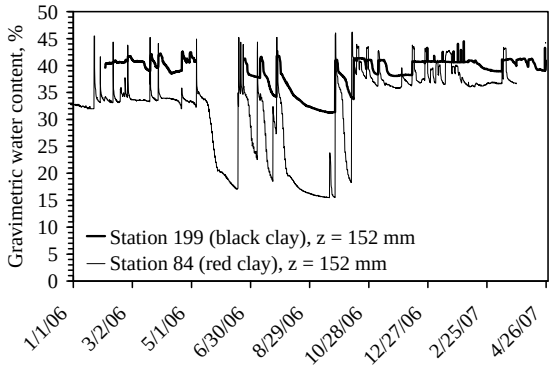

Figure 7.17: Comparisons between surface gravimetric water content measurements in the drainage ditch

7.6 Implications of results

The gravimetric water content measurements indicate that moisture fluctuations can occur rapidly during wetting of clays of high plasticity. However, the results indicate that moisture migration is negligible from the drainage ditch to the center of the pavement due to the limited pathways for moisture migration. In fact, the fluctuations in gravimetric water content were not even observed under the edge of seal coat of the pavement. Due to the contrast in water content fluctuations from the shoulder of the road to those made under the road, a differential change in volume can be expected. The location of the changes may have implications on the application of geogrid reinforcement in expansive subgrades. Geogrid reinforcement can be used to increase the stiffness of the soil near the edge of the pavement, with the goal of withstanding volume changes in the subgrade during moisture fluctuations. The geogrid should extend into the shoulder of the pavement to prevent the shoulder from pulling the pavement apart laterally. The geogrid may also provide increased tensile stress to the neutral axis of the pavement upon bending.

7.7 Conclusions

This study summarized moisture monitoring results in the subgrade under an instrumented highway in eastern Texas, with the goal of investigating the mechanisms of longitudinal cracking in expansive clay subgrades. The moisture sensors used in this study were found to work well in the harsh environment of a pavement subgrade (high temperature, high compaction strain, volumetric changes), and were inexpensive enough to permit replacement if damaged by straining or animals. Field measurements of gravimetric water content indicate that moisture fluctuations occur primarily in the drainage ditch adjacent to the pavement. However, little moisture migration was observed from the shoulder to the center of the pavement. Although structural damage has not been observed in the pavement in the year and a half of service, the moisture trends support the phenomena of differential volume change as the cause of longitudinal cracking.

Chapter 8. Guidelines for Testing, Design, and Specifications

8.1 Introduction

This chapter provides a review of current TxDOT specifications and testing methods for using geosynthetics in unbound base course of flexible pavements. A discussion is provided on the tests that should be retained from current specifications. Further, it also lists some tests that should be considered for compiling new specifications. This chapter has three main sections. The first section deals with current status of geogrid testing as per TxDOT specifications. Then the second section reports the current body of literature on the various testing methods available to quantify the soil and geosynthetic properties for their application to pavement design. Finally, the third section outlines the specification for new test that can be used along with current specifications for quantifying the mechanisms involved in geosynthetic reinforced pavements.

8.2 TxDOT specifications

The TxDOT specifications regarding design of geogrids in pavements are listed in three main categories:

1. TEX 621-J: Testing geogrids (Chemical test procedures)
2. TEX 735-I: Sampling Construction Fabrics (Structural test procedures)
3. DMS 6240: Geogrid for base/embankment reinforcement

8.2.1 Review of Specifications

As per current TEX 621-J, geogrid is defined as a synthetic planar structure formed by a regular network of *tensile members* with *appropriate apertures* to allow *interlocking* with surrounding soil or aggregate for the purpose of *reinforcement* and or segregation.

The test procedures for the following tests are described

1. Aperture size
2. Percent open area
3. Thickness
4. Flexure rigidity
5. Tensile strength and modulus
6. Junction strength and efficiency

The TEX 735-I specifications deal with the collection of the sample from field as shown in Table 8.1.

Table 8.1: TEX 735-1 specification for sampling geogrids

Width	Sample
<1 meter	1.2 m in length across full width
>1 meter	0.6 m long across full width of roll

The DMS 6240 governs the material composition, quality, sampling, and testing. It divides geogrids into two categories as type 1 and type 2 for different loads. It is not clearly specified how this division is made and what the appropriate load levels are. The current TxDOT specifications give the minimum design values for these tests as shown in Table 8.2.

Table 8.2: DMS 6240 specifications for geogrids

Tests	**Type 1**	**Type 2**
Aperture size	1.0-2.0 in	1.0-2.0 in
% open area	70% minimum	70% minimum
Thickness		
Machine direction ribs	0.03 in minimum	0.05 in minimum
Cross-machine direction	0.025 in minimum	0.045 in minimum
Junction	0.06 in minimum	0.10 in minimum
Tensile modulus at 2% elongation		
Machine and cross machine	14000 N/m	20000 N/m
Junction efficiency, % of rib ultimate tensile strength		
Machine and cross machine	90% minimum	90% minimum

8.2.2 Comparison of Specification and Geogrid Properties

An attempt was made to understand how the current TxDOT specifications and geogrid properties fit together. The comparison of the current geogrid definition and properties of the geogrid is provided in Table 8.3.

Table 8.3: Comparison of geogrid properties and specification

Property	**Specification**
Determine tensile strength	Tensile strength/Modulus
Appropriate apertures	Aperture size/Thickness of rib
Allow interlocking	% open area/Junction strength
Reinforcement	--not specified--
Stiffness	Flexural rigidity

Based on this comparison, the two main gaps in the current TxDOT specifications can be found. There is no test to quantify the reinforcement function of the geogrids. Further, the relevant property measured by flexural rigidity test as shown in Figure 8.1 is not clear. According to Koerner (1998), stiff geogrids generally made from polyethylene or polypropylene are characterized by having flexural rigidity values greater than 1000 g-cm whereas flexible geogrids—which are made of polyester, nylon and fiberglass yarns—are characterized by having flexural rigidity values less than 1000 g-cm. But how this property can be used in application to pavement reinforcement is still not clear. Further, all the current tests described in TxDOT specification are performed under unconfined conditions. But the actual geogrid application in the pavements is under confined conditions and there is no test to quantify this behavior. Finally, there are no tests to quantify the soil/aggregate properties for their application to the pavement.

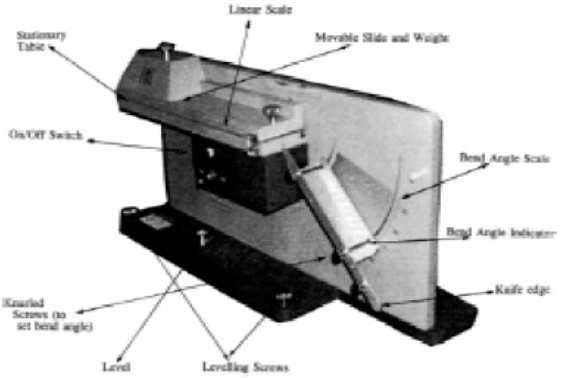

Figure 8.1: Bending stiffness test as per TxDOT specifications

Based on the discussion, it can be seen that the current TxDOT specifications lack mechanism based approach. Thus, there is no synergy between various components involved in pavement design. To fill the current gap, a literature review of the current testing methodologies was conducted for geogrids, soil, and geogrid-soil for their application to flexible pavement design.

8.3 Current review of literature

8.3.1 Geogrid Testing

As explained in Chapter 2, geogrids are a geosynthetic material consisting of connected parallel sets of tensile ribs with apertures of sufficient size to allow strike through of surrounding soil, stone, or other geotechnical material (Koerner, 1998). The tests done to determine their properties are as shown in Table 8.4.

Table 8.4: Geogrid tests based on properties being measured

Physical Properties	Mechanical properties	Degradation properties
Structure	Single Rib test	Temperature effects
Junction type	Junction Strength	Oxidation effects
Aperture size	Wide width tensile strength	Hydrolysis effects
Thickness	Shear test	Chemical effects
Mass per unit area	Pullout test	Radioactive effects
Flexural rigidity	**Endurance properties**	Biological effects
	Installation damage	Sunlight (UV) effects
	Tension-Creep behavior	Stress-crack resistance

The current TxDOT specification does a good job of incorporating the properties of geogrid, which are useful for the pavement design such as aperture size, thickness, single rib test, junction strength. But it still lacks *the wide width tensile strength and installation damage test*. The advantage of using wide width tensile test is it can be used to measure the properties of other geosynthetics especially geotextiles in pavement application. Even for geogrids, the wide width test can serve as an important indicator in studying the interaction of ribs with junction by observing the failure mode during the test. The way to incorporate installation damage in the current testing is explained in Chapter 9. Further the flexural rigidity test that is in the current specifications does not really quantify the property relevant to application of geogrids to pavement design.

8.3.2 Soil Testing

The guidelines set up by NCHRP Project 1-28A (NCHRP 2000) recommend performing resilient modulus test on the unbound base course material to be used in the flexible pavement.

8.3.3 Soil and Geosynthetic Interface Testing

Based on the laboratory and field studies conducted for geosynthetic reinforcement of flexible pavements, it has been demonstrated that the principal effect of the geosynthetics is to provide lateral confinement to the aggregate or base course layer of pavement (Bender and Barenberg, 1978; Kinney and Barenberg, 11982; Perkins 1999; Perkins and Edens, 2002). Interaction between the geosynthetics and the aggregates under traffic wheel loading causes development of interface shear stress between them leading to transfer of load from aggregate to the geosynthetic. Further as per Perkins 2004, as the cycle of traffic load is applied, there is both a resilient or recoverable shear stress and a permanent sear stress that exists when the traffic load is removed. The permanent interface shear stress continues to grow as repeated traffic loads are applied, meaning that the lateral confinement of the aggregate base layer becomes greater with increasing traffic load repetitions. Han et al. (2007) stated that the geosynthetic-soil confinement depends not only on the macro structure and index properties of geosynthetics but also on the properties of soil and most importantly the interaction between geosynthetics and soil particles. A number of test methods that can quantify directly or indirectly the confinement effect of soil-

geosynthetic interface has been developed recently. Table 8.5 shows the four main categories in to which these tests can be divided.

Table 8.5: Soil-geosynthetic confinement tests

Unconfined test	**Confined-Monotonic test**	**Confined-cyclic**	**Field test**
Aperture rigidity	In soil test device	Cyclic plate load	Field trafficking
Junction efficiency	Modified direct shear test	Modified Asphalt pavement analyzer	Accelerated pavement analyzer
Biaxial loading	Triaxial	Bending stiffness	
Wide width tensile	Zero span test	Cyclic pullout test	
	Plane strain UCD		
	Automatic Plane strain		
	In soil creep test		
	Pullout test		
	Push test		

Each test category has its relative advantages and disadvantages. The unconfined tests are easy to run but cannot be used for all geosynthetics. Further, it would give the same result independent of the soil type used in the project. The confined monotonic tests are easy to conduct and fast. They can serve as an index for quantifying the confinement effect of the geosynthetic. However, because they do not involve the actual load as in real pavement, they cannot capture the exact mechanism. The confined cyclic tests are expensive compared to the confined monotonic test but they replicate the field phenomenon more closely. Currently, repeatability of these tests has been an issue too. The field tests are time consuming and expensive but would give the exact behavior of the pavement. The following section provides details for the unconfined and confined monotonic tests and recommendations for their use in TxDOT specifications.

Table 8.6: Salient features of tests used for soil-geosynthetic confinement

Features	Unconfined test	Confined-monotonic test	Confined-cyclic test	Field test
Applicable to geosynthetics	Possible	Yes	Yes	Yes
Soil used	No	Yes	Yes	Yes
Index property	Yes	Yes	No	No
Actual property	No	No	Yes	Yes
Repeated Loading	No	No	Yes	Yes
Ease of use	Yes	Yes	No	No
Repeatability	Yes	Yes	Possible	Possible
Time consuming	No	No	Yes	Yes
Inexpensive	Yes	Yes	No	No

8.4 Recent advances in soil-geosynthetic testing

8.4.1 Unconfined Testing

The recent advances in pavement engineering have seen a rapid increase in the use of biaxial geogrids. The standard test procedures restricted to uniaxial testing and conventional analytical techniques do not easily allow the load-strain characteristics of the materials in two orthogonal directions to be mathematically combined (McGown et al., 2005). Further, the geogrids are produced by a variety of manufacturing processes thus their load-strain behavior may vary significantly in the two axes of principal stiffness. Two new tests have been reported for their specific application to the pavement design recently: the torsional rigidity test and biaxial loading test.

8.4.4.1 Torsional Rigidity Test

The torsional rigidity test is an index test for geogrids to determine the resistance of a geogrid to the given distortion and to compare the response of one geogrid to another. It has been adopted as a design parameter by Giroud and Han (2004) as a design parameter for unpaved reinforced roads. Currently this test method is under review by ASTM D 35 committee and they recommend using it for geogrid products with an aperture size of no more than 2.9 in. (75 mm) or less than .59 in. (15 mm) parallel to any rib.

Kinney and Yuan (1995) developed the initial testing apparatus and procedure for measuring torsional rigidity or in plane rotational stiffness of the geogrids. It was done to correlate the performance of large scale geogrid reinforced paved road tests conducted by US

Army Corps of Engineers at the Waterways Experiment Station with the relevant laboratory property of geogrids for base reinforcement.

The procedure of the test involves fixing an unsupported square geogrid specimen on its four sides in a horizontally oriented containment box as shown in Figure 8.2. The central node is then clamped by a device that simultaneously applies torque and measures the resulting rotation of the geogrid. The value of modulus of the rotation obtained from the moment curve is the desired value of geogrid stiffness in units of N-m/deg. As per Kinney the aperture stability modulus is calculated at a torque of 2 N-m, which corresponds to large angular rotations, whereas Geosynthetic Research Institute recommends reporting initial tangent modulus at small torques and offset tangent modulus and angular rotation at large torques.

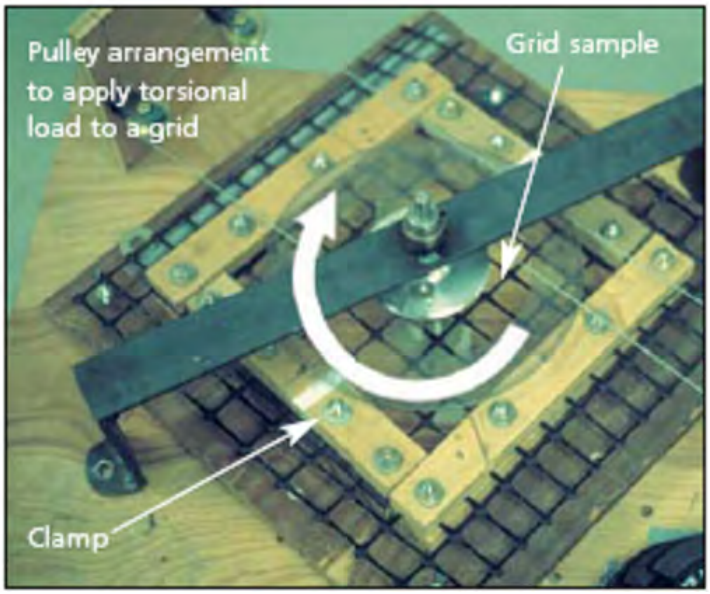

Figure 8.2: Torsional rigidity apparatus (Tensar website)

This test was an initial attempt to determine or quantify the interlocking capacity of the geogrid. But the relationship between geogrid torsional rigidity and the performance of the geogrid reinforced road sections could not be established. Further, this test method also tended to demonstrate a substantially higher torsional rigidity for stiff geogrids as compared to flexible geogrids. A study conducted by Texas Research Institute TRI (2001) reported that there was no correlation between torsional rigidity and confinement performance of the geogrids.

8.4.4.2 Biaxial Loading Test

The properties of the tensile ribs and junctions contribute to the behavior of geogrids in a complex manner, influencing both their load-strain-time and soil interaction properties. Thus a new biaxial test method has been developed by Kupec and McGown. The test specimens were prepared with 5 ribs in each direction and so 25 junctions within the central section of the test specimen (see Figure 8.3). This generally results in overall cruciform test specimen dimensions of some 20x20 inch (500 x 500 mm), with central test areas of 3.9 to 8.6 in. (100 to 220 mm) square. The test specimens were held in suitable clamps, which prevented slippage and specimen damage during testing. The loads were applied to the test specimens under isotropic rate of deformation conditions of .04 in./min (1 mm/min). Deformations were measured at the clamps

by means of linear vertical displacement transducers and at various positions on the test specimen using digital photogrametry.

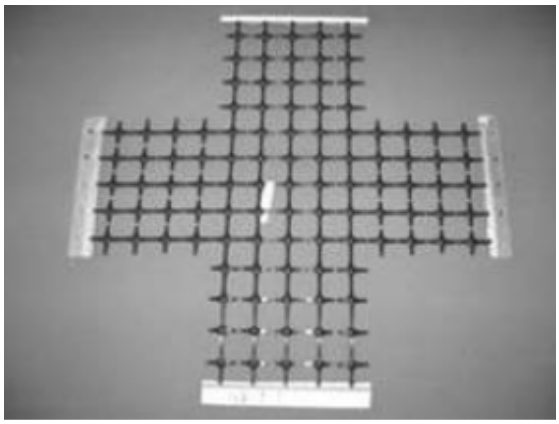

Figure 8.3: Geogrid specimens for biaxial testing

8.4.2 Confined-Monotonic Soil-Geosynthetic Testing

The direct measurement of the capacity of a geogrid to effectively interlock the soils has been the focus of research since early 1980s. In 1998, FHWA published a report on this topic titled "Development of Protocols for Confined Extension/creep Testing of Geosynthetics for Highway Applications." It listed a number of tests that can be conducted to obtain the confined stress strain properties of geogrids and geotextiles. It finally developed a testing protocol for confined extension and creep testing of the geosynthetic reinforcement materials. Based on the data generated, it stated that the unconfined response is overly conservative and confined response should significantly improve the characterization of geosynthetic material in engineering application. Recently there has been an attempt by Matys and Beslik, 2005, to develop an index test to measure these confined stress strain properties using a push test. It involved pushing a cone through a layer of geogrid and base course material and measuring the resistance to cone penetration. They stated that when granular soil particles are compacted over these geogrids, they partially penetrate the apertures to create a strong interlock. Confining effect occurs together with interlocking, thereby increasing the strength of the soil. These mechanisms were characterized by an increase in bearing capacity onto sub-base surface and reduction in its vertical deformations. Matys and Beslik argued that this can be used to distinguish the performance of geogrids with different polymers and opening size. Further, it would help distinguish among geogrids that cannot generate the same very efficient interaction and confinement of the aggregate. All the tests that can be listed under this category are shown in Table 8.7.

Table 8.7: Confined monotonic soil geosynthetic test methods

Test Method	Reference
In soil test device	McGown et al. (1982)
Zero span tests	Christopher et al. (1986)
Pullout test	Holtz et al. (1971), Juran (1991)
Triaxial test	Ling (1991), Wu (1991)
Plane strain UCD	Boyle (1995)
Automatic Plane strain	Whittle (1993)
Modified Direct shear test	Lechinsky (1997)
In soil creep test	Fock and McGown (1987)
Push test	Matys and Beslik (2005)

8.4.3 Confined Cyclic Test

These tests involve applying a cyclic load to the geosynthetic-soil system and measuring its response. These tests represent the wheel loading conditions close to the actual field conditions. Generally, the benefit of reinforcement is reported as the ratio of the deformation response measured for a reinforced section when compared with an unreinforced section. These tests generally require more expensive equipment than the confined monotonic test and repeatability of results has been an issue.

8.4.4 Suggested Test

Based on the review of the current literature and testing methods available, the research team concluded that soil-geosynthetic confinement was the key property to be determined for quantifying benefits of geosynthetics in pavement. Further, to understand the confinement effect of the geosynthetics, it was hypothesized that the confined stiffness (or confined stress-strain properties) of the soil-geosynthetic system under low strains would be relevant parameter.

According to Perkins and Cuelho (1999), the direct shear device and the pullout apparatus can be used for determination of shear stress-shear displacement interaction relationships of soil and geosynthetic. But the direct shear device is typically used for assessing soil-geosynthetic shear interaction parameters where soil is sliding relative to an essentially fixed geosynthetic layer. Soil-geosynthetic parameters determined from a direct shear device are commonly used to assess the stability of sloped soil-geosynthetic layers in landfills. The use of a direct shear device, to assess the parameters describing shear stress-shear displacement interaction on an elemental volume, suffers from problems similar to those encountered when attempting to use a soil direct shear device for the purpose for determining intrinsic soil constitutive properties. Further, Abramento and Whittle (1995) stated that if the inclusion is rigid (inextensible), it can be assumed that the shear resistance is mobilized uniformly over the embedded surface area under the pullout load. However, for extensible reinforcements (including most geosynthetics), the deformations of the inclusion can introduce a progressive failure

mechanism, in which the shear resistance varies with position. The presence of edge effects and non-uniform boundary conditions restrict the use of this device for this application.

Therefore, the confined monotonic pullout test is suggested as the test to be conducted to determine this property.

8.5 New test for TxDOT use

Based on the preceding discussion, it can be seen that current TxDOT specifications have appropriate tests to determine the physical properties of the geogrid. But still there is no test specification on quantifying the confined stress strain properties of the geogrids for their application to the pavements. Therefore, the current research proposes the use of pullout tesst to determine these properties.

8.5.1 Introduction

The increasing use of geosynthetics in pavement has necessitated an evaluation of its reinforcement interaction parameters, typically the coefficient of interface friction. A number of factors can influence the measured properties. As per the Louisiana Transport research report (2004), these factors are testing equipment and associated boundary effects, soil-properties and compaction procedures, geosynthetic type and geometry and confining pressure. The soil-geosynthetic reinforcement interaction mechanism is complex and raises difficulties in interpreting the pullout test results. The confined stress strain of the geosynthetic during pullout is significantly affected by its geometry, length, extensibility, and the amount of soil confinement. Pullout resistance of geotextile reinforcement is provided mainly by friction resistance along the soil-geotextile interface. On the other hand, the pullout resistance of a geogrid is due mainly to soil frictional resistance and passive bearing resistance against its transverse members. Furthermore, non-uniform shear stress strain distribution is developed along the geosynthetic specimen during pullout due to the coupled effect of its elongation and interface shear. Various theoretical and empirical procedures have been developed in order to model the soil-geosynthetics interface mechanism during pullout. These models vary in their assumptions with respect to the constitutive material-properties, the load transfer mechanism at the interface, and the shape of the load-strain curve during pullout. The objective of this research was to evaluate the pullout performance of geogrids and geotextiles embedded in both base course and subgrade soil. Laboratory tests were performed on the geosynthetic specimens that were the same as those used in the field case study. In all tests, the soil was compacted to 95 percent of its standard proctor density at optimum moisture content. The section describes the pullout testing equipment used to conduct large scale pullout testing on geosynthetics at The University of Texas at Austin. It further explains the methodology adopted for sample preparation and running the test. Finally, it describes the analysis of results obtained by the various tests conducted at the laboratory.

8.5.2 Pullout Apparatus

UT Austin’s pullout equipment was used to conduct the test; it consists of a box with internal dimensions of 60 inches length, 24 inches width, and 12 inches height. The various components of the pullout box are as shown in Figure 8.4.

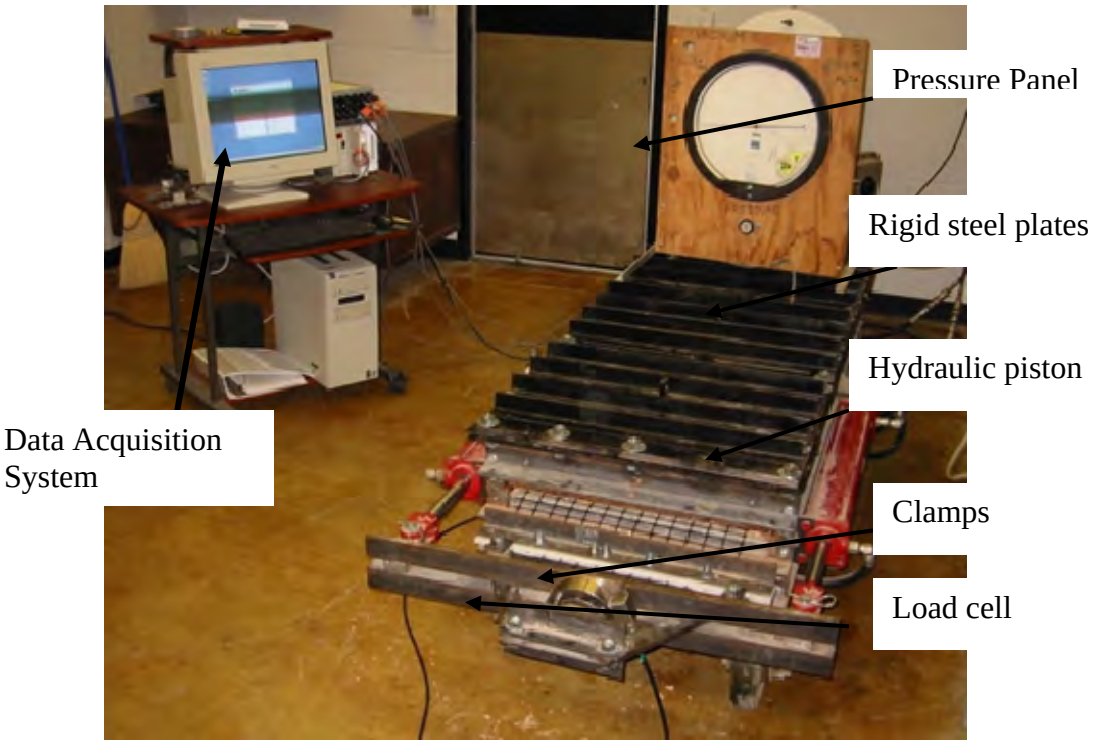

Figure 8.4: Large-scale pullout testing device

8.5.2.1 Hydraulic system for pullout test

The force application system of this equipment is composed of hydraulic cylinders, a hydraulic pump, and a regulating valve as shown in Figure 8.5. The pump injects hydraulic oil to the cylinders and promotes the movement of the pistons that generate the pullout force. The pump generates compressed air and is controlled by the regulating valve of air pressure. The volume of oil that flows to the pump can be adjusted by means of needle valves attached to the piston such that the set of cylinders move at a constant displacement rate. The direction of piston movement can then be regulated using the three way ball valve. The pressure gauges mounted on the sides of the valve can be used to monitor the pressure in individual pistons.

a) Needle valve

b) Air pump

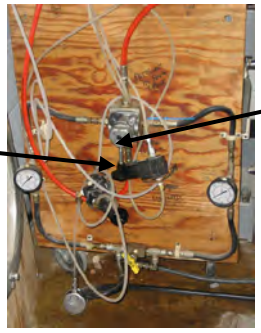

c) 3-way ball valve

Figure 8.5: Hydraulic system to control piston movement in the pullout box

8.5.2.2 Normal air pressure application device

A flexible pneumatic device was used to apply and maintain a uniform normal stress over the entire pullout box area. This device consists of one manometer, one control valve, two rubber sheets, connections, and hoses. The air pressure is controlled by the control valve, measured by the manometer, and applied between the two rubber sheets that are bolted at their edges to the steel plates. It is considered that the pressure measured by the manometer is the same applied to the soil by the air bag composed by the rubber sheets. This confining load is applied on the surface of the soil sample from the reaction force generated by inflatable air bag, placed between the soil surface and the cover of the box made of the steel plates as shown in Figure 8.6.

a) Rubber sheet

b) Valve

Figure 8.6: Rubber membrane to apply normal pressure during pullout test

8.5.2.3 Instrumentation

The instrumentation used during this test consisted of a load cell and linear variable displacement transducers (LVDTs) as shown in Figure 8.7. The load cell measured the pullout force applied by the movement of the hydraulic cylinders attached to the rigid clamps. It was manufactured and commercialized under the name of Omega LCH-20K. The maximum capacity of the load cell is 20000 lbs. The LVDTs were used to measure the displacements of the geosynthetic embedded in the soil. They were manufactured by Schaevtiz and had a measurement range of 3 inches.

a) Load cell to measure pullout force

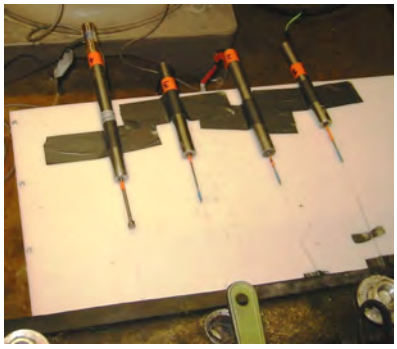

b) LVDTs to measure displacement

Figure 8.7: Instrumentation system for pullout test

8.5.2.4 Compaction equipment

To compact the soil in the pullout box, a vibratory hammer was used with different extension rods as shown in Figure 8.8. The wide plate compaction rod was used to compact the subgrade soil that mainly consisted of silty sand, whereas the sheep foot roller compaction rod was used to compact the clayey soil. The excavation chisel was used to remove the soil at the completion of the test.

a) Vibratory Hammer

b) Wide plate compaction rod

c) Sheep foot compaction rod

d) Cutting chisel

Figure 8.8: Equipment used for soil compaction during pullout testing

8.5.3 Pullout Test Preparation

The specimen preparation for the pullout test consisted of preparing the geogrid specimen to be attached to the clamps, preparing the soil to required moisture content, attaching the tell tales to the geogrids, and then finally compacting the soil in the pullout box.

8.5.3.1 Soil Preparation

The amount of soil required for the given test was calculated based on the volume of the pullout box and soil density from the proctor test. Based on the corresponding water content for the given density was obtained from the proctor test. The soil was mixed with the required amount of water to obtain the soil to be used in the test, which was then stored in the plastic drums with lids to prevent loss of water. This also helped the moisture to equilibrate within the soil specimen. The water content for the soils in the drums was checked before every pullout test.

8.5.3.2 Geosynthetic Specimen Preparation

The geosynthetic of the required dimensions was cut and then joined to plastic plates by means of epoxy glue. The set up was compressed under weights and left for 24 hours for the epoxy to dry. During the test, the plastic plates with the geosynthetic were clamped to the two steel L-sections with bolts. This provides a rigid grip throughout the geosynthetic specimen thus

preventing differential slip of the element. Clamps were used to connect the hydraulic cylinders and the test specimen without slipping or breaking of the specimens. The clamping device consisted of a sandwich of two 26 inch (660 mm) wide L-section steel pieces and two plastic plates, with a series of holes where bolts and nuts are used in order to hold the test specimen between the plates. The clamp allows the specimen to remain horizontal during loading and not interfere with the pullout/shear surface. Epoxy was used to attach the plastic plates with the geogrid. This provides uniform tension on all of the stressed geogrid ribs extending from the clamp into the pullout box. The external connecting device allows the pulling force to be distributed evenly throughout the width of the sample.

8.5.3.3 Displacement measurements

In order to obtain displacement measurements, tell tale wires were attached to the embedded geosynthetic. Then the wires were passed through the pullout box to its back end inside a protective sheathing tube. This free end of the tell tale wire was then attached to the LVDTs. During the test, as the geosynthetic was pulled, it caused the tell tale wire to move, which was measured by change in the voltage response of the corresponding LVDT. For current testing, three tell tales were attached in staggered pattern, separated from each other by 6 inches (150 mm).

8.5.3.4 Compacting the soil and geosynthetic placement

To distribute the compactive effort equally throughout the soil in the pullout box, it was decided to compact soil in four layers of 3 inch thickness each. The weight of soil required for each layer was calculated and then compacted to the required height using the Bosch hammer as shown in Figure 8.9(a). The surface of second layer was made as flat as possible. It was necessary to temporarily anchor the back end of the geogrid specimen so as to maintain its horizontal position on the surface of second layer as shown in Figure 8.9(b). After the placement of geogrid, the clamping plastic was inserted between two wide L section steel plates and clamped with five bolts and nuts. Then the tell tales were attached at the required junctions of the geosynthetic as shown in Figure 8.9(c). The other two layers of the soil were then compacted in 3 inch increments as shown in Figure 8.9(d). The rubber membrane was then placed at the top of the compacted soil layer and enclosed by steel plates and air pressurized to the required normal load level. When the bolts and nuts did not fasten tightly, air leaked out through the crack between two rubber plates thereby reducing the normal pressure on the soil. Therefore, significant effort was placed to fasten the bolts and nuts tightly enough to maintain the uniform air pressure.

8.5.3.5 Data acquisition system

The load cell and the LVDTs were then connected to the data acquisition system ports. Labview 7.0 software developed by National Instruments was used to acquire data from the instruments.

a) Compaction of soil in layers

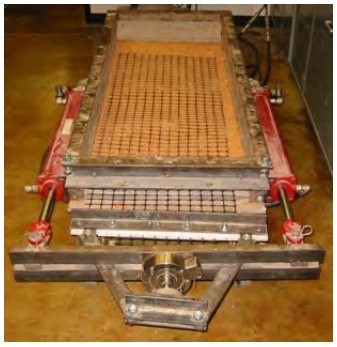

b) Placement of geogrid at end of second layer

c) Attaching tell tales to the geogrid

d) Soil compaction on top of the clamped geogrid

e) Rubber membrane and steel plates over compacted soil

f) Removing soil at end of test and embedded geogrid

Figure 8.9: Procedure for conducting pullout test

8.5.4 Test Procedure

The pullout test was started by turning the data acquisition system on and loading virtual instrument program called “pullout test.vi.” At the same time, air pressure to the air bag was applied for generating normal pressure. Initial loading continued for twenty minutes so that it equilibrated throughout the rubber membrane before starting the test. After twenty minutes of initial loading, the hydraulic pistons were activated by applying air pressure to the hydraulic jack, which applied pullout force on the embedded geosynthetic. During this stage, pullout resistance and displacement of geosynthetic were measured from the load cell and LVDTs respectively. The test was continued until the geogrid failed in pullout or tension mode. Pullout mode of failure was assumed to occur when displacements at all locations became equal to one another while the pullout force was constant or decreasing. Tensile mode of failure was assumed to occur if the geogrid slipped at the clamping end or when the ribs slipped from the junctions during the test as shown in Figure 8.10. After the test was finished, a file was created using the data acquisition system software that contained the data from all the instruments at one-second intervals during the test. Further, the normal air pressure was removed and the metal plates and air bag were disassembled. The soil was removed and stored in the drum. The condition of the geogrid was checked to determine the kind of failure that occurred in the specimen during the test.

a) Tensile mode of failure at the grips

b) Tensile mode of failure at end of test

Figure 8.10: Tensile failure of specimen during pullout test

8.5.5 Testing Matrix

Based on the testing materials and testing procedures explained earlier, sixteen pullout tests were conducted. Pullout tests were conducted on two different geogrids, both in machine and cross-machine direction with two different normal pressure and two different interface materials. The testing matrix adopted for the current study is shown in Table 8.8. The abbreviation used for the tests indicate type of geosynthetic (T for Tensar and M for Mirafi), testing direction (M for machine direction and X for cross machine direction), confining material (B for base course and S for sub-base course), and normal load (1 for 1 psi and 3 for 3 psi). Therefore, Tensar geogrid (T) pulled in machine direction (M) with confining material as base course (B) under confining pressure of 1 psi (1) is indicated as TMB1.

Table 8.8: Testing matrix for large scale pullout testing

S.NO	GEOSYNTHETIC	TESTING DIRECTION	CONFINING MATERIAL	NORMAL LOAD	ABBREVATION
1	TENSAR	MD	Base course	1 psi	TMB1
2	TENSAR	XD	Base course	1 psi	TXB1
3	TENSAR	MD	Base course	3 psi	TMB3
4	TENSAR	XD	Base course	3 psi	TXB3
5	TENSAR	MD	Subgrade	1 psi	TMS1
6	TENSAR	XD	Subgrade	1 psi	TXS1
7	TENSAR	MD	Subgrade	3 psi	TMS3
8	TENSAR	XD	Subgrade	3 psi	TXS3
9	MIRAFI	MD	Base course	1 psi	MMB1
10	MIRAFI	XD	Base course	1 psi	MXB1
11	MIRAFI	MD	Base course	3 psi	MMB3
12	MIRAFI	XD	Base course	3 psi	MXB3
13	MIRAFI	MD	Subgrade	1 psi	MMS1
14	MIRAFI	XD	Subgrade	1 psi	MXS1
15	MIRAFI	MD	Subgrade	3 psi	MMS3
16	MIRAFI	XD	Subgrade	3 psi	MXS3

8.5.6 Test Results

The data obtained from the pullout tests was used to obtain the magnitude of pullout force at the front of the geosynthetic and corresponding displacements at each LVDT. The results for all sixteen pullout tests on Tensar geogrid and Mirafi geogrid with base course and clay as confining material are attached in Appendix B. The typical results from a given pullout test on Mirafi geogrid in Machine direction with clay as the confining material under 1 psi of confining pressure is shown in Figure 8.11. The frontal displacement and displacement of LVDTs embedded in the geogrid is represented by d0, d1, d2, and d3 respectively and is plotted against the frontal pullout force Fo.

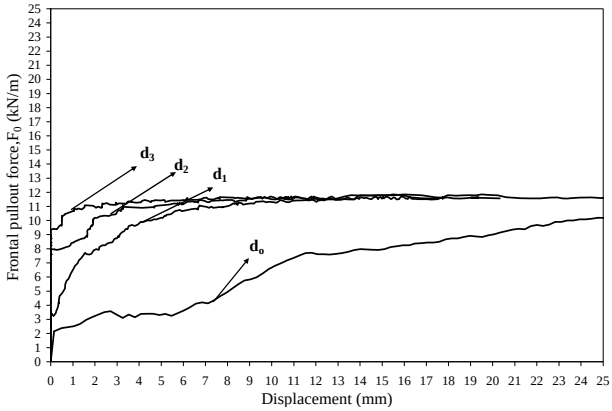

Figure 8.11: Pullout test load-displacement curves

8.5.7 Analysis of Results

8.5.7.1 Maximum Pullout force

The results obtained from the testing were analyzed to determine the maximum pullout resistance offered by the geogrids under different confining pressure for both base course material and clay material as shown in Table 8.9.

It was found that the maximum pullout resistance of geogrids increased as the confining pressure increased as shown in Figure 8.12. Further, both the geogrids had higher maximum pullout resistance when they were confined within the subgrade material as compared to base course material.

Table 8.9: Maximum pullout resistance

Test No.	Geogrid Type	Max. Pullout force	Max. tensile strength	Failure mode
		kN/m	kN/m	
1	TMB1	7.0	12.4	Pullout
2	TXB1	6.0	18.9	Pullout
3	TMB3	11.0	12.4	Pullout
4	TXB3	14.0	18.9	Tensile
5	TMS1	11.5	12.4	Pullout
6	TXS1	12.0	18.9	Pullout
7	TMS3	13.4	12.4	Tensile
8	TXS3	13.4	18.9	Tensile
9	MMB1	7.0	29.1	Pullout
10	MXB1	5.0	29.1	Pullout
11	MMB3	25.0	29.1	Tensile
12	MXB3	26.0	29.1	Tensile
13	MMS1	11.9	29.1	Pullout
14	MXS1	11.8	29.1	Pullout
15	MMS3	24.0	29.1	Pullout
16	MXS3	24.6	29.1	Pullout

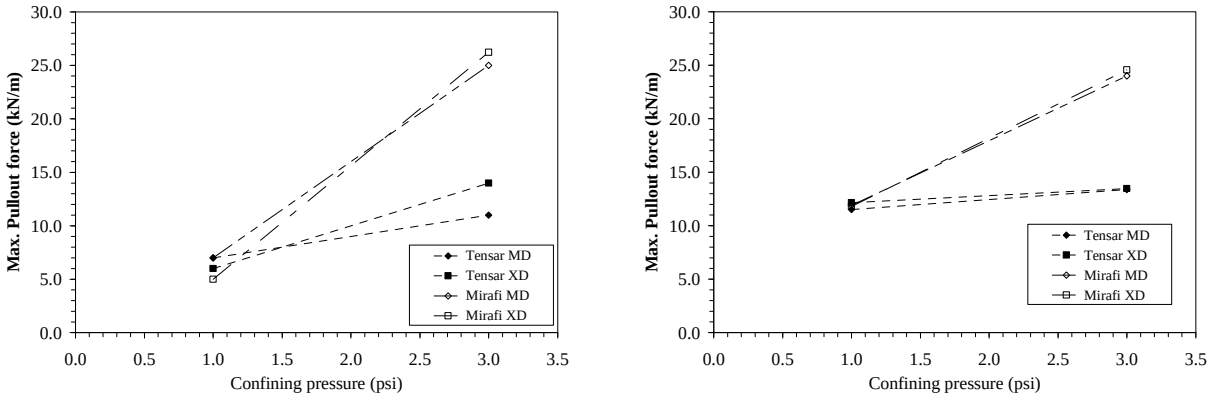

(a) Base course (b) Subgrade

Figure 8.12: Variation of maximum pullout force with confining pressure when a) Base course b) Subgrade is used as confining material

8.5.7.2 Coefficient of interaction,C_i

The coefficient of interaction $C_{i,}$ for each case was calculated as

$$C_i = \tan\delta \big/ \tan\phi \tag{8.1}$$

$$\tan\delta = \frac{P_{\max}}{2.A_{grid}} \tag{8.2}$$

where P_{max} is the maximum pullout force in kN/m per unit width of the specimen, A_{grid} is the area of grid in meter^2, δ is the apparent angle of interaction between the geogrid and the confined material and Ø, which is the friction angle of the confining material was assumed as 34^0 for base course and 30^0 for subgrade material. See Table 8.10.

Table 8.10: Coefficient of interaction from pullout test

Test No.	Geogrid type	tan δ	tan Ø	C_i
1	TMB1	0.83	0.67	1.2
2	TXB1	0.72	0.67	1.1
3	TMB3	0.44	0.67	0.7
4	TXB3	0.56	0.67	0.8
5	TMS1	1.37	0.58	2.4
6	TXS1	1.45	0.58	2.5
7	TMS3	0.53	0.58	0.9
8	TXS3	0.54	0.58	0.9
9	MMB1	0.83	0.67	1.2
10	MXB1	0.60	0.67	0.9
11	MMB3	0.99	0.67	1.5
12	MXB3	1.19	0.67	1.8
13	MMS1	1.42	0.58	2.5
14	MXS1	1.41	0.58	2.4
15	MMS3	0.95	0.58	1.7
16	MXS3	0.98	0.58	1.7

Effect of confining pressure

As the confining pressure increased, C_i reduced for both Tensar geogrid for both base course and subgrade material. But C_i increased for Mirafi geogrid when the confining material was base course and reduced when the confining material was subgrade with increase in the confining pressure.

Effect of confining material

C_i was greater when the confining material was subgrade as compared to base course for both Tensar and Mirafi geogrid as shown in Figure 8.13(a) and (b).

Effect of geogrid type

The C_i was same for both Tensar and Mirafi geogrid in base course and subgrade material for low confining pressure but it increased for the Mirafi geogrid under high confining pressure.

Effect of machine and cross machine direction

The C_i had similar values for both machine and cross machine direction for Tensar geogrid in base course and subgrade material. But Mirafi geogrid had different values in machine and cross machine direction when the confining material is base course.

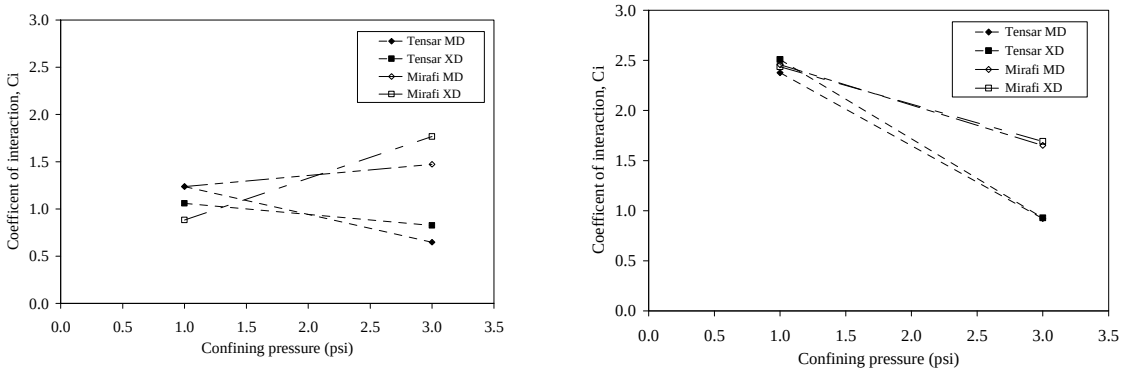

(a) Base course (b) Subgrade

Figure 8.13: Variation of coefficient of interaction with confining pressure for GG1 and GG2 in machine and cross machine direction a) Base course b) Subgrade

8.5.7.3 Confined modulus from pullout test

Confined modulus of the geogrid (M_c) is defined as the ratio of the frontal pullout force (in kN/m) to the displacement at LVDT d_1 (in mm). Figure 8.14 shows the plot of frontal pullout force with corresponding displacement at LVDT 1 for Tensar and Mirafi geogrid with confining medium of base and subgrade soil. M_c was calculated corresponding to the displacement of .04 in. (1 mm) and .2 in. (5 mm) for each of the tests as shown in Table 8.11 and Table 8.12 respectively.

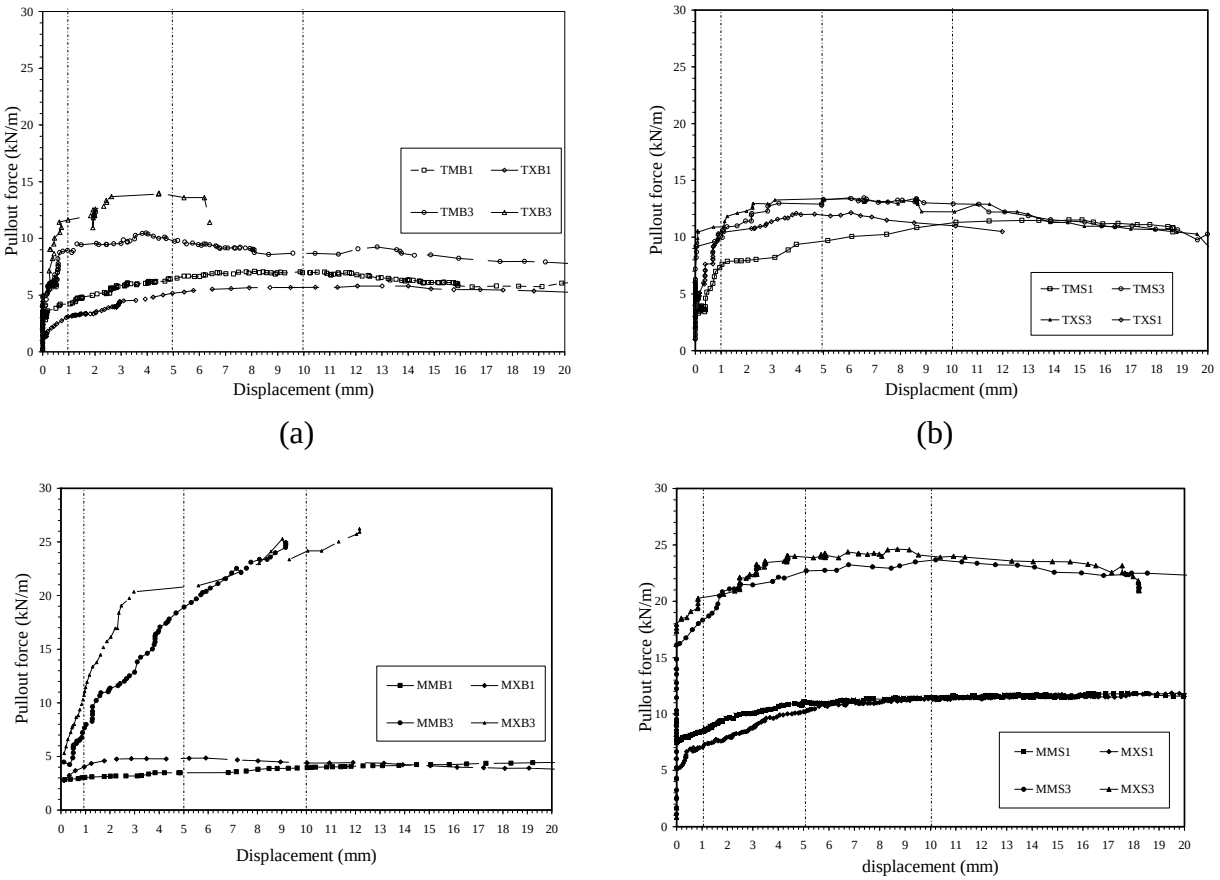

Figure 8.14: Pullout force variation with displacement at LVDT 1 for geogrid at different confining pressures in machine and cross machine direction a) Tensar geogrid in base course b) Tensar geogrid in subgrade c) Mirafi geogrid in base course d) Mirafi geogrid in subgrade

Table 8.11: Confined modulus (Mc) for 1mm displacement

Test No.	Geogrid type	Pullout force (kN/m)			Modulus (kN/m^2)
		At 0 mm	At 1 mm	Difference	M_c
1	TMB1	2.82	4.20	1.38	1380.00
2	TXB1	1.30	3.12	1.82	1820.00
3	TMB3	4.05	8.80	4.75	4750.00
4	TXB3	5.19	11.75	6.56	6560.00
5	TMS1	3.30	7.50	4.20	4200.00
6	TXS1	4.60	10.43	5.83	5830.00
7	TMS3	7.20	9.96	2.76	2760.00
8	TXS3	9.59	10.90	1.31	1310.00
9	MMB1	2.83	3.11	0.28	280.00
10	MXB1	2.76	4.35	1.59	1590.00
11	MMB3	4.48	7.92	3.44	3440.00
12	MXB3	5.30	11.46	6.16	6160.00
13	MMS1	7.60	8.40	0.80	800.00
14	MXS1	5.10	7.10	2.00	2000.00
15	MMS3	16.20	18.00	1.80	1800.00
16	MXS3	17.98	20.50	2.52	2520.00

Table 8.12: Confined modulus (Mc) for 5 mm displacement

Test No.	Geogrid type	Pullout force (kN/m)			Modulus (kN/m^2)
		At 0 mm	At 1 mm	Difference	M_c
1	TMB1	2.82	6.45	3.63	726.00
2	TXB1	1.30	5.20	3.90	780.00
3	TMB3	4.05	10.47	6.42	1284.00
4	TXB3	5.19	13.98	8.79	1758.00
5	TMS1	3.30	9.50	6.20	1240.00
6	TXS1	4.60	12.03	7.43	1486.00
7	TMS3	7.20	13.40	6.20	1240.00
8	TXS3	9.59	13.25	3.66	732.00
9	MMB1	2.83	3.48	0.65	162.50
10	MXB1	2.76	4.8	2.04	510.00
11	MMB3	4.48	18.9	14.42	3605.00
12	MXB3	5.30	20.35	15.05	3762.50
13	MMS1	7.60	11.10	3.50	700.00
14	MXS1	5.10	10.20	5.10	1020.00
15	MMS3	16.20	22.5	6.30	1260.00
16	MXS3	17.98	23.90	5.92	1184.00

Effect of confining pressure

As the confining pressure increased, M_C increased for both Tensar and Mirafi geogrid in base course material. But when the confining medium was subgrade, it reduced for the Tensar geogrid. In general, the increase in confining pressure led to increase in the confined modulus of the geogrid.

Effect of confining material

At confining pressure of 1 psi, M_C value was greater for both Tensar and Mirafi geogrid when the confining medium was subgrade. But for higher confining pressure of 3 psi, the base course had higher M_C value than that obtained from the subgrade for both geogrids.

Effect of geogrid type

Tensar geogrid had higher values of M_C at low confining pressure as compared to Mirafi geogrid. But for higher confining pressure Mirafi geogrid had higher M_C values than Tensar geogrid. Therefore, low confining pressure Tensar geogrid was found stiffer in response to Mirafi geogrid.

Effect of machine and cross machine direction

For Tensar geogrid both the machine and cross-machine direction had similar values of M_C. But for Mirafi geogrid M_C value for cross machine direction was greater than that of machine direction.

Effect of displacement interval selected

M_C values for lower displacement interval of .04 in. (1 mm) were higher as compared to displacement interval of .2 in. (5 mm).

8.5.8 Confined Stiffness (J_C)

8.5.8.1 Introduction

The results obtained from the analysis of pullout test data shown earlier for maximum pullout force and coefficient of interaction are useful for design of structures at limit state as they predict the soil-geogrid interaction behavior at failure. But for the design of reinforced pavements, as discussed earlier, the properties of geogrid at low strains are critical. Though M_C values can be used as an index for describing such behavior, the pullout force used for calculating M_C does not correspond to the actual force at which displacement is measured. Therefore, to better define the confined modulus at low strains, which would take into account the confined pullout force at the point of displacement measurement, confined stiffness parameter needs to be evaluated. This requires an appropriate stiffness model to predict the shear displacement-force relation under confined conditions. This would then help to define the force at a given confined point inside the pullout box and corresponding strain at it. The slope of this curve can then be used to determine the confined stiffness of the soil-geosynthetic system.

8.5.8.2 Objective

The analysis of pullout test was done to calculate the confined modulus at low strains. Attempts were made to obtain the initial confined stiffness of the geogrid. It was envisioned that this would provide basis for developing a confined strength–strain curve for the geogrid. This would further help to:

1. Quantify the effect of geogrid reinforcement on pavement;
2. Provide basis for comparison of performance of various geogrids in reinforced pavements.

8.5.8.3 Equivalent model

The analysis for confined stiffness obtained by pullout test can be compared to linear elastic model used for defining relationship between tensile force (F_T) and low strain (ε_T) at any point x_i, in an unconfined tensile testing of geogrids, which is expressed as

$$F_T(x_i) = J_U * \varepsilon_T(x_i) \tag{8.3}$$

Similarly, the pullout force (F_P) and strain (ε_P) relationship for pullout test at any point x_i, can be expressed as

$$F_P(x_i) = J_c * \varepsilon_P(x_i) \tag{8.4}$$

Out of the three main mechanisms involved during the pullout of the geogrid from the soil, the initial confined stiffness, Jc, quantifies two mechanisms, i.e., tensile stress mechanism (J_u) and shear stress mechanism (J_s), during pullout test at low strains. The bearing mechanism is assumed not to have significant contribution at low strain values. Expressing the ratio of frontal displacement to the displacement at any point x_i in pullout test as J_s, equation 8.5 can be written as

$$J_C = J_U * J_S \tag{8.5}$$

where J_U represents the initial tensile stiffness and J_S represents the initial shear stiffness during the pullout test.

The stiffness of the combined soil-geogrid system in the pullout test consists of three main components, which are stiffness of the geogrid, stiffness of the soil and stiffness of the combined soil geogrid system.

$$J(soil - geogrid.system) = f(J_{soil}, J_{geogrid}, J_{soil-geogrid}) \tag{8.6}$$

$$J_{geogrid} = f(J_U) \tag{8.7}$$

$$J_{soil-geogrid} = f(J_S) \tag{8.8}$$

$$J_C = f(J_U, J_S) = f(J_{geogrid}, J_{soil-geogrid}) \tag{8.9}$$

Thus, J_C is not the stiffness of the geogrid alone but of the geogrid and soil-geogrid system combined together during a pullout test.

8.5.8.4 Degree of confinement

The confined stiffness obtained during the pullout test can also be expressed as a product of unconfined stiffness and the confinement factor F_C, where F_C is defined as the ratio of displacement rate during pullout test to the displacement rate at any point x_i.

$$J_C = J_U * F_C \tag{8.10}$$

The value of F_C equal to 1 would then represent no confinement or in-air tensile test and values greater than 1 would quantify the degree of confinement obtained in a soil-geosynthetic system. For geotextiles, F_C greater than 1 would quantify the value of shear stress mobilized during the pullout test and for geogrids it would help in quantifying the interlock and interface friction mobilized during the pullout test.

8.5.8.5 Conclusions

The current research at The University of Texas at Austin is focused on developing a model that would capture the shear displacement-force relationship under confined conditions. Further, a modified pullout test apparatus has been developed as explained in the next chapter in which the force is assumed to be constant throughout the entire length of embedded geosynthetic. This then helps to determine the confined force-strain relationship easily.

Chapter 9. New Test Procedures

9.1 Introduction

Traditional pullout tests use large pullout devices that conform to minimum recommendations of ASTM D6706. However, these pullout tests still require considerable effort to execute. On average, the volume of soil used in the common pullout tests ranges from 0.3 to 0.5 m3 and the mounting, executing, and dismounting procedures of a test require five or six days. In order to provide less expensive and more expeditious but still reliable tests, small pullout test devices have been developed by the works of Nakamura 2003, Kakuda et al. 2006, and Ju et al. 2006. The small pullout box used in this study was constructed by Teixeira (2003) and the feasibility of this small pullout box was demonstrated by Kakuda et al. (2006). In the present study, modifications were made in the small pullout box to allow the direct measurement of displacements throughout the geosynthetic specimen during the pullout test.

A new approach was developed for the obtained small pullout test results in order to apply them for pavement reinforcement purposes. This approach is different from the approach to the results of the large pullout tests presented in the previous chapter.

This chapter is organized as follows: first, the small pullout equipment device is described. Second, a correction of the grain size distribution curve of the base course soil is showed and justified. Third, the new approach for the small pullout test results is explained. Fourth, curves for pullout force vs. displacement are presented in order to validate the results obtained from the modified small pullout box. Then an evaluation is completed of the unconfined rigidity compared to the confined rigidity of each geosynthetic tested. Finally, a comparative analysis is performed among the confined rigidity of the geosynthetics used in the experimental testing program.

9.2 Test setup

9.2.1 Description of the Small Pullout Equipment

The small pullout box used in the experimental program has internal dimensions of 10 in. (250 mm) length, 12 in. (300 mm) width, and 6 in. (150 mm) height as shown in Figure 9.1. The volume of soil in this box is 0.01125 m^3; namely, 13% of the volume used for a device according to the minimum dimensions recommended by ASTM 6706. The frontal wall has a .3 in. (8 mm) aperture for the exit of the geosynthetic to the loading system. In this study, we made two openings of 1.6 by .12 in. (40 by 3 mm) at the back wall of the box in order to measure the displacement of two reference points in the geosynthetic specimen. All the internal walls were covered with two layers of a thin and rigid plastic. Grease was used between the walls and the first plastic layer and between the two plastic layers. This procedure was done to prevent friction between soil and box walls. The overload is applied by compressed air in a bag attached to the cover of the box.

A thin non-woven geotextile was placed on the top of the base course soil to protect the air bag responsible for the overload application, and then the box cover was attached. Pieces of a thin nonwoven geotextile were bonded on the geogrid ribs or on the area of the woven geotextile tested in contact with the grip. For the nonwoven geotextile tested specimens, a steel bar was

also used bonded to the geotextile specimen. These procedures were adopted to prevent slippage inside the grip of the geosynthetic specimen during pullout tests. Figure 9.2 shows the pullout test layout, which was executed at the same rate (.12 in. or 3 mm / min) of the large pullout tests.

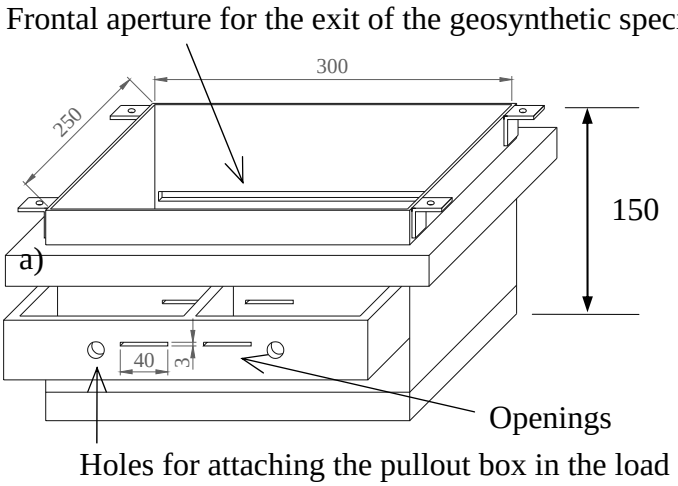

Figure 9.1: Cross section of the small pullout box used in the study (dimensions in mm).

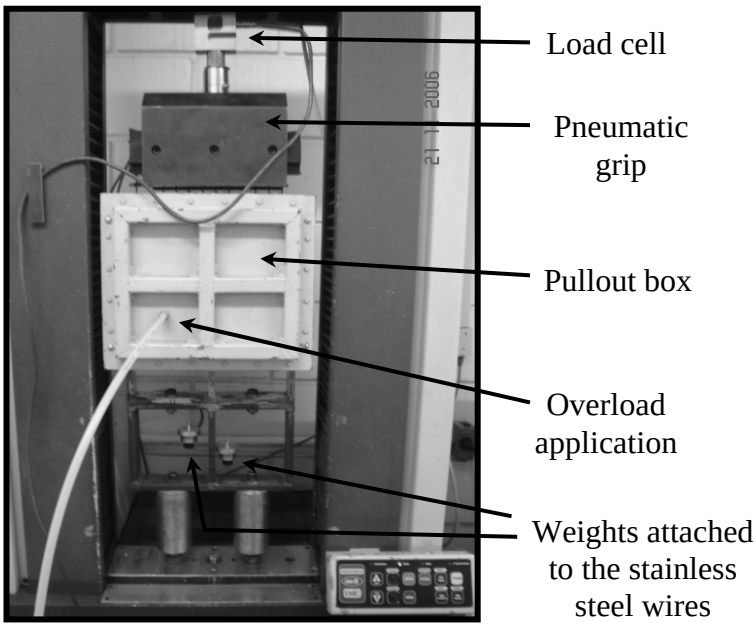

Figure 9.2: Small dimension pullout test layout

9.2.2 Correction of the Grain Size Distribution Curve of the Base Course Material

Correction was done in the grain size distribution curve of the base course soil to minimize interferences on the contour condition of the pullout tests and to follow the recommendations of ASTM D6706. The ASTM D6706 presents minimum relationships between (i) the wall dimensions of pullout box and the soil maximum diameter and between (ii) the wall

dimensions of pullout box and the diameter correspondent to 85% of the soil particles finer by weight. The values of these relationships for the small pullout box and soils are shown as dashed lines in Figure 9.3. The soils were compacted at the optimum water content and 100% of compaction grade at Proctor energy.

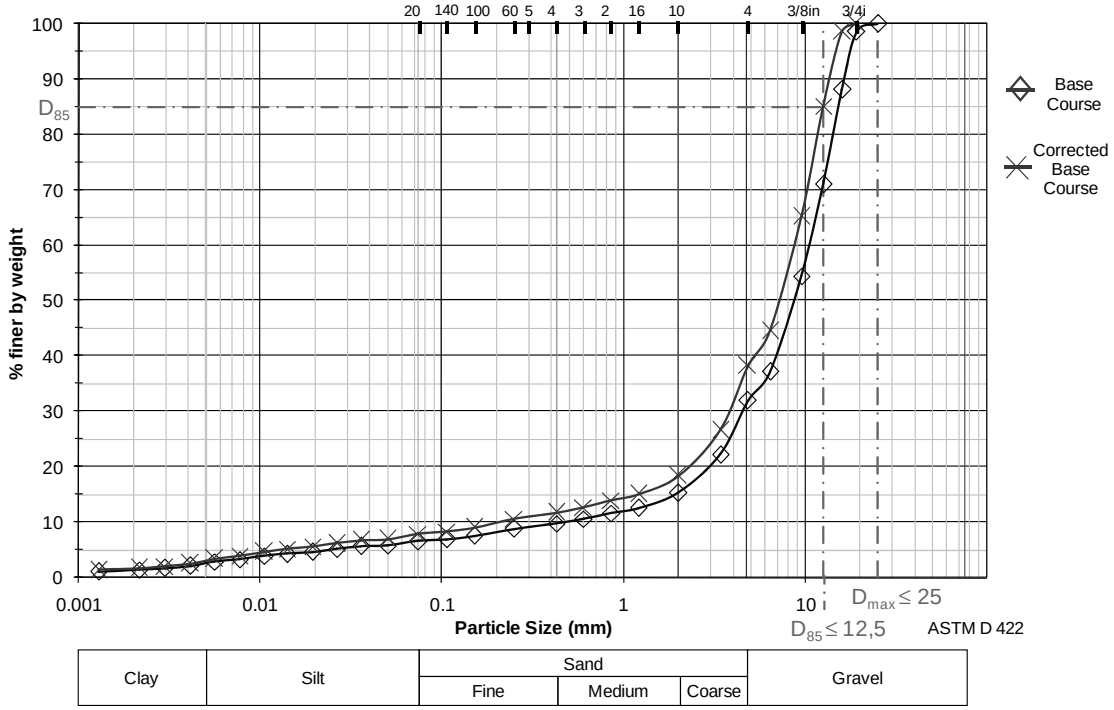

Figure 9.3: Modified gradation curve of the base course material for use with the small pullout box

9.3 Confined rigidity

9.3.1 Confined Rigidity Modulus (J_C) and Unconfined Rigidity Modulus (J_U)

The new approach to use the pullout test results for pavement reinforcement is to define a confined rigidity modulus (J_C). J_C is the pullout force divided by the correspondent deformation of the geosynthetic specimen. Equation 9.1 presents the definition of J_C.

$$J_C = \frac{\text{Pullout Force (kN/m)}}{\text{Deformation (\%)}} \qquad (9.1)$$

The geosynthetic specimen is entirely mobilized in the beginning of the small pullout test due to the small size of this specimen. Because of this entire mobilization in the beginning of the pullout test, we assume that it is not necessary to calculate the forces applied to the geosynthetic specimen at the points of measurement displacement. Whether these forces applied to the geosynthetic specimen at these measurement points are accounted, the difference between these forces and the pullout force would be very small. Consequently, the pullout force was directly used in Equation 9.1 to simplify the calculation of J_C. Additionally, the results of the pullout tests

applied in the Equation 9.1 were the results related only to the initial slope of the curve pullout force vs. displacement.

Similarly to J_C, the unconfined rigidity modulus (J_U) is defined as the tensile force (kN/m) divided by the correspondent deformation of the geosynthetic specimen (Equation 9.2) in the ultimate tensile strength test.

$$J_U = \frac{\text{Tensile Force (kN/m)}}{\text{Deformation (\%)}} \quad (9.2)$$

9.3.2 Validation of the Pullout Test Results

Pullout tests were executed with varying soils and geosynthetics. The geosynthetics were tested in both directions. We performed the tests with overloads of 7 and 21 kPa (1 and 3 psi, respectively) in order to make the overloads compatible to the normal tension occurred in road pavements. These overloads are the same for the large pullout tests performed. Table 9.1 summarizes the small pullout tests performed and their respective configuration.

All pullout force vs. displacement curves obtained from the small pullout tests have similar behavior to those curves reported in literature. This was observed because the reference displacement point closer to the pullout force applying point is mobilized before the reference displacement point more distant to the pullout force applying point. Additionally, the small pullout test curves are characterized for presenting a maximum value of pullout resistance and tending to stabilize in this maximum value or suffering a small and progressive decrease after the peak of the curve.

Typical pullout force variation with displacement curves obtained from small pullout equipment are presented in Figures 9.4 to 9.6 as examples of curves with similar behavior to those reported in literature. The differences among these tests are the configuration of the soil layers. Tests 1 and 2 were executed with subgrade soil in the bottom and upper layers. In tests 5 and 6 the bottom layer is subgrade soil and the upper layer is base course soil. In tests 15 and 16, the base course soil was placed in both layers. The geosynthetic used in these tests was the PP geogrid performed in the cross direction.

Table 9.1: Testing matrix for the small pullout tests performed.

Test	Bottom Layer	Geosynthetic/ Testing Direction	Upper Layer	Overload (kPa)
1	Subgrade	PP GG / Cross Direction	Subgrade	7
2	Subgrade	PP GG / Cross Direction	Subgrade	21
3	Subgrade	PP GG / Machine Direction	Base Course	7
4	Subgrade	PP GG / Machine Direction	Base Course	21
5	Subgrade	PP GG / Cross Direction	Base Course	7
6	Subgrade	PP GG / Cross Direction	Base Course	21
7	Subgrade	PET GG / Machine Direction	Base Course	7
8	Subgrade	PET GG / Machine Direction	Base Course	21
9	Subgrade	PET GG / Cross Direction	Base Course	7
10	Subgrade	PET GG / Cross Direction	Base Course	21
11	Subgrade	PP GT / Machine Direction	Base Course	7
12	Subgrade	PP GT / Machine Direction	Base Course	21
13	Subgrade	PP GT / Cross Direction	Base Course	7
14	Subgrade	PP GT / Cross Direction	Base Course	21
15	Base Course	PP GG / Cross Direction	Base Course	7
16	Base Course	PP GG / Cross Direction	Base Course	21
17	Base Course	PET GG / Machine Direction	Base Course	7
18	Base Course	PET GG / Machine Direction	Base Course	21
19	Base Course	PET GG / Cross Direction	Base Course	7
20	Base Course	PET GG / Cross Direction	Base Course	21

Note: PP—Polypropylene; PET—Polyester; GG—Geogrid; GT—Geotextile.

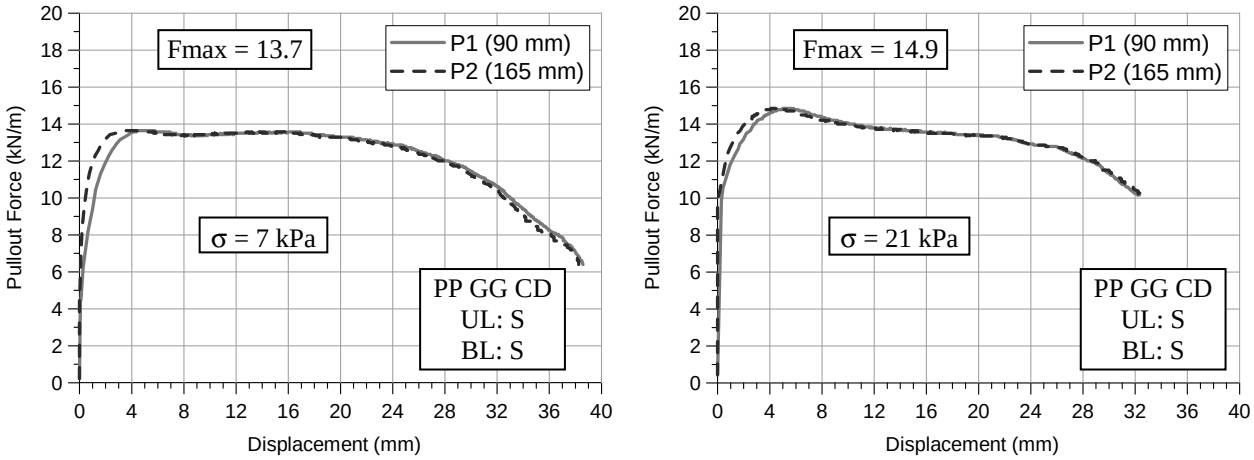

(a) Test 1 b) Test 2

Figure 9.4: Curves pullout force vs. displacement obtained from small pullout equipment

Note:

Number between parenthesis—point distance from the frontal wall of the small pullout box;

Fmax—Maximum pullout force;

σ —Overload;

BL—Bottom layer;

UL—Upper layer;

S—Subgrade;

PP—Polypropylene;

GG—Geogrid;

CD—Cross Direction.

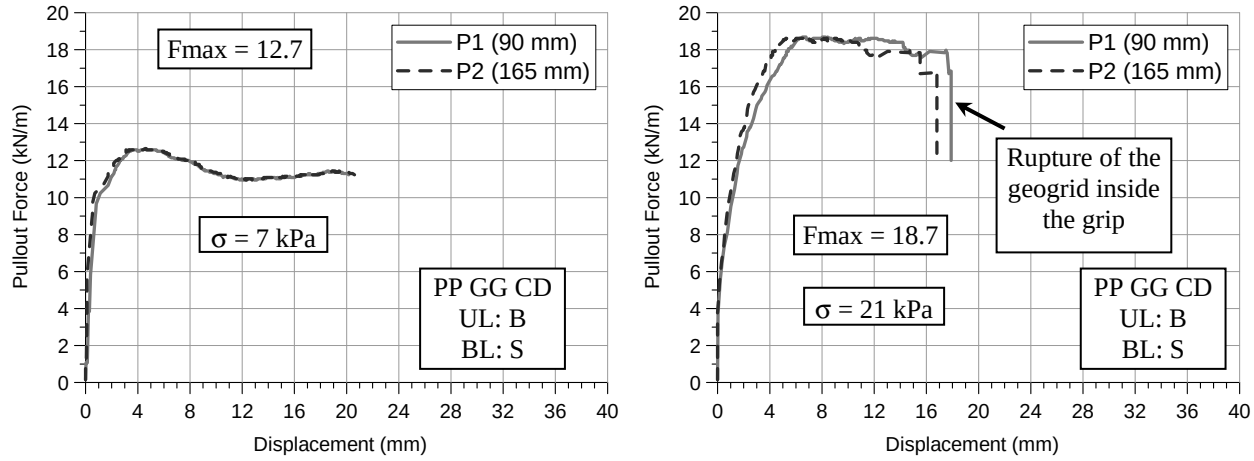

(a) Test 5 (b) Test 6

Figure 9.5: Curves pullout force vs. displacement obtained from small pullout equipment

Note:

Number between parenthesis—point distance from the frontal wall of the small pullout box;

Fmax—Maximum pullout force;

σ —Overload;

BL—Bottom layer;

UL—Upper layer;

S—Subgrade;

B—Base course;

PP—Polypropylene;

GG—Geogrid;

CD—Cross Direction.

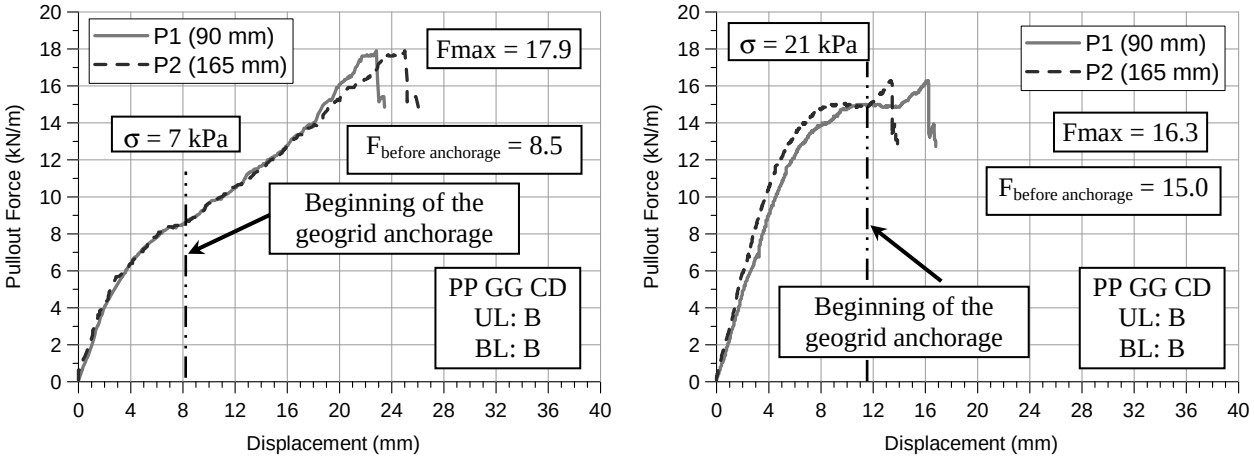

(a) Test 15 (b) Test 16

Figure 9.6: Curves pullout force vs. displacement obtained from small pullout equipment

Note:

Number between parenthesis—point distance from the frontal wall of the small pullout box;

Fmax—Maximum pullout force;

σ —Overload;

BL—Bottom layer;

UL—Upper layer;

B—Base course;

PP—Polypropylene;

GG—Geogrid;

CD—Cross Direction.

In the preceding figures, we can see that the curves reach a constant value and then start to increase again. This behavior is more evident in Figure 9.6(a) and (b). The unexpected second upward trend in the curves is due to the anchorage of the geogrid at the exit of the pullout box. The anchorage occurred because the maximum diameter of the particles of the granular soil (.75 in. / 19 mm) is bigger than the aperture of the frontal wall of the small pullout box (.3 in. / 8 mm). However, this phenomenon of anchorage of the geogrid only starts with relatively large displacements. In tests 15 and 16 the anchorage occurred when the reference point P2 presented displacements close to .3 and .5 in. (8 and 12 mm), respectively. Therefore, we can admit that the constant value that the pullout force vs. displacement curve reaches before to the anchorage of the geogrid is the "maximum natural value of the pullout resistance of the test." This anchorage occurs when the first transverse rib of the geogrid goes out from the pullout box, and then is hindered to move in some points by the soil particles arrested at the frontal aperture of the box. Also, as the anchorage phenomenon only occurs for large displacements (.3 in. / 8 mm at least) in the small pullout test, and the data used in Equation 9.1 were those only related to the initial slope of the curve pullout force vs. displacement; the calculated deformation of the geosynthetic is not affected by the anchorage phenomenon. Moreover, the calculation of the geosynthetic deformation is valid because the geosynthetic specimen is entirely mobilized in the beginning of the small pullout tests.

Figure 9.7 shows the anchorage in small pullout tests; Figure 9.8 depicts the results of entire mobilization of the geosynthetic specimen during the pullout tests.

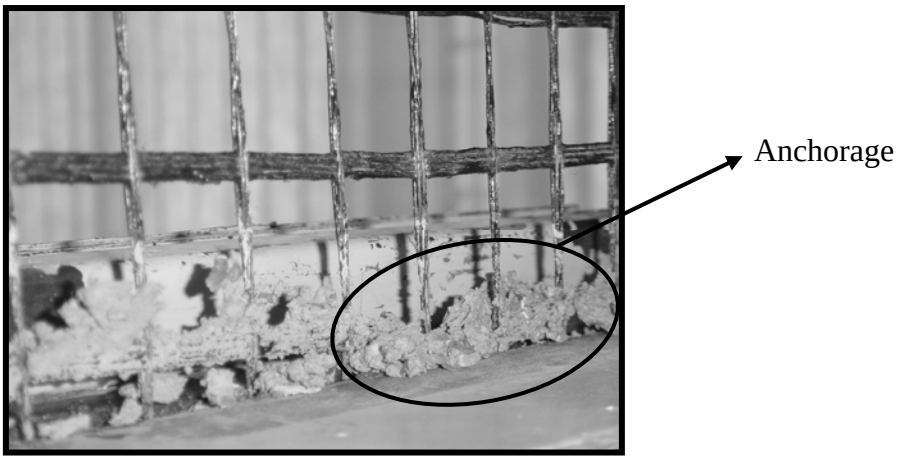

Figure 9.7: Anchorage in small pullout tests: Anchorage of the PET geogrid specimen at the exit of the small pullout box during test 17

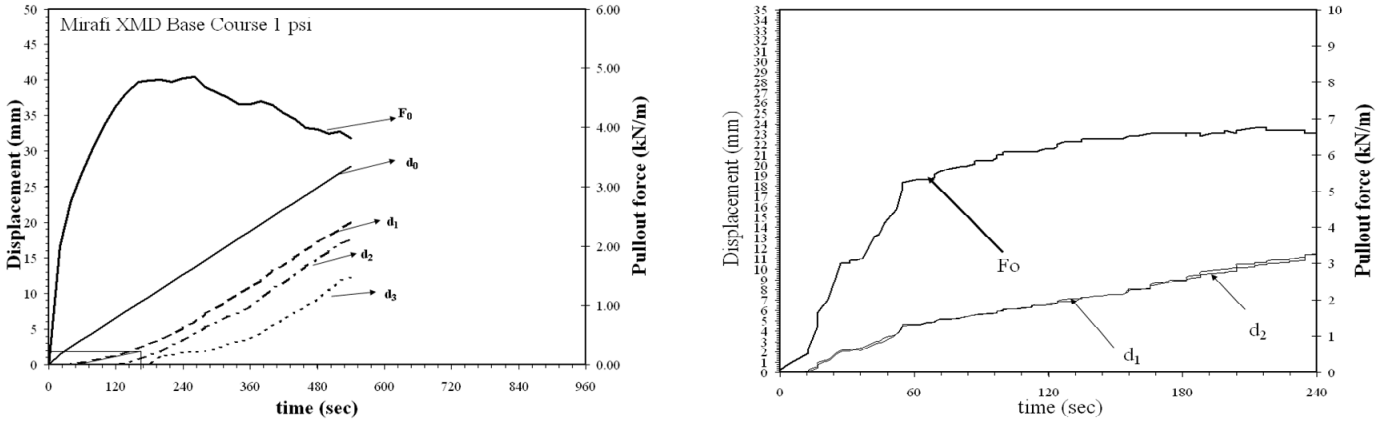

(a) Large pullout test (b) Small pullout test

Figure 9.8: Entire mobilization of the geosynthetic specimen during the small pullout test and comparison with large pullout test.

Note: Configuration of both tests: PET geogrid used in cross direction, base course soil in both layers of the pullout box and overload of 7 kPa.

In the large pullout test the displacement reference points of the geosynthetic specimen (d_1, d_2, d_3) start to move one after other with a delay. Moreover, the last point, d_3, begins to move only after approximately 180 seconds. This delay shows that the large geosynthetic specimen is progressively mobilized. Besides the small geosynthetic specimen is also progressively mobilized, the displacement reference point d_2 starts to move just after the first displacement reference point d_1. Therefore, the small geosynthetic specimen is entirely mobilized in the beginning of the pullout test.

9.3.3 Comparison of the Confined Rigidity Moduli (J_C) of the Geosynthetics

Figures 9.9 and 9.10 presents the confined rigidity moduli (J_C) of the geosynthetics tested in the machine direction with overloads of 7 and 21 kPa. This figure shows that, among the geosynthetics used with the soils of the testing program, the PP geogrid had the best performance

for pavement reinforcement purpose. This best performance occurs because the PP geogrid presented the highest J_C for all levels of deformation in comparison with the other geosynthetics tested. However, the GG geogrid has the lowest unconfined rigidity among the geosynthetics used. Figure 9.11 shows the comparison of the J_U of the geosynthetics tested in the machine direction. The maximum value of the x-axis was limited to 2% because the highest deformation presented by the geosynthetics was less than 2% in the confined situation. Accordingly, Figure 9.11 b shows that the GG geogrid has the lowest J_U for all values of deformation. In contrast, the PET geogrid is the geosynthetic with the highest J_U. However, the J_U of this geogrid becomes lower than the J_U of the PP geotextile starting from deformation of 0.85%.

Based on the relative behavior of the geosynthetics tested in confined and unconfined situation, we concluded that the soil-reinforcement interaction was more efficient for the PP geogrid than for the PET geogrid or the PP geotextile. This same relative behavior was found when the geosynthetics were tested in the cross machine direction. The PP geogrid presented the highest J_C due to its better interaction with the soils used in the study. This good performance of the PP geogrid occurs because of its geometric characteristics and its junction strength. Specifically, the relation between the aperture size (machine and cross directions) and the grain size distribution of the soils was favorable to the PP geogrid than to the PET geogrid.

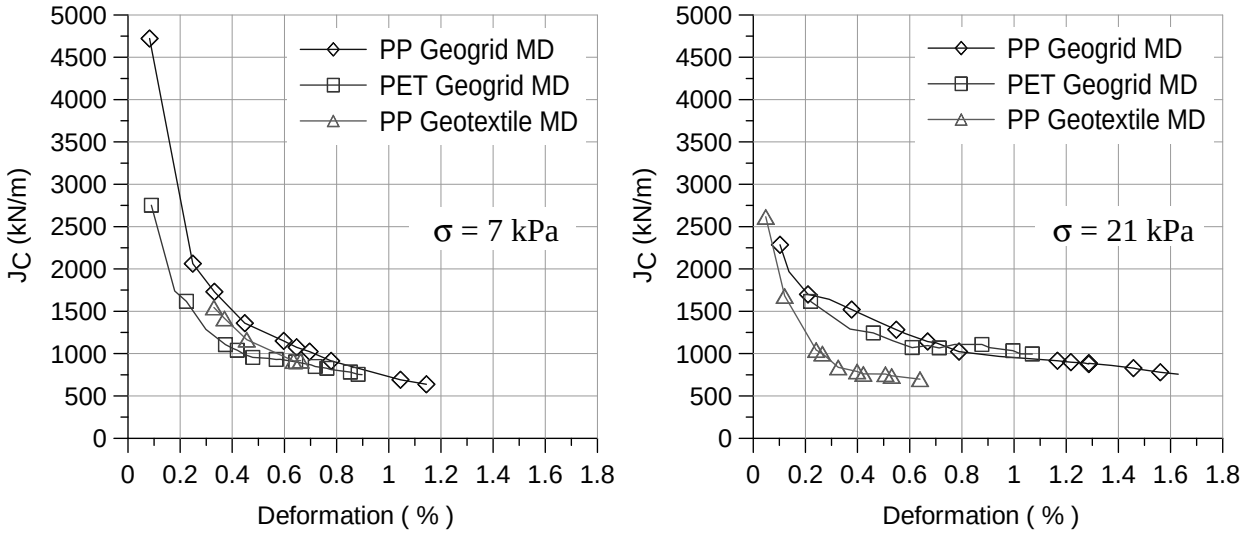

(a) Overload of 7 kPa (b) Overload of 21 kPa

Figure 9.9: Confined rigidity modulus (J_C) vs. Deformation curves of the geosynthetics tested in machine direction with subgrade soil in the bottom and base course soil in the upper layers of the pullout box

Note: PP—Polypropylene; PET—Polyester; MD—Machine Direction; σ—Overload.

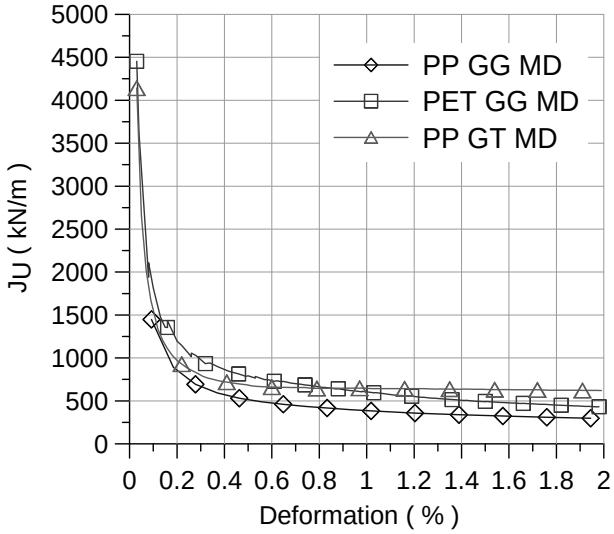

Figure 9.10: Comparison among the unconfined rigidity moduli (J_U) of the geosynthetics tested in the machine direction

Note: PP—Polypropylene; PET—Polyester; GG—Geogrid; GT—Geotextile; MD—Machine Direction.

Additionally, the junction strength of the PP geogrid is higher than the junction strength of the PET geogrid. Tests made by the laboratory of transportation of TxDOT showed that the PP geogrid has 15.4 kN/m of junction strength and that the PET geogrid has 5.8 kN/m of junction strength. Hence, although the high unconfined rigidity is the prime characteristic required to a geosynthetic to be used in pavement reinforcement, the soil-reinforcement interaction is also determinant for the performance of a geosynthetic as reinforcement of road pavements.

In addition to the tests with the geogrids, we also tested a PP woven geotextile. Accordingly, the PP geotextile presented higher J_C than the PET geogrid for overload of 7 kPa , but for overload of 21 kPa , the PP geotextile presented lower J_C than the PET geogrid. This occurred because the geogrid performs as a confinement element for the soil. For overload of 7 kPa, which is a low pressure, the geotextile is better because of its bigger area available for developing skin friction between soil and reinforcement. For this level of overload, the mechanisms of bearing capacity and the cutting action of the geogrid bearing members are not highly mobilized. However, for overload of 21 kPa, the soil contact through the aperture size of the geogrid increases thus making it harder for developing the cutting action of the geogrid bearing members and, consequently, raising the bearing capacity of these members. Consequently, these mechanisms of skin friction and bearing capacity of the PET geogrid became higher than the skin friction of the PP geotextile.

On the other hand, the behavior of the PP geotextile for overload of 21 kPa was lower than its behavior for overload of 7 kPa. This unexpected result may have been caused by the steel bar used against slippage inside the grips for the test with 21 kPa of overload. The explanation of this slippage phenomenon is addressed in the next section.

9.3.4 Confined Rigidity vs. Unconfined Rigidity Analysis of the Geosynthetics

Figure 9.11 shows the unconfined (J_U) and confined (J_C) rigidity moduli of the geosynthetics used in the machine direction. In the confined condition, all tests were performed using subgrade soil in the lower layer and base course soil in the upper layer, with overloads of 7

and 21 kPa. In the unconfined condition, the J_U presented is from the specimen considered as the "average specimen" of the ultimate tensile strength tests.

The benefits of the confinement for the PET geogrid are shown in Figure 9.11 b. These benefits are provided by the relative behavior among the curves where the J_U of the PET geogrid is lower than its J_C at 7 kPa, which is lower than its J_C at 21 kPa. This relative behavior occurs because the soil-geosynthetic interaction limits the reinforcement deformation in a confined condition. Additionally, as the overload applied on the top of the soil block increases, the confinement also increases making it harder for the geosynthetic to deform. This same behavior is found for the PP geogrid starting from deformations of about 0.4%. We believe that initially, the rearrangement of the soil particles in the interaction with the PP geogrid may have influenced the results of J_C at 21 kPa of overload. However, for the PP geotextile the very low behavior of J_C at 21 kPa of overload may have been caused by the device used against slippage inside the grips for this specimen. This slippage may have occurred during the pullout test because of adjustment of the steel bar used to prevent it. For some reason, this adjustment did not influence the curve pullout force vs. displacements but was decisive for the deformation behavior of the geosynthetic. The small pullout test performed with PP geotextile highlighting the steel bar used to prevent slippage of the geotextile specimen inside the grip (see Figure 9.12). Figure 9.11(c) shows the pullout force vs. displacement curve of this PP geotextile pullout test, providing that this curve was unaffected by the adjustment of the steel bar in the grip during the test.

Furthermore, using granular soil instead of using cohesive soil may also increase the confined rigidity of the geosynthetic. Figure 9.13 illustrates this increase by presenting the J_U and J_C curves of the PP geogrid tested in the cross direction. One J_C curve was obtained using the subgrade soil in the upper layer in the pullout box, while the other J_C curve was obtained using the base course soil in the upper layer in the pullout box. In both of the confined tests used to obtain these J_C curves, an overload of 21 kPa was applied. The results show that the confined rigidity of the PP geogrid increases when the upper layer of subgrade soil is replaced by a layer of base course soil. We found two reasons to explain this increase.

First, the soil-reinforcement interaction is different when the upper layer of cohesive soil (subgrade) is replaced by granular soil (base course). With the granular soil in the upper layer of the pullout box, the bearing strength developed by the transverse members is higher than with the cohesive soil in the upper layer. In addition, the granular soil used in this study is a sandy-silty gravel with angular particles, which may result in higher interface shear strength in comparison to the cohesive soil used. Hence, due to the soil-reinforcement interaction, the base course soil placed in the upper layer of the pullout box increases the rigidity of the geogrid specimen more than the subgrade soil does.

Second, the geosynthetic specimen is nailed when the base course soil is compacted in the upper layer of the pullout box and the subgrade soil is in the bottom layer of the box. This nailing is heterogeneous so the geosynthetic specimen is not throughout submerged in the subgrade layer at the same depth. Consequently, this nailing causes a pre-stress in the geogrid specimen increasing the initial rigidity of this specimen. This nailing phenomenon was realized during the dismounting procedure of the pullout tests. Additionally to the geosynthetic nailing, the particles of the base course soil submerged into the subgrade soil through the apertures of the geogrid specimen. Specifically, the biggest particles of the base course soil, which were half submerged in the subgrade soil, made harder the development of the cutting action of the transverse members. As a result, the bearing strength developed by these transverse members

was increased. The same behavior was found for the pullout tests performed with 7 kPa of overload.

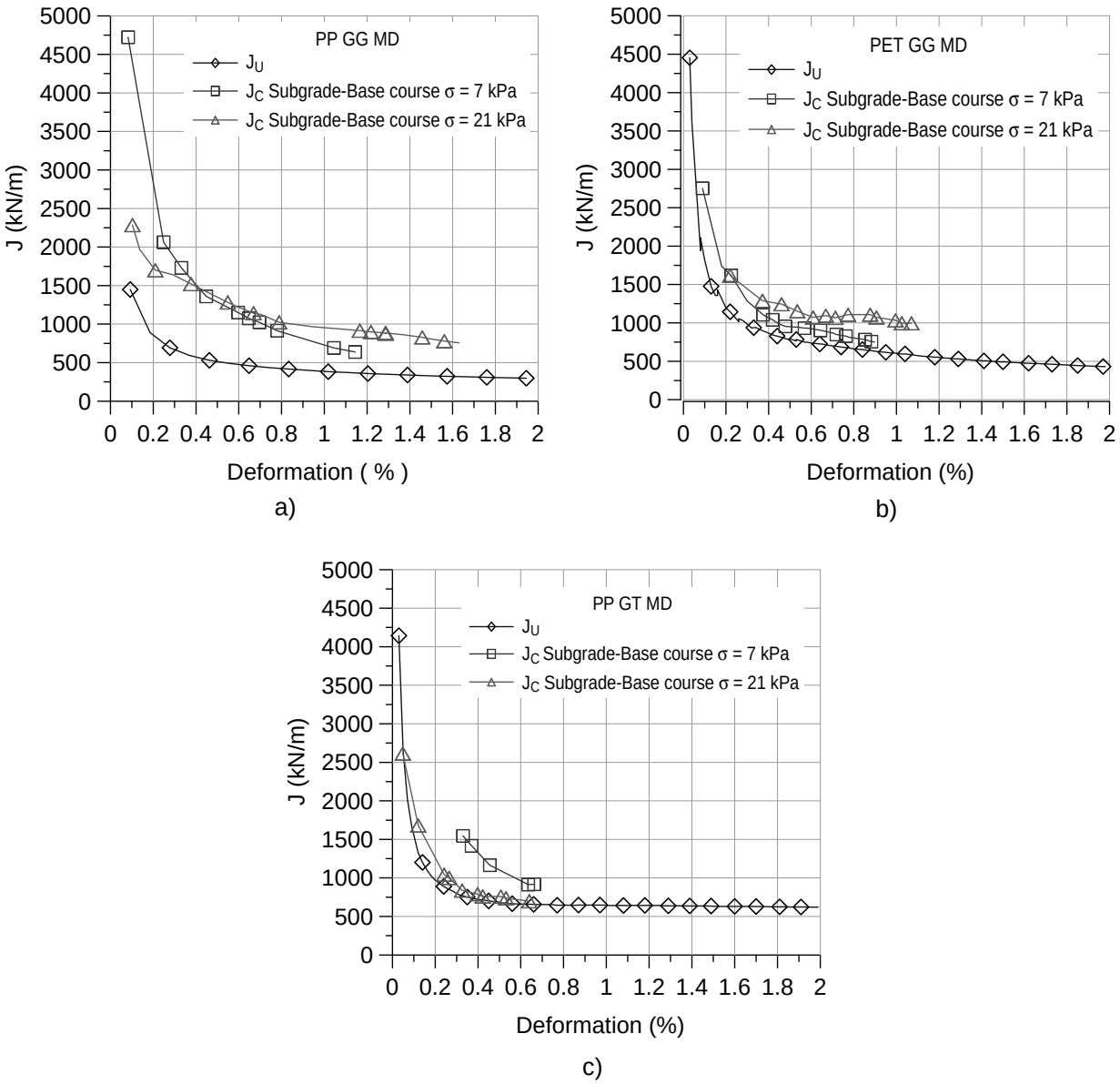

Figure 9.11: Comparisons among unconfined (J_U) and confined (J_C) rigidity moduli of the geosynthetics tested in the machine direction a) Polypropylene Geogrid b) Polyester Geogrid. c) Polypropylene Woven Geotextile

a)

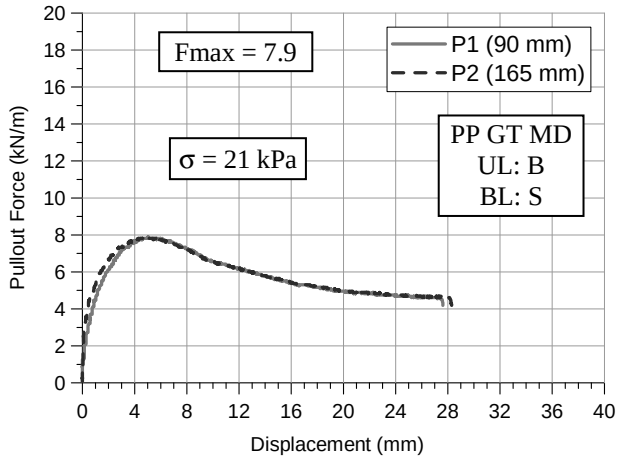

b)

Figure 9.12: Small pullout test of the PP geotextile with 21 kPa of overload, subgrade and base course soils in the bottom and the upper layers, respectively (Test 12) a) Photo of the test with the steel bar highlighted used for prevent slippage of the geosynthetic specimen during pullout test b) Curve pullout force vs. displacement of test 12

Note:
Number between parenthesis—point distance from the frontal wall of the small pullout box;
Fmax—Maximum pullout force;
σ —Overload;
BL—Bottom layer;
UL—Upper layer;
S—Subgrade;
B—Base course;
PP—Polypropylene;
GT—Geotextile;
MD—Machine Direction.

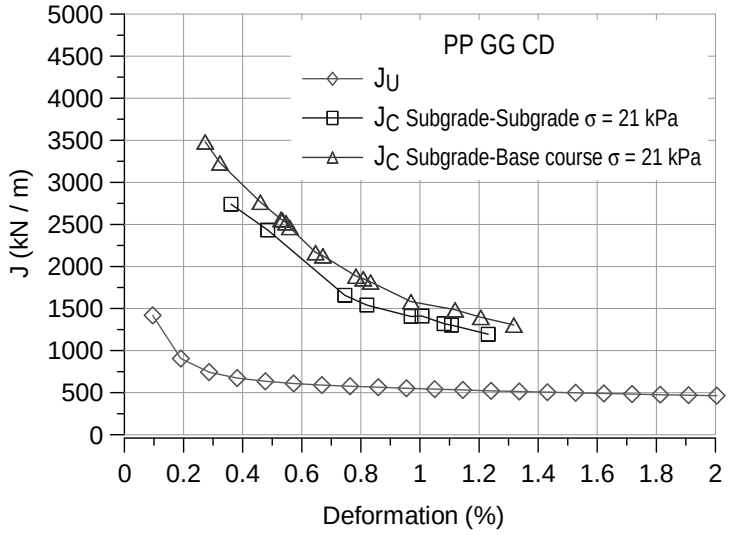

Figure 9.13: Unconfined (J_U) and confined (J_C) rigidity moduli of the PP grid

Note: the polypropylene geogrid tested in the cross direction with subgrade soil in the bottom layer of both pullout tests and subgrade and base course soils in the upper layer of pullout tests 2 and 6, respectively. GG—Geogrid; PP—Polypropylene; CD—Cross Direction; σ—Overload.

9.4 Summary of test results

Three geosynthetics were evaluated for pavement reinforcement purposes. The geosynthetics tested included polypropylene and polyester geogrids; and a polypropylene woven geotextile. The evaluation was done by using pullout tests in small pullout equipment. An approach was developed in order to apply the results of the small pullout tests in road pavement reinforcement. Clay and sandy-silty gravel were used to study the performance of the geosynthetics placed between the subgrade and base course layers of a road pavement. The main conclusions that can be drawn from this study include:

- The junction strength is the most important factor influencing the confined stiffness of geogrids. This parameter was more important for confined stiffness than the unconfined stiffness of the geosynthetics used in this study. Consequently, the soil-reinforcement interaction was favorable for the PP geogrid and there is good evidence that this geogrid is better for pavement reinforcement than the other geosynthetics used in this work. Further research is needed to confirm this observation in the field.
- The reasons related to the low performance of one geosynthetic when compared with another can be attributed to its low junction strength, high sensitivity to installation damage, high manufacturing variability, and low friction coefficient. These factors are related to geometric characteristics and manufacturing procedures.

Chapter 10. Summary and Conclusions

10.1 Summary of research objectives

The goal of this study was to identify the material properties governing the design of geosynthetic-reinforced pavements and to develop appropriate material specifications. The study shows that the soil-geosynthetic confinement is the relevant property that should be determined for design of geosynthetic-reinforced pavements. Specifically, the stiffness of the soil-geosynthetic system under low strains, which can be obtained using the suggested new test, can be used as an index for comparing and predicting the performance of geosynthetics in pavements. By developing a small pullout box and a simple model that requires straightforward interpretation of data, this research aims to quantify soil-geosynthetic confinement in a reasonable time frame. This would help to promote the use of experimentally derived project specific properties to be used in design of geosynthetic reinforced pavements in Texas.

10.2 Conclusions from the study

The specific objectives stated in the beginning of this report were achieved as follows:

- Current reinforced pavement design methodologies were reviewed, with particular emphasis on their suitability for conditions typical of TxDOT pavements and Texas materials and environmental conditions was conducted. Based on this review, the current state of practice for the geosynthetic reinforced pavements in Texas was summarized. The relevant mechanisms responsible for better performance of geosynthetic reinforced pavements were identified.
- A one-page statewide survey was conducted. The information survey summarizing the experience gained by TxDOT to date on the use of geosynthetic reinforcement in pavement systems was presented. Based on the comments received on the survey forms, it was found that the engineers had no specifications for designing geogrid reinforced roads. They only had a single TxDOT specification regarding testing methodology to be adopted to determine which geogrid should be used in pavement for reinforcement purposes, but no such specification existed for geotextiles. Further, the best location for the placement of geosynthetics and construction guidelines to place them in the field were not specified.
- Quantification of the structural conditions of in-situ pavement sections constructed by TxDOT was carried out in order to identify the variables responsible for observed differential pavement performance in the field. The research indicated adequate field evidence that geogrid reinforcement provides benefits by stabilizing pavement over clays of high plasticity. But still there is need for new laboratory tests that can provide insight into field performance of these sections. Further, new methods for the analysis of FWD testing need to be developed that can better predict the field performance of geogrid reinforced and unreinforced section
- The information collected in this study was used to validate existing methodologies and develop a new methodology for the design of geosynthetic reinforced base courses. Based on the laboratory and field studies conducted for geosynthetic

reinforcement of flexible pavements, it was demonstrated that the principal effect of the geosynthetics is to provide lateral confinement to the aggregate or base course layer of pavement.

- The testing procedures and specifications based on quantification of soil-geosynthetic interaction under low strains were established. Due to mobilization of the entire specimen in the small pullout test, the forces applied to the geosynthetic specimen at the points of measurement displacement could be easily measured. This data can then be used to compute the confined stiffness of the system by determining the initial slope of the pullout force and displacement curve.
- To translate the finding of this research into construction and material guidelines suitable to TxDOT's needs, a new test method has been suggested. A confined-monotonic test setup involving a pullout box and a simple model that requires straightforward interpretation of data is explained. This aims to quantify soil-geosynthetic confinement in a reasonable time frame, using the apparatus commonly available in most TxDOT testing laboratories.
- When comparing the performance of one geosynthetic with another for reinforced pavement application, a number of factors besides soil-geosynthetic should also be considered. The reasons related to the low performance of one geosynthetic can be attributed to its low junction strength, high sensitivity to installation damage, high manufacturing variability, and low friction coefficient. These factors are related to geometric characteristics and manufacturing procedures. Consequently, improving these aspects would help develop geosynthetics for pavement reinforcement

Chapter 11. Path Forward

11.1 Introduction

Use of geosynthetics for unbound base courses can lead to improved performance and reduced costs in pavement systems. However, appropriate selection of geosynthetics is compromised by the difficulty in associating their relevant properties to pavement performance. The current project included survey, analytical, experimental, and field components aimed at identifying the geosynthetic properties that govern their use in a pavement system. Specifically, a new test device was developed to allow characterization of the soil-geosynthetic interaction under low strain levels.

For this project, a new testing device was developed, and a monitoring program was initiated to evaluate the performance of geosynthetics used as reinforcement for unbound base courses. The purpose of the further research should be to conduct a pilot implementation using the new testing device. The testing should involve a modified pullout device for characterization of the confined stiffness in geosynthetic reinforcements. The project should also provide continued monitoring of 32 experimental test sections constructed on FM 2 (Bryan District) for the purposes of correlating field performance with material characterization. The field component of this implementation project should involve continued condition survey, moisture monitoring, FWD testing, and weather data gathering in order to establish the threshold of the proposed parameter in the new specification based on field performance.

11.2 Validation of new laboratory testing procedure

The objective of this task should be to validate the testing procedures established for quantification of soil-reinforcement interaction under low strains. The property suitable to evaluate the performance of geosynthetic-reinforced pavements was determined to be the confined stiffness of the geogrid. The testing program of the geosynthetic should be designed to complement tests conducted so far, including conventional tests for characterization of geosynthetics as well as the recently developed small-scale pullout test.

11.3 Monitoring test sections

In addition, and in order to validate the experimental results against field performance, the structural condition of pavement sections constructed by TxDOT should be continually monitored. Emphasis should be placed on monitoring the 32 recently constructed geogrid-reinforced pavement sections on FM 2 (Bryan District), although additional locations can also be considered according to TxDOT needs, particularly where pavement failures are identified. Field monitoring program should include: (i) continued FWD testing to be conducted at least four times a year to assess the effect of moisture seasonal variations in the pavement performance, (ii) continued field monitoring of moisture sensor profiles that have already been installed to monitor the horizontal (under the pavement) and vertical moisture fluctuations, (iii) continued condition surveying to document and quantify the field performance of the sections, (iv) continued gathering and evaluation of relevant weather data, and (v) quantification and assessment of cracks and deterioration that may develop in the 32 monitored sections. This should also include trenching at locations of identified failures.

References

American Society for Testing and Materials (2003). Standard Test Method for Measurement of Soil Potential (Suction) Using Filter Paper, D 5298-03.

Ayad, R., Konrad, J.-M., and Soulie, M. (1997). "Desiccation of a Sensitive Clay: Application of the Model CRACK." Canadian Geotechnical Journal, V 34, pp 943-951.

Chen, F.H. (1988). Foundations on Expansive Soils. Elsevier Science Publishers B.V.

Fredlund, D.G., and Morgenstern, N.R. (1976). "Constitutive Relations for Voume Change in Unsaturated Soils." Canadian Geotechnical Journal, Vol. 13, No. 3, pp 21-276.

Fredlund, D. G., and Rahardjo, H. (1993). Soil Mechanics for Unsaturated Soils. John Wiley & Sons, Inc., New York.

Freund, L. B. (1978) "Stress Intensity Factor Calculations Based on a Conservation Integral." International Journal of Solids Structures, Vol. 14, pp. 241-250.

Harison, J. A., Hardin, B. O., and Mahboub, K. (1994). "Fracture Toughness of Compacted Cohesive Soils Using Ring Test." Journal of Geotechnical Engineering, Vol. 120, No. 5, pp 872-891.

Jayatilaka, R., and R. L. Lytton (1997). Prediction of Expansive Clay Roughness in Pavements with Vertical Moisture Barriers. Research Report FHWA/TX-98/187-28F, Texas Transportation Institute, Texas A&M University, College Station, Texas.

Konrad, J. M., and Ayad, R. (1997). "Desiccation of a sensitive Clay: Field Experimental Observations." Canadian Geotechnical Journal, V 34, pp 929-942.

Konrad, J. M., and Cummings, J. (2001). "Fracture Toughness of Frozen Base and Subbase Soils in Pavement." Canadian Geotechnical Journal, V 38, pp 967-981.

Lawn, B. (1993). Fracture of Brittle Solids. Cambridge University Press, Cambridge.

Lee, F., Lo, K., and Lee, S. (1988). "Tension Crack Development in Soils." Journal of Geotechnical Engineering, ASCE, Vol. 114, No. 8, pp 915-929.

Lytton, R. L. (1977). "The Characterization of Expansive Soils in Engineering." Presentation at the Symposium on Water Movement and Equilibria in Swelling Soils, American Geophysical Union, San Francisco, California.

Lytton, R. L. (1995). "Foundations and Pavements on Unsaturated Soils." Proceedings of the First International Conference on Unsaturated Soils, Paris, France, pp 1201-1220.

Lytton, R. L, Aubeny, C., and Bulut, R. (2004). Design Procedure for Pavements on Expansive Soils, Research Report FHWA/TX-05/0-4518-1, Texas Transportation Institute, Texas A&M University, College Station, Texas.

McKeen, R. G. (1980). "Field Studies of Airport Pavements on Expansive Clay." Proceedings of the Fourth International Conference on Expansive Soils, Denver, Colorado, V. 1, pp 242-261.

Mitchell, P. W. (1979). The Structural Analysis of Footings on Expansive Soil. Research Report No. 1, Kenneth W. G. Smith and Associates, Adelaide, south Australia.

Mitchell, P. W. (1980). "The Concepts Defining the Rate of Swell of Expansive Soils." Proceedings of the Fourth International Conference on Expansive Soils, Denver, Colorado, V. pp 106-116.

Mobasher, B., Mamlouk, M. S., and Lin, H. M. (1997). "Evaluation of Crack Propagation Properties of Asphalt Mixtures." Journal of Transportation Engineering, Vol. 123, No. 5, pp 405-413.

Mojekwu, E. C. (1979). A Simplified Method for Identifying the Predominant Clay Mineral. Master Thesis, Department of Civil Engineering, Texas Tech University, Lubbock, Texas.

Morris, P. H., Graham, J., and Williams, D. J. (1992). "Cracking in Drying Soils." Canadian Geotechnical Journal, V 29, pp 263-277.

Nyangag, F. N. (1996). Developing A Model to Predict Pavement Roughness Development on Expansive Soils. Ph.D. Dissertation, Texas A&M University, College Station, Texas.

Paris, P. C., and Sih, G. C. (1965). "Stress Analysis of Cracks." Fracture Toughness Testing and its applications. ASTM Spec. tech. Publ. 381, pp 30.

Rice, J. R. (1968). "A Path Independent Integral and the approximate Analysis of Strain Concentration by Notches and Cracks." Journal of Applied Mechanics, V. 35, pp 379-386.

Sebesta, S. (2002). Investigation of Maintenance Base Repairs over Expansive Soils: Year 1 Report. Research Report FHWA/TX-03/0-4395-1, Texas Transportation Institute, Texas A&M University, College Station, Texas.

Tada, H., Paris, P. C., and Irwin, G. R. (2000). The Stress Analysis of Cracks Handbook. The American Society of Mechanical Engineers, New York.

Thornthwaite, C. W. (1948). "An Aproach toward a Rational Classification of climate." Geographical Review, V. 18, pp 54-94.

Wray, W. K., B. M. El-Garhy, and A. a. Youssef (2005). "Three-Dimensional Model for Moisture and Volume Changes Prediction in Expansive Soils." Journal of Geotechnical and Geoenvironmental Engineering, vol. 131, No. 3, pp 311-324.

Wray, W. K. (1978). Development of a Design Procedure for Residential & Light Commercial Slabs-on-Ground Constructed over Expansive Soils. Ph.D. Dissertation, Texas A&M University, College Station, Texas.

Decagon Devices, inc. (2006). *ECH$_2$0 Dielectric Probes vs. Time Domain Reflectometry (TDR)*. Application Note.

Mitchell, J.K. and Dermatas, D. (1992). Clay Soil Heave Caused by Lime-Sulfate Reactions. *Innovations and Uses for Lime* ed. Walker DD. ASTM. West Conshohoken, PA.

Sebesta, S.D., Scullion, T., and Estakhri, C.K. (2004). Selection of Maintenance Repair Methods on Expansive Subgrades. Texas Transportation Institute, College Station, TX.

Zornberg, J.G., Gupta, R., and Prozzi, J. (2008). Geogrid Reinforcement of Pavements over Expansive Clay Subgrades. *GeoAmericas 2008*. Cancun, Mexico.

ASTM D 6706. Standard test method for measuring geosynthetic pullout resistance in soil, American Society for Testing and Materials, West Conshohocken, Pennsylvania, USA.

Ju, J.W., Park, J.B., Song, C.S., Chun, S., Cho, S.D. and Kim, J.H. (2006). New definition of pullout constant. 8ICG, GS, Yokohama, Japan, 1437-1441.

Kakuda, F.M., Bueno, B.S. and Teixeira, S.H.C. (2006). Geogrid pullout tests using small scale equipment. 8ICG, IGS, Yokohama. Japan, 1443-1446.

Nakamura, T., Mitachi, T. and Ikeura, I. (2003). Estimating method for the in-soil deformation behavior of geogrid based on the results of direct box shear test. Soil and Foundations, 43: 47-57.

Teixeira (2003). Estudo da interação solo-geogrelha em testes de arrancamento e a sua aplicação na análise e dimensionamento de maciços reforçados. PhD dissertation, Dept. of Geotechnical Engineering, Engineering School of Sao Carlos, Univ. of Sao Paulo (in Portuguese).

Appendix A

A.1 Condition Survey for FM 2, Grimes County, Texas

FM 2 (Farm to Market 2) is a low-volume road located in Grimes County, Texas. This road extends east from SH 6 (State Highway 6) to FM 362 and is approximately 10 miles south of Navasota, Texas. It is primarily used by residential traffic and has had a history of severe longitudinal cracking. Two years ago, the road and sub-layers were excavated and test sections were installed to determine the best combination of sub-grade and textile to eliminate the previously mentioned longitudinal cracking. The road was constructed with 16 test sections included (8 east bound side, 8 west bound side). Each test section consists of a different base mixture accompanied by a layer of either Geo grid or Geosynthetics. A chip seal was applied to the surface to provide a measure of protection from the elements and vehicle traffic.

Along with moisture and density testing, a visual condition survey was conducted approximately every three months. This interval was selected to provide data for cold, hot, rainy, and dry periods throughout the evaluation. The condition survey consisted of walking along the edge of the road, the length of the test sections, while measuring the distance walked with a measuring wheel, at the same time visually inspecting the roads surface for distresses (cracking, potholes, etc.). When a distress was noticed several aspects of that distress were recorded, the type of distress, location along the test section, and the dimensions (length, wide, depth). This information was used to monitor and evaluate the distresses over time providing a means to determine whether the distress's severity remained the same or increased over time.

The overall condition of the road is fairly good. Due to the chip seal the road is extremely raveled in several places especially were driveways along the road are present. The small potholes that are present are due to something being dragged along the road (Chain, trailer, etc.) not from a breakdown of the chip seal. Similarly the presence of edge cracking is caused by the exposed base mixture eroding away, possibly due to vehicle traffic and/or rain.

A.2 Summary of Observations and Survey Data

A.2.1 August 2006

The first evaluation was conducted in August of 2006. There were no major distresses present on the road surface. The road has evidence of edge cracks, possibly due to erosion of the base materials along the edge of the road. There were also several small potholes that were caused by vehicular traffic on the road. The most severe distresses seen were large longitudinal cracks on the shoulder of the road.

Table A.1: Survey Data from August 2006

FM 362

Dist	Desc	Length	Width	Depth	Notes
Test Section 1▼					
350	Edge Cracking	6'	6"		
Test Section2▼					
450	Edge Cracking	73'	6"		
648	Edge Cracking	6"	6"		
740	Edge Cracking	6"	6"		
871	Edge Cracking	6"	6"		
Test Section 3▼					
Test Section 4▼					
1125	Edge Cracking	35'	6"		
Test Section 5▼					
Test Section 6▼					
2311	Edge Cracking	25'	6"		
Test Section 7▼					
2700	Edge Cracking	27'	6"		
2775	Edge Cracking	6"	6"		
Test Section 8▼					
3168	Edge Cracking	18"	6"		
3590	Edge Cracking	10'	6"		
Test Section 9▼					
Test Section 10▼					
Test Section 11▼					
Test Section 12▼					
Break in Test Sections					
Test Section 13▼					
63	Longitudinal Crack	32'	0.0625		≈ 12"from SH
224	Edge Cracking	3.5'	6"		
314	Longitudinal Crack	90'	0.0625		≈ 12"from SH
Test Section 14▼					
Test Section 15▼					
918	Edge Cracking	6"	6"		
1045	Small Pothole	2"	2"		≈ 12"from SH
1046	Small Pothole	1"	1"		≈ 12"from SH
1048	Small Pothole	1"	1"		≈ 12"from SH
Test Section 16▼					
1434	Edge Cracking	6"	6"		
1450	Edge Cracking	8"	6"		
1475	Edge Cracking	4'	6"		
1589	Longitudinal Crack	31'	0.0625		≈ 12"from SH
1722	Edge Cracking	2"	6"		

Dist	Desc	Length	Width	Depth	Notes
Test Section 17▼					
Test Section 18▼					
Test Section 19▼					
1009	Edge Cracking	14.3'	6"		
Test Section 20▼					
Test Section 21▼					
Test Section 22▼					
Test Section 23▼					
Test Section 24▼					
Test Section 25▼					
Test Section 26▼					
Test Section 27▼					
Test Section 28▼					
Test Section 29▼					
Test Section 30▼					
Test Section 31▼					
Test Section 32▼					

SH 6

A.2.2 November 2006

There is no significant change in the road condition from the first survey. All of the distress noticed on the previous survey was still present and had not increased in severity.

Table A.2: Survey Data from November, 2006

FM 362										
Dist	**Desc**	**Lgth**	**Width**	**Depth**	**Notes**	**Dist**	**Desc**	**Lgth**	**Width**	**Depth**	**Notes**
Test Section 1▼						**Test Section 17▼**					
0	Edge Cracking	321	6"			**Test Section 18▼**					
Test Section2▼											
641	Sign - Warning for Stop Sign					**Test Section 19▼**					
Test Section 3▼											
Test Section 4▼						**Test Section 20▼**					
1395	Diagonal Crack	6'	0.125		Starts at Shoulder						
1738	Edge Cracking	15'	10"			**Test Section 21▼**					
Test Section 5▼											
1883	Sign - Highway Inter					**Test Section 22▼**					
2131	Mailbox # 2837										
2184	Data Logger					**Test Section 23▼**					
2191	Longitudinal Crack	14'	.0125"								
2226	Previous Crack Marking	25'			Crack Not Visible	**Test Section 24▼**					
2248	Longitudinal Crack	14	.125"			**Test Section 25▼**					
Test Section 6 ▼						3224	Data Logger				
Test Section 7▼						3382	Edge Cracking	49'	6"		
2977	Mailbox # 3004					**Test Section 26▼**					
3001	Longitudinal Crack	40'	6-8"		5.5' off E Strip	3661	Data Logger				
Test Section 8▼						3882	Edge Cracking	41"	6"		
3163	Longitudinal Crack	13'	1"		4' 0ff E Strip	**Test Section 27▼**					
3270	Longitudinal Crack	8'	1"		6.5' off E Strip	**Test Section 28▼**					
Test Section 9▼											
3818	Longitudinal Crack	11'	0.25		2.5' from Sh						
Test Section 10▼											
4333	Mailbox # 3252										
Test Section 11▼											
4585	Data Logger										
Test Section 12▼											
5400	End										
Break in Test Sections											
Test Section 13▼						**Test Section 29▼**					
0	Start Marked - 98+00					0	Start Marked 98+00				
203	Edge Crack	6'	.125"		2.5' off E Strip	**Test Section 30▼**					
Test Section 14▼						**Test Section 31▼**					
857	Small Pothole	2"	3"	0.5	≈ 12" in from Sh	**Test Section 32▼**					

875	Small Pothole	1"	1"	0.5	≈ 12" in from Sh	1800	End Marked 80+00
884	Small Pothole	1"	1"	0.5	≈ 12" in from Sh		
Test Section 15▼							
Test Section 16▼							
1357	Longitudinal Crack	28'	0.125				
1409	Longitudinal Crack	8'	.125"		1' off Edge Strip		
1809	End Marked - 80+00						

SH 6

A.2.3 February 2007

During this survey several transverse cracks had starting to form, mostly in test sections 17-28. They were merely hairline cracks at the time of this survey. These cracks extended from the shoulder to the center strip. They was no change in the pre-existing distresses except for one of the previously noticed cracks had disappeared. This was likely due to changes in temperature from when the crack was first noticed.

TableA.3: Survey Data for February, 2007

FM 362

Dist	Desc	Lgth	Wide	Depth	Notes
Test Section 1▼					
0	Start - Marked 221+00				
91.9	Edge Cracking				
429.3	Sign - Camp Allen				
Test Section2▼					
566.3	Mailbox # 2533				
703.7	Sign - Gross Weight				
887.7	Sign				
Test Section 3▼					
Test Section 4▼					
1383.4	Longitudinal Crack	28.1	0.25		18" of Edge Strip
1477.4	Diagonal Crack	4.4	0.25		
1623.9	Mailbox # 2726				
Test Section 5▼					
1852.4	Edge Crack	16.1	0.125		6" off Edge strip
2004.7	Sign - highway intersection				
2147	Transverse Crack	14.5	0.125		SG to CS
2232	Transverse Crack	18.5	0.125		SG to CS
Test Section 6▼					
2267.3	Mailbox #2837				
2320.9	Data Logger				
2364.6	Previous Long Crack				Not Visible
2491.1	Longitudinal Crack	47.3	0.125		3' off edge strip
Test Section 7▼					
Test Section 8▼					
Test Section 17▼					
0	Start - Marked 221+ 00				
Test Section 18▼					
693.8	Sign - Gross Weight				
Test Section 19▼					
Test Section 20▼					
Test Section 21▼					
Test Section 22▼					
Test Section 23▼					
2430.2	Transverse Crack	8'	0.0625		SH to CS
2471	Transverse Crack	8'	0.0625		SH to CS
Test Section 24▼					
2722.5	Transverse Crack	4'	0.0625		SH to CS
2941	Transverse Crack	4'	0.0625		SH to CS
Test Section 25▼					
3182	Transverse Crack	4'	0.0625		SH to CS
3302.1	Transverse Crack	4'	0.0625		SH to CS
3388.9	Data Logger				
3595.3	Longitudinal Crack	19.6'	0.125		4' off edge Strip
3595.3	Transverse Crack	4'	0.125		SH to Edge
Test Section 26▼					
3671.6	Longitudinal Crack	9.5'	0.125		4' off edge Strip
3730	Transverse Crack	4'	0.125		SH to Edge
3857.4	Data Logger				
Test Section 27▼					

3159.2	Mailbox # 3004					**Test Section 28▼**	
3185.8	Longitudinal Crack	40	4"		4-5" off Edge Strip	5654.11	End Marked 167+ 00
Test Section 9▼							
3894.3	Gouge	2'	2"	0.5			
Test Section 10▼							
4311.4	Longitudinal Crack	23.2	0.25		3' off edge strip		
Test Section 11▼							
4594.9	Mailbox # 3252						
4863.5	Data Logger						
Test Section 12▼							
5561.6	Mailbox # 3394						
5698.1	End Marked 167+00						
Break in Test Sections							
Test Section 13▼						**Test Section 29▼**	
0	Start - Marked 98+ 00					0	Start - Marked 98+00
Test Section 14▼						**Test Section 30▼**	
909	Small Pothole	1"	1"	0.5		769.6	Approx Middle of Large Culvert Geo Grid
937.7	Small Pothole	1"	1"	0.5		**Test Section 31▼**	
937.7	Small Pothole	2"	3"	0.5		1886	End Marked 80+ 00
1128.7	Approx Middle of Large Culvert					**Test Section 32▼**	
Test Section 15▼							
1490.4	Longitudinal Crack	5'	.125"		1' off Edge Strip		
1568.3	Transverse Crack	4'	0.06 25				
1591.8	Transverse Crack	4'	0.06 25				
Test Section 16▼							
1912.7	End - Marked 80+ 00						
SH 6							

A.2.4 May 2007

During this survey more transverse cracks were noticed, primarily forming in test sections 17-28, with the majority of them being in test section 28. Some of the previous transverse cracking was no longer visible, most likely due to changes in the temperature from one survey to the next. The new cracks that formed appeared to be forming in the same manner as the previous ones. These cracks extended from the shoulder and terminated at the center strip.

Table A.4: Survey Data from May 2007

FM 362											
Dist	Desc	Lgth	Wdth	Depth	Notes	Dist	Desc	Lgth	Wdth	Depth	Notes
Test Section 1▼						**Test Section 17▼**					
0	Marked 221+00					0	Marked 221+00				
9	Crack		0.0625		YL to YL (Center Strip)	**Test Section 18▼**					
84	Transverse Crack	15'	.0625		Sh to YL	721	Pothole	3"	2"		2" in From YL
409	Camp Allen Sign					751	Pothole	12"	12"		6" in From YL
Test Section2▼						760	Pothole	3"	4"		6" in From YL
538	Mailbox #2533					786	Pothole	4"	4"		4' in from YL
667	Gross Weight Sign					**Test Section 19▼**					
840	Stop Warning Sign					1147	Transverse Crack	4'	.0625		SH to WL
Test Section 3▼						1209	Survey Marker				
Test Section 4▼						**Test Section 20▼**					
1392	Diagonal Crack	4'	0.325			1578	Transverse Crack	3'	.0625		SH to WL
1514	JCT FM 362 Sign					1646	Transverse Crack	3'	.0625		SH to WL
1528	Mailbox #2726					1661	Transverse Crack	3'	.0625		SH to WL
1740	Edge Cracking	12'	6"			**Test Section 21▼**					
Test Section 5▼						1805	Transverse Crack	2'	.0625		SH to EDGE
2130	Mailbox #2837					**Test Section 22▼**					
2183	Data Logger					2328	Transverse Crack	3'	.0625		SH to WL
2188	Longitudinal Crack	14'			2.5' off WL	2519	Data Logger				
Test Section 6▼						**Test Section 23▼**					
Test Section 7▼						2839	Transverse Crack	4'	.0625		SH to WL
2969	Mailbox # 3004					2919	Survey Marker				
2993	Longitudinal Crack	40'	4"		4' off WL	**Test Section 24▼**					
3069	Longitudinal Crack	18'	.325		3' of WL	**Test Section 25▼**					
Test Section 8▼						3776	Survey Marker				
Test Section 9▼						**Test Section 26▼**					
Test Section 10▼						**Test Section 27▼**					
4202	Longitudinal Crack	4'	.25		2.5' off WL	**Test Section 28▼**					
4323	Mailbox # 3252					5015	Transverse Crack	4'	.0625		SH to WL
Test Section 11▼						5117	Transverse Crack	4'	.0625		SH to WL
4575	Data Logger					5141	Transverse Crack	4'	.0625		SH to WL
Test Section 12▼						5208	Transverse Crack	4'	.0625		SH to WL
5234	Mailbox # 3394					5227	Transverse Crack	4'	.0625		SH to WL
						5253	Transverse Crack	4'	.0625		SH to WL
						5268	Transverse Crack	4'	.0625		SH to WL
						5283	Transverse Crack	4'	.0625		SH to WL
						5307	Transverse Crack	4'	.0625		SH to WL
						5400	Transverse Crack	4'	.0625		SH to WL
Break in Test Sections											
Test Section 13▼						**Test Section 29▼**					
0	Marked 96+00					0	Marked 96+00				
337	Edge Cracking	34'	Various			**Test Section 30▼**					

Test Section 14▼				
853	Pothole	2"	2"	Gouge
853	Pothole	1"	1"	Gouge
853	Pothole	.5"	.5"	Gouge
870	Pothole	2"	2"	Gouge
880	Pothole	1"	1"	Gouge
Test Section 15▼				
Test Section 16▼				
1395	Longitudinal Crack	4'	0.0625	12' off WL
1494	Transverse Crack	3'		SH to WL
1800	End - Marked 80+00			

Test Section 31▼			
1084	Edge Cracking	31	
1192	Pot hole	1"	1"
1382	Edge Cracking	14'	8"
1429	Edge Cracking	5'	10"
Test Section 32▼			
1800	End Marked 80+00		

SH 6

Section No. 1Wa

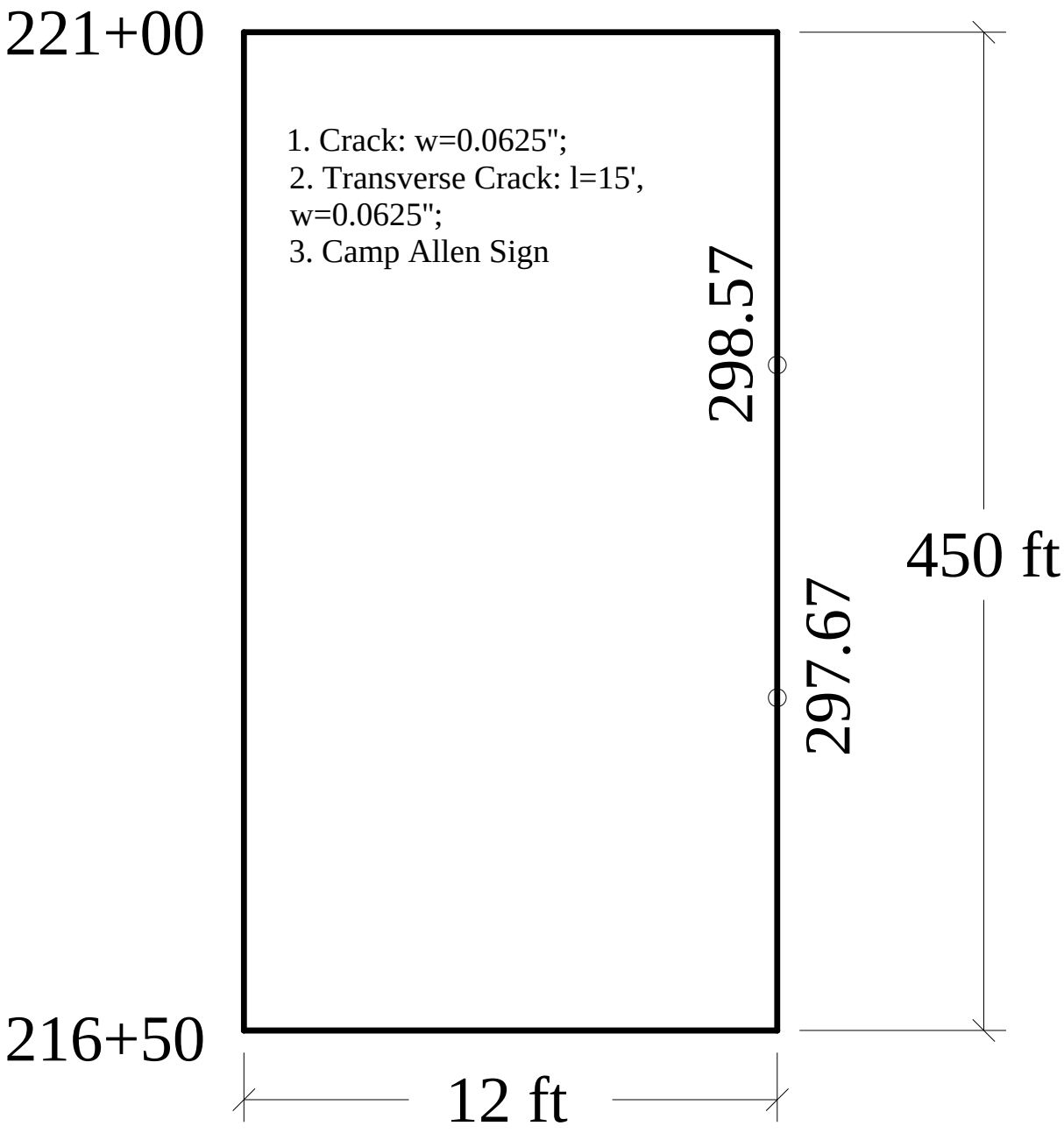

Section No. 2Wa

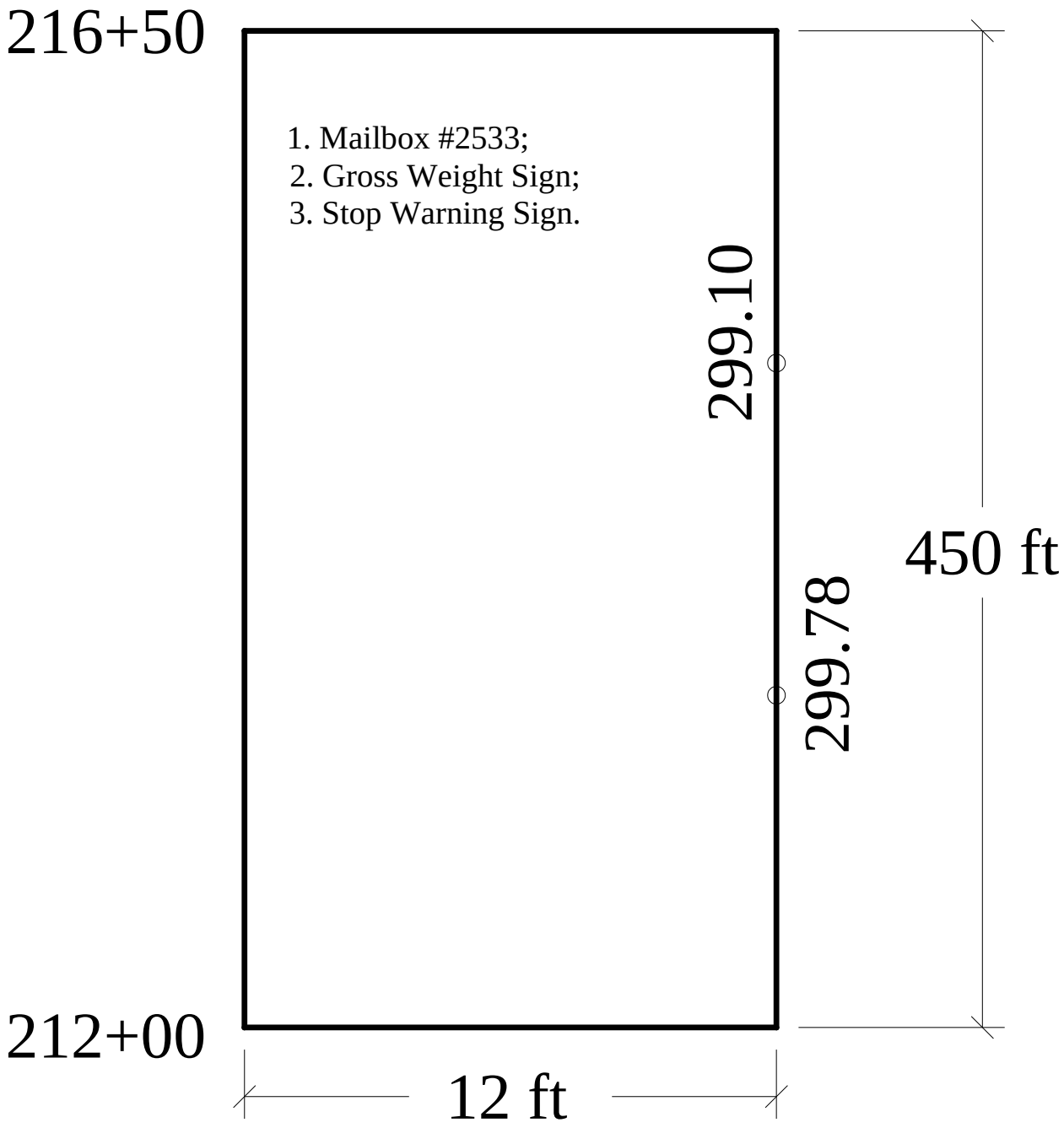

Section No. 3Wa

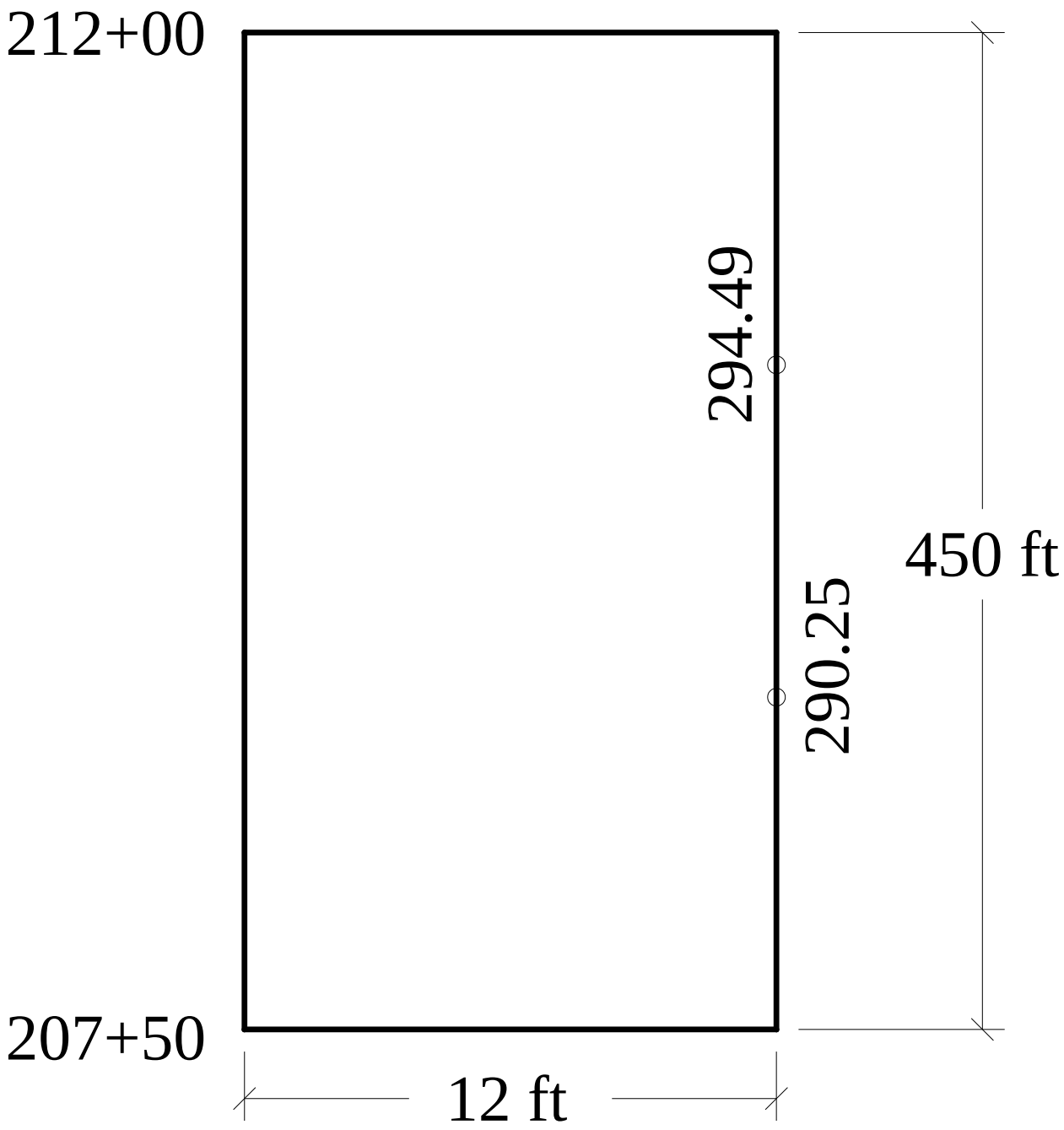

Section No. 4Wa

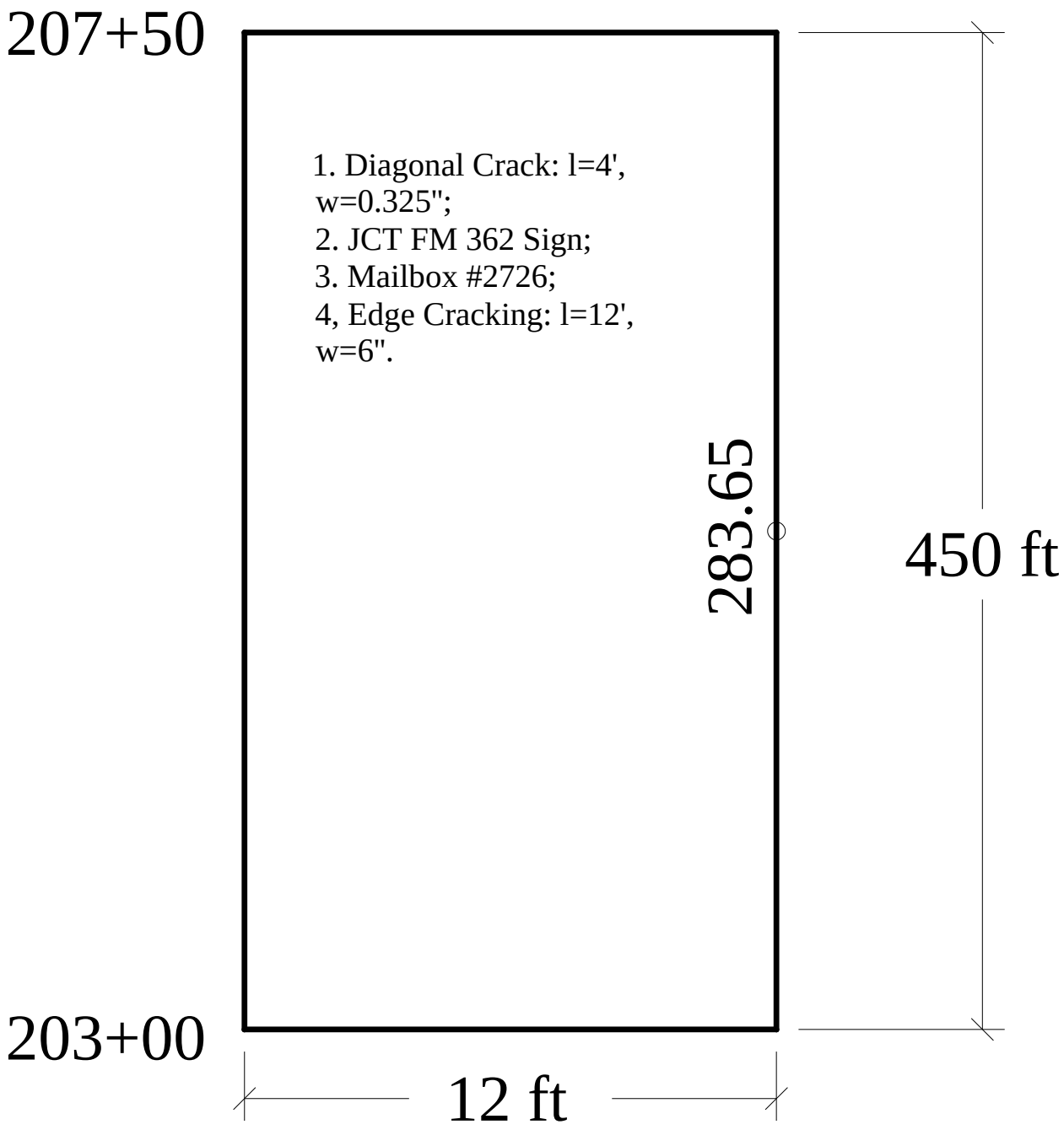

Section No. 5Wa

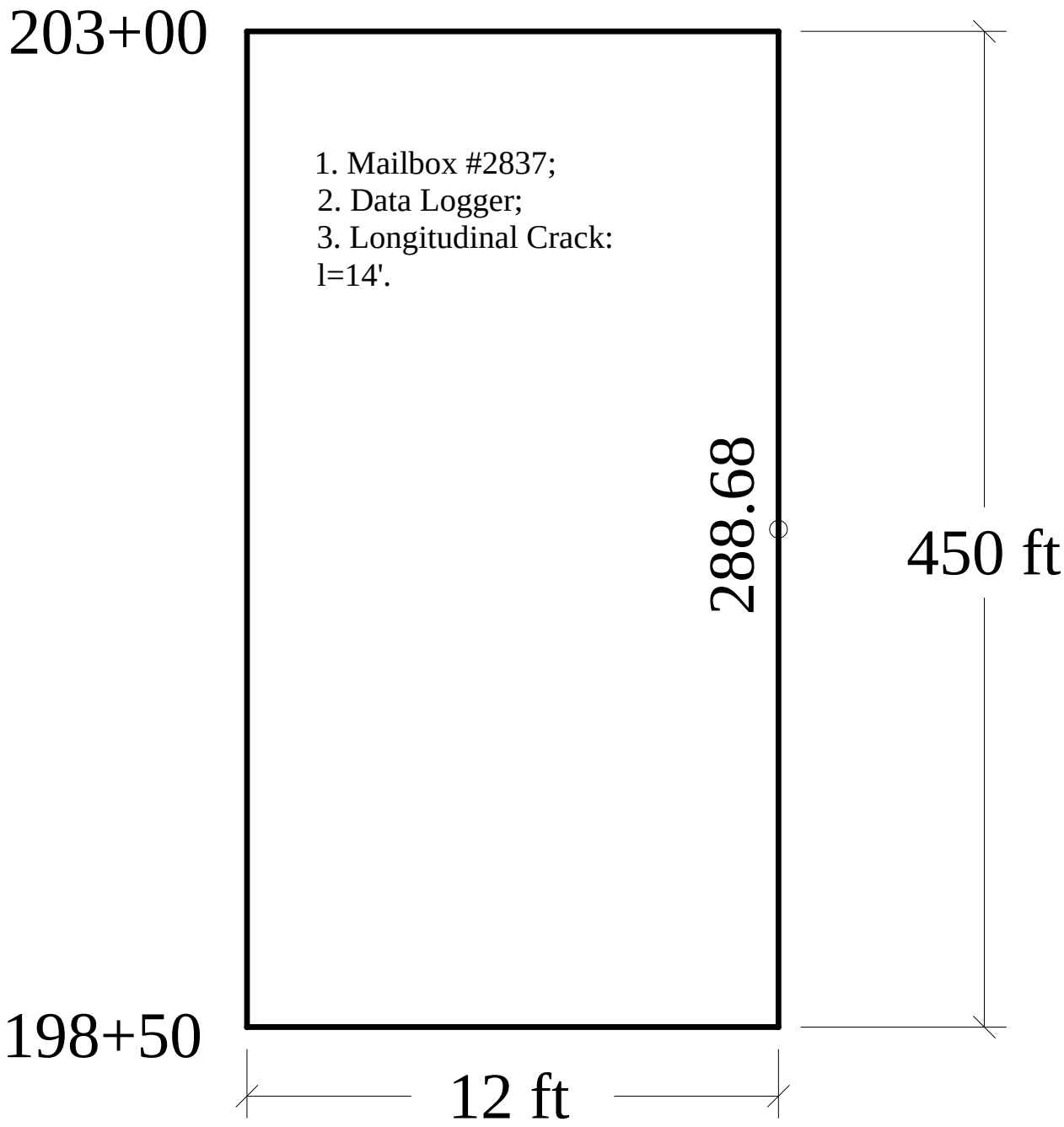

Section No. 6Wa

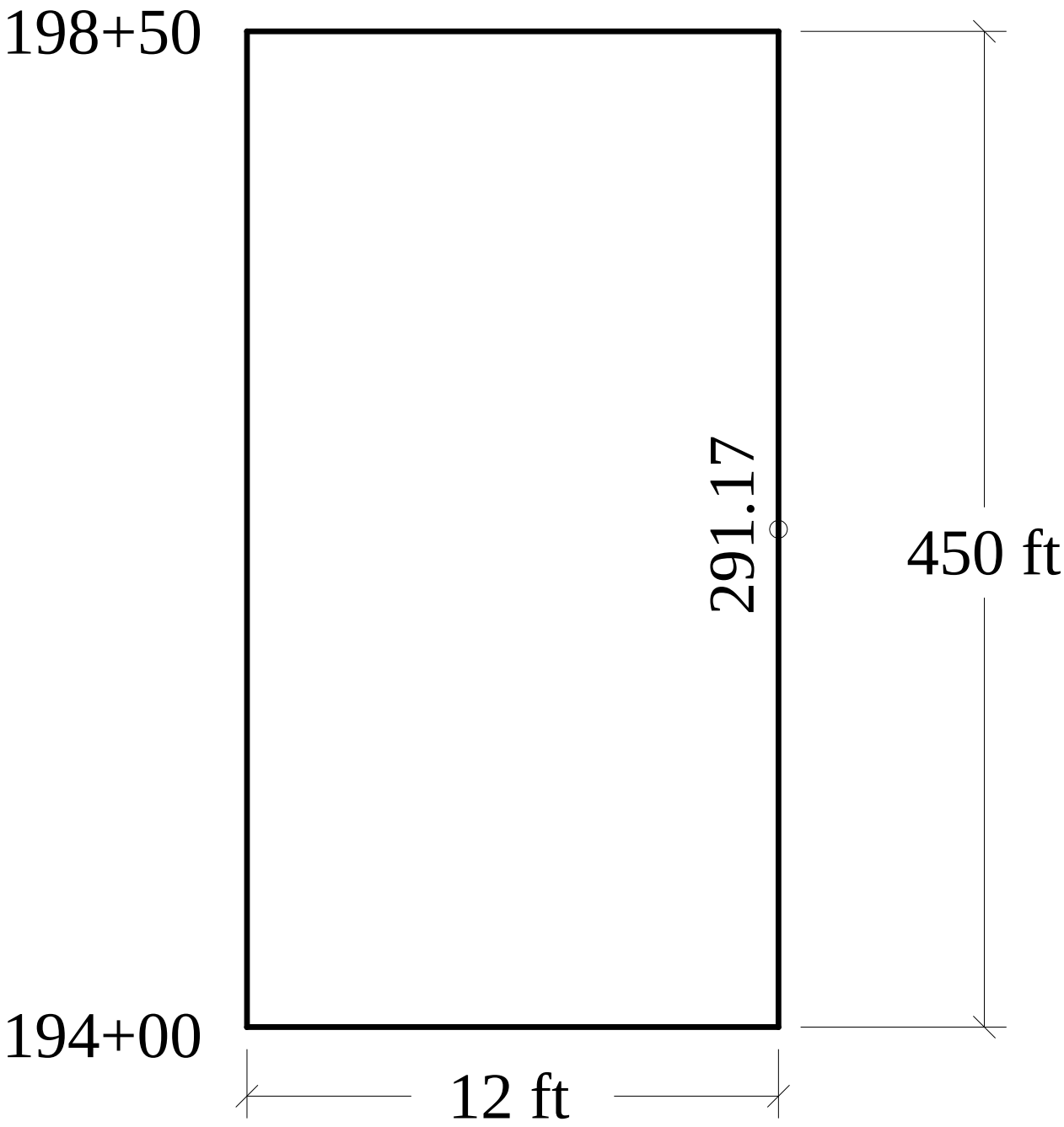

Section No. 7Wa

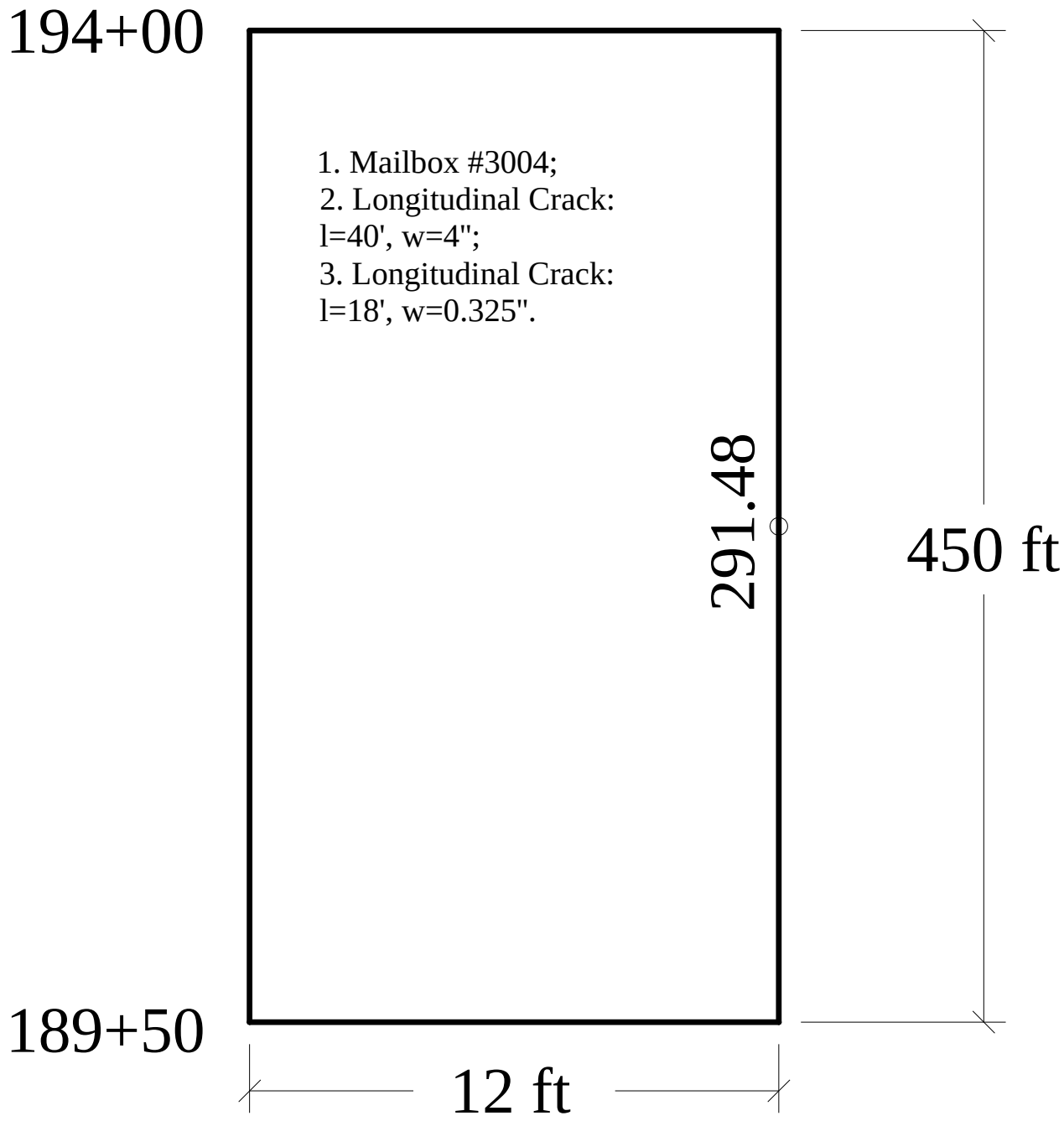

Section No. 8Wa

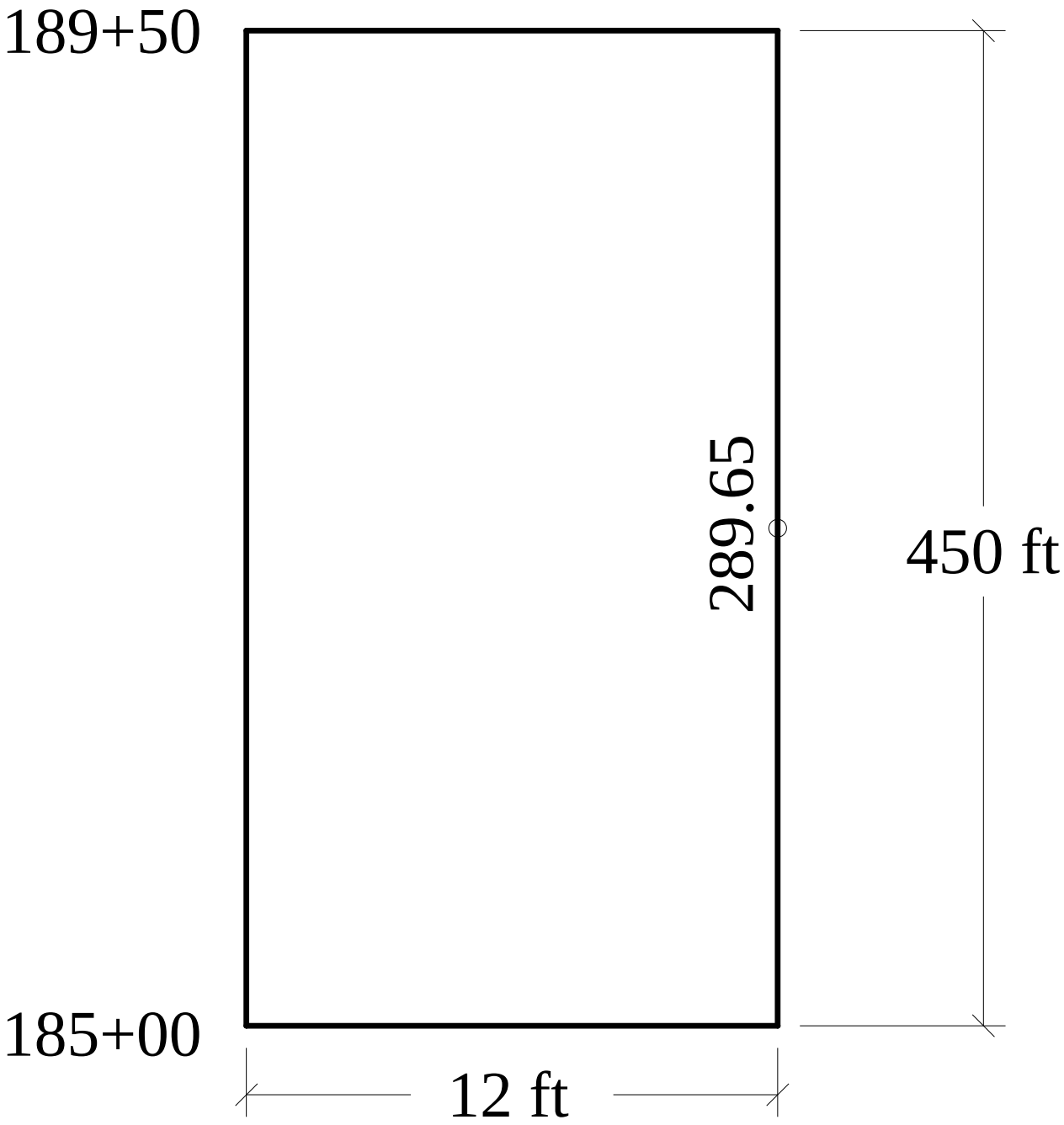

Section No. 1Wb

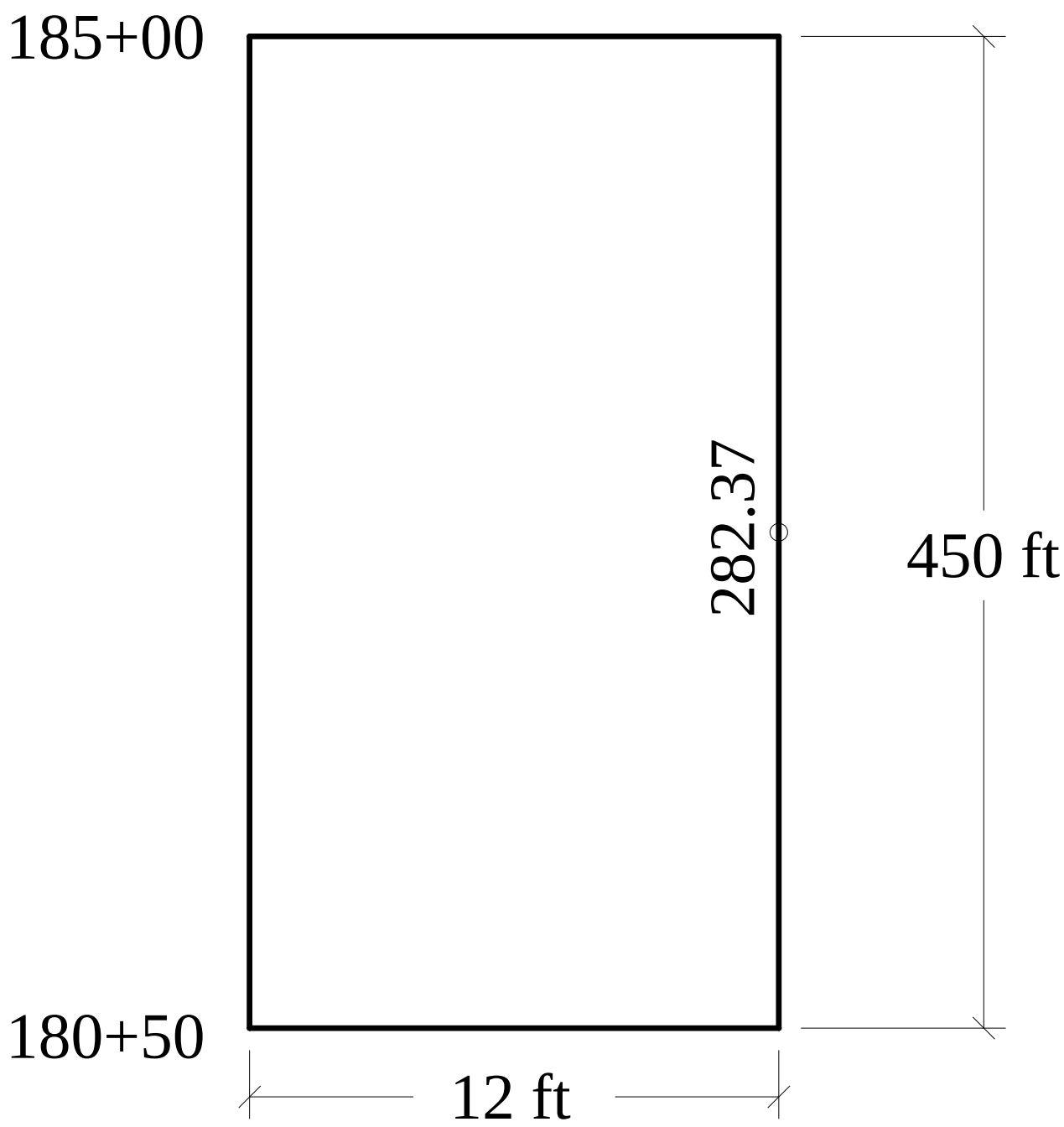

Section No. 2Wb

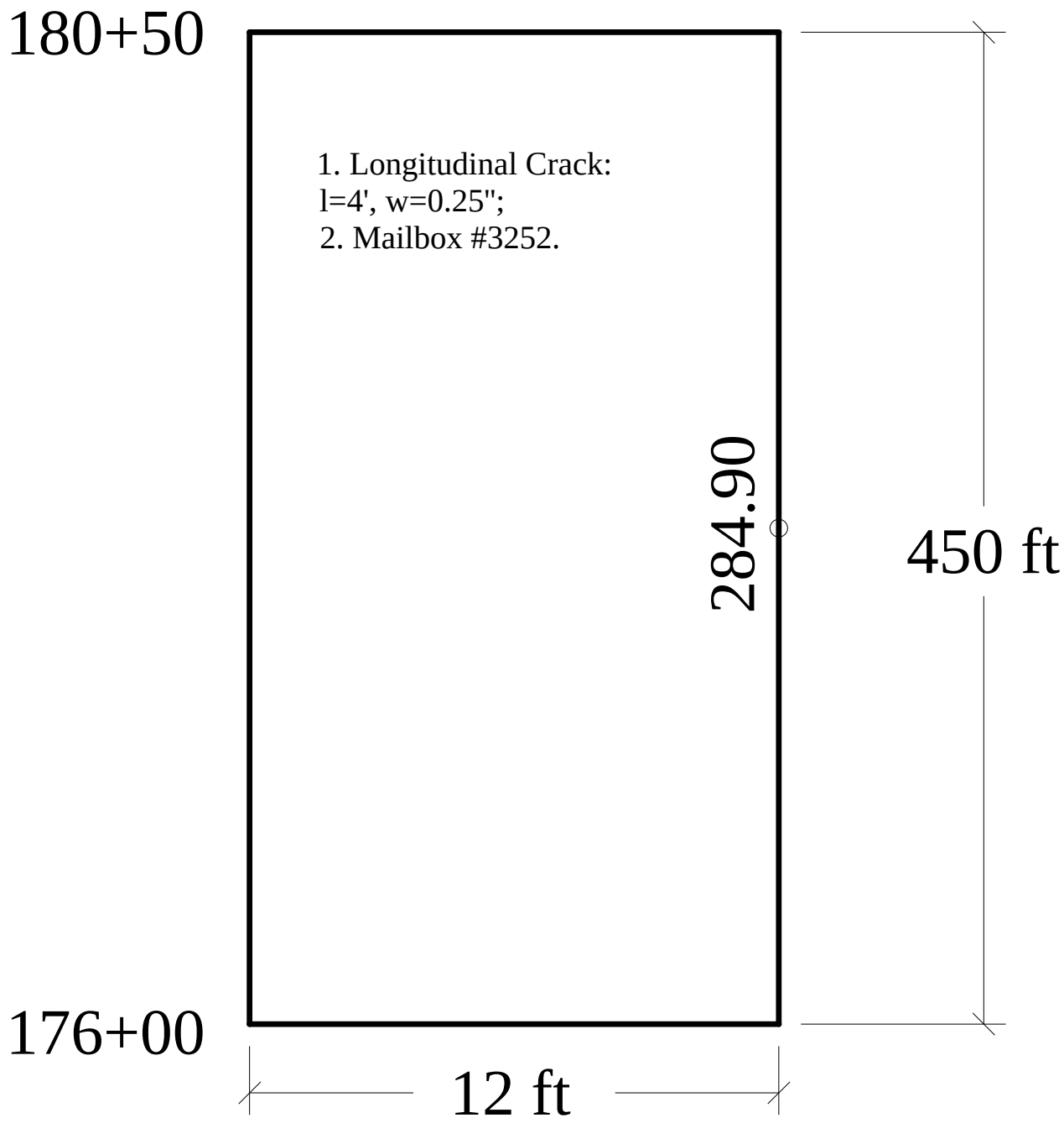

Section No. 3Wb

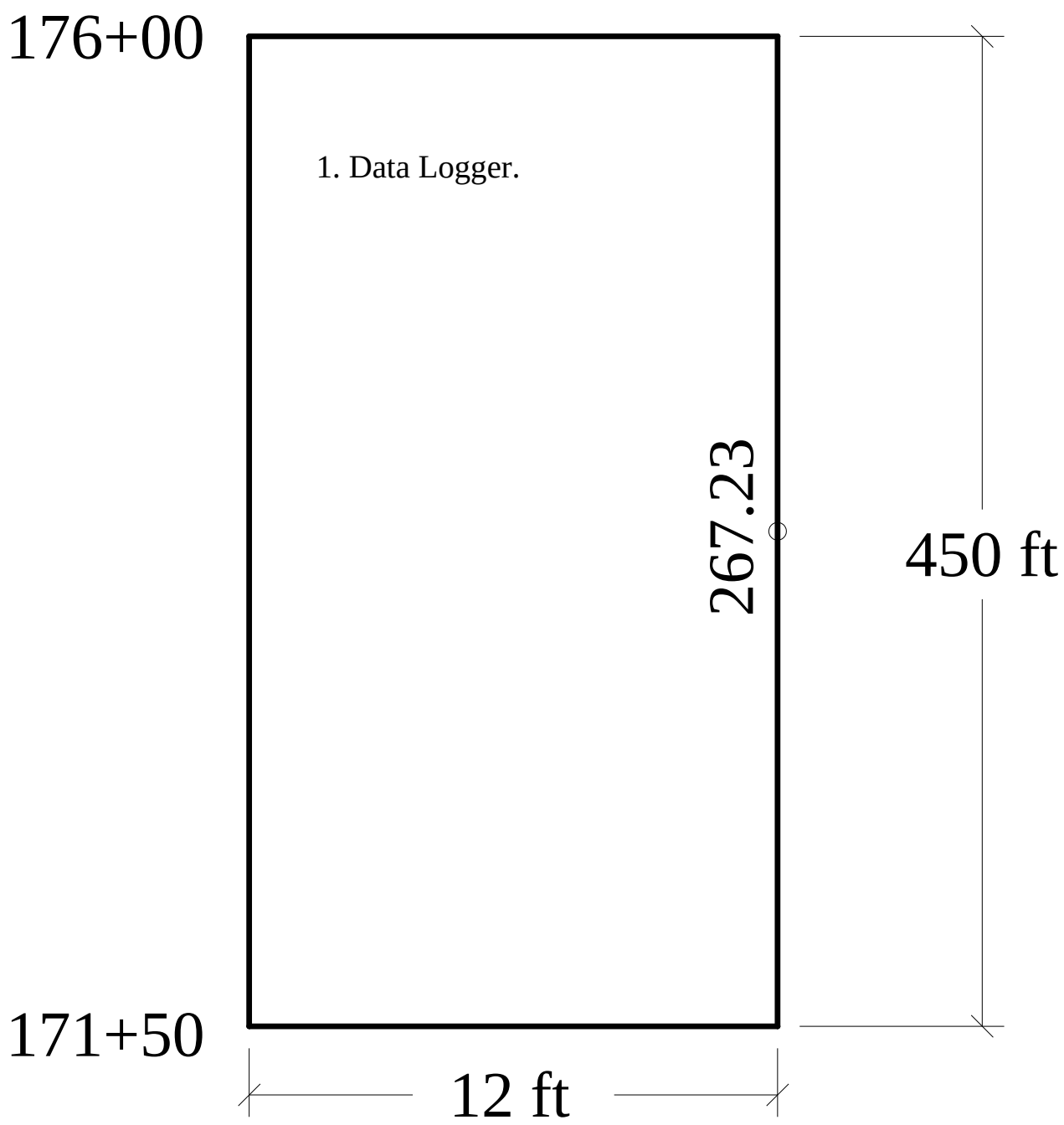

Section No. 4Wb

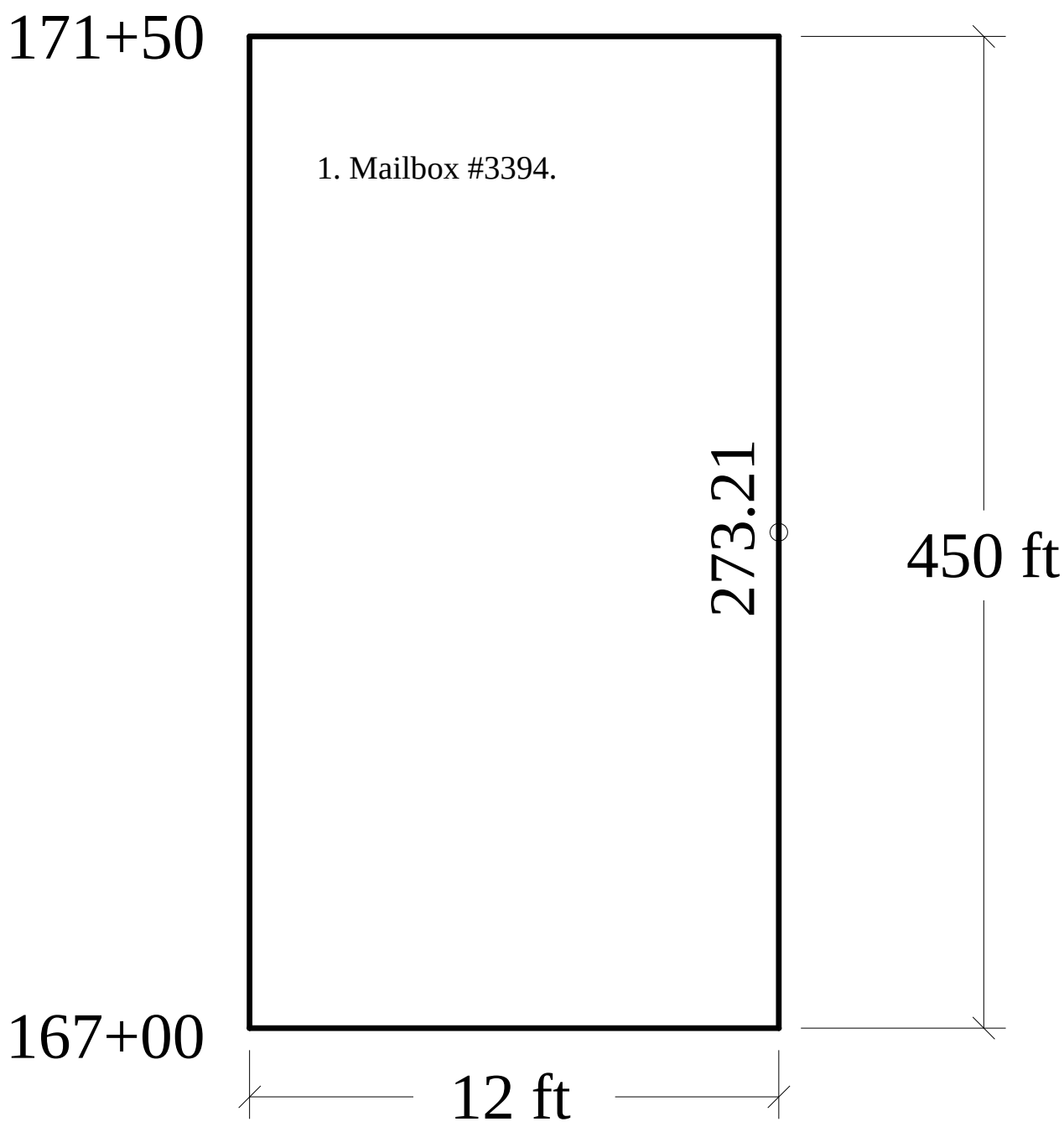

Section No. 5Wb

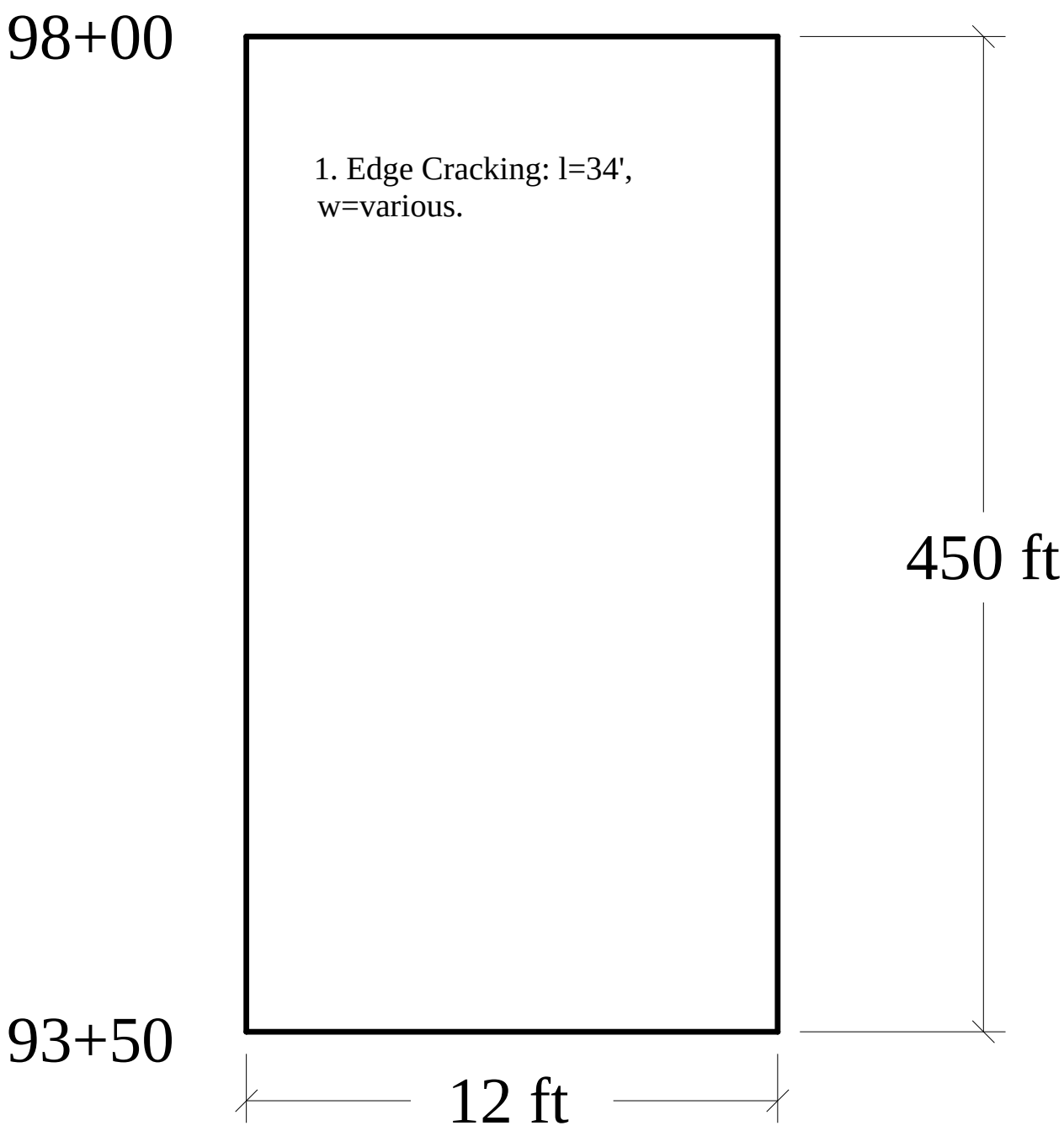

Section No. 6Wb

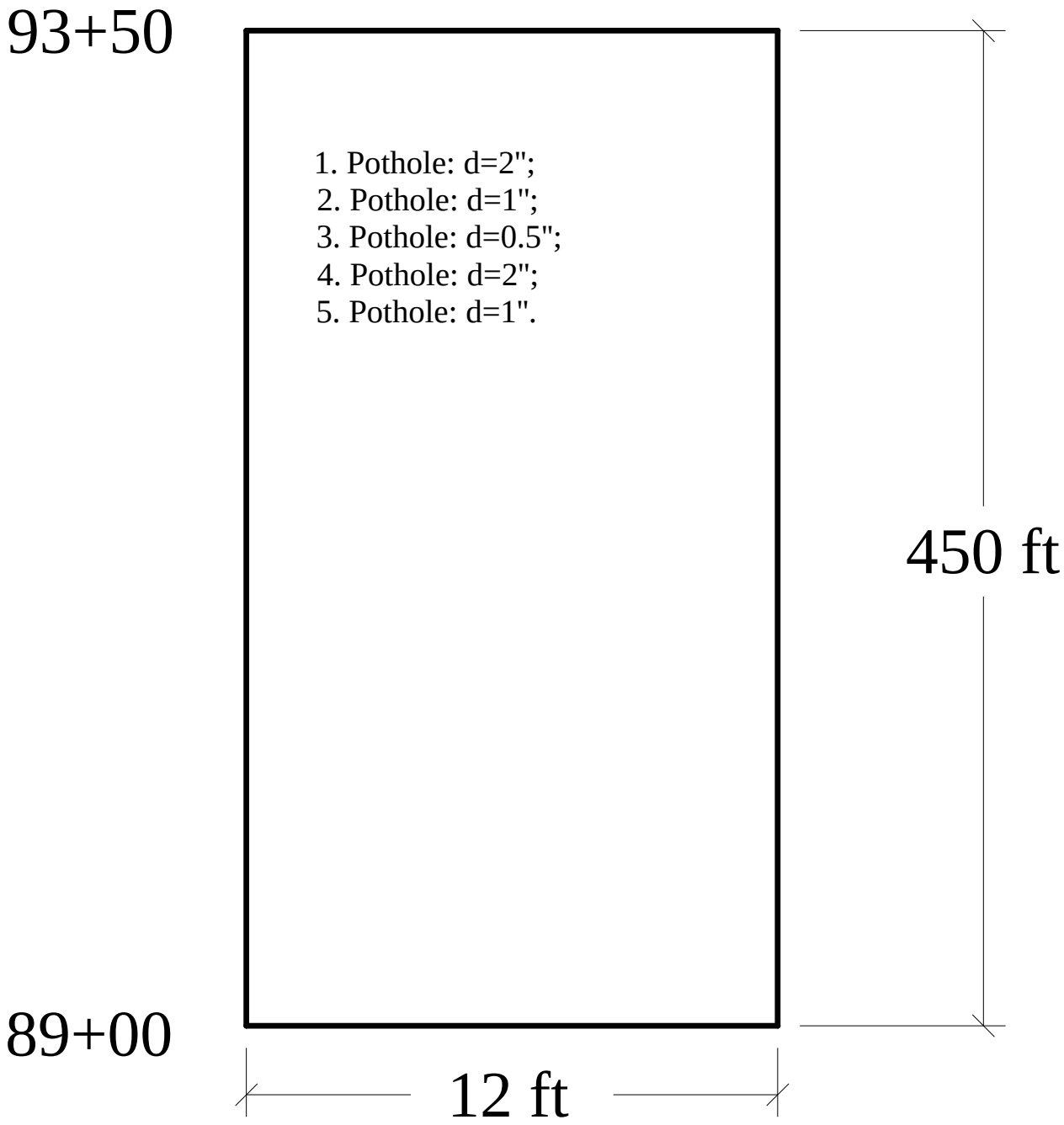

Section No. 7Wb

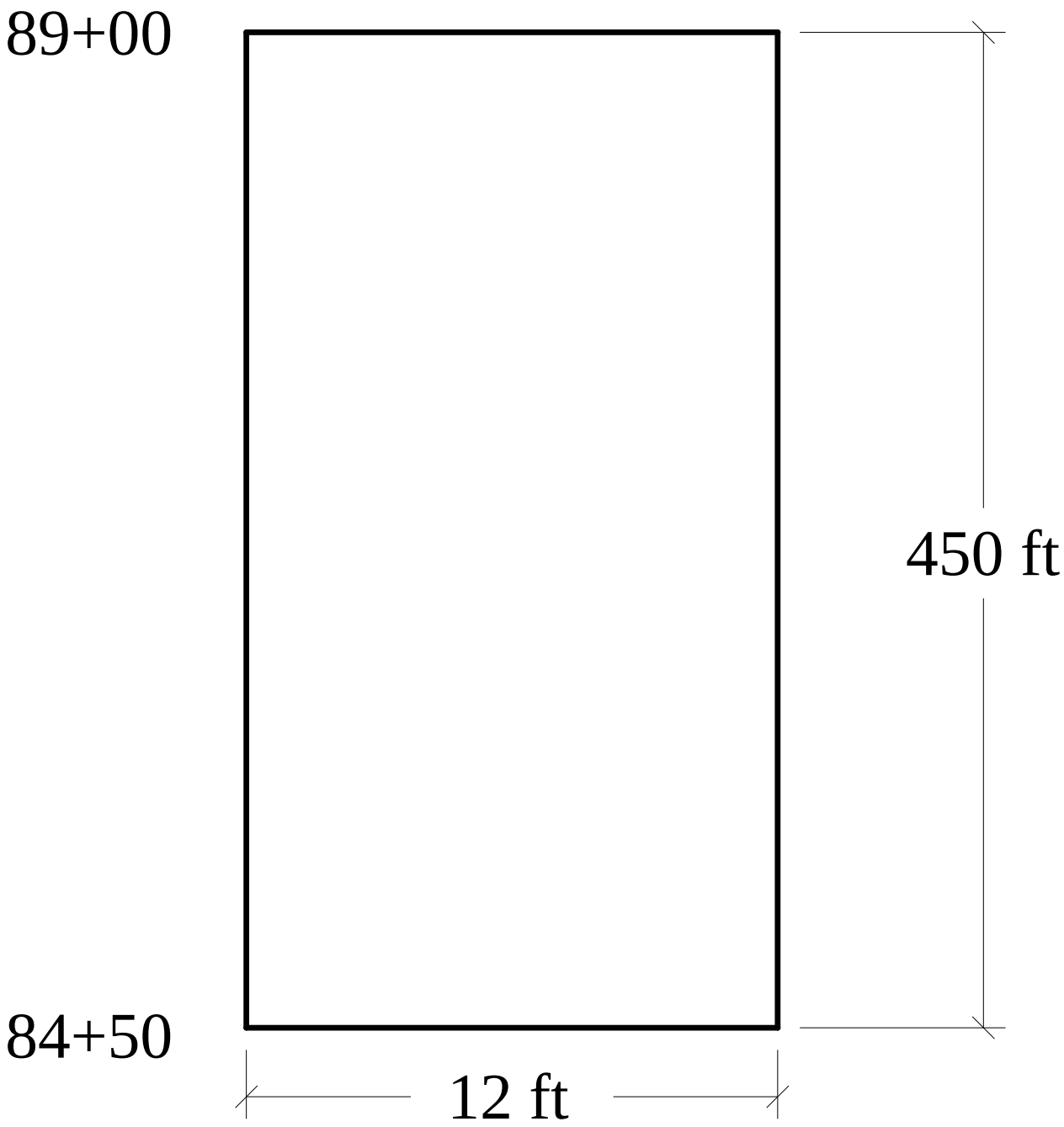

Section No. 8Wb

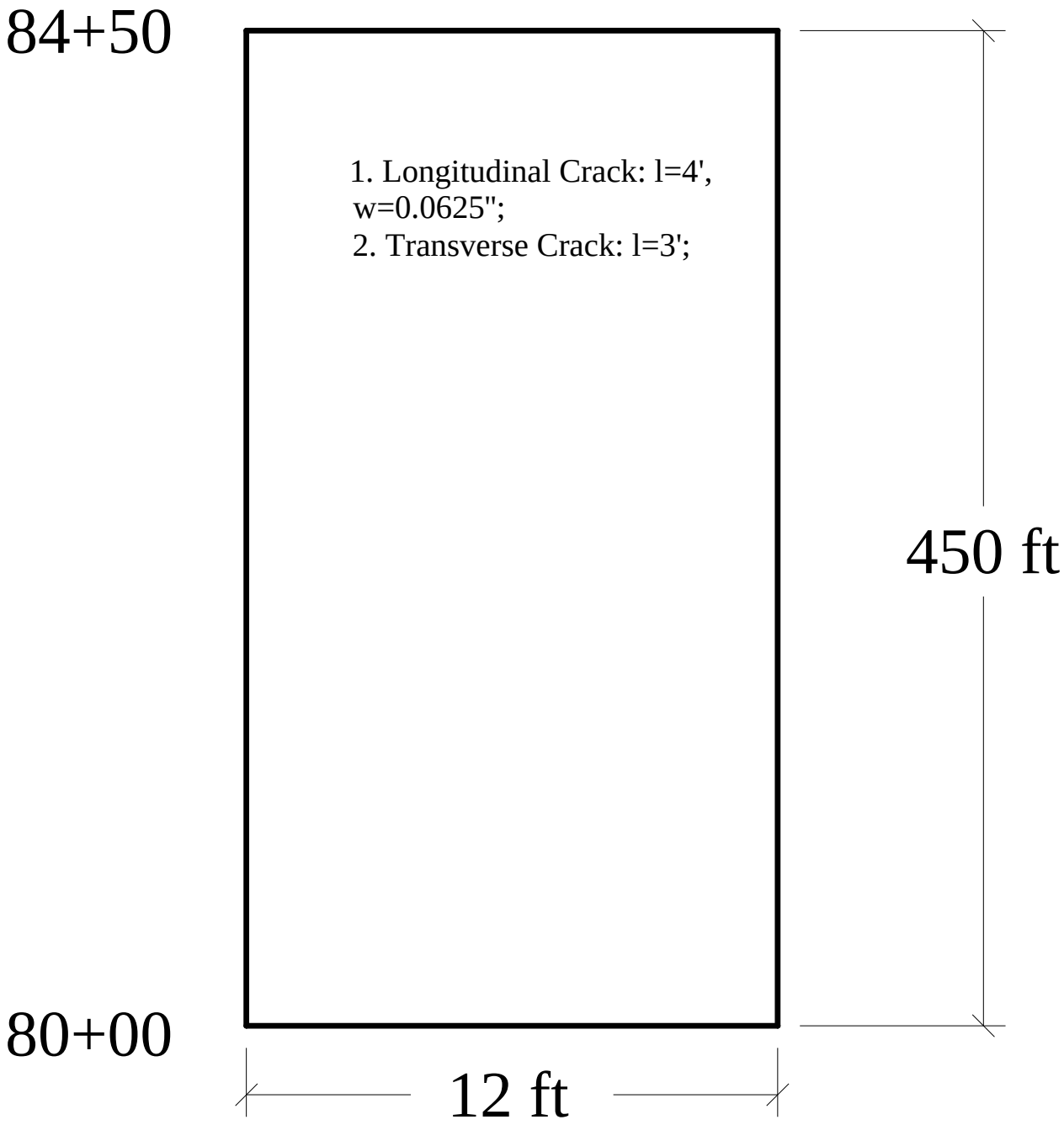

Section No. 2Ea

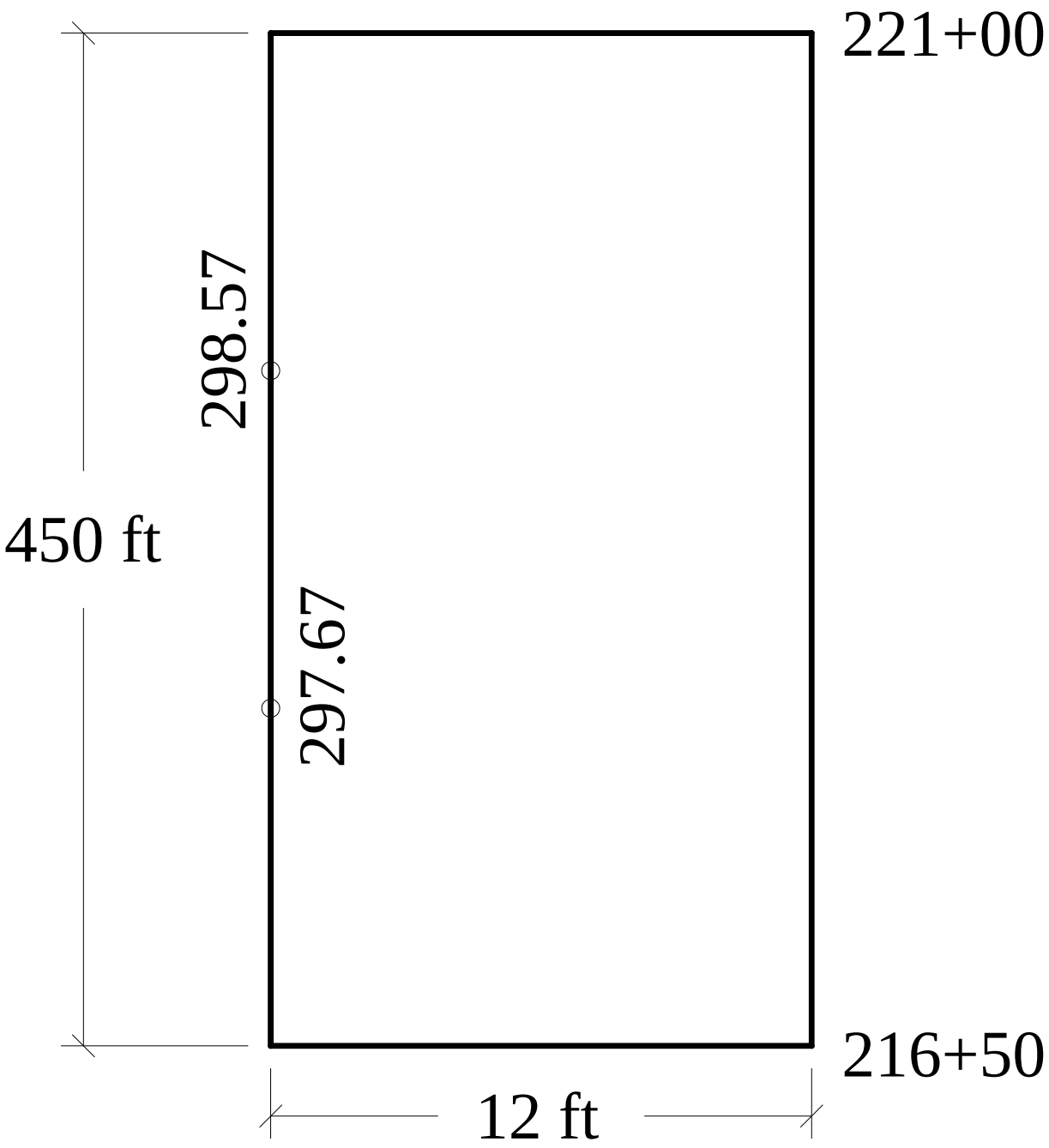

Section No. 3Ea

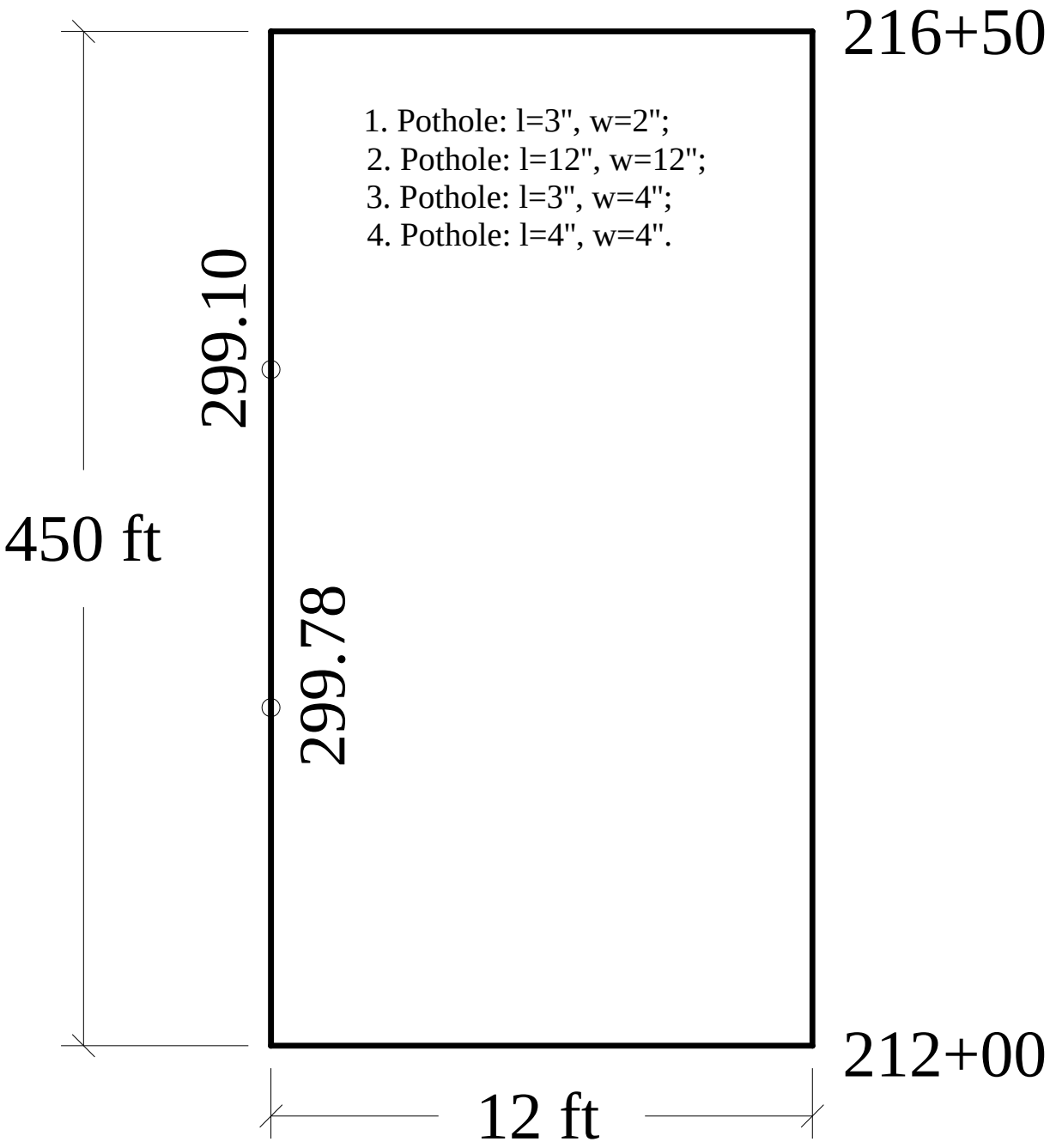

Section No. 4Ea

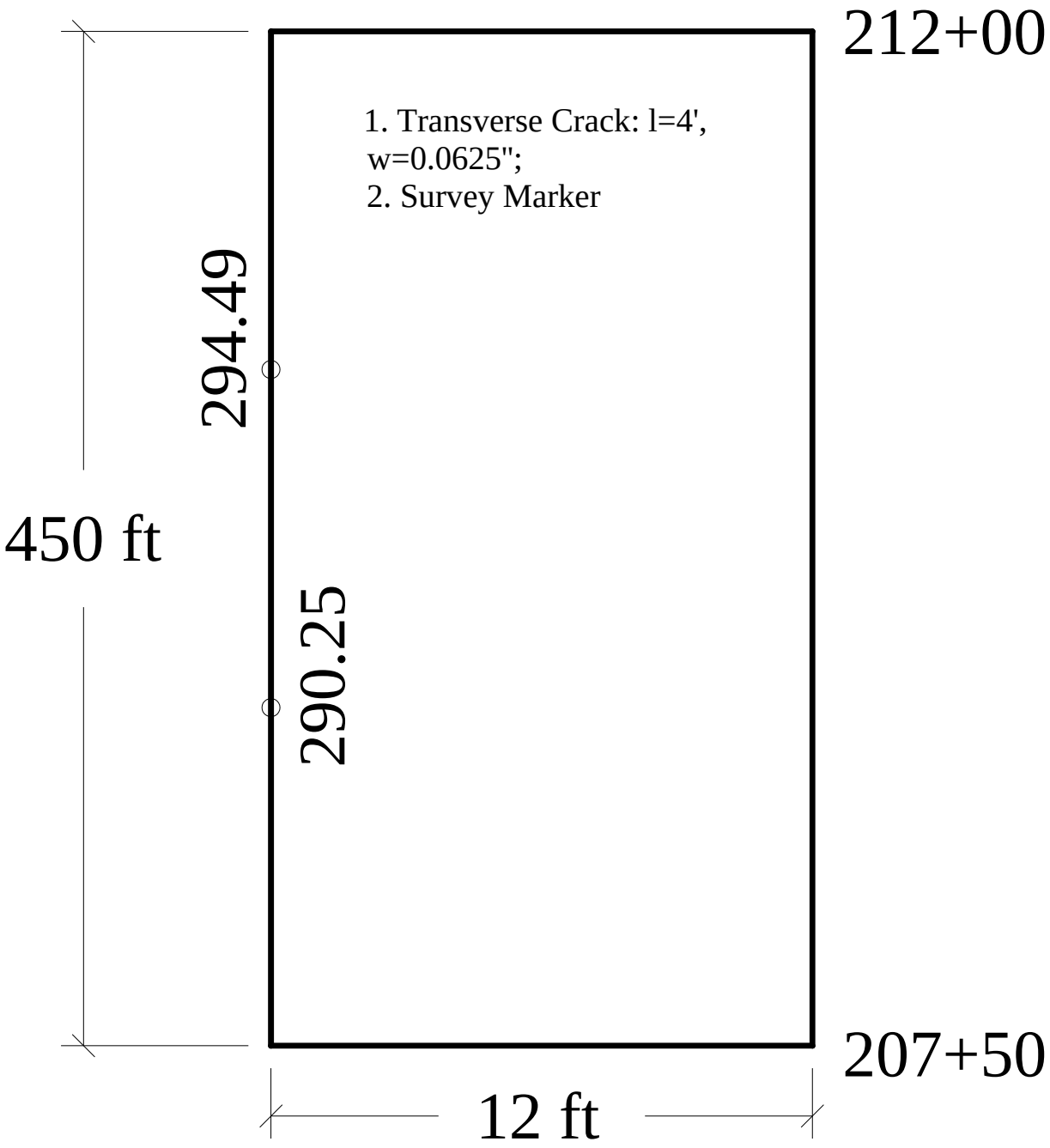

Section No. 1Ea

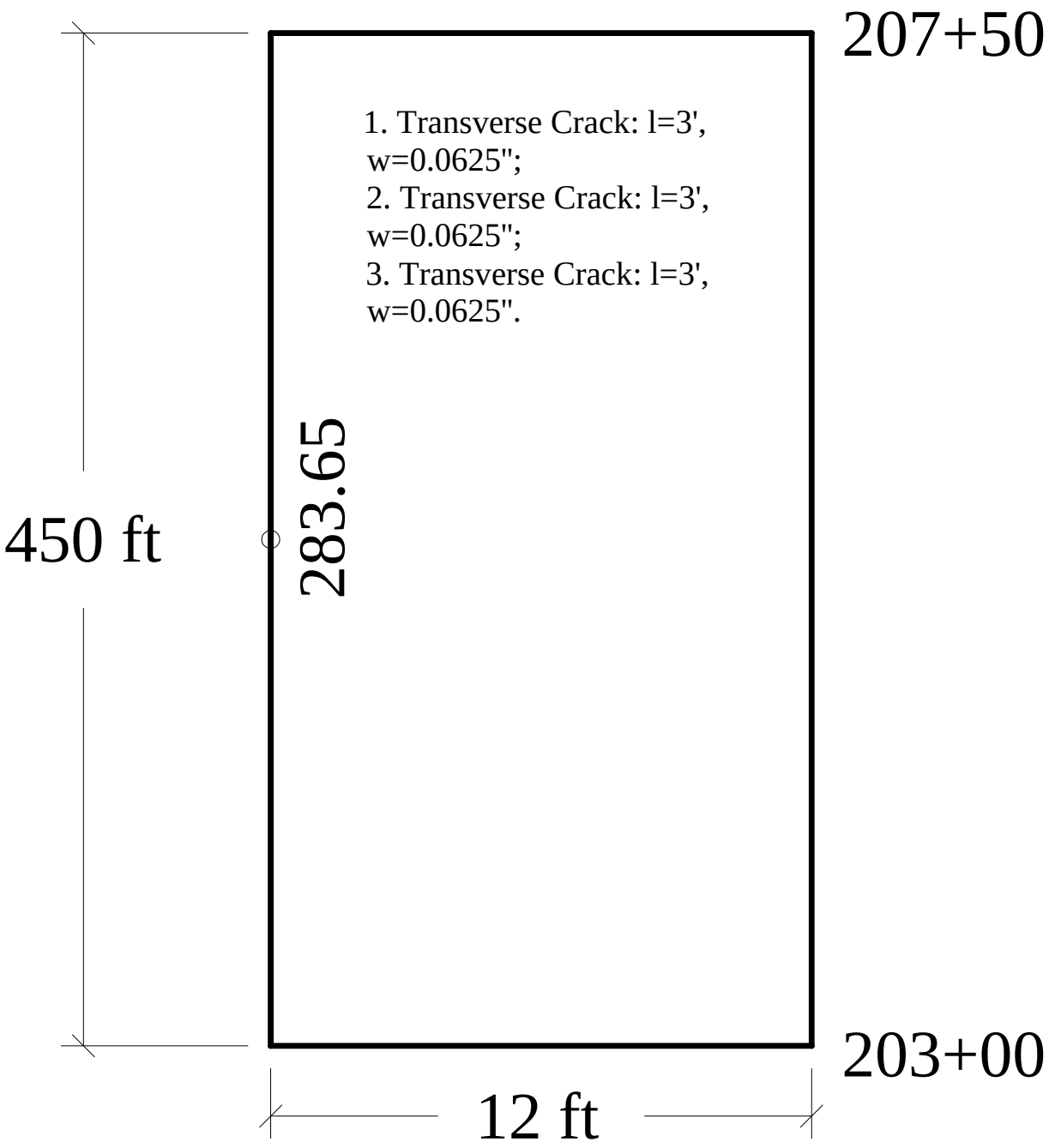

Section No. 6Ea

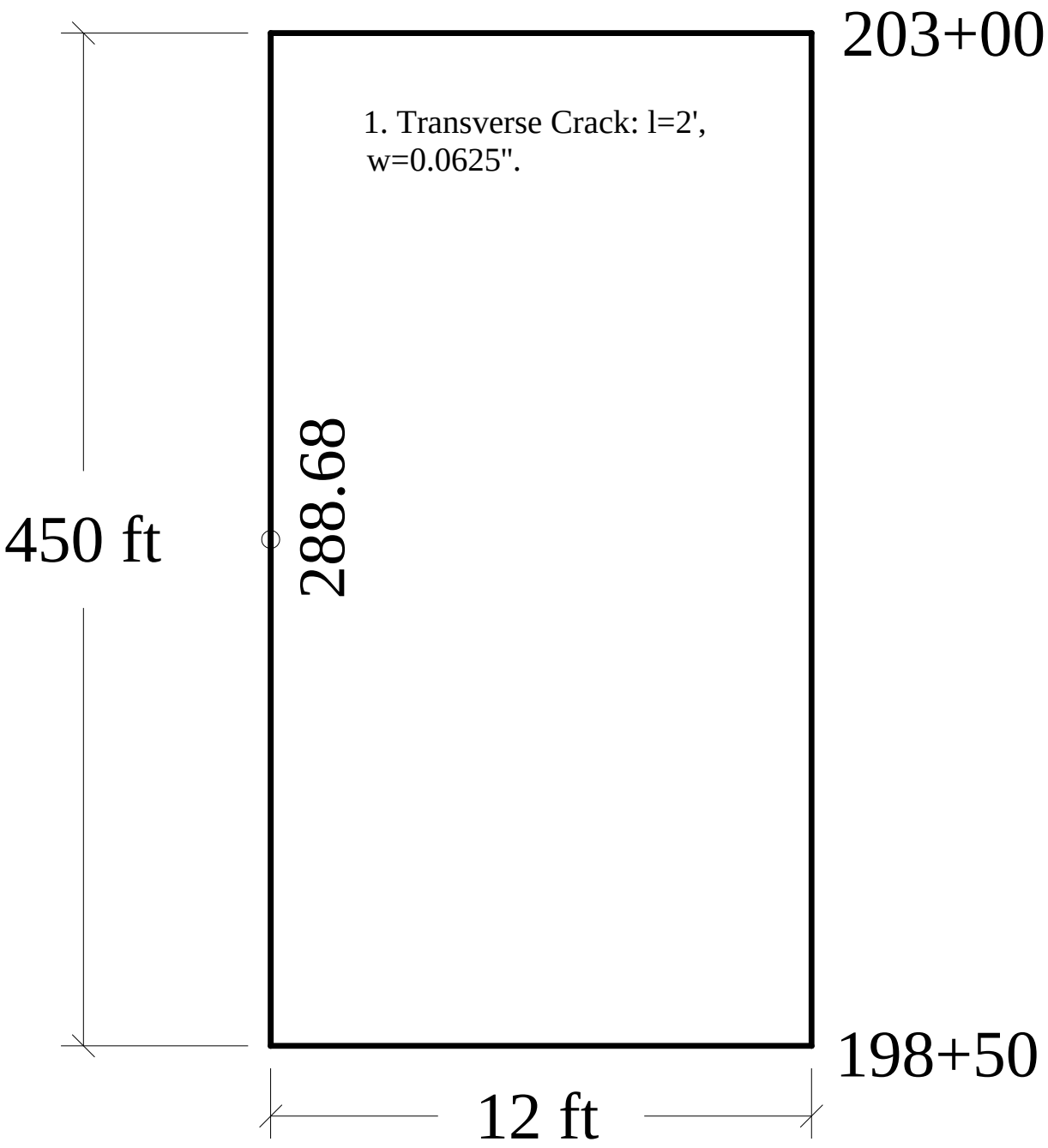

Section No. 7Ea

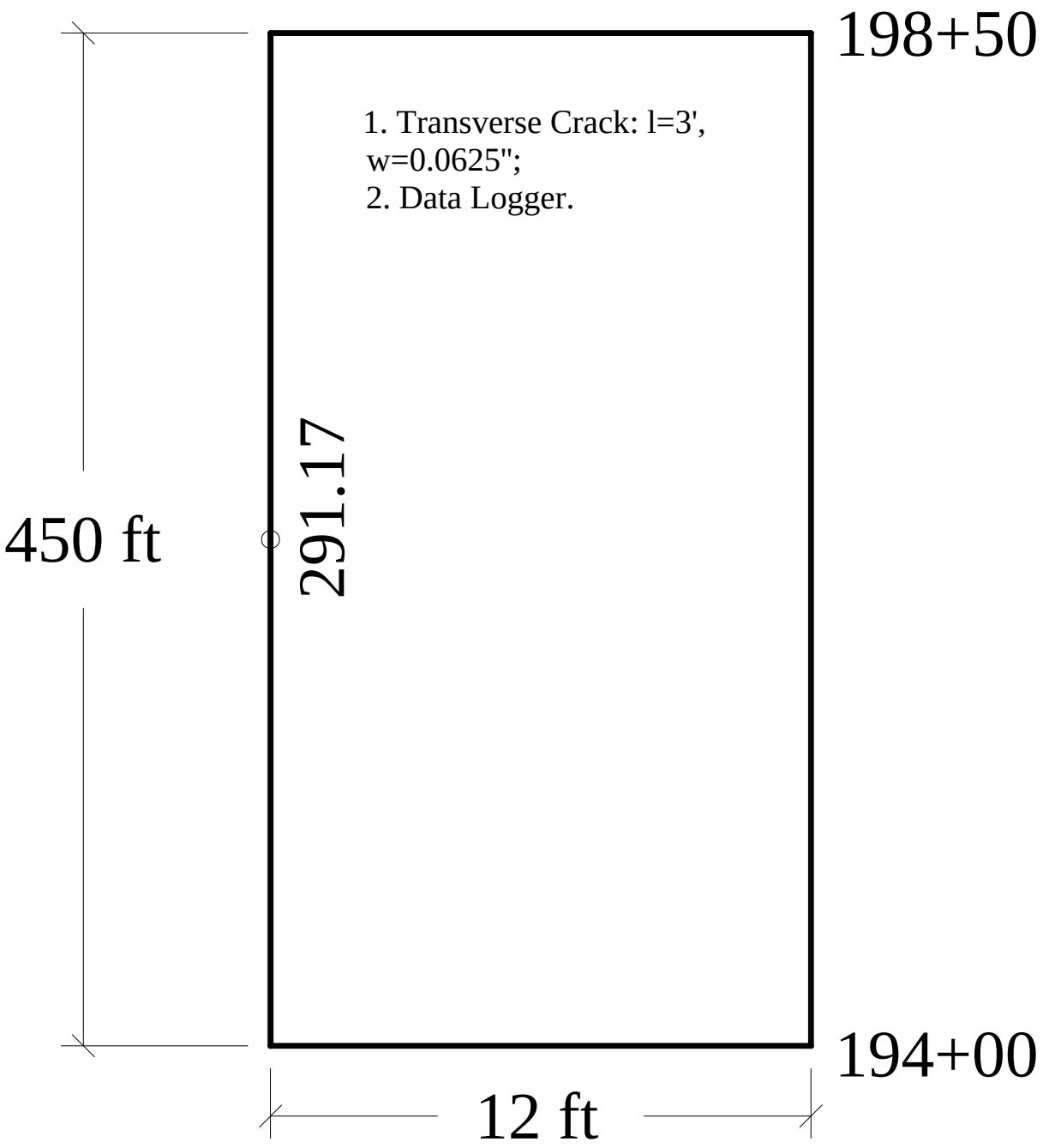

Section No. 8Ea

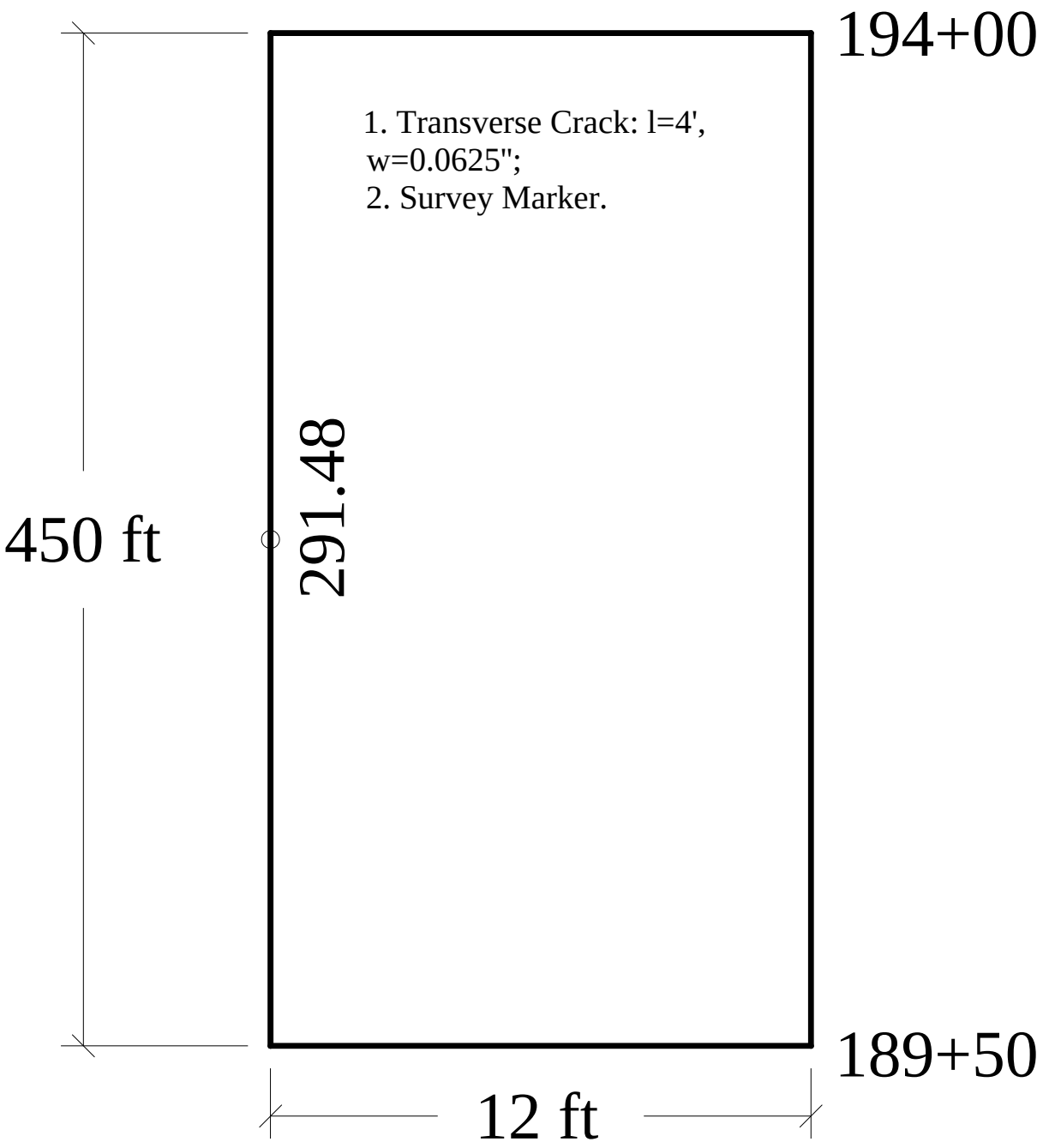

Section No. 5Ea

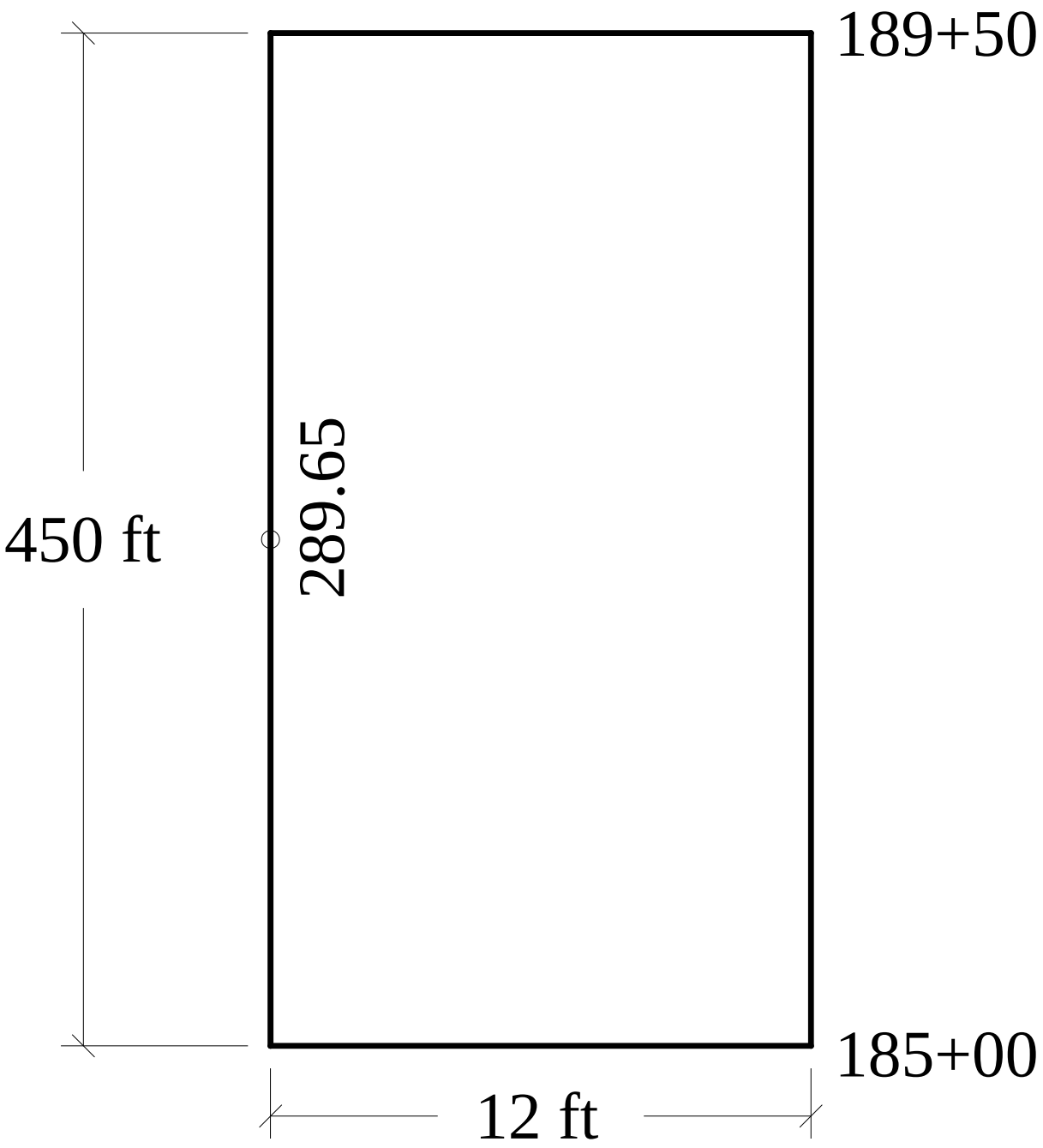

Section No. 3Eb

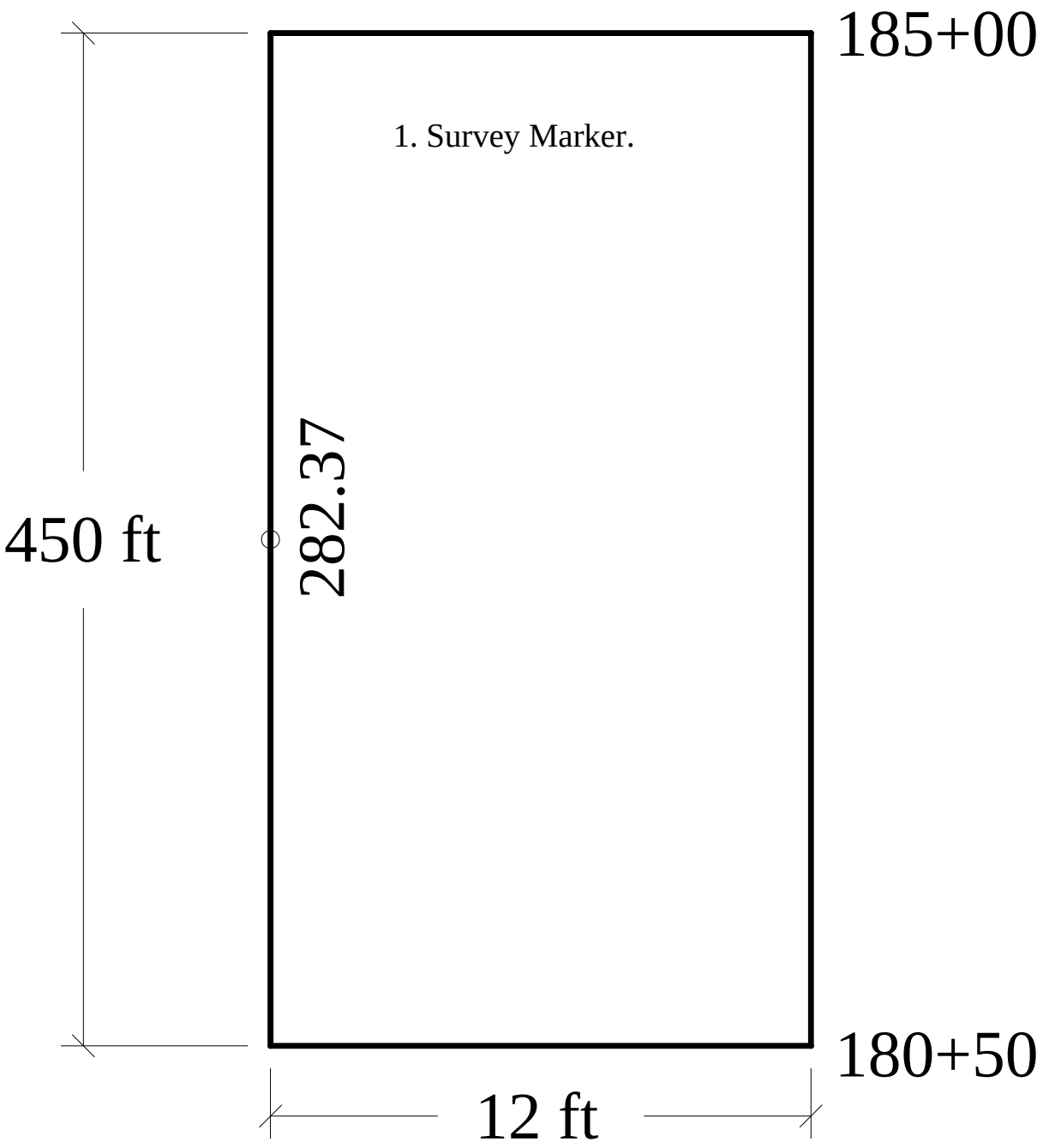

Section No. 4Eb

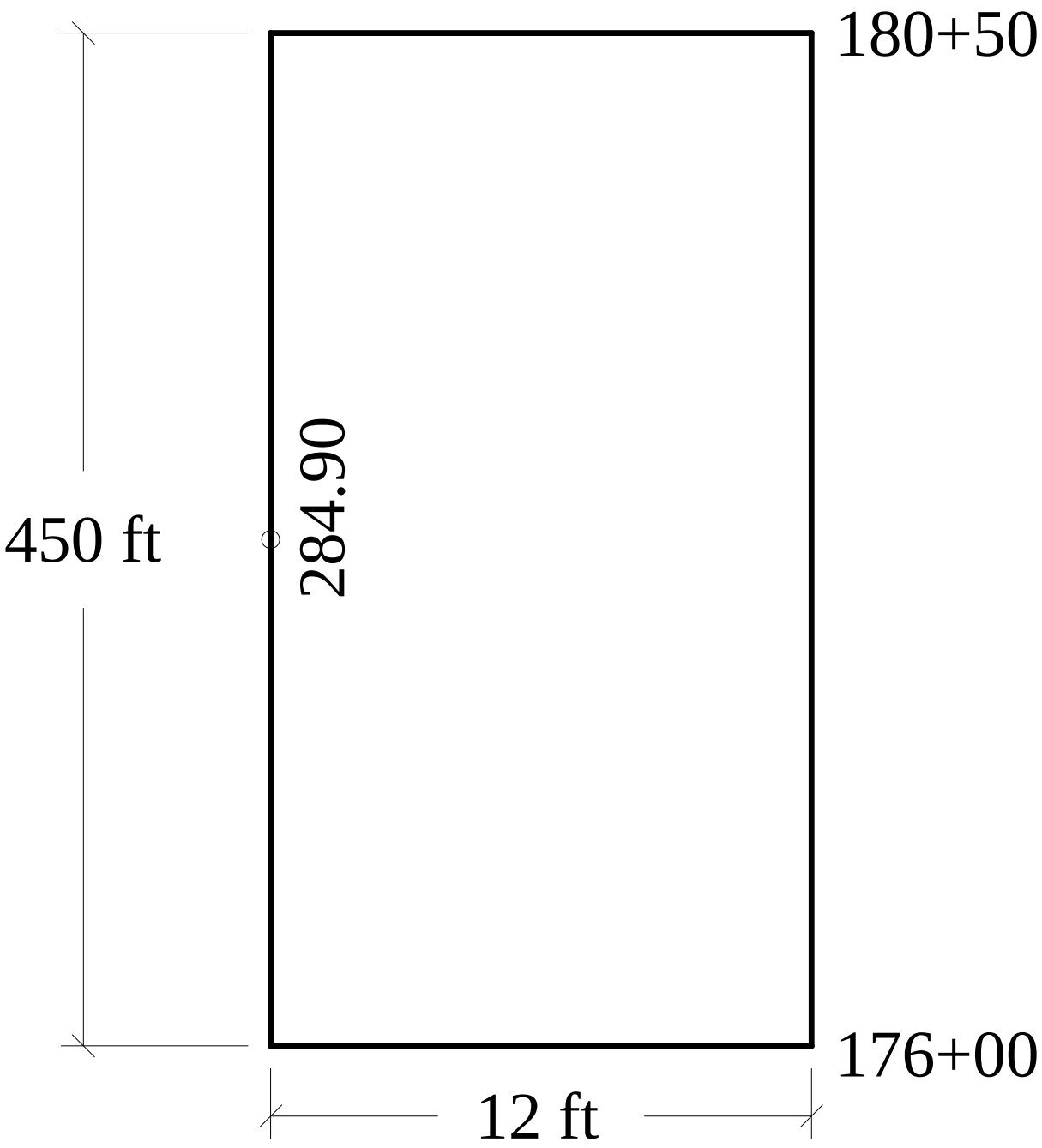

Section No. 1Eb

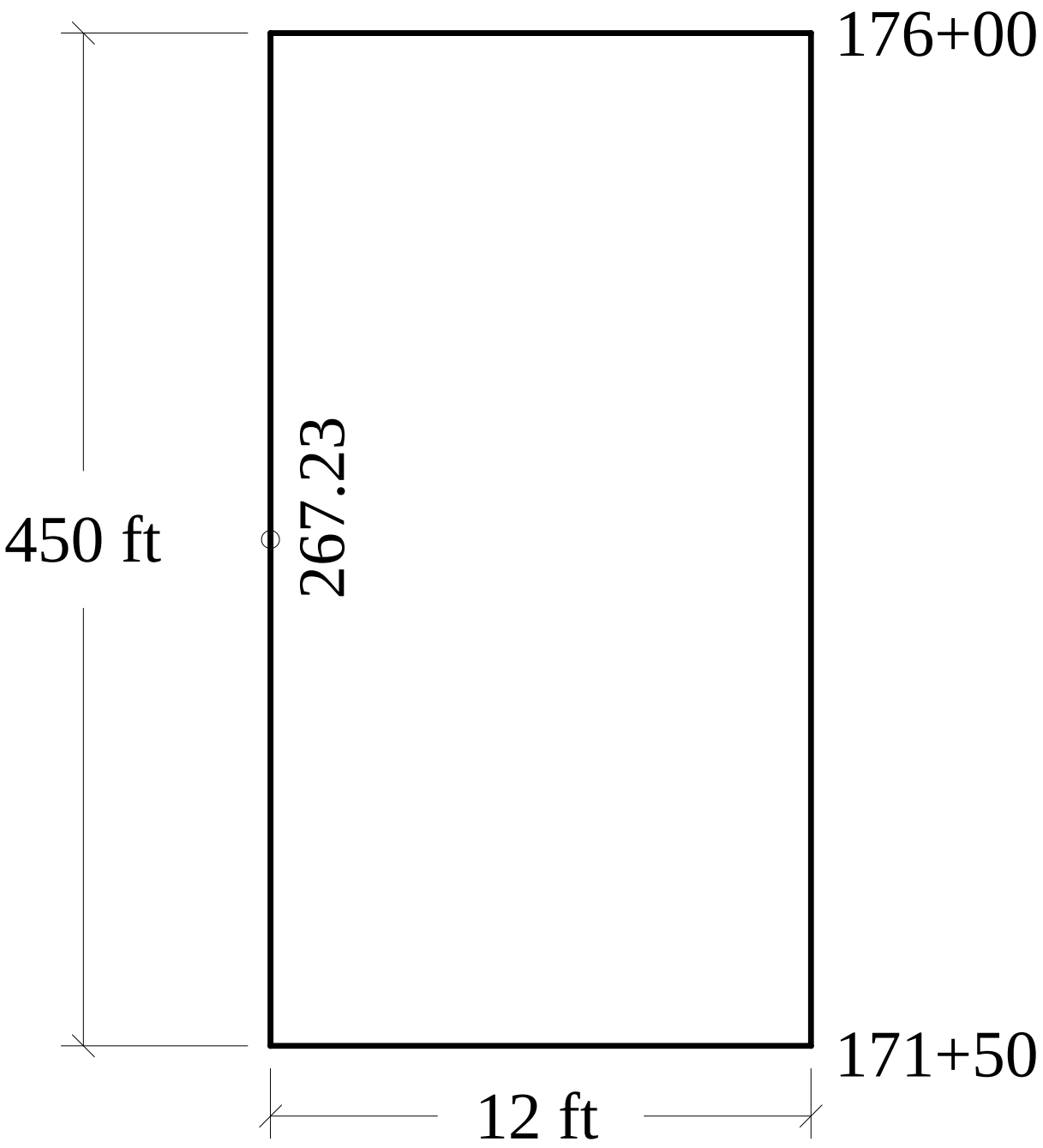

Section No. 2Eb

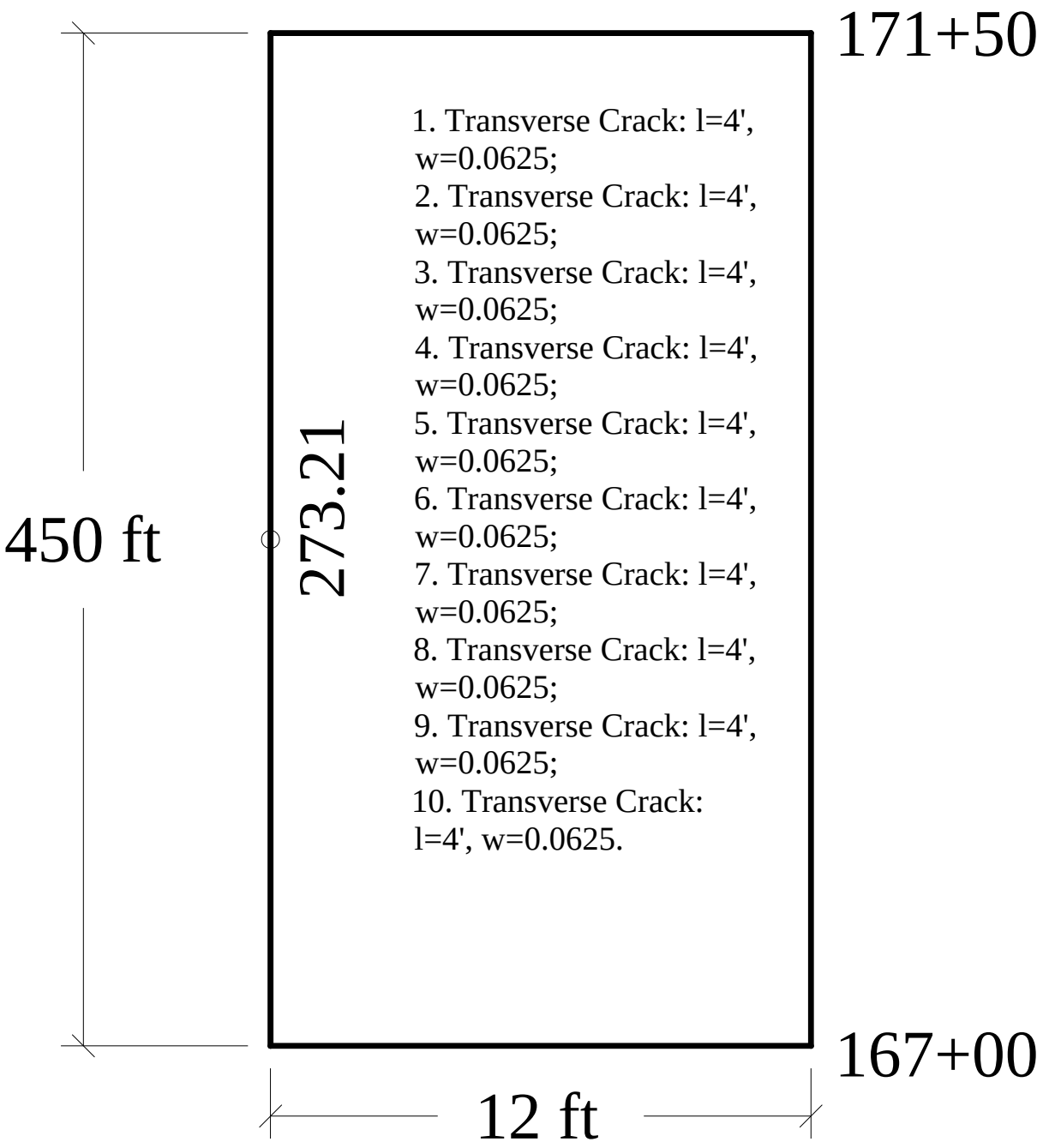

Section No. 7Eb

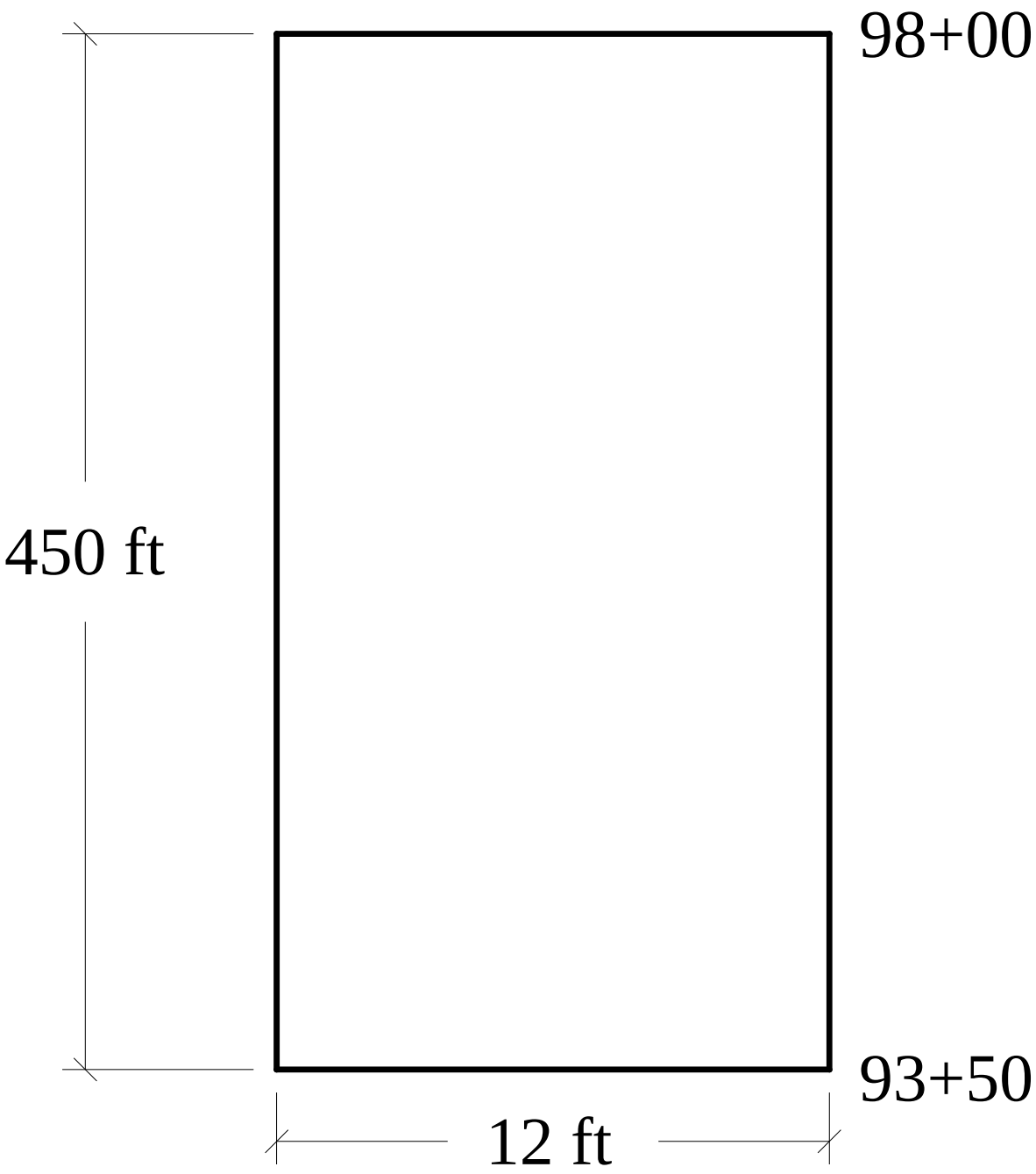

Section No. 8Eb

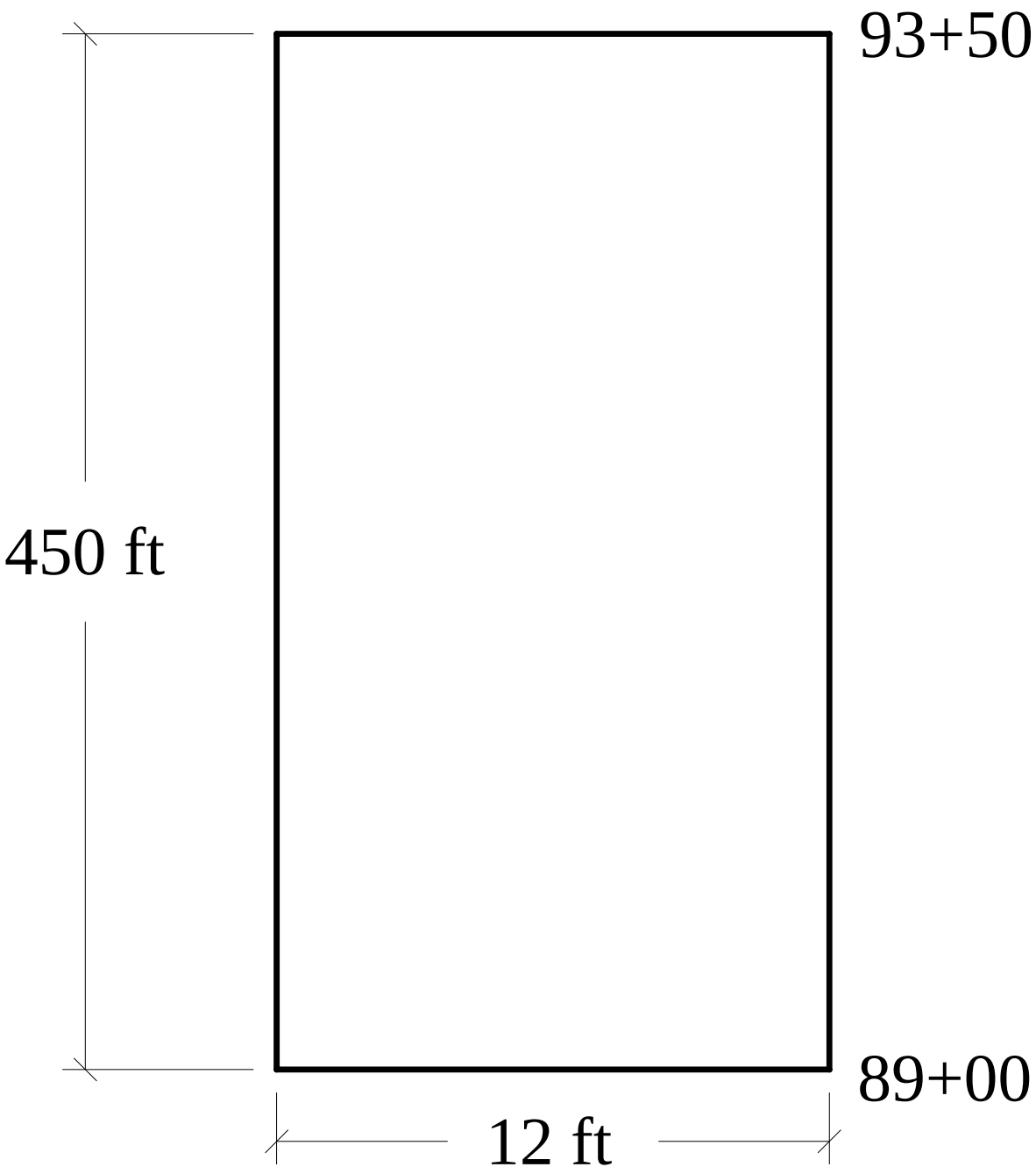

Section No. 5Eb

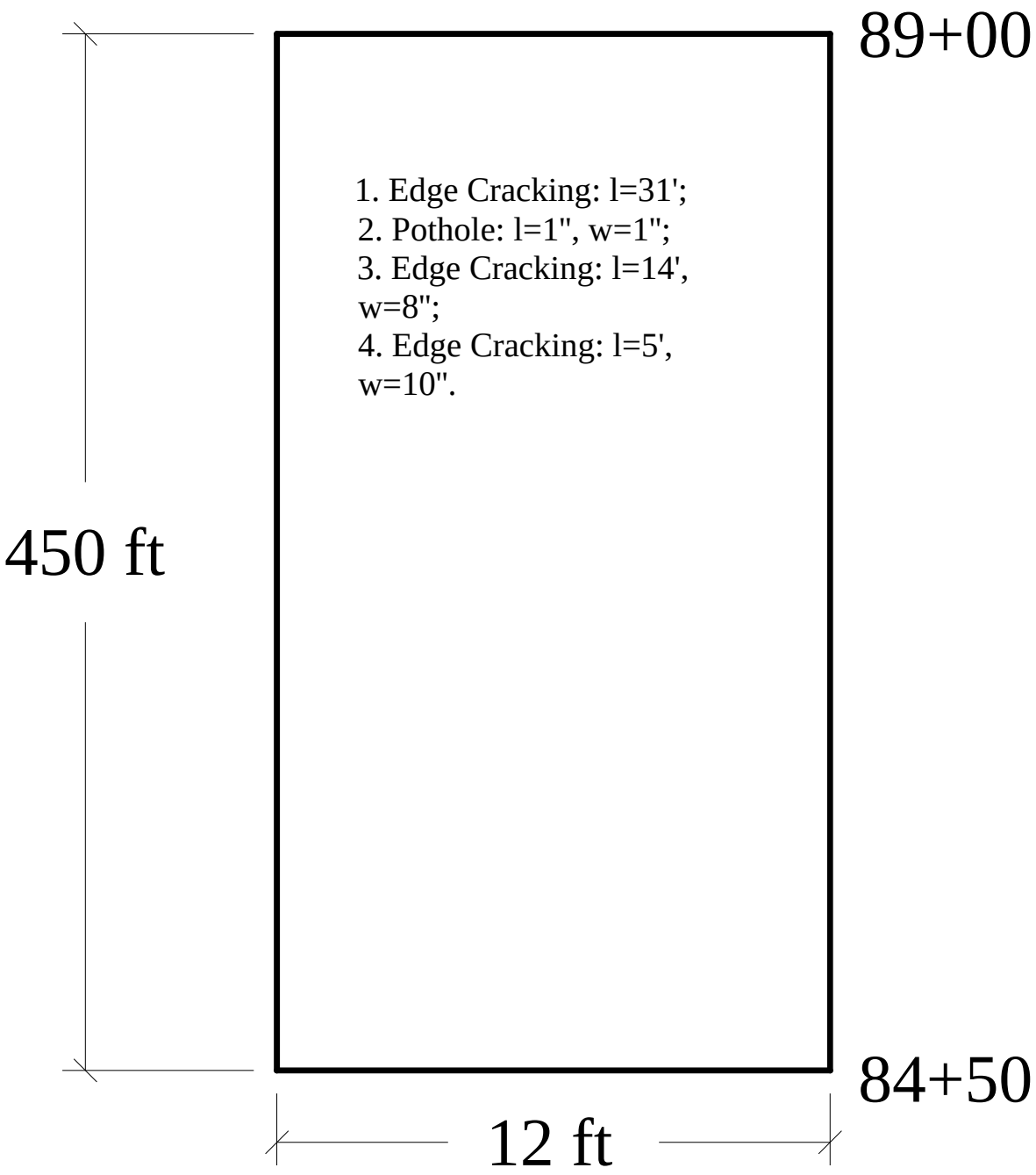

Section No. 6Eb

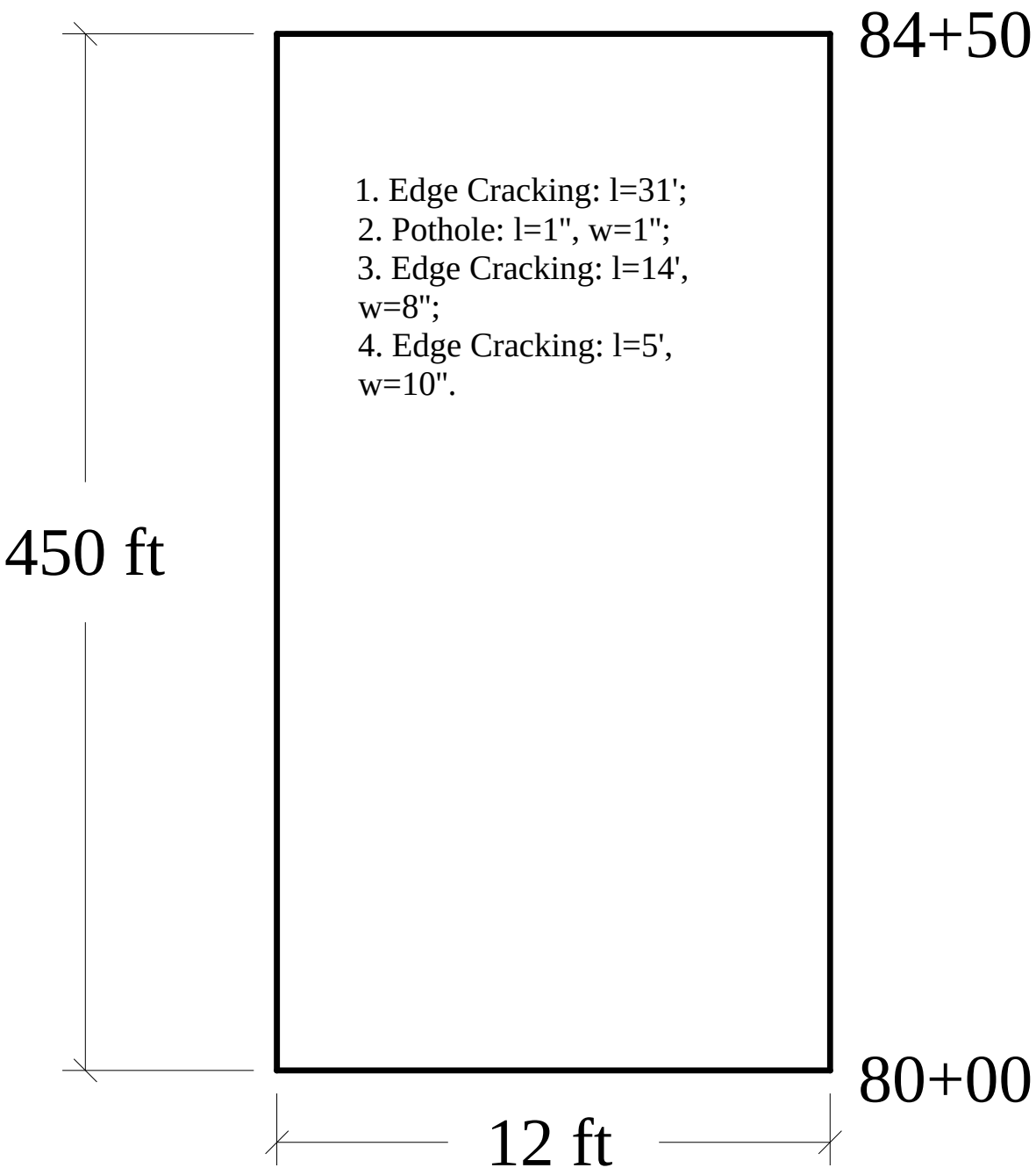

Appendix B

Appendix B.1

The following appendix includes the large pullout tests conducted to quantify the soil-geosynthetic interaction. The results of a series of 16 tests are provided here.

Table B.1: Testing matrix for large scale pullout testing

S.NO	GEOSYNTHETIC	TESTING DIRECTION	CONFINING MATERIAL	NORMAL LOAD	ABBREVATION
1	TENSAR	MD	Base course	1 psi	TMB1
2	TENSAR	XD	Base course	1 psi	TXB1
3	TENSAR	MD	Base course	3 psi	TMB3
4	TENSAR	XD	Base course	3 psi	TXB3
5	TENSAR	MD	Subgrade	1 psi	TMS1
6	TENSAR	XD	Subgrade	1 psi	TXS1
7	TENSAR	MD	Subgrade	3 psi	TMS3
8	TENSAR	XD	Subgrade	3 psi	TXS3
9	MIRAFI	MD	Base course	1 psi	MMB1
10	MIRAFI	XD	Base course	1 psi	MXB1
11	MIRAFI	MD	Base course	3 psi	MMB3
12	MIRAFI	XD	Base course	3 psi	MXB3
13	MIRAFI	MD	Subgrade	1 psi	MMS1
14	MIRAFI	XD	Subgrade	1 psi	MXS1
15	MIRAFI	MD	Subgrade	3 psi	MMS3
16	MIRAFI	XD	Subgrade	3 psi	MXS3

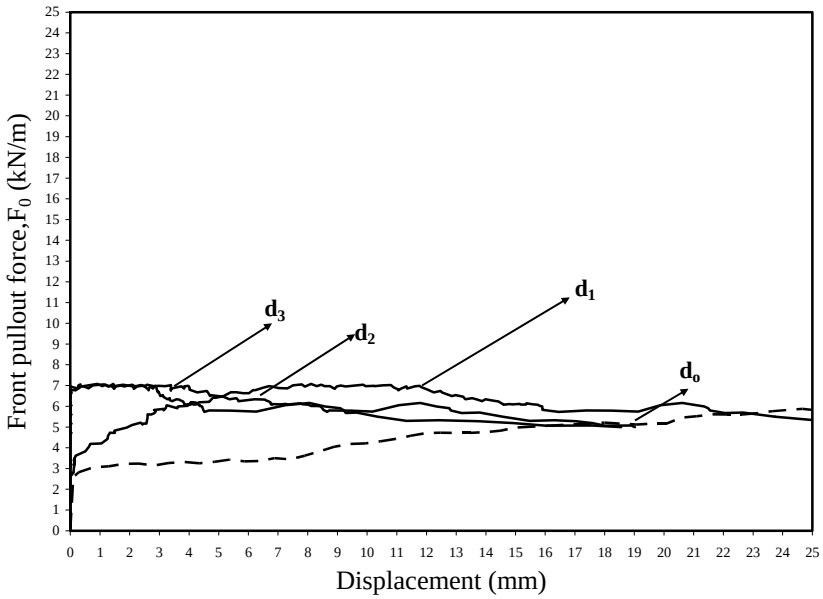

Figure B.1: Pullout test results for TMB1

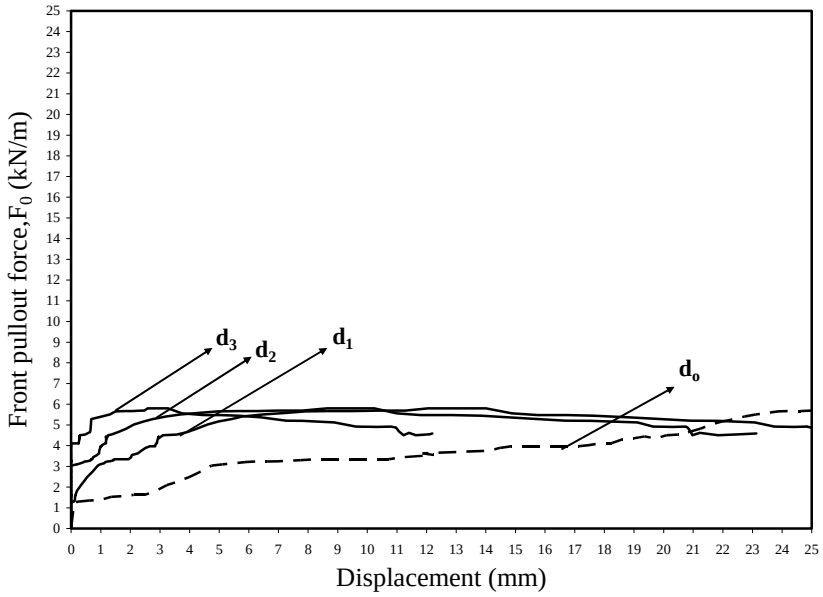

Figure B.2: Pullout test results for TXB1

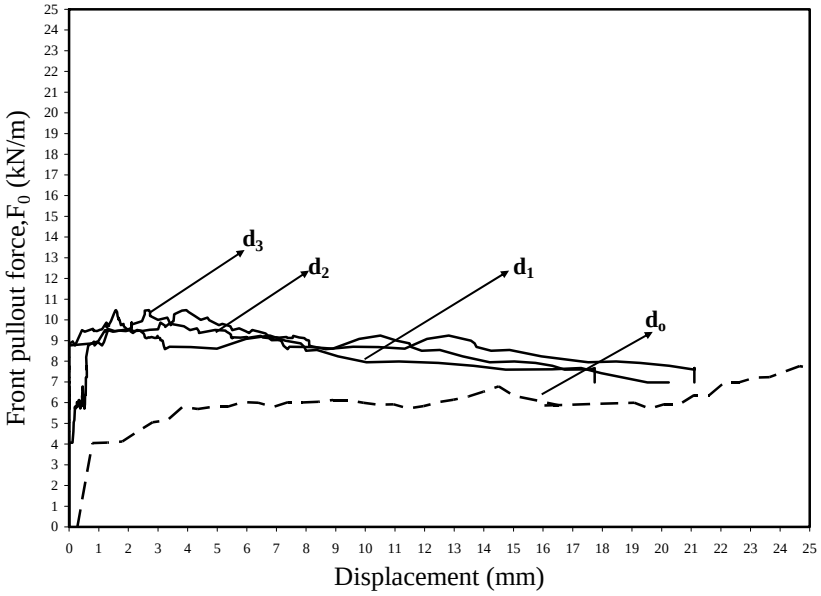

Figure B.3: Pullout test results for TMB3

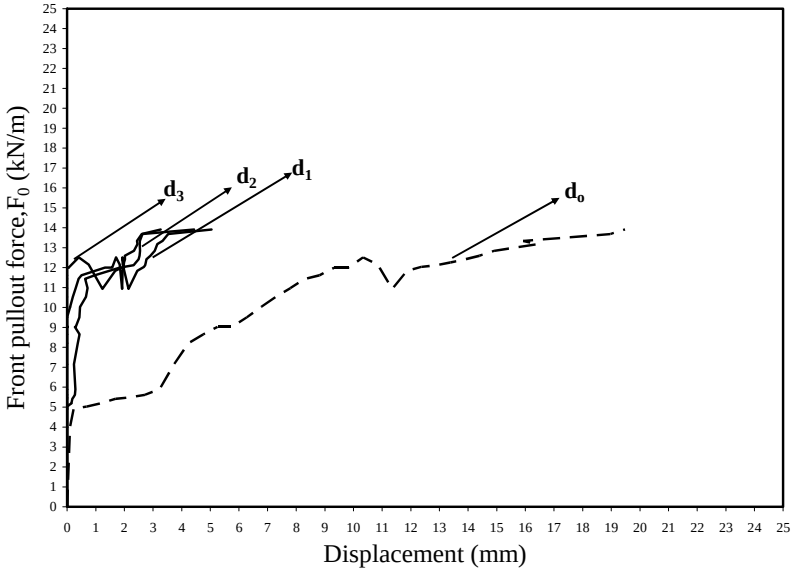

Figure B.4: Pullout test results for TXB3

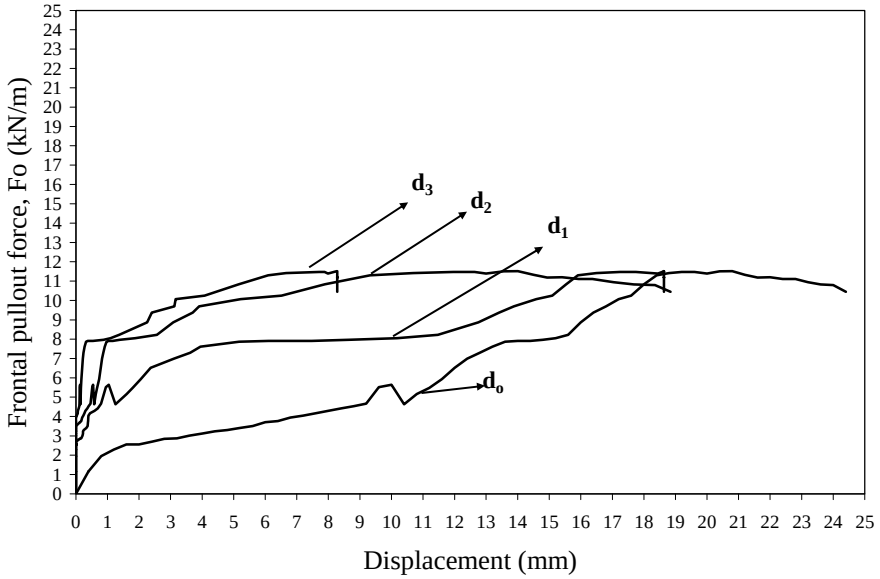

Figure B.5: Pullout test results for TMS1

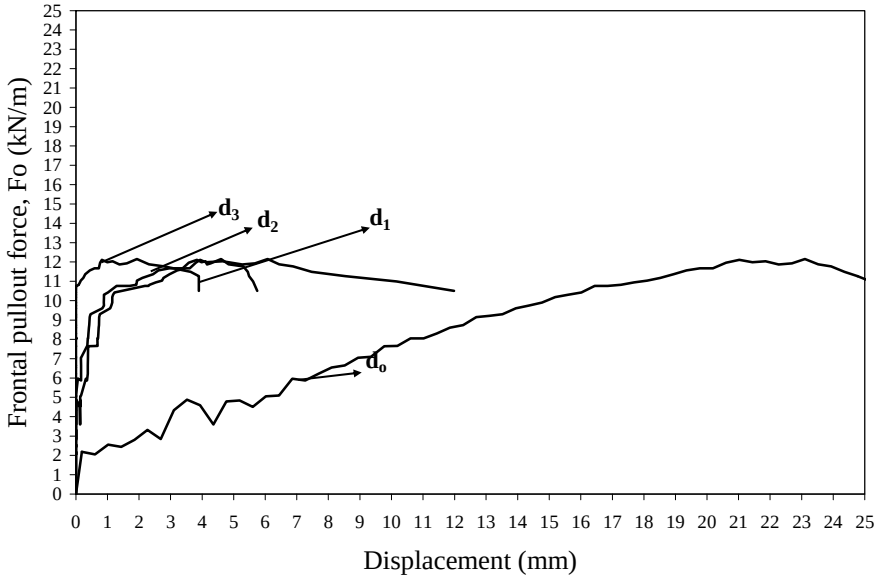

Figure B.6: Pullout test results for TXS1

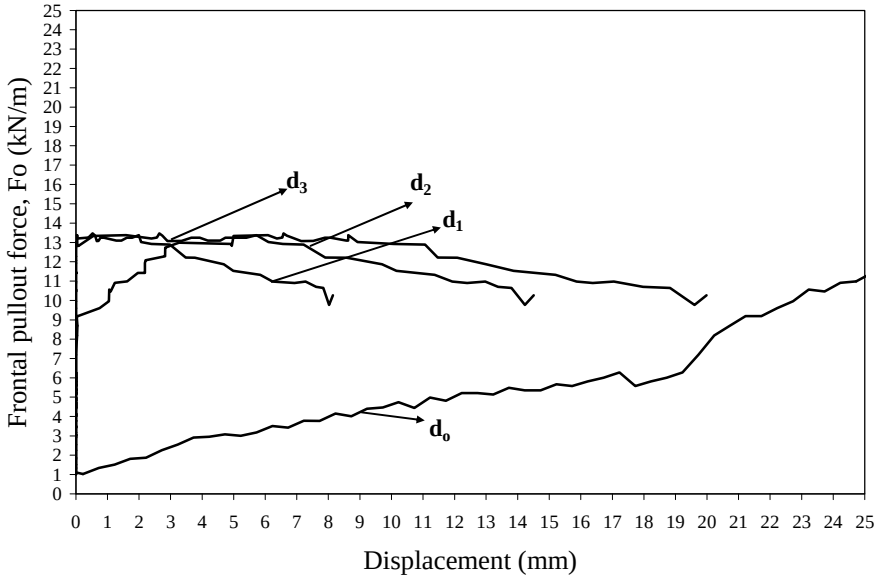

Figure B.7: Pullout test results for TMS3

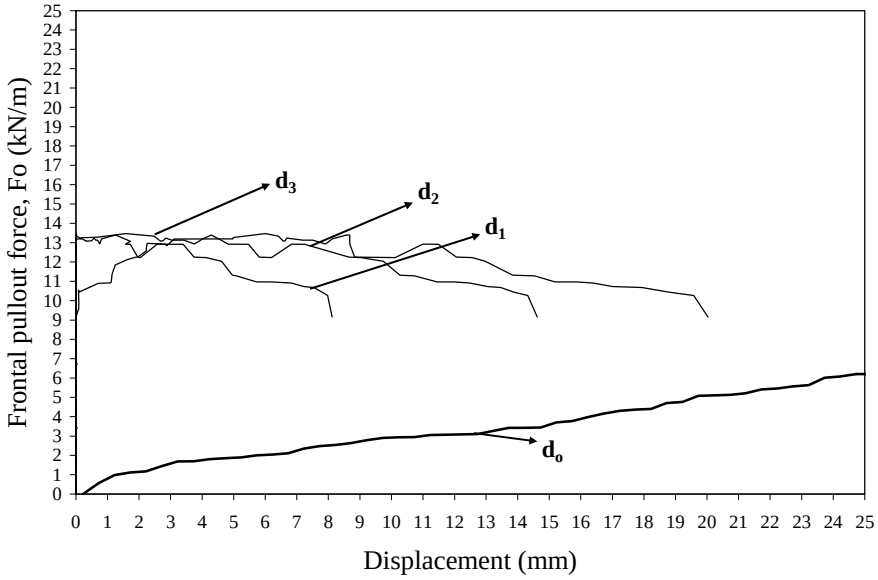

Figure B.8: Pullout test results for TXS3

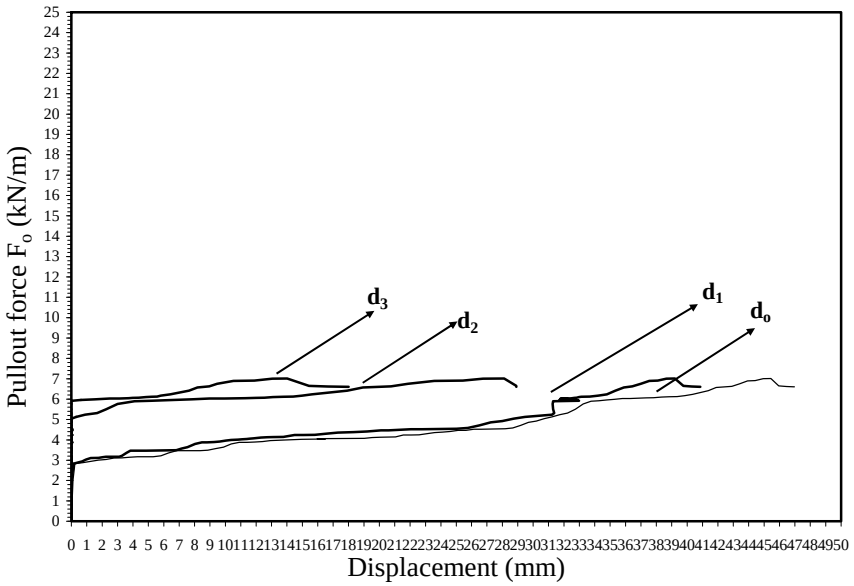

Figure B.9: Pullout test results for MMB1

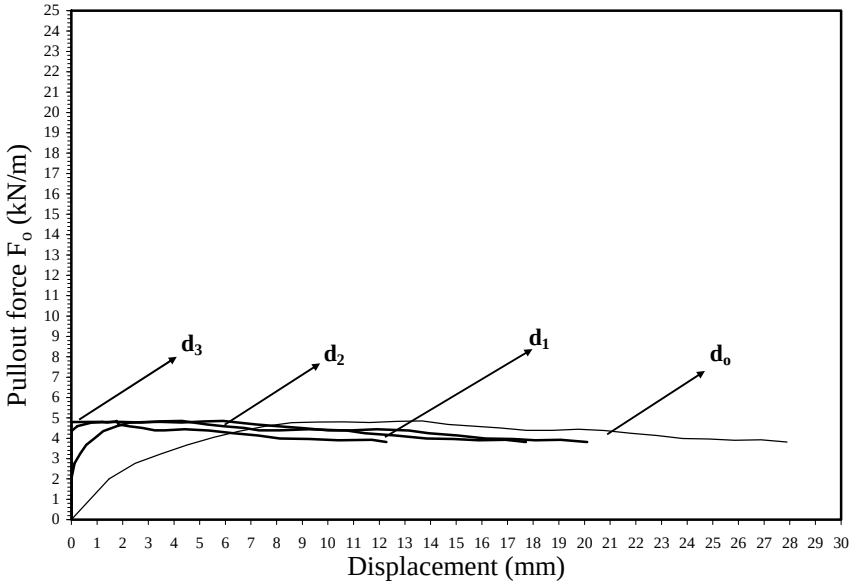

Figure B.10: Pullout test results for MXB1

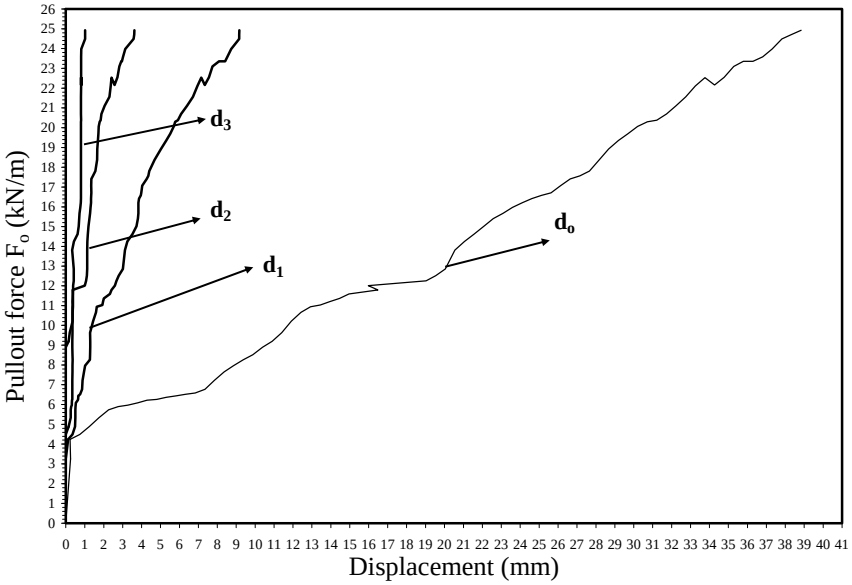

Figure B.11: Pullout test results for MMB3

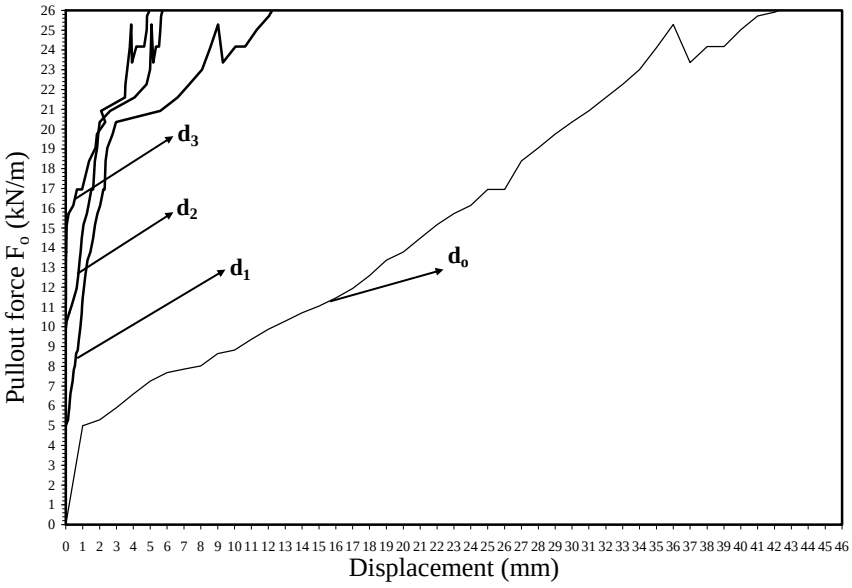

Figure B.12: Pullout test results for MXB3

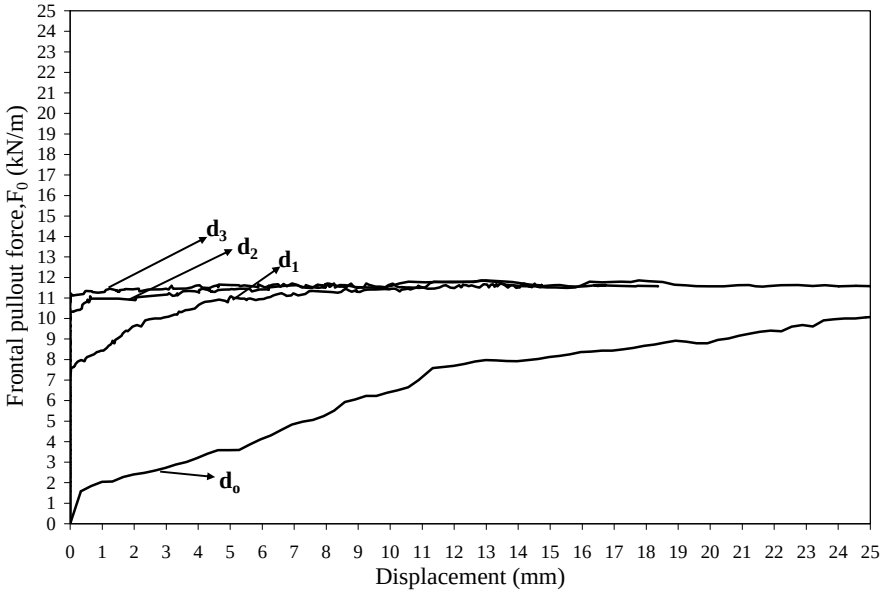

Figure B.13: Pullout test results for MMS1

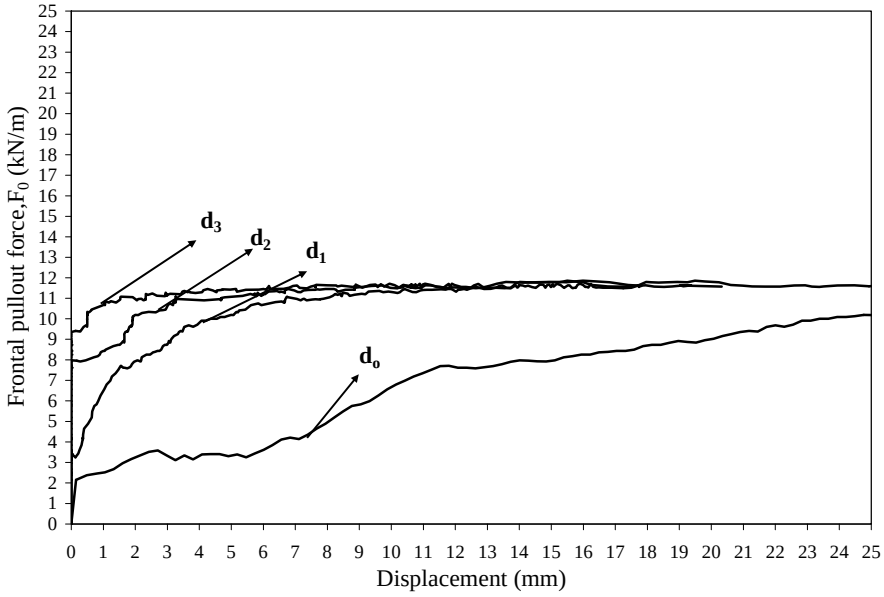

Figure B.14: Pullout test results for MXS1

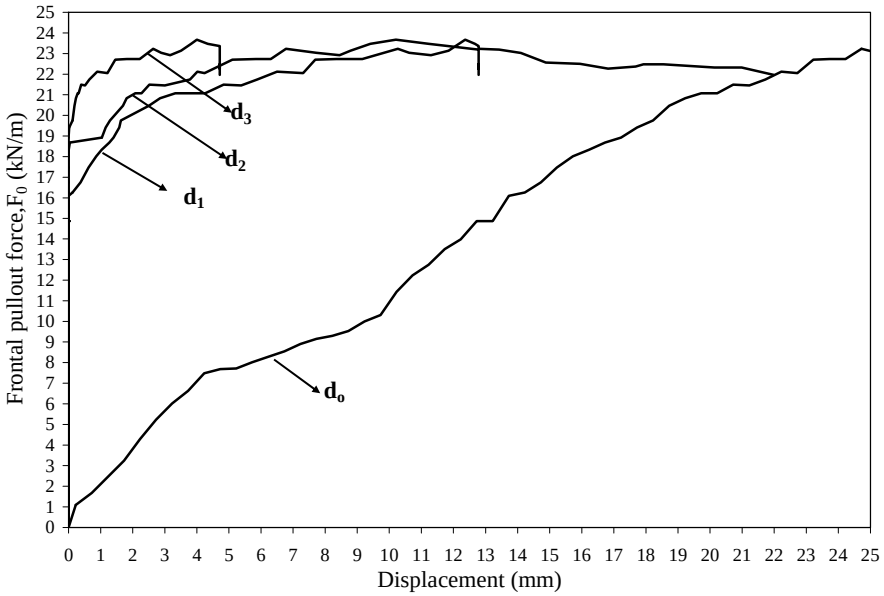

Figure B.15: Pullout test results for MMS3

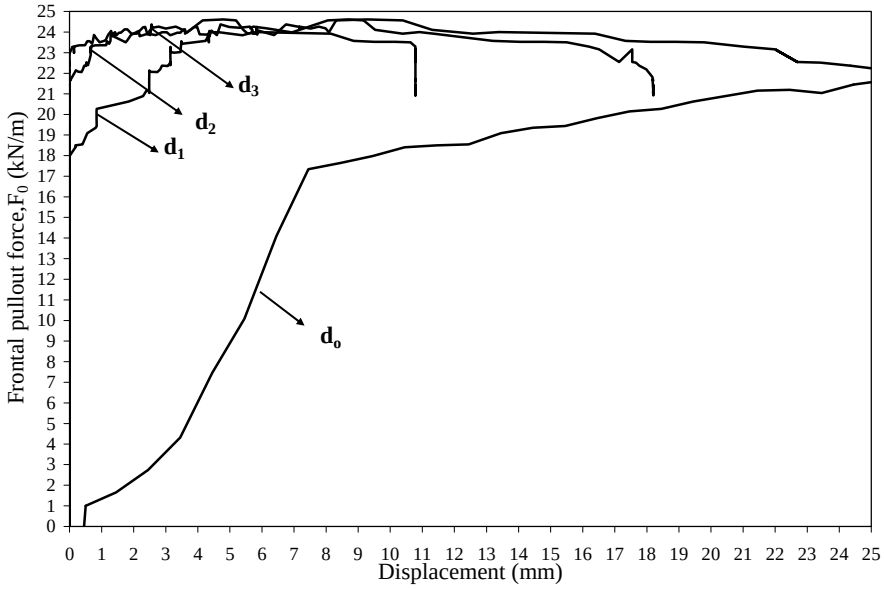

Figure B.16: Pullout test results for MXS3